

**Solution-Processing of Organic Solar Cells:  
From In Situ Investigation to Scalable Manufacturing**

Dissertation by  
Maged Abdelsamie

In Partial Fulfillment of the Requirements

For the Degree of  
Doctor of Philosophy

King Abdullah University of Science and Technology  
Thuwal, Kingdom of Saudi Arabia

© November, 2016

Maged Abdelsamie

All Rights Reserved

The dissertation of Maged Abdelsamie is approved by the examination committee.

Committee Chairperson: Professor Aram Amassian

Committee Member: Professor Husam Alshareef

Committee Member: Professor Omar F. Mohammed

Committee Member: Professor Pedro M. Da Costa

Committee Member: Professor Pierre M. Beaujuge

Committee Member: Professor Natalie Stingelin

**ABSTRACT****Solution-Processing of Organic Solar Cells:****From In Situ Investigation to Scalable Manufacturing**

Maged Abdelsamie

Photovoltaics provide a feasible route to fulfilling the substantial increase in demand for energy worldwide. Solution processable organic photovoltaics (OPVs) have attracted attention in the last decade because of the promise of low-cost manufacturing of sufficiently efficient devices at high throughput on large-area rigid or flexible substrates with potentially low energy and carbon footprints. In OPVs, the photoactive layer is made of a bulk heterojunction (BHJ) layer and is typically composed of a blend of an electron-donating (D) and an electron-accepting (A) materials which phase separate at the nanoscale and form a heterojunction at the D-A interface that plays a crucial role in the generation of charges. Despite the tremendous progress that has been made in increasing the efficiency of organic photovoltaics over the last few years, with power conversion efficiency increasing from 8% to 13% over the duration of this PhD dissertation, there have been numerous debates on the mechanisms of formation of the crucial BHJ layer and few clues about how to successfully transfer these lessons to scalable processes. This stems in large part from a lack of understanding of how BHJ layers form from solution. This lack of understanding makes it challenging to design BHJs and to control their formation in laboratory-based processes, such as spin-coating, let

alone their successful transfer to scalable processes required for the manufacturing of organic solar cells. Consequently, the OPV community has in recent years sought out to better understand the key characteristics of state of the art lab-based organic solar cells and made efforts to shed light on how the BHJ forms in laboratory-based processes as well as in scalable processes. We take the view that understanding the formation of the solution-processed bulk heterojunction (BHJ) photoactive layer, where crucial photovoltaic processes take place, is the one of the most crucial steps to developing strategies towards the implementation of organic solar cells with high efficiency and manufacturability. In this dissertation, we investigate the mechanism of the BHJ layer formation during solution processing from common lab-based processes, such as spin-coating, with the aim of understanding the roles of materials, formulations and processing conditions and subsequently using this insight to enable the scalable manufacturing of high efficiency organic solar cells by such methods as wire-bar coating and blade-coating. To do so, we have developed state-of-the-art in situ diagnostics techniques to provide us with insight into the thin film formation process. As a first step, we have developed a modified spin-coater which allows us to perform in situ UV-visible absorption measurements during spin coating and provides key insight into the formation and evolution of polymer aggregates in solution and during the transformation to the solid state. Using this method, we have investigated the formation of organic BHJs made of a blend of poly(3-hexylthiophene) (P3HT) and fullerene, reference materials in the organic solar cell field. We show that process

kinetics directly influence the microstructure and morphology of the bulk heterojunction, highlighting the value of in situ measurements. We have investigated the influence of crystallization dynamics of a wide-range of small-molecule donors and their solidification pathways on the processing routes needed for attaining high-performance solar cells. The study revealed the reason behind the need of empirically-adopted processing strategies such as solvent additives or alternatively thermal or solvent vapor annealing for achieving optimal performance. The study has provided a new perspective to materials design linking the need for solvent additives or annealing to the ease of crystallization of small-molecule donors and the presence or absence of transient phases before crystallization. From there, we have extended our investigation to small-molecule (p-DTS (FBTTh<sub>2</sub>)<sub>2</sub>) fullerene blend solar cells, where we have revealed new insight into the crucial role of solvent additives. Our work has also touched upon modern polymers, such as PBDTTPD, where we have found the choice of additives impacts the formation mechanism of the BHJ. Finally, we have performed a comparative study of the BHJ film formation dynamics during spin coating *versus* wire-bar coating of p-DTS(FBTTh<sub>2</sub>)<sub>2</sub>: fullerene blends that has helped in curbing the performance gap between lab-based and scalable techniques. This was done by implementing a new apparatus that combines the benefits of rapid thin film drying common to spin coating with scalability of wire-bar coating. Using the new apparatus, we successfully attain similar performance of solar cell devices to the ones fabricated by spin coating with dramatically reduced material waste.

## ACKNOWLEDGEMENTS

I would like to express my sincere appreciation to my advisor professor Aram Amassian for supporting me and providing guidance and constructive feedback that have shaped my research skills and views. I am grateful to him for the valuable scientific training throughout my Ph.D. I am thankful for his trust in me and encouraging me for taking challenges and creative thinking. I am thankful to professor McGehee for hosting me in his research lab and the scientific training provided by his group members that helped me to take the first steps in organic photovoltaics field. I am thankful to our collaborators, professors. Gui Bazan, Natalie Stingelin, Pierre Beaujuge and Iain Mcculloch, for their helpful discussions and contributing to my research by valuable experimental work from their groups. Special thanks to professor Gui Bazan for his valuable discussions and providing insightful feedback that helped the progress of our collaborative projects. I am grateful to professor Detlef Smilgies and Dr. Ruipeng Li for the training on X-ray scattering techniques and their guidance at the D1 beam-line at Cornell High Energy Synchrotron Source (CHESS).

I am thankful to my committee members, professors. Husam Alshareef, Omar F. Mohammed, Pedro M. Da Costa, Pierre Beaujuge and Natalie Stingelin, for taking the time to assess this work and provide helpful feedback.

I would like to thank my group mates, especially Ahmed Kirmani, for their advice and guidance throughout my Ph.D.

My deepest gratitude is to my family and my parents for the support and encouragements, especially my wife (Rokaia Mohamed) for sharing the journey with me.

## TABLE OF CONTENTS

Abstract.....	3
Acknowledgements.....	6
Table of contents.....	7
List of illustrations.....	9
List of Tables.....	18
<b>Chapter 1 Introduction</b> .....	<b>19</b>
<b>Chapter 2 Morphology development in bulk heterojunction organic photovoltaics: A literature review</b> .....	<b>26</b>
2.1 Organic semiconductors .....	26
2.2 Organic photovoltaics.....	30
2.3 Strategies for controlling the active layer morphology in BHJ solar cells .....	39
2.4 In situ monitoring and process diagnostics .....	52
<b>Chapter 3 Methodology and general description of the work</b> .....	<b>72</b>
3.1 Introduction .....	72
3.2 <i>In situ</i> characterization techniques .....	72
3.3 <i>Ex situ</i> characterization techniques .....	82
3.4 Solar cell devices fabrication and characterization .....	84
<b>Chapter 4 In situ UV-visible absorption during spin-coating of organic semiconductors: a new probe for organic electronics and photovoltaics</b> .....	<b>88</b>
4.1 Introduction .....	88
4.2 Design of the new spin coater setup for <i>in situ</i> UV-vis absorption measurements .....	90
4.3 Stages of thin film formation during spin coating .....	91
4.4 Neat P3HT in toluene for organic thin film transistors.....	93
4.5 P3HT:PC <sub>61</sub> BM blend in oDCB for organic solar cells .....	101
4.6 Conclusions .....	110
<b>Chapter 5 Roles of the donor crystallization dynamics and pathway on bulk heterojunction formation in small-molecule organic solar cells</b> .....	<b>112</b>
5.1 Introduction .....	112
5.2 Roles of the donor crystallization in small-molecule organic solar cells .....	114
5.3 The need of flash differential scanning calorimetry (F-DSC) for detecting the metastable phases.....	115
5.4 Liquid crystalline mesophase of p-DTS(FBTTh <sub>2</sub> ) <sub>2</sub> .....	119

5.5 Generalization of the relationship between the ease of crystallization of donor molecules and the need for additives .....	130
5.6 Conclusion .....	144
<b>Chapter 6 Impact of solvent additives on the mechanism of film formation in small-molecule bulk heterojunction solar cells.....</b>	<b>147</b>
6.1 Introduction.....	147
6.2 Effects of solvent additives on solar cell devices performance and BHJ morphology.....	149
6.3 Monitoring microstructure evolution during solution processing .....	156
6.4 Relative solubility of BHJ components/phases in DIO.....	164
6.5 Mechanism of the solvent additive effect on microstructure evolution .....	170
6.6 Conclusions.....	174
<b>Chapter 7 Polymer-fullerene bulk heterojunction solar cells: Role of solvent additives in fullerene aggregation.....</b>	<b>176</b>
7.1 Introduction.....	176
7.2 Effects of solvent additives on solar cell devices performance.....	178
7.3 Effects of solvent additives on the BHJ morphology .....	180
7.4 Effects of solvent additives on the carrier mobility.....	184
7.5 Monitoring microstructure evolution during solution processing .....	186
7.6 Mechanism of additive-mediated bulk heterojunction formation .....	199
7.7 Conclusions.....	203
<b>Chapter 8 Lessons for scalable processing of small-molecule bulk heterojunction solar cells while achieving microstructural and performance parity .....</b>	<b>206</b>
8.1 Introduction.....	206
8.2 Wire-bar coating and blade-coating of p-DTS(FBTTh <sub>2</sub> ) <sub>2</sub> :PC <sub>71</sub> BM films .....	208
8.3 Crystallization dynamics of p-DTS(FBTTh <sub>2</sub> ) <sub>2</sub> during wire-bar coating of p-DTS(FBTTh <sub>2</sub> ) <sub>2</sub> :PC <sub>71</sub> BM films.....	210
8.4 Introducing modified wire-bar coating.....	215
8.5 Conclusions.....	227
<b>Chapter 9 Conclusions and Future Work.....</b>	<b>229</b>
9.1 Summary.....	229
9.2 Future work .....	237
<b>Bibliography.....</b>	<b>239</b>



## LIST OF ILLUSTRATIONS

<b>Figure 2.1</b> Molecular structures of organic semiconductor materials (small-molecules and medium-size molecules on the top, polymers on the bottom).....	29
<b>Figure 2.2</b> Schematics represent organic photovoltaics architecture in bilayer and BHJ configuration in (a) & (b), respectively. Donor and acceptor phases are represented in dark green and red, respectively. ....	33
<b>Figure 2.3</b> (a) & (b) Simplified schematics represent the main processes for light harvesting into electricity in organic BHJ photovoltaics. ....	37
<b>Figure 2.4</b> Schematic represents the possible pathways for free charge carriers generation from excited states (left) to separated states (right). ....	37
<b>Figure 2.5</b> Schematic representing the J-V characteristic of solar cell devices and the associated figures of merit, including $J_{sc}$ , $V_{oc}$ , FF and PCE. ....	39
<b>Figure 2.6</b> (a) & (b) Schematics represent integrated knife coater with drying setup and laser reflectometry setup, respectively. Photovoltage vs time measured <i>in situ</i> during blade-coating of at 15 °C and air speed of 0.1 and 0.5 m/s in (c) and (d) respectively. (e) Calculated time-dependent film thickness from (c) and (d). ....	54
<b>Figure 2.7</b> Normalized specular interference and off-specular light scattering during spin coating of PDPP5T: PC <sub>70</sub> BM from pure CF (blue) and CF with 5 vol% oDCB (red) in (a) & (b), respectively. (c) Schematic represents the role of co-solvent preventing large-scale liquid-liquid phase separation by inducing early polymer aggregation at high solvent contents. <sup>[24]</sup> .....	57
<b>Figure 2.8</b> (a) The thickness evolution of a P3HT:PCBM blend film as a function of time for blade coating blend films from CB onto a substrate held at a temperature of 30, 40 and 50 °C. ( b) Replot the data shown in (a) for 30 °C substrates with showing the three stages of film formation. (c) The evolution of extinction coefficient (k) at specific wavelengths during drying for 30 °C sample.....	59
<b>Figure 2.9</b> Time evolution of $\lambda_{max}$ during blade coating of P3HT:PCBM from various solvents. ...	60
<b>Figure 2.10</b> Absorption spectra in the (a) 250-300 nm range and (b) 600-900 nm range as a function of time after spin-coating for 10 s at 2000 rpm from TCB with 2% DIO in 90 s intervals (black and blue) and then 10 min intervals (red).....	62
<b>Figure 2.11</b> (a) Normalized Raman spectrum of P3HT: PCBM films before and after solvent vapor annealing. (b) Time evolution of the FWHM of symmetric C=C stretching mode of P3HT (at 1440 cm <sup>-1</sup> ) during solvent vapor annealing of pure P3HT and P3HT: PCBM. ....	64
<b>Figure 2.12</b> FWHM of symmetric C=C stretching mode of P3HT versus temperature obtained by in situ Raman spectroscopy during heating and cooling cycles of of P3HT: PCBM films in (a) and static Raman at room temperature of annealed samples as a function of annealing temperature in (b). ....	65
<b>Figure 2.13</b> (a) Normalized GIWAXS and GISAXS scattering intensities as a function of the spinning time during spin-coating of P3HT: PCBM (62.5 wt%:37.5 wt%) on the top and time-	

resolved thickness for the same sample on the bottom. (b) The onset of film formation ( $t_{\text{onset}}$ ) and its duration ( $\Delta t_{\text{formation}}$ ) for different P3HT:PCBM blend ratios.....	67
<b>Figure 2.14</b> (a) Evaluation of total scattered intensities from the alkyl stacking peak (blue) and the amorphous region (red) versus time after spin coating of PCPDTBT:PC70BM from CB containing 3% ODT. (b) Time-evolution of the peak position of the (100) peak (blue) and the (100)' peak (red) of the same sample in (a). (c) Schematic represents the morphology of PCPDTBT:PC <sub>70</sub> BM with and without additives. ....	69
<b>Figure 3.1</b> Schematic represents the interaction of an incident linearly polarized light with a sample.....	74
<b>Figure 3.2</b> (a) Simplified schematic represents the scattering experiment; diffraction peak appear when the reciprocal-space of a crystal (black dot) intersects the Ewald sphere. (b) Schematic represents GIWAXS experiments; scattering is collected by 2D detector. $q_z$ and $q_{xy}$ correspond to the scattering in the out-of-plane and in-plane directions, respectively. $\alpha_i$ , $\theta_f$ and $\alpha_f$ correspond to incident angle, out-of-plane scattering angle and in-plane scattering angle, respectively.....	78
<b>Figure 3.3</b> Schematics represent 2D GIWAXS scattering of crystallites at different orientations. The crystallites are represented as red lines corresponding to crystallographic planes with spacing ( $d$ ) between the planes. (a-d) Crystallites with crystallographic planes: (a) oriented parallel to the substrate, (b) oriented in both directions, parallel and vertical to the substrates, (c) oriented with an angular distribution around the horizontal alignment, and (d) randomly oriented crystallites. Schematics are adapted from reference .....	81
<b>Figure 3.4</b> (a) Schematics of the devices structure for electron-only and hole-only devices. (b) Illustration of MIS-CELIV extraction currents transients. ....	87
<b>Figure 4.1</b> Schematic represents the newly developed spin coater combined with in situ UV-vis absorption. An actual photo of the setup is shown in the inset of the figure.....	91
<b>Figure 4.2</b> (a) Time resolved <i>in situ</i> UV-vis absorbance spectra obtained during spin-coating of P3HT:PCBM (1 : 1) blend solution in o-DCB at 900 rpm for 120 s. (b) Time evolution of absorption intensity at the solution peak (460 nm) and at the aggregation peaks ( (0-1) at 550 nm and (0-0) at 605 nm. ....	92
<b>Figure 4.3</b> Time resolved <i>in situ</i> UV-vis absorbance spectra obtained during spin-coating of (a) a well-dissolved solution of P3HT in warm toluene (stirred overnight at 65 °C) and spin coated at 900 rpm for 30 seconds, (b) a pre-aggregated solution of P3HT in toluene (stirred overnight at room temperature) and spin coated at 900 rpm for 30 s. (c) Time evolution of the aggregation peak ( $\lambda = 605$ nm, namely 0-0 transition) during spin-coating for the well-dissolved and pre-aggregated solutions. (d) Time evolution of solution and film thickness.....	95
<b>Figure 4.4</b> Absorption spectra of P3HT subjected to Spano model analysis for dry films coated from (a) well-dissolved P3HT in toluene and (b) pre-aggregated P3HT in toluene.....	96
<b>Figure 4.5</b> Transfer characteristics of top-contact, bottom gate OFET devices [ $(I_D)^{1/2} - V_G$ ]. ....	99

- Figure 4.6** Atomic force microscopy (AFM) and transmission electron microscopy (TEM) micrographs for P3HT thin films prepared from a pre-aggregated P3HT solution (a and b) and a well dissolved P3HT solution (c and d), respectively. The insets of (b) and (c) show selected area electron diffraction (SAED) patterns for the same samples. The normalized intensity line scans obtained from the SAED images are plotted in (e)..... 100
- Figure 4.7** (a) Time evolution of solution and film thickness during spin coating of P3HT: PC<sub>61</sub>BM (1 : 1) blends in different processing conditions. Spin coating of the solution of P3HT:PC<sub>61</sub>BM (1:1) in o-DCB was performed at 900 rpm for 45 s (black), 900 rpm for 120 s (red) and 1200 rpm for 120 s (blue). (b) & (c) Time evolution of absorption at the solution peak (460 nm) and at the intermolecular aggregation peak (605 nm), respectively..... 102
- Figure 4.8** (a) Absorption spectra of the dried films normalized to the PC<sub>61</sub>BM absorption peak (at 330 nm). The inset in (a) shows the actual absorption spectra of the dried films. Absorption spectra of P3HT subjected to Spano model analysis for P3HT: PC<sub>61</sub>BM dry films coated from oDCB at 1200 rpms for 120 s in (b), at 900 rpms for 120 s in (c) and 900 rpms for 45 s in (d). Absorption spectra of P3HT were obtained by subtraction of PC<sub>61</sub>BM absorption from P3HT:PCBM (1:1) absorption. .... 105
- Figure 4.9** (a) J–V characteristics of P3HT:PCBM BHJ solar cells fabricated from coated films at 900 rpm for 45 s (black), 900 rpm for 120 s (red) and 1200 rpm for 120 s (blue). (b) External quantum efficiency (EQE) spectra for these devices. .... 107
- Figure 4.10** Atomic force micrographs and transmission electron micrographs, respectively, of P3HT:PC<sub>61</sub>BM blend thin films spin-cast at (a, b) 900 rpm for 45 s, (c, d) 900 rpm for 120 s and (e, f) 1200 rpm for 120 s, respectively. Selected area electron diffraction (SAED) showing the (020) diffraction ring of P3HT are shown as insets in the respective electron micrographs. The corresponding normalized intensity line scan profiles are shown in (g). .... 109
- Figure 5.1** Molecular structure of the materials in the study. .... 114
- Figure 5.2.** (a-c) UV-Vis absorption spectra of solution (dark curve) and dry film (red curve) of neat p-DTS(FBTTh<sub>2</sub>)<sub>2</sub> [T1] in (a), p-SIDT(FBTTh<sub>2</sub>)<sub>2</sub> [H1] in (b) and X2 in (c). (d-f) Time evolution of absorption at the vibronic peak marked by the black arrows in (a-c), which corresponds to an absorption characteristic of the photo-physical aggregates. The start and end of aggregation during film formation are marked by red and blue arrows, respectively..... 118
- Figure 5.3.** Heating thermograms at rate (100 K s<sup>-1</sup>) of p-DTS(FBTTh<sub>2</sub>)<sub>2</sub> (black), p-SIDT(FBTTh<sub>2</sub>)<sub>2</sub> (red) and X2 (blue). The onset of melting for the three molecules is marked as asterisk. .... 119
- Figure 5.4** Differential scanning calorimetry thermograms of p-DTS(FBTTh<sub>2</sub>)<sub>2</sub> at different heating (a) and cooling (b) rates revealing the liquid crystalline nature of the molecule. .... 121
- Figure 5.5** Cross-polarized transmission optical microscopy (X-POM) of neat p-DTS(FBTTh<sub>2</sub>)<sub>2</sub> film cast from CB in (a), p-DTS(FBTTh<sub>2</sub>)<sub>2</sub> :PC<sub>71</sub>BM film cast from CB in (b) and CB with 1.5% DIO in (c). .... 123

- Figure 5.6** Cross-polarized transmission optical microscopy (XPOM) of neat p-DTS(FBTTh<sub>2</sub>)<sub>2</sub> film during heating on top and cooling in bottom. Differential scanning calorimetry thermograms during heating and cooling in the middle. .... 124
- Figure 5.7** Time evolution of p-DTS(FBTTh<sub>2</sub>)<sub>2</sub> crystallization from LC phase. (a) 2D plot of GIWAXS of neat p-DTS(FBTTh<sub>2</sub>)<sub>2</sub> as cast from pure CB (LC phase) on left, after 7 days (crystal phase) on right and time resolved integrated intensity of GIWAXS measurements over days on the middle. (b) 2D image plots of GIWAXS of p-DTS(FBTTh<sub>2</sub>)<sub>2</sub> film cast from CB soaked for two days after casting at incident angle 0.04° (below critical angle of X-ray beam) on left , 0.15° (above critical angle of X-ray beam) on right and integrated scattering intensity of GIWAXS performed at different incident angles on the middle. .... 126
- Figure 5.8** *In situ* 2D GIWAXS image plots (Integrated scattering intensity is shown in logarithmic color scale versus  $q$  (nm<sup>-1</sup>) and time(s)) of spin-casting neat p-DTS(FBTTh<sub>2</sub>)<sub>2</sub> and p-DTS(FBTTh<sub>2</sub>)<sub>2</sub>:PC<sub>71</sub>BM blends form CB with 0.4 % DIO, in (a) and (b), respectively..... 128
- Figure 5.9** (a) Energy-filtered transmission electron micrographs (EFTEM) with elemental mappings of carbon (284 eV) and sulfur (165 eV) performed on the plan-view of p-DTS(FBTTh<sub>2</sub>)<sub>2</sub>:PC<sub>71</sub>BM film, coated from CB with 1.5% DIO. (b) Composite color image of EF-TEM image in (a). Red and green colors represent carbon rich phase [PC<sub>71</sub>BM], sulfur rich phase [p-DTS(FBTTh<sub>2</sub>)<sub>2</sub>], respectively..... 129
- Figure 5.10** Differential scanning calorimetry thermograms at different heating (a) and cooling (b) rates of p-SIDT(FBTTh<sub>2</sub>)<sub>2</sub> . .... 132
- Figure 5.11** Differential scanning calorimetry thermograms at different heating (a) and cooling (b) rates of X2..... 134
- Figure 5.12** Heating and cooling thermograms at rate (100 K s<sup>-1</sup>) of p-SIDT(FBTTh<sub>2</sub>)<sub>2</sub>, X2, and p-DTS(FBTTh<sub>2</sub>)<sub>2</sub>. .... 135
- Figure 5.13** Integrated intensity of alkyl stacking peak derived from *in situ* GIWAXS during spin coating of the three molecules blends with PC<sub>71</sub>BM; p-SIDT(FBTTh<sub>2</sub>)<sub>2</sub>:PC<sub>71</sub>BM from CB and CB with 0.4% DIO in (a), p-DTS(FBTTh<sub>2</sub>)<sub>2</sub>:PC<sub>71</sub>BM from CB and CB with 0.4% DIO in (b) and X2: PC<sub>71</sub>BM from CF and CF with 0.4% DIO in (c). The thickness of the coated film in (a), (b) and (c) is ~ 100 nm, ~ 103 nm and ~ 108 nm, respectively. .... 137
- Figure 5.14** 2D GIWAXS image plots of as cast p-SIDT(FBTTh<sub>2</sub>)<sub>2</sub>:PC<sub>71</sub>BM film from CB in (a) and CB with 0.4% DIO in (c). Time evolution of integrated scattering intensity of *in situ* GIWAXS performed during spin coating of p-SIDT(FBTTh<sub>2</sub>)<sub>2</sub>:PC<sub>71</sub>BM from CB in (b) and CB with 0.4% DIO in (d). .... 138
- Figure 5.15** 2D GIWAXS image plots of as cast p-DTS(FBTTh<sub>2</sub>)<sub>2</sub>:PC<sub>71</sub>BM film from CB in (a) and CB with 0.4% DIO in (c). Time evolution of integrated scattering intensity of *in situ* GIWAXS performed during spin coating of p-DTS(FBTTh<sub>2</sub>)<sub>2</sub>:PC<sub>71</sub>BM from CB in (b) and CB with 0.4% DIO in (d). .... 139

- Figure 5.16** 2D GIWAXS image plots of as cast X2:PC<sub>71</sub>BM film from CF in (a) and CF with 0.4% DIO in (c). Time evolution of integrated scattering intensity of *in situ* GIWAXS performed during spin coating of X2:PC<sub>71</sub>BM from CF in (b) and CF with 0.4% DIO in (d). ..... 140
- Figure 5.17** (a) Current density-voltage (J-V) characteristics of two champion solar cells, both exhibiting PCE = 7.6%, fabricated using X2:PC<sub>71</sub>BM blend spin-cast from pure chloroform (open circles) and from chloroform with 0.4 % DIO (solid circles). (b) & (c) Composite color image of energy-filtered transmission electron micrographs (EFTEM) with elemental mappings of carbon (284 eV) and sulfur (165 eV) performed on the plan-view of X2:PC<sub>71</sub>BM film coated from CF (b) and CF with 0.4 % DIO (c). The film thicknesses in (a) and (b) are ~ 108 nm and ~ 109 nm respectively. Green and red colors represent sulfur rich phase [X2] and carbon rich phase [PC<sub>71</sub>BM], respectively. .... 143
- Figure 6.1** Current density- Voltage (J-V) curves of solar cell devices fabricated from p-DTS(FBTTh<sub>2</sub>)<sub>2</sub>:PC<sub>71</sub>BM blends cast from pure CB (black), CB with 0.4% DIO (red), and CB with 1.0% DIO (blue). ..... 149
- Figure 6.2** Cross-polarized optical microscopic (X-POM) images of p-DTS(FBTTh<sub>2</sub>)<sub>2</sub>:PC<sub>71</sub>BM films cast from CB in (a), CB & 0.4% DIO in (b) and CB & 1.0% DIO in (c). Composite color images of EF-TEM with elemental mappings of carbon (284 eV) (red) and sulfur (165 eV) (green) performed on the plan-view of p-DTS(FBTTh<sub>2</sub>)<sub>2</sub> : PC<sub>71</sub>BM film coated from CB in (d), CB & 0.4% DIO in (e) and CB & 1% DIO in (f). ..... 151
- Figure 6.3** (a) External quantum efficiency of solar cell devices fabricated from p-DTS(FBTTh<sub>2</sub>)<sub>2</sub>:PC<sub>71</sub>BM blends cast from pure CB (black), CB with 0.4% DIO (red), and CB with 1.0% DIO (blue). Fitting of the charge transfer (CT) states intensity is shown in dashed lines for the three cases. (b) The electronic coupling term (f) versus DIO content calculated from fitting CT states in (a)..... 153
- Figure 6.4** (a) The thickness evolution during and thereafter spin-coating p-DTS(FBTTh<sub>2</sub>)<sub>2</sub>:PC<sub>71</sub>BM from CB solution and with different DIO content (0.4% and 1%). (b) The calculated retained solvent in the “wet” film during and thereafter spin-coating for the three cases in (a). ..... 157
- Figure 6.5** Time-resolved UV-vis absorption color plot (absorption intensity is shown as logarithmic color scale versus wavelength ( $\lambda$ ) and time (s)) of coating p-DTS(FBTTh<sub>2</sub>)<sub>2</sub> : PC<sub>71</sub>BM from CB in (a) , CB with 0.4 % DIO in (b) and CB with 1.0 % DIO in (c). ..... 159
- Figure 6.6** (a) UV-vis absorption spectra of as cast dry films of p-DTS(FBTTh<sub>2</sub>)<sub>2</sub>:PC<sub>71</sub>BM coated from CB (black), CB with 0.4 % DIO (red) and CB with 1.0 % DIO (blue). (b) The vibronic ratio with respect to time for the donor represented as the ratio of absorption at  $\lambda_2 = 682$  nm and  $\lambda_1 = 625$  nm for the three formulations. The point at which CB is removed is indicated by a black asterisk and the saturation of photo-physical aggregation in the presence of DIO is marked with red asterisks. .... 161

- Figure 6.7** (a) *In situ* GIWAXS color image plot (Integrated scattering intensity is shown in logarithmic color scale versus  $q$  ( $\text{nm}^{-1}$ ) and time(s)) of casting p-DTS(FBTTh<sub>2</sub>)<sub>2</sub>: PC<sub>71</sub>BM from CB in (a) , CB with 0.4 % DIO in (b) and CB with 1.0 % DIO in (c). ..... 162
- Figure 6.8** UV-Vis absorption spectra of PC<sub>71</sub>BM: PMMA (40: 60) in solution and solid state (normalized to PC<sub>71</sub>BM absorption peak ( $\lambda_1 = 465$  nm)). (b) Time-evolution of PC<sub>71</sub>BM aggregation as represented by the ratio of absorption peak intensities at  $\lambda_2 = 550$  nm and  $\lambda_1$  during spin-coating of a PC<sub>71</sub>BM: PMMA blend. In all experiments reported here, spin-coated lasted 60 seconds, while *in situ* measurements were performed for at least one hour..... 164
- Figure 6.9** (a) Schematic figure represents drop-spin experiment in which DIO is dropped on a dry film followed by spinning the sample, while acquiring UV-vis absorption measurements. Spin coating was done at two steps; initially at low speed (600 rpms) for 20 s in order to achieve uniform distribution of DIO followed by spinning at 1750 rpms for 5 min. UV-vis absorption of as cast and DIO treated films of neat p-DTS(FBTTh<sub>2</sub>)<sub>2</sub> prepared from CB in (b) and CB with 0.4 % DIO in (c). In the inset of figure (b), GIWAXS of as cast film from CB and after treatment indicates the transformation of the liquid crystal phase to crystal phase upon treatment with DIO. UV-vis absorption of as cast and DIO treated films of p-DTS(FBTTh<sub>2</sub>)<sub>2</sub>:PC<sub>71</sub>BM prepared from CB in (d) and CB with 0.4 % DIO in (e). (f) Schematic summarizing the solubility of different components of the BHJ in DIO relatively. .... 167
- Figure 6.10** Time evolution of the relative absorption intensity at the two vibronic peaks, V2 (at 682 nm) and V1 (at 625 nm), of the drop-spin experiment on neat p-DTS(FBTTh<sub>2</sub>)<sub>2</sub> films in (a) and p-DTS(FBTTh<sub>2</sub>)<sub>2</sub>: PC<sub>71</sub>BM films in (b). Initial values of the as cast films are shown as black triangle (CB) and red triangle (CB & 0.4% DIO) at  $t=0$  and dashed line for comparison..... 169
- Figure 6.11** Schematic representation of thin film microstructure just after evaporation of the process solvent (CB) in two scenarios of DIO content (0.4% and 1%). The top row shows a molecular-level view of the LC to crystal transformation accompanied by segregation of PCBM and p-DTD(FBTTh<sub>2</sub>)<sub>2</sub> phases in the presence of DIO. The middle and bottom rows show a more microscale picture of crystallization of the as-cast LC phase (LC disclinations shown for illustration purposes) of p-DTD(FBTTh<sub>2</sub>)<sub>2</sub> and its phase separation from PC<sub>71</sub>BM for low (0.4%) and high (1%) DIO content scenarios. The aggregation and phase separation processes are both faster and more complete in the presence of large amounts of DIO, and tend to promote formation of microscale fibrils of p-DTD(FBTTh<sub>2</sub>)<sub>2</sub>..... 173
- Figure 7.1** Molecular structure of the materials in the study. .... 178
- Figure 7.2** Current density- Voltage (J-V) curves of solar cell devices fabricated from PBDTPD: PC<sub>71</sub>BM blends processed from pure CB (black), CB with 5% CN (red), and CB with 5% OT (blue). ..... 179
- Figure 7.3** TEM images of PBDTPD : PC<sub>71</sub>BM films coated from: (a) CB, (b) CB with 5% CN, and (c) CB with 5% OT. Composite color images of EF-TEM with elemental mappings of carbon (284 eV) (red) and sulfur (165 eV) (green) performed on the plan-view of PBDTPD : PC<sub>71</sub>BM films

- coated from; (d) CB, (e) CB with 5% CN, and (f) CB with 5% OT. EF-TEM in (f) was performed on the marked area with red square in the inset of the figure (f)..... 181
- Figure 7.4** (a-c) 2D GIWAXS plot of PBDTTPD: PC<sub>71</sub>BM films coated from; (a) pure CB, (b) CB with 5% CN, and (c) CB with 5% OT.(d) Line cuts of integrated scattering intensity versus  $q$  ( $\text{nm}^{-1}$ ) of the three samples (a-c). Inset of (d) shows zoomed-in plot highlighting scattering from BDTTPD lamellar-stacking peak (100)..... 183
- Figure 7.5** MIS-CELIV extraction currents transients of the charge carriers injected into: (a) electron-only extraction devices; ITO/MgF<sub>2</sub>/ PBDTTPD: PC<sub>71</sub>BM /Ca/Al and (b) hole-only extraction devices; ITO/MgF<sub>2</sub>/ PBDTTPD: PC<sub>71</sub>BM /MoO<sub>3</sub>/Ag. The active layer of PBDTTPD: PC<sub>71</sub>BM was processed from; pure CB (red curves), CB with 5% CN (blue curves), and CB with 5% OT (green curves)..... 185
- Figure 7.6** (a) The thickness evolution during spin-coating and subsequent drying for PBDTTPD: PC<sub>71</sub>BM spin-cast from pure CB, CB with 5% CN, and CB with 5% OT. (b) The calculated retained solvent in the “wet” film during and thereafter spin-coating for the three cases in (a). ..... 187
- Figure 7.7** UV-Vis absorption spectra of PC<sub>71</sub>BM: PS (60:40) in solution and solid state (normalized to PC<sub>71</sub>BM absorption peak ( $\lambda_1 = 465$  nm)). (b) Time-evolution of PC<sub>71</sub>BM aggregation as represented by the ratio of absorption peak intensities at  $\lambda_2 = 550$  nm and  $\lambda_1$  during spin-coating and thereafter of a PC<sub>71</sub>BM: PS blend. The values of  $\text{Abs}(\lambda_2)/\text{Abs}(\lambda_1)$  of the dry additive-processed films are shown as asterisks in figure (b) (right). PS with high Mw (650 KDa) was used in this experiment..... 190
- Figure 7.8** *In situ* GIWAXS color plots (Integrated scattering intensity is shown in logarithmic color scale versus  $q$  ( $\text{nm}^{-1}$ ) and time(s)) of casting PBDTTPD: PC<sub>71</sub>BM from: (a) pure CB, (b) CB with 5% CN, and (c) CB with 5% OT. .... 194
- Figure 7.9** Line-cuts of the integrated scattering intensity versus  $q$  during spin coating of PBDTTPD: PC<sub>71</sub>BM at 6 s (top) and at 10 s (bottom) from start spin coating, showing that PBDTTPD crystallites formation occurs early in solution for additive-free and additive processed samples. The scattering around ( $q \sim 5 \text{ nm}^{-1}$ ) corresponds to a Kapton foil that was used as shield against ink splashes during spin coating. The broad scattering ( $q \sim 10\text{-}18 \text{ nm}^{-1}$ ) corresponds to solvent scattering..... 194
- Figure 7.10** (a) Evolution of the integrated scattering intensity of the lamellar stacking scattering peak (100) of PBDTTPD during casting of PBDTTPD: PC<sub>71</sub>BM from pure CB (black), CB with 5% CN (red), and CB with 5% OT (blue). (b) Evolution of the peak position of the lamellar stacking peak (100) of PBDTTPD versus time (s) for the three condition in (a). The values of the integrated scattering intensity and peak position of the complete dry films are shown as asterisks on the right of the plots (a,b) with the corresponding colors of the three conditions. Line-cuts of the integrated scattering intensity versus  $q$  of the as cast and vacuum dried PBDTTPD: PC<sub>71</sub>BM films processed from CB with 5% CN (c), and CB with 5% OT (d)..... 195
- Figure 7.11** (a-c) 2D GIWAXS color plot of integrated scattering intensity of PBDTTPD lamellar stacking peak (100), shown in logarithmic color scale, versus time(s) and azimuth angle ( $^\circ$ ) from

out-of-plane direction at ( $0^\circ$ ) to in-plane direction at ( $90^\circ$ )); GIWAXS measurements were performed *in situ* during casting PBDTPD: PC<sub>71</sub>BM from: (a) pure CB, (b) CB with 5% CN, and (c) CB with 5% OT. (d-f) Line-cuts of the evolution of the integrated scattering intensity in the out-of-plane direction and in-plane direction versus time for the three conditions in (a-c); (d) pure CB, (e) CB with 5% CN, and (f) CB with 5% OT. Line-cuts were taken at the dashed lines in (a-c). (g) Line-cuts of the integrated scattering intensity versus azimuth angle ( $^\circ$ ) of the as cast films in (a-c). (h-i) Line-cuts of the integrated scattering intensity versus azimuth angle ( $^\circ$ ) of the as cast and vacuumed dried films of the additive-processed samples; (h) CB with 5% CN, and (i) CB with 5% OT. .... 198

**Figure 7.12** Schematics represents the mechanisms of film formation of PBDTPD: PC<sub>71</sub>BM blends when they are cast from pure CB, CB with CN, and CB with OT. PBDTPD is represented as rods (dark red), PC<sub>71</sub>BM is represented as blue dots, and all solvents are transparent. (a) Schematic represents the solution-state showing PBDTPD self-assembly in CB solution for the three conditions. (b) Schematic represents the formation of PBDTPD fibril-network during CB evaporation for pure CB case. (c) Schematic represents the formation of PBDTPD fibril-networks during CN evaporation for CN-processed films revealing the formation of more fibril-networks which reduces the inter-spacing between these networks, and thus reduces PC<sub>71</sub>BM domains. (d) Schematic represents the as cast wet film, swollen with OT, for OT-processed films, revealing segregation of PC<sub>71</sub>BM into large-domains. .... 202

**Figure 8.1** (a) POM image of p-DTS(FBTTh<sub>2</sub>)<sub>2</sub>:PC<sub>71</sub>BM films coated by wire-bar coating from CB with 21 % w/w (DIO/solutes). (b) POM image near the edge of the sample in (a) showing coffee-ring effect. (c) TEM image of p-DTS(FBTTh<sub>2</sub>)<sub>2</sub>:PC<sub>71</sub>BM films coated from CB with 21 % w/w (DIO/solutes). .... 209

**Figure 8.2** (a) 2D GIWAXS image of p-DTS(FBTTh<sub>2</sub>)<sub>2</sub>: PC<sub>71</sub>BM film wire-bar coated from at room temperature. (b) Line cuts of integrated scattering intensity versus  $q$  ( $\text{nm}^{-1}$ ) of wire-bar coated samples at room temperature (black), at  $45^\circ\text{C}$  (red) and spin-coated reference sample (blue). All samples were processed with identical DIO content; 21 % w/w (DIO/solutes). Inset of (b) shows zoomed-in plot highlighting scattering from p-DTS(FBTTh<sub>2</sub>)<sub>2</sub> alkyl-stacking peak (001). (c) & (e) 2D GIWAXS color plot (Integrated scattering intensity is shown in logarithmic color scale versus  $q$  ( $\text{nm}^{-1}$ ) and time(s)); measured *in situ* during wire-bar coating of p-DTS(FBTTh<sub>2</sub>)<sub>2</sub>: PC<sub>71</sub>BM from CB with 21 % w/w (DIO/solutes) at room temperature and at  $45^\circ\text{C}$ , respectively. (d) & (f) Integrated scattering intensity of solvent scattering (black) and p-DTS(FBTTh<sub>2</sub>)<sub>2</sub> alkyl-stacking scattering ( $X_{001}$ ) (red) calculated from *in situ* GIWAXS in (c) & (d), respectively. .... 213

**Figure 8.3** (a) 2D GIWAXS image of p-DTS(FBTTh<sub>2</sub>)<sub>2</sub>: PC<sub>71</sub>BM film wire-bar coated from pure CB at room temperature. (b) 2D GIWAXS colour plot (Integrated scattering intensity is shown in logarithmic colour scale versus  $q$  ( $\text{nm}^{-1}$ ) and time(s)); measured *in situ* during wire-bar coating of p-DTS(FBTTh<sub>2</sub>)<sub>2</sub>: PC<sub>71</sub>BM from pure CB at room temperature. .... 215

**Figure 8.4** Schematics represents the stages of spin coating process; namely (a) deposition, (b) spin-up, (c) spin-off and (d) evaporation. .... 217



- Figure 8.5** Schematic of the apparatus for high-throughput and high-speed thin film coating. Substrate is placed on a temperature controller (1). Wire-bar coater is used to coat the solution on the substrate (2). Representation of the wire-bar coater is shown in the inset of the figure. Drying of the wet film is controlled by spinning the surrounding gas on top of the wet film by supplying vacuum or drying gas through rotating slit in a cylindrical rotating head (3). Vacuum or drying gas is supplied via stationary tube (4). ..... 220
- Figure 8.6** POM images of p-DTS(FBTTh<sub>2</sub>)<sub>2</sub>:PC<sub>71</sub>BM films coated by: (a) spin coating (total solutes concentration = 35 mg/mL), (b) conventional wire-bar coating (total solutes concentration = 35 mg/mL), (c) modified wire-bar coating (total solutes concentration = 35 mg/mL), and (d) modified wire-bar coating ((total solutes concentration = 12.5 mg/mL). All samples were coated from CB with 21 % w/w (DIO/solutes). The thickness of the films in (a), (b), (c), and (d) is 100+/- 5 nm, 290 +/- 10 nm, 275 +/- 10 nm, and 115+/-5 nm, respectively. .... 222
- Figure 8.7** 2D GIWAXS images of p-DTS(FBTTh<sub>2</sub>)<sub>2</sub> : PC<sub>71</sub>BM films coated by spin coating (a), and modified wire-bar coating (b). (c) Line cuts of integrated scattering intensity versus q (nm<sup>-1</sup>) of p-DTS(FBTTh<sub>2</sub>)<sub>2</sub>:PC<sub>71</sub>BM samples coated by modified wire-bar coating (black curve) and spin coated (red curve). Both samples were processed with identical DIO content; 21 % w/w (DIO/solutes)..... 224
- Figure 8.8** Current density- Voltage (J-V) curves of solar cell devices fabricated from p-DTS(FBTTh<sub>2</sub>)<sub>2</sub>:PC<sub>71</sub>BM blends coated by spin coating with total solute concentration 35 mg/mL (black), new wire-bar coating at different concentrations; 35 mg/mL (red), 25 mg/mL (blue), 17 mg/mL (pink), and 12.5 mg/mL (green). All sample were coated in air from CB with 21 % w/w (DIO/solutes). Notably, fabricated solar cell devices in glove-baox by spin coating have higher performance ( PCE > 7%). ..... 226

## LIST OF TABLES

<b>Table 4.1</b> Spano model parameters of P3HT films coated from well-dissolved and pre-aggregated solutions.....	98
<b>Table 4.2</b> Field effect transistor performance of P3HT transistor devices.....	98
<b>Table 4.3</b> Spano model parameters for P3HT : PC <sub>61</sub> BM films.....	104
<b>Table 4.4</b> Solar cell device parameters for P3HT:PC <sub>61</sub> BM solar cells.....	107
<b>Table 5.1</b> Average device parameters of solar cell devices fabricated from X2:PC <sub>71</sub> BM.....	143
<b>Table 5.2</b> Comparison of the ability of crystallization, crystallization behavior and processing routes between p-SIDT(FBTTh <sub>2</sub> ) <sub>2</sub> , p-DTS(FBTTh <sub>2</sub> ) <sub>2</sub> and X2.....	146
<b>Table 7.1</b> Device performance parameters of the solar cells fabricated from PBDTTPD: PC <sub>71</sub> BM blends processed from pure CB and CB with solvent additives.....	179
<b>Table 7.2</b> Summary of the relative crystallinity and crystalline correlation length of PBDTTPD in the dry blend films, calculated from lamellar-staking (100) scattering.....	184
<b>Table 7.3</b> Calculated electron and hole mobilities of PBDTTPD: PC <sub>71</sub> BM films coated with and without additives.....	186
<b>Table 7.4</b> Summary of the relative crystallinity and crystalline correlation length of PBDTTPD in the as cast blend films, calculated from lamellar-staking (100) scattering.....	196
<b>Table 8.1</b> Summary of the relative crystallinity and crystalline correlation length of p-DTS(FBTTh <sub>2</sub> ) <sub>2</sub> , calculated from the alkyl-stacking peak (001).....	214
<b>Table 8.2</b> Summary of the relative crystallinity and crystalline correlation length of p-DTS(FBTTh <sub>2</sub> ) <sub>2</sub> , calculated from the alkyl-stacking peak (001).....	224
<b>Table 8.3</b> Device performance parameters of the solar cells fabricated from p-DTS(FBTTh <sub>2</sub> ) <sub>2</sub> : PC <sub>71</sub> BM by spin coating versus the new wire-bar coating apparatus.....	227

## Chapter 1

### Introduction

Our planet continues to experience increasing global energy demand and consumption. Consequently, there is increasingly a tremendous need for the development of renewable energy resources which can supply a significant fraction of society's energy needs. Solar photovoltaic (PV) technologies are near the top in the renewable energy mix needed to make a societal impact. Silicon based solar cells currently prevail in the photovoltaic market. However, they have large energy payback time and their manufacturing incur environmental hazards due to the chemicals released during processing.<sup>[1,2]</sup> Although silicon based solar cells technology suffered from high cost for decades, its fabrication cost has reduced substantially in the last few years.<sup>[1]</sup> Second generation thin film inorganic PV technologies that have the second share of the market, such as CdTe, CdS and CIGS, have challenges of using rare materials and/ or poisonous heavy metals, and utilize capital intensive vacuum-based deposition processes.<sup>[3,4]</sup> Alternative PV technologies were developed that make use of abundant materials and which allow to achieve low cost manufacturing on large area, flexible substrates, using solution processing methods compatible with roll-to-roll methods.<sup>[4-9]</sup> Over the past two decades, various technologies have emerged which can make this vision a reality, including organic, quantum dot, dye-sensitized and hybrid perovskite light absorbers, all of which can be solution processed.<sup>[6-12]</sup> Amongst these

technologies, OPVs, being carbon based materials, have several advantages such as availability, flexibility, lightweight and low-cost. <sup>[6-9]</sup> Besides, OPVs have potentially low energy payback time and ease of fabrication into large-area, flexible and rigid substrates, and can be applied as transparent solar panels into windows. However, organic semiconductors have the main disadvantage of a low dielectric permittivity. <sup>[13]</sup> Therefore, upon absorbing light, Coulomb-bound electron-hole pairs instead of free carriers are generated due to the low screening of the photo-generated charge carriers. <sup>[14-18]</sup> Short lifetime and a very limited diffusion length of the generated strongly bound excitons are key characteristics of organic solar cells. Thus, donor and acceptor materials with properly chosen energy levels are blended – instead of forming a planar heterojunction – into an intricate network known as the bulk heterojunction (BHJ) with interfaces acting complementarily to separate the bound excitons into free carriers, which then diffuse to the respective electrodes. <sup>[6]</sup> Another disadvantage of OPVs arises from the complexity of the BHJ photoactive layer compared to classical thin film light harvesters, which makes it challenging for scalable fabrication. <sup>[6]</sup> In addition, OPVs suffer from large voltage losses which lead to large energy losses by wasting part of the energy of the absorbed light. <sup>[19,20]</sup>

A major challenge in the development of OPV devices is identifying a viable route for controlling the morphology in order to achieve a reproducible and optimal performance. The morphology strongly depends on the processing approach. To date, spin coating has

been the most widely used processing technique in both academia and in industrial research units. However, its major drawback is its incompatibility to industrial commercialization.<sup>[21]</sup> Besides the fact that it is extremely inefficient in material usage, its low throughput makes the process incompatible with roll-to-roll processing. In contrast to spin coating, other alternative techniques, such as blade-coating and slot-die coating, are highly efficient in material usage and easily transferable to roll-to-roll coating environment.<sup>[21]</sup> However, these techniques had received little attention in the context of organic solar cells at the start of this Ph.D work. Reproducibility and parity of device performance remain the biggest challenges. The lack of knowledge of how the BHJ forms when the film is cast through these techniques constitutes the main obstacle in attaining satisfactory performance. To overcome this limitation, it is necessary to gain both quantitative and qualitative understanding of how the final film morphology is attained and how this morphology depends on the processing route. We take the view that scale-up from spin-coating first involves deep scientific insight into the thin film formation mechanisms in state of the art solar cells. Understanding the development of morphology in BHJs should offer a viable route to enabling the scalable manufacturing of efficient organic solar cells in the future.

The kinetics of solution drying and phase transformation during the solution process is of crucial importance for tuning morphology of the BHJ and to optimizing the performance of organic solar cells.<sup>[22,23]</sup> However, one key limitation at the start of this Ph.D dissertation was the lack of availability of in situ metrology techniques to

investigate the solution-to-solid phase transformation in the context of solution processing, especially for spin-coating. Laser reflectometry was used recently to reveal the mechanism of phase separation during spin coating of BHJ films by monitoring the light scattering out of specular direction, allowing detecting micron-scale phase separation.<sup>[24,25]</sup> Our group reported the first study of the morphological evolution including crystalline behavior and phase separation of P3HT:PCBM BHJ was monitored during spin coating using grazing incidence wide angle x-ray scattering (GIWAXS) and grazing incidence small angle x-ray scattering (GISAXS).<sup>[22]</sup> However, there were no other reports related to spin-coating, possibly because of the significant engineering challenge to overcome in performing in situ metrology during spin-coating. Consequently, the community has directly investigated “easier” processes, but this does not help the spin-coating process - the most successful solution process in the field of OPVs – be better understood. In another study, solution to solid-state formation during blade-coating of P3HT:PCBM films was monitored using spectroscopic ellipsometry and GIWAXS.<sup>[26]</sup> In that work, kinetics of film drying, evolution of P3HT aggregation state and crystalline behavior were monitored simultaneously.<sup>[26]</sup>

Perhaps the most common implementation among all in situ process monitoring tools are optical ones, because of their compatibility with liquid and vapor environments and do not require vacuum, unlike many other surface and thin film characterization methods. The time-evolution of thickness during solution drying has been measured in different solution processing techniques, such as spin coating and blading, with laser

reflectometry, spectroscopic reflectometry and spectroscopic ellipsometry being the most common methods. Spectroscopic ellipsometry requires full modeling of the optical properties (extinction coefficient and refractive index) in order to extract film thickness. The extinction coefficient, a parameter closely related to absorbance, strongly correlates to the presence J and H photophysical aggregates in conjugated materials, which are due to wavefunction overlap between adjacent conjugated units, e.g., in a polymer, and which play a crucial role in mediating carrier transport through the organic semiconductor.<sup>[26,27]</sup> Knowledge of the optical properties can therefore provide a link between solution and solid states of organic semiconductor materials and their device performance. The number and “quality” of photophysical aggregates in terms of backbone planarity and conjugation length can be estimated in conjugated polymers via modeling, making this a powerful method to monitor polymer conformation and aggregation during solution processing.<sup>[27,28]</sup> Ultraviolet-visible (UV-Vis) absorption provides similar insight into photophysical aggregation with the advantage that unlike ellipsometry it is a direct measurement that does not require tedious modeling. It also provides absorption data from the first moment of solution processing through the bulk solution, whereas ellipsometry only works when the solution thickness approaches its last micron. As such, UV-Vis absorption can track pre-aggregation of solutes in the solution. UV-Vis absorption has not been implemented in situ during spin-coating at the start of this Ph.D dissertation. It was used to monitor the transition from solution to solid-state of spin coated films after interrupting spin coating and moving the sample to

the measurement stage.<sup>[29]</sup> However, this does not capture the process kinetics realistically, since spinning enhances solvent evaporation kinetics. Raman spectroscopy also provides insight into ordering of conjugated materials. The sensitivity of Raman modes to the degree of ordering and  $\pi$ -electron delocalization has been reported.<sup>[30,31]</sup> These optical methods are spectroscopic in nature and offer only an indirect link to crystalline structure, order and to phase separation of the components of the blend. To access this information more directly, one must also perform X-ray scattering measurements. X-ray diffraction and related scattering methods become a very useful complementary technique. In particular, grazing incidence X-ray scattering has been used successfully to probe the molecular packing structure as well as nanoscale and mesoscale phase morphology over a wide range of length scales.<sup>[22]</sup>

In this dissertation, we will use in situ measurement techniques, combined with ex situ measurement capabilities, to investigate the spin coating process in the context of OPVs. Then, we extend our investigation to production-compatible processing methods (such as wire-bar coating). We aim to translate knowledge gained in understanding the formation from spin coating of the bulk heterojunction layer to more scalable solution processing methods. This will enable the emergence of pathways that will bridge the gap between lab-based non scalable processes and commercially viable solution processing methods.

In the following chapters of this dissertation, we provide an overview of the morphology development in bulk heterojunction organic photovoltaics in chapter 2. Then, we discuss



in the third chapter the general methodology of this work. Afterwards, we will discuss our approach to overcome the above mentioned problems by applying in situ investigation of bulk heterojunction formation of solution processed organic solar cells aiming to scalability of device fabrication in chapters 4-8. Finally, we conclude in chapter 9 the general outcomes of the dissertation. The chapters are as follows:

Chapter2. Morphology development in bulk heterojunction organic photovoltaics: A literature review

Chapter3. Methodology and general description of the work

Chapter4. In situ UV-visible absorption during spin-coating of organic semiconductors: a new probe for organic electronics and photovoltaics

Chapter5. Roles of the donor crystallization dynamics and pathway on bulk heterojunction formation in small-molecule organic solar cells

Chapter6. Impact of solvent additives on the mechanism of film formation in small-molecule bulk heterojunction solar cells

Chapter7. Polymer-fullerene bulk heterojunction solar cells: Role of solvent additives in fullerene aggregation

Chapter8. Lessons for scalable processing of small-molecule bulk heterojunction solar cells while achieving microstructural and performance parity

Chapter9. Conclusions and Future Work

## Chapter 2

### **Morphology development in bulk heterojunction organic photovoltaics: A literature review**

In this chapter, we provide an overview of the field of organic solar cells highlighting the strategies used to control the active layer morphology and the techniques used to monitor the active layer formation. At the start of this Ph.D dissertation in 2011, little research was published in this area. This review focuses on the state of the art around that time and also includes some more recent results which were published by other groups during the completion of this PhD dissertation. We start by a brief introduction to organic semiconductors and organic photovoltaics. We discuss the semiconducting properties of organics and the main differences that distinguish them from inorganics. We go through the development of the bulk heterojunction concept of organic photovoltaics and the main optoelectronic processes of harvesting light into electricity in bulk heterojunction solar cells. Then, we provide an overview of the main strategies that have been developed to control the bulk heterojunction microstructure. Finally, we review the state-of-the-art in situ diagnostic techniques that have been implemented in the monitoring of bulk heterojunction formation during solution processing.

#### **2.1 Organic semiconductors**

Semiconducting properties in organic semiconductors originate from delocalized  $\pi$ -electrons in  $\pi$ -conjugated systems.<sup>[32,33]</sup> To get a sense of the conjugated system, let us

discuss first the double bond between two adjacent carbon atoms (i.e. C=C bond which is a key unit in conjugated system). In each carbon atom, the 2s and two of the 2p orbitals form three sp<sup>2</sup> hybridized orbitals with a planar trigonal structure, whereas the third p<sub>z</sub> orbital remains perpendicular to the hybridized orbitals plane. The double bond between two adjacent carbon atoms consists of a  $\sigma$ -bond and a  $\pi$ -bond. A  $\sigma$ -bond is formed from head-on overlapping of two sp<sup>2</sup> orbitals from each carbon atom whereas the shared electrons remain localized between the two bonded atoms. On the other hand,  $\pi$ -bond is formed from overlapping of the p<sub>z</sub> orbitals forming a much weaker bond wherein the electrons are delocalized and can move in and out of the space between the two  $\pi$ -bonded atoms. This weakness of  $\pi$ -bonding is attributed to the reduced overlap between p<sub>z</sub> orbitals due to their parallel orientation. In conjugated systems, of which several examples are shown in **Figure 2.1**, the overlap of p-orbitals is extended along the system constituting a delocalized electron cloud.

The quantity and quality of aggregation, including short range order and long range crystalline order and the molecular packing motif in aggregated organic semiconductors determine the extent of  $\pi$ -bond overlap and delocalization of  $\pi$ -electrons, with significant implications on their energetics and optoelectronic properties.<sup>[34-36]</sup> The conjugation and delocalization also determine whether the semiconductor has the ability to transport charge carriers, along which directions and at what carrier mobility. Considering P3HT, historically the most commonly investigated reference material in

the world of conjugated polymers, an increase in degree of ordering and backbone planarity of P3HT is accompanied by an increase in the conjugation length which also causes a red shift in absorption spectrum.<sup>[28,37]</sup> Moreover, the increase of polymer aggregation/crystallization has been shown to result in enhanced charge carrier mobility, especially in high Mw polymers, where long polymer chains act as so-called tie-molecules that connect the polymer aggregates.<sup>[38,39]</sup> For small-molecules, crystallization is crucial for ensuring intermolecular interactions required for the efficient charge transport, unlike polymer donors which have charge transport pathways through both interchain and intra-chain interactions.<sup>[17,38-40]</sup> In addition, for various small-molecules, different polymorphs exhibit extreme differences in their optoelectronic properties.<sup>[41]</sup> Several studies reported that a change in crystal packing structure can give rise to significant differences in charge carrier mobility.<sup>[41,42]</sup> Overall, evaluating and controlling the degree and nature of ordering in organic semiconductors are critical for attaining the appropriate optoelectronic properties needed for the relevant optoelectronic applications.

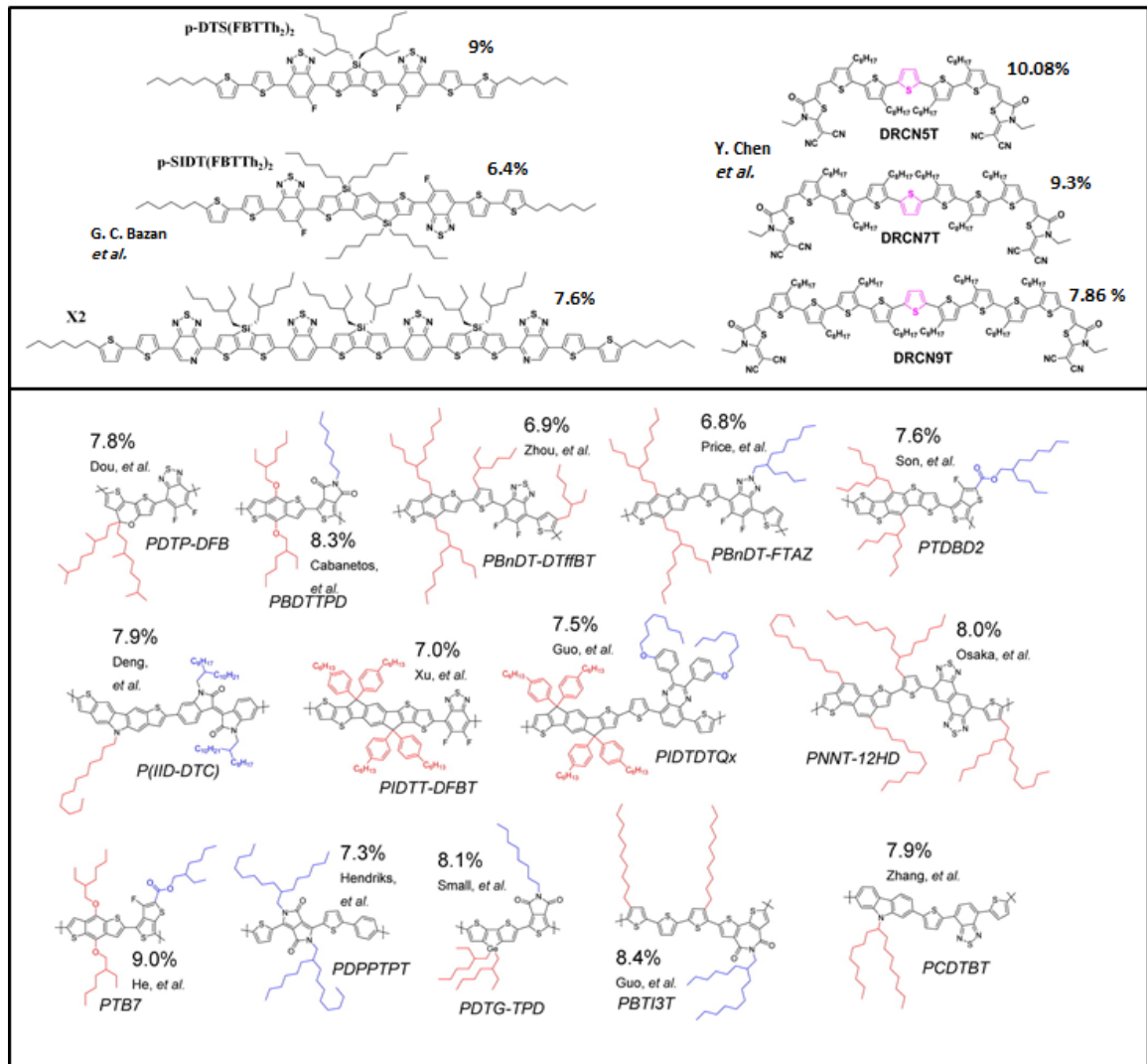


**Figure 2.1** Molecular structures of organic semiconductor materials (small-molecules and medium-size molecules on the top, polymers on the bottom). Figures are adapted from references <sup>[43,44]</sup>. All are used as donor materials for high performing OPVs.

## 2.2 Organic photovoltaics

Currently, the market of photovoltaics devices is dominated by inorganic-based solar cells; mainly silicon-based solar cells. However, their manufacturing has challenges related to the materials consumption, fabrication costs and environmental issues. Some PV technologies require huge materials consumption and manufacturing costs such as the first generation solar cells based on silicon, whereas others rely on rare earth elements and/ or toxic materials such as the second generation thin film solar cells including CIGS, CdTe and CdS.<sup>[1-4]</sup> The latter, regardless of being thin films with much less materials consumption, still incurs large energy consumption during their manufacturing requiring vacuum processes and/or high temperature treatments.<sup>[3]</sup> Thus, alternative photovoltaics technologies, what's called third generation solar cells, were developed aiming to overcome these challenges by using abundant low-cost materials that can be manufactured by cost effective solution processing techniques compatible with roll-to-roll manufacturing.<sup>[4-6]</sup> Amongst these technologies, organic photovoltaics, besides being carbon-based materials, have several advantages such as availability, flexibility, light-weight, low-cost and compatibility with roll-to-roll solution processing techniques.<sup>[6-9]</sup>

There are major differences that should be considered for organic photovoltaics as compared to inorganic materials. First of all, one advantage for organic semiconductors is that they are chemically synthesized from abundant carbon-based materials.<sup>[6-9]</sup> This

opens the opportunity for creating infinite number of novel semiconducting materials with highly tunable optoelectronic properties.<sup>[6,7,9]</sup> On the other hand, organic photovoltaics have a major drawback of being excitonic solar cells which don't effectively screen the interaction between the electrons and holes upon absorption.<sup>[14-18]</sup> In a polarizable material, such as a semiconductor, the polarization of neutral atoms around oppositely charged electrons and holes screens the attraction between them. The dielectric constant of the material is a key factor that determines the degree of screening of the columbic attraction between the photo-generated electrons and holes.<sup>[43,44]</sup> Unfortunately, organic semiconductors have relatively low dielectric constants as compared to their inorganic counterparts.<sup>[13]</sup> For instance, most of organic semiconductors have dielectric constant on the order of 2 to 4, whereas, for silicon, it has a dielectric constant around 12.<sup>[13]</sup> To give sense of the numbers, electron-hole pair in an organic semiconductor with a dielectric constant of 4 tends to feel attracted 3 times more than it does in Silicon. Basically, photon excitation leads to the formation of strongly bound electron-hole pairs, namely excitons, in low dielectric constant materials such as organic semiconductors whereas, it leads to the formation of free charges immediately in high dielectric constant materials such as silicon. That's why organic photovoltaics are considered excitonic solar cells. One more aspect that we should consider is the charges diffusion length, a parameter related to the average length a carrier diffuses throughout the semiconductor between photo-generation and recombination.<sup>[17,18,47]</sup> Typically, in organic semiconductors, the exciton diffusion length

is limited to a few tens of nanometers, whereas, the carriers diffusion length is significantly higher in silicon that can be as high as hundreds of microns.<sup>[17,48,49]</sup> Moreover, lower diffusion length is indicative of shorter lifetime.<sup>[18,50]</sup> Thus, a major challenge is designing the organic photovoltaics device so that the excitons can be separated into free charges during their short lifetime before recombination.

The organic photovoltaics active layer is designed from a combination of a donor (D) and acceptor (A) materials. Nevertheless, more than one donor or acceptor can be used such as in ternary or quaternary systems.<sup>[51-53]</sup> At the early stages of organic photovoltaics, a stacked bilayer of pure D/A materials was used as the active layer, see **Figure 2.2a.**<sup>[54]</sup> However, the devices efficiency remained very low because of the short exciton diffusion length that significantly limit charges extraction at bilayer configuration. At this configuration, the number of excitons that can reach the interface of the bilayer is too low leading to significant recombination losses.<sup>[54]</sup> To effectively split the excitons before they recombine, the active layer should be limited within around 10 nm from both sides of D/A interface.<sup>[55]</sup> However, the active layer should be thick enough to effectively absorb most of the incident light; generally several hundreds of nm thick active layer is needed.

To overcome this problem, the bulk heterojunction (BHJ) concept was introduced in which the active layer is formed from an interpenetrating network of donor and



acceptor domains with length scales comparable to the typical diffusion length of excitons, see **Figure 2.2b**.<sup>[56]</sup> BHJ active layers can be fabricated by solution processing in which the D & A materials are blended in solutions of a given solvent or co-solvents and are allowed to partially phase separate during solvent drying. The BHJ morphology can be tuned by several pre and post deposition techniques that will be discussed in the following sections.<sup>[6]</sup> BHJ active layers can also be processed by co-evaporation of D/A materials (mostly small-molecules). There are also less common techniques of making BHJ films via annealing initially coated bilayer films allowing diffusion and mixing of D/A components to form BHJ.

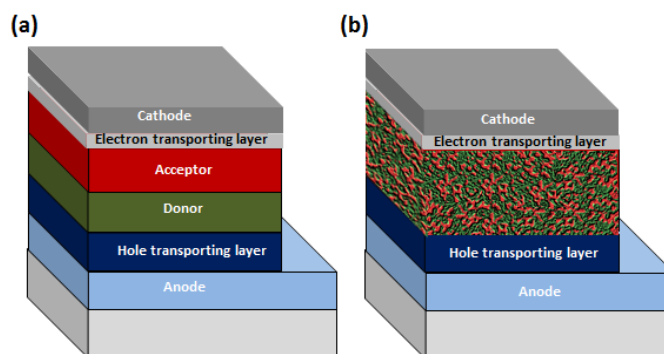


**Figure 2.2** Schematics represent organic photovoltaics architecture in bilayer and BHJ configuration in (a) & (b), respectively. Donor and acceptor phases are represented in dark green and red, respectively.

The main processes for light harvesting into electricity in organic BHJ photovoltaics can be summarized in the following successive steps and as shown in **Figure 2.3**:

- 1. Light absorption and exciton formation;** an incident light with appropriate energy promotes the excitation of electron from HOMO to an excited state leading to exciton formation.<sup>[14]</sup> The minimum energy required for the excitation is equivalent to the HOMO-LUMO gap minus the exciton binding energy, namely the optical gap.<sup>[14]</sup> Excited electrons with high energy states undergo vibrational relaxation to lower energy states. Several parameters affect the light absorption including the band gap, absorption coefficient and thickness. Luckily, organic semiconductors have high absorption coefficient so that a few hundreds of nanometers are enough to absorb most of the light.<sup>[57]</sup> Since organic semiconductors have tunable band gap, the light harvesting can be significantly improved through the integration of multiple materials with complementary absorptions, such as in ternary systems.<sup>[52]</sup> Although the most common acceptors based on fullerene derivatives have wide band gap and doesn't contribute much to the absorption, the development of new acceptors with complementary absorption to the donor has improved the overall absorption in organic photovoltaic systems.<sup>[58-61]</sup> Dyes as a ternary component with donor: fullerene systems were also used to improve the absorption.<sup>[51]</sup> Furthermore, through device engineering, the absorption can be increased by means of mirrors and textured electrodes.<sup>[62]</sup>
- 2. Exciton diffusion:** for effective charge generation, the excitons have to diffuse to the D/A interface before their decay by radiative or non-radiative recombination processes.<sup>[63]</sup> D/A domains purity and size are key factors that should be tuned

carefully to reduce the recombination losses.<sup>[64,65]</sup> Notably, this diffusion process is affected by the intrinsic properties of donors and acceptors, such as exciton diffusion length and lifetime.

3. **Exciton dissociation:** this process occurs at the D/A interface where the energy cascade at the interface provides the driving force for the excitons separation.<sup>[66]</sup> Once the excitons reach D/A interface, they form charge transfer complexes (at interfacial CT states).<sup>[67,68]</sup> Afterwards, they can either decay to the ground state by recombination processes or produce free carries at charge separated (CS) states. Once carriers become in the CS states, they can move freely in the active layer after overcoming the binding energy. More detailed picture of the exciton dissociation processes is illustrated in **Figure 2.4**. The nanostructure morphology near the interface plays a critical role in facilitating or hindering the dissociation process. For example, the high local mobility and the appropriate energy offsets near the interface can significantly favor the dissociation process.<sup>[66]</sup>
4. **Carrier transport to the electrodes for extraction:** once free carriers are generated after excitons dissociation, they migrate towards their respective electrodes guided by the work-functions of the electrodes. Electrons diffuse towards the low work function cathode whereas the holes diffuse towards the high work function anode for collection. This process is affected by multiple factors such as carrier mobility within donor and acceptor domains as well as D & A domains purity and connectivity. Bi-continuous domains of D/A phases with sufficient phase purity and high carrier

mobility are crucial for effective charge transport and minimum recombination losses of the carriers while they are migrating to their respective electrodes. <sup>[64,65,69]</sup> Impure D/A phases and discontinuous pathways are detrimental to the efficiency of charge transport and extraction. An optimum active layer thickness is also important for efficient charge collection. Although increasing the thickness is beneficial for light absorption as mentioned in step (1), it can introduce recombination losses because the charges have to migrate larger distance to reach the electrodes.

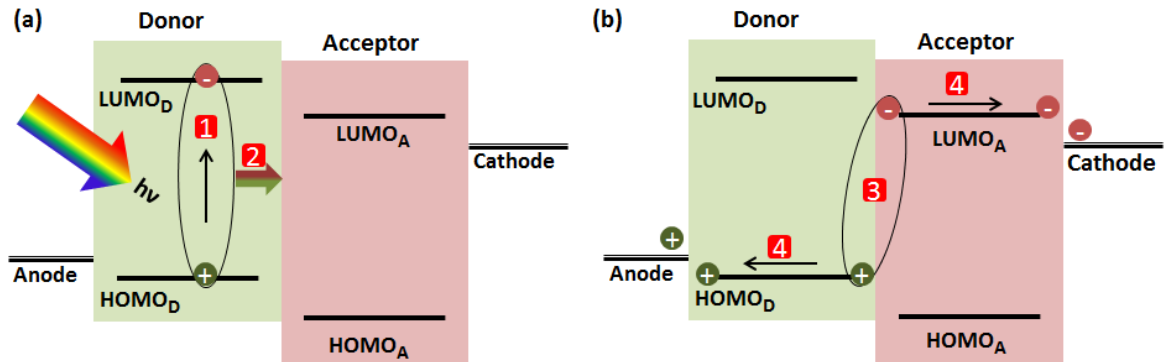


**Figure 2.3** (a) & (b) Simplified schematics represent the main processes for light harvesting into electricity in organic BHJ photovoltaics.

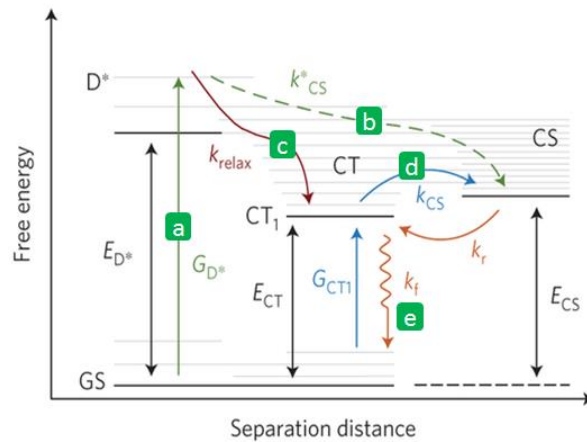


**Figure 2.4** Schematic represents the possible pathways for free charge carrier generation from excited states (left) to separated states (right).<sup>[67]</sup> (a) Photo-excitation by a photon with energy higher than energy gap ( $E_{D^*}$ ) of a donor semiconductor, generates the donor excited state  $D^*$  at a rate  $G_{D^*}$ . (b) Pathway for generation of free carriers at charge-separated states (CS) at a rate ( $k^*_{CS}$ ), also called hot exciton dissociation.<sup>[67,68]</sup> This pathway (b) occurs for high-energy (hot) delocalized excited

states, where excess energy after photo-excitation assist to bypass vibrationally relaxed and lowest energy CT states ( $CT_1$ ). Another pathway for free carrier generation via (c-d); (c) Thermal relaxation to  $CT_1$  states at a rate ( $k_{relax}$ ), (d) Dissociation form  $CT_1$  to CS at rate ( $k_{CS}$ ). (e) Radiative decay from  $CT_1$  to the GS. Other processes such as relaxation form CS to  $CT_1$  at rate  $k_r$  or optical excitation into  $CT_1$  at  $G_{CT_1}$  are possible. This illustration is adapted from reference <sup>[67]</sup>.

Overall, the performance of the photovoltaic device is evaluated by the power conversion efficiency (PCE) which is calculated from the current density voltage (J-V) curve under standard conditions; see **Figure 2.5**. The solar cell device delivers power under illumination in the region between short circuit condition (at  $V = 0$ ,  $J=J_{sc}$ ) and the open circuit condition (at  $V = V_{oc}$ ,  $J=0$ ). It is important to define two main characteristics of the J-V curve; the maximum power point and fill factor (FF). The maximum power point is the point at which the solar cell delivers the maximum extractable power density, determined by point of the maximum product of J and V. The fill factor, a parameter related to the efficiency of charge collection in the solar cell, is determined by the ratio of the maximum power density to the product of the  $J_{sc}$  and  $V_{oc}$ . PCE of a solar cell is the ratio of the maximum extractable power density to the power density of the incident light ( $P_{in}$ ) which involves the product of  $J_{sc}$ ,  $V_{oc}$  and FF divided by  $P_{in}$ , see **Figure 2.5**. An improvement in PCE requires enhancement in the three parameters ( $J_{sc}$ ,  $V_{oc}$  & FF) simultaneously.

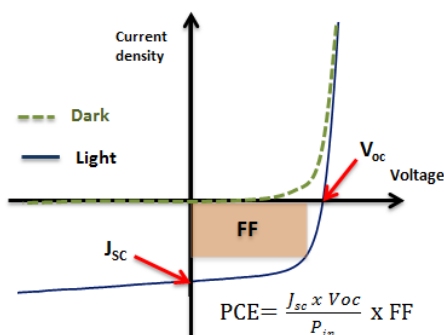


**Figure 2.5** Schematic representing the J-V characteristic of solar cell devices and the associated figures of merit, including  $J_{sc}$ ,  $V_{oc}$ , FF and PCE.

### 2.3 Strategies for controlling the active layer morphology in BHJ solar cells

The active layer morphology in BHJ organic solar cells depends on the interplay between multiple variables including intrinsic properties related to the pure D & A domains as well as the interaction parameters between both components. Domain size and purity play a crucial role in defining the efficiency of charge generation and extraction, as discussed above.<sup>[65,69]</sup> The D/A domains have to be small enough to increase the interfacial area and to ensure that the charges can reach the interface. The latter is limited by the diffusion length of charge carriers. Furthermore, the domains have to be large enough to ensure the connectivity of D/A domains creating percolation pathway for the charges through the entire film. Phase purity of donor and acceptor domains is another factor that has to be considered carefully. Impure phases can lead to severe recombination losses, thus formation of D/A domains with sufficient phase purity is a must for achieving high performance BHJ solar cells. Nevertheless, the presence of a

mixed phase at the D/A interface is found to be beneficial for charge separation.<sup>[66]</sup> It has been shown that having an energy offset at the interface derived by the presence a mixed phase at the D/A interface leads to supreme charge dissociation probability as compared to having sharp energy levels at the interface. At the presence of an energy offset at the interface, it becomes more energetically favorable for both electrons and holes to move from the highly disordered interface to the pure phases.<sup>[66]</sup>

Several thin film processing strategies have been used to tune the BHJ morphology including the choice of the solvent or co-solvents, the processing conditions and the post-treatments such as solvent or thermal annealing.<sup>[6]</sup> In the following sections, we discuss in details the most common thin film processing strategies for controlling BHJ morphology. There are other strategies that involve chemical modifications such as cross-linking and modification of main chains and side chains of oligomers and polymers but are not discussed here.<sup>[6]</sup>

### **2.3.1 Choice of solvent approach**

One of the main key parameters for tuning the BHJ morphology in solution processed BHJ solar cells is the choice of the solvent. The main aspects that should be considered when selecting a solvent involve thermodynamics aspects such as solubility of D & A materials in the solvent as well as the mutual interactions between solvent: D: A and kinetics aspects such as the boiling point and the vapor pressure of the solvent besides the coating conditions which define the drying kinetics.<sup>[70,71]</sup> Generally, chlorinated



solvents such as chlorobenzene (CB), 1,2-dichlorobenzene (DCB), 1,2,4-trichlorobenzene (TCB), and chloroform (CF) and aromatic solvents such as xylene and toluene are found to be good solvents for wide-range of organic semiconductors.

The role of D & A solubility in the casting solvent on the BHJ morphology was reported in a variety of BHJ systems.<sup>[70–74]</sup> For MDMO-PPV:PCBM, samples coated from CB were finely mixed whereas samples coated from toluene exhibited large features that were identified as large domains of PCBM.<sup>[74,75]</sup> The study revealed the formation of these large PCBM domains to the poor solubility of PCBM in toluene. On the other hand, the high solubility of PCBM in CB prevented the formation of the over-sized PCBM domains. These findings were generalized in another study that investigated the morphology of MDMO-PPV:PCBM blend films coated from several solvents; namely CB, CF, toluene, carbon disulfide, pyridine, trichloroethylene, and 1-methyl pyrrole.<sup>[73]</sup> Over-sized PCBM grains (on the order of hundreds of nanometers) were observed for samples coated from solvents that are poor solvents for PCBM such as pyridine and toluene. Similar findings were reported for P3HT:PCBM blends. A study reported the formation of large PCBM domains when the blends were cast from poor solvents for PCBM such as toluene and xylene.<sup>[76]</sup> These large domains were absent from samples coated from good solvents such as CB and DCB. Another example that highlights the importance of solvent selection was reported for PCDTBT: PC<sub>71</sub>BM blends; a system that can achieve PCE as high as 7.5%.<sup>[77–79]</sup> Again, casting the blends from poor solvents for PC<sub>71</sub>BM such

as CF resulted in large PC<sub>71</sub>BM domains.<sup>[79]</sup> DCB was found to prevent the over segregation of PC<sub>71</sub>BM and enhance the formation of PCDTBT fibrils leading to optimal devices performance.

Several studies have considered the role of the drying kinetics which determines how fast the solution to solid-state transformation occurs.<sup>[80–82]</sup> Volatile solvents with low boiling points tend to evaporate faster than high boiling point solvents. It was found in P3HT:PCBM blend that crystallization of P3HT is highly dependent on the solvent.<sup>[80]</sup> A study reported the dependence of P3HT crystal size in P3HT:PCBM BHJ blends coated from CF, toluene, CB and xylene, showing that P3HT crystallites sizes were larger for higher boiling point solvents.<sup>[76]</sup> Similar observation was reported for other polymers such as PCPDTBT and PTB7.<sup>[81,82]</sup>

Although, several studies have considered the effect of the processing solvent on BHJ morphology at early stage of the development of BHJ concept when BHJ films were typically cast from one solvent, the usage of co-solvents was adopted later that was found to be more effective in attaining the desired morphology. The latter will be discussed below in section 0.

### **2.3.2 Thermal annealing approach**

Thermal annealing is one of the most common techniques used for tuning the BHJ morphology and enhancing the device performance of variety of BHJ systems. It is typically used when the as cast film morphology is far from optimum requiring post-

processing treatments. For P3HT:PCBM system, thermal annealing can increase the photo-physical aggregation and crystallinity of P3HT. Simultaneously, thermal annealing was found to drive the phase separation of the P3HT and PCBM.<sup>[83–85]</sup> Thermal annealing of P3HT:PCBM can be done either before or after the deposition of the cathode, namely pre-annealing and post-annealing, respectively.<sup>[83]</sup> A detailed comparative study of the as cast versus pre-annealed versus post-annealed P3HT:PCBM thin films has revealed detailed morphological changes driven by the two annealing methods.<sup>[83]</sup> For the as cast films, the samples suffered from poor P3HT ordering and poor phase separation as revealed by high resolution transmission electron microscopy (TEM), small angle neutron scattering (SANS) and grazing incidence X-ray scattering (GIXS). Upon annealing for both methods, phase separation of P3HT and PCBM was detectable leading to nanoscopic, bicontinuous morphology with a characteristic length scale of  $\sim 10$  nm domains. At the same time, an increase in P3HT crystallinity was observed with enhancement in lamellar stacking ordering as well as development of  $\pi$ -stacking ordering. Although both crystals with edge-on and face-on orientations were observed in both annealing conditions, post-annealing was found to promote more crystallites formation with face-on orientation, compared with pre-annealing. In addition, the concentration of components at the cathode interface was different in the two cases revealed by dynamic secondary ion mass spectroscopy (DSIMS). An enhancement in the P3HT concentration at the cathode interface was observed for the pre-annealed sample, on the other hand, the opposite was observed for the post-annealed sample. In another

study, the post-annealing treatment of P3HT:PCBM blends was found to increase both the  $J_{sc}$  and FF leading to improvement in devices performance.<sup>[83]</sup> Another work reported an increase in carrier mobility upon post-annealing treatment which was correlated to the enhancement of the efficiency.<sup>[84]</sup> Further studies confirmed the correlation between the thermal annealing treatments and the increase in P3HT crystallinity and consequently P3HT:PCBM phase separation; the net result is an enhancement in overall devices performance.<sup>[85–88]</sup> Overall, these studies revealed strong correlation between the devices performance and bulk and interfacial morphologies derived by the annealing treatments.

Further studies have reported the effectiveness of thermal annealing in improving the device performance of wide-range of systems. For instance, thermal annealing was utilized to improve the device performance of PSBTBT:PCBM system leading to an increase in PCE.<sup>[89–92]</sup> Morphological studies have shown that the crystallization of PSBTBT and phase separation were initially developed during spin coating, whereas thermal annealing further increased the polymer crystallinity and the phase segregation as revealed by GIXD and SANS.<sup>[92]</sup> Pre-annealing and post-annealing treatments of PSBTBT:PCBM system have resulted in differences in vertical phase segregation.<sup>[92]</sup> For as cast samples, PSBTBT was found to be segregated at the free surface. Pre-annealing was found to further increase PSBTBT concentration at the top surface before coating the cathode layer. On the other hand, post-annealing treatment has resulted in

enrichment of PCBM concentration at the cathode interface. Improvement in device performance was observed for post-annealing treatment only. However, pre-annealing has decreased the device performance. These results strongly correlate with what is expected for the morphology. Notably, it is beneficial for the charge collection to have the donor segregated at the anode and the acceptor segregated at the cathode interfaces.

Thermal annealing was used to attain one of the highest performance solar cells devices based on the small-molecule system (DRCN7T: PCBM). Thermal annealing has given rise to an increase of PCE from ~ 3.5% to 9.3%.<sup>[43,93]</sup> Morphological studies have revealed an increase in crystallinity and enhancement in fibrillar networks after annealing, revealed by GIXS and TEM, respectively.<sup>[93]</sup> The hole mobility increased by an order of magnitude upon annealing. The significant increase in PCE was mainly due to an increase in both FF and Jsc.

### **2.3.3 Solvent annealing approach**

Solvent vapor annealing (SVA) is another effective method that can be used to manipulate the BHJ morphology in which the as cast film is subjected to a solvent vapor that can diffuse into the film inducing morphological development. The solvent vapor, upon its diffusion into the film, increases the mobility of BHJ components that can in turn lead to crystallization and phase segregation of the D & A phases.

This method has been used extensively to optimize the morphology of P3HT: PCBM blends. Generally solvent annealing enabled the P3HT crystallization and consequently PCBM segregation.<sup>[94–97]</sup> A study reported an increase in P3HT ordering, revealed by an enhancement in photo-physical aggregation after vapor treatment of 1,2-dichlorobenzene (DCB) which resulted in enhanced hole mobility.<sup>[97]</sup> In another study, the solubility of BHJ components in the solvent vapor was considered in P3HT: PCBM blends. The effects of using good solvents for P3HT such as (chlorobenzene (CB), chloroform (CF) and DCB) and poor solvents such as (acetone and methylene chloride) on the BHJ morphology and devices performance were investigated.<sup>[96]</sup> All solvents have resulted in improved performance as compared to the as cast film but the poor-solvent-annealed devices exhibited higher performances than good-solvent-annealed ones. The gain in the hole mobility achieved by the solvent treatment was almost identical for all solvents. Although the samples prepared by the good solvents treatment exhibited an increase in P3HT ordering, they have suffered from excessive phase separation resulted in an increase in recombination losses; the excitons recombine before reaching the D/A interface due to the over domains coarsening. Poor solvents treatment was more effective in gaining balanced mobility without increasing the recombination losses thanks to the enhanced P3HT ordering and the balanced phase separation.

In another work, three-Dimensional nanoscale morphology of P3HT: PCBM BHJ was resolved using transmission electron microscopy tomography.<sup>[94,95]</sup> The impact of SVA

on the microstructure was investigated. SVA resulted in the formation of 3D nanoscale networks of interpenetrating P3HT crystalline fibrils. Also, SVA has led favorable vertical phase separation with appropriate concentration gradients of both P3HT and PCBM through the thickness of the photoactive layer, where P3HT fibrils were accumulated at the anode layer and PCBM domains were segregated at the cathode layer. The formation of favorable vertical phase separation upon SVA treatment was supported by another study using time-of-flight secondary ion mass spectrometry (ToF-SIMS) which confirmed the accumulation of PCBM at the top surface (near the cathode interface) whereas P3HT is concentrated at the bottom surface (near the anode interface).<sup>[94]</sup>

In another study, PCE over 9.0% was achieved for small-molecules (BTR:PC<sub>71</sub>BM) BHJ system using SVA by tetrahydrofuran (THF).<sup>[98]</sup> The PCE was doubled for SVA devices as compared to the as cast non-treated ones, mainly due to an increase in FF and J<sub>sc</sub>. Both electron and hole motilities were enhanced significantly by one order of magnitude after SVA, matching with the devices performance enhancement. TEM images revealed larger and more well-defined domains for SVA samples. TEM tomograms revealed the formation of larger and inter-connected domains constituting 3D networks throughout the whole active layer after SVA. THF SVA treatment was found to improve the crystallinity of BTR as revealed by GIWAXS measurements. Moreover, texture of  $\pi$ -stacking was evolved from the random orientation into well-defined edge-on and face-on arrangements after SVA, which was argued to be more beneficial for 3D charge

transport. Overall, these enhancements to the BHJ morphology driven by the SVA treatment were responsible for achieving one of the highest performing solar cell devices in the literature. Notably, this system can afford achieving remarkable performance (high fill factor of ~70% and high PCE of ~8% ) with very thick active layer ( up to 400 nm thick ), which is an empirical requirement for roll-to-roll manufacturing.

#### **2.3.4 Solvent additives**

Solvent additive processing has been adopted for a decade to tune the BHJ morphology that has been proven to be successful in attaining the desired microstructure for efficient solar cells in wide-range of systems.<sup>[99]</sup> It involves incorporation of higher boiling solvent than the host solvent into the coating solution prior coating. One key benefit for solvent additive processing is reducing the steps of the fabrication of the active layer into one step process, unlike thermal annealing and SVA that require added step after coating. Thus, it is compatible with roll-to-roll manufacturing more than the other two techniques. However, mostly it involves usage of toxic halogenated solvents as the solvent additive that remains an obstacle for environment-friendly processing. Using either green solvents or designing D/A materials that can be processed in additive-free and annealing-free environment are key solutions towards environment-friendly roll-to-roll fabrication of organic photovoltaics.<sup>[100]</sup>

The mutual interactions between the host solvent, solvent additives and D/A materials define how solvent additive processing impacts the BHJ morphology. Empirically, two



general guidelines were adopted for host solvent and additives selection.<sup>[99]</sup> First, the solvent additives usually have selective solubility to one of the BHJ components, whereas the host solvents usually have high solubility to both D/A materials. Second, solvent additives typically have higher boiling points than host solvents. Therefore, predicating and/or quantifying the solubility of BHJ components in a given solvent can facilitate the choice of the suitable co-solvents for additive processing. One way to predict the solubility can be achieved by calculating Hansen solubility parameters which are derived from the cohesive energy density parameters, including energy from dispersion forces, dipolar intermolecular forces, and hydrogen bonding.<sup>[70,73,101]</sup> The solubility can be quantified experimentally by loading the solutes into the solvent and quantifying the dissolved and non-dissolved parts or by exposing the coated films of a given component to the vapor of the solvent and tracking their interaction.<sup>[102,103]</sup>

Generally, the influence of the solvent additives on the crystallinity in most BHJs is mainly improving the overall crystallinity, though it varies from system to another in the crystallization behavior; i.e., the number of crystallites, size and texture of the crystals and the interlayer-spacing. The solvent additives effect on the phase separation is more complicated. The additives can improve the phase separation in some systems, whereas they can suppress the oversized phase separation in others.<sup>[99]</sup>

For P3HT based solar cells, the additives were usually used to improve P3HT crystallinity and the D/A phase separation. The impacts of the additive octanedithiol (ODT) on the

crystal structure in P3HT:PCBM blend system were investigated by GIXS.<sup>[104,105]</sup> The additive ODT has led to enhanced crystallinity and the formation of larger crystallites. Also, ODT resulted in contraction of the lamellar spacing of P3HT crystallites which is also observed in separate studies. The crystallites remained with preferential edge-on orientation for both with and without ODT cases.<sup>[104]</sup> In another similar BHJ blend of P3HT: indene-C<sub>70</sub>-bisadduct (IC<sub>70</sub>BA), the additives of 3-hexylthiophene (HT) and 3-methylthiophene (MT) were used to improve the PCE from 5.80% for additive-free devices to 6.35% and 6.69% for devices processed with HT and MT additives, respectively.<sup>[106]</sup> Both additives resulted in enhanced absorption, crystallinity, and improved film morphology forming bi-continuous interconnected domains of P3HT and IC<sub>70</sub>BA.

In another study, DIO promoted the phase separation in the blend system of PCPDTBT:PC<sub>71</sub>BM. Morphological investigations have shown null phase separation of PCPDTBT:PC<sub>71</sub>BM films processed without additives, the microstructure appeared homogeneous with null contrast by TEM and AFM, revealing high degree of inter-mixing of PCPDTBT and PC<sub>71</sub>BM. On the other hand, the microstructure appeared with reasonable phase separation when DIO was used. TEM images revealed the formation of fibril-like domains of PCPDTBT and larger-sized inter-connected domains of both PCPDTBT and PC<sub>71</sub>BM. Similar behavior where additives improved the phase separation was also reported in other BHJ systems.<sup>[107–111]</sup>

On the other hand, in some polymer-fullerene systems, large-scale phase segregation on the order of hundreds of nanometers is attained when they are cast in additive-free conditions.<sup>[112–115]</sup> Solvent additive processing was utilized to suppress the oversized phase separation for variety of systems. For example, PTB7:PC<sub>71</sub>BM BHJ blends cast from pure CB solvents exhibited very coarse domains with sizes over hundred nm.<sup>[112,114]</sup> Incorporation of DIO resulted in reduced phase separation with more homogeneous nanomorphology. Quantitative analysis of the composition of phase-separated domains revealed that PC<sub>71</sub>BM was segregated into phase-separated domains with droplet shape.<sup>[116]</sup> These pristine PC<sub>71</sub>BM droplets were embedded in polymer-rich matrixes with (PTB7:PC<sub>71</sub>BM ~ 70:30 wt%).<sup>[116]</sup> Using DIO resulted in reduction of the dominant domain size from 177 nm to 34 nm. No significance change in crystalline behavior of PTB7 was observed for both additive-free and DIO-processed films.

In the context of small-molecule solar cells, the additives were mainly used to induce crystallization and increase the phase separation with a few exceptions.<sup>[117–121]</sup> For instance, DIO was used to promote the donor crystallization and phase separation in the small molecular-fullerene blends, such as p-DTS(PTTh<sub>2</sub>)<sub>2</sub>, p-DTS(FBTTh<sub>2</sub>)<sub>2</sub> and p-SIDT(FBTTh<sub>2</sub>)<sub>2</sub> blends with PC<sub>71</sub>BM.<sup>[119–121]</sup> On the other hand, DIO has resulted in reduced phase separation in porphyrin based molecule (DPPEZnP-O) blended with PCBM.<sup>[122]</sup> Nevertheless, DIO improved the crystallinity of the DPPEZnP-O in the film.

Similar behavior was observed for CNDPP:PCBM blend system, in which DIO has resulted in suppression of the domains over-coarsening.<sup>[123]</sup>

## **2.4 In situ monitoring and process diagnostics**

Understanding the mechanisms and the kinetics of film formation and morphology evolution during processing and post-treatments is of crucial importance for tuning the morphology of BHJ organic solar cells and improving their performance. Substantial ex situ and in situ studies have been done that have revealed general concepts about the relationship between processing parameters, output film morphology and devices performance. In situ studies, in particular, have shown to be more reliable in monitoring the film formation dynamics on real time and more effective in detecting the presence of intermediate phases on the route. In this section, we provide an overview of the in situ characterization techniques that have been used in the context of solution processed BHJ solar cells.

### **2.4.1 Spectroscopic reflectometry**

Spectroscopic reflectometry is a common technique for thickness measurement in many industrial applications as well as academia.<sup>[24,25,124–127]</sup> The technique involves usage of light source, white light or laser, in which the scattered light from the sample carries information about the thickness and the macrostructure. Thickness measurements can be calculated by analyzing the specular constructive and destructive interferences of the

reflected light.<sup>[124]</sup> Off specular scattering can provide information about microscale phase separation.<sup>[24,25]</sup>

Generally, spectroscopic reflectometry has been widely used in solution processing to monitor the drying kinetics *in situ* during thin film processing. A study reported systematic dependency of P3HT: PCBM film morphology on the kinetics of film formation by knife coating, as shown in **Figure 2.6**. Laser reflectometry was used to monitor the thickness evolution at different drying kinetics that was controlled by varying the temperature and flow gas rate. Thickness calculation was performed by means of transfer matrix formulation of specular interferences. At low air flow, higher phase separation was attained due to the slower drying kinetics. Similar behavior was observed when lower temperature (*ca* 15 °C) was used as compared to higher temperature (*ca* 25 °C). The improved aggregation and phase separation at low temperature was attributed to both slower kinetics and temperature-induced aggregation.<sup>[124]</sup>

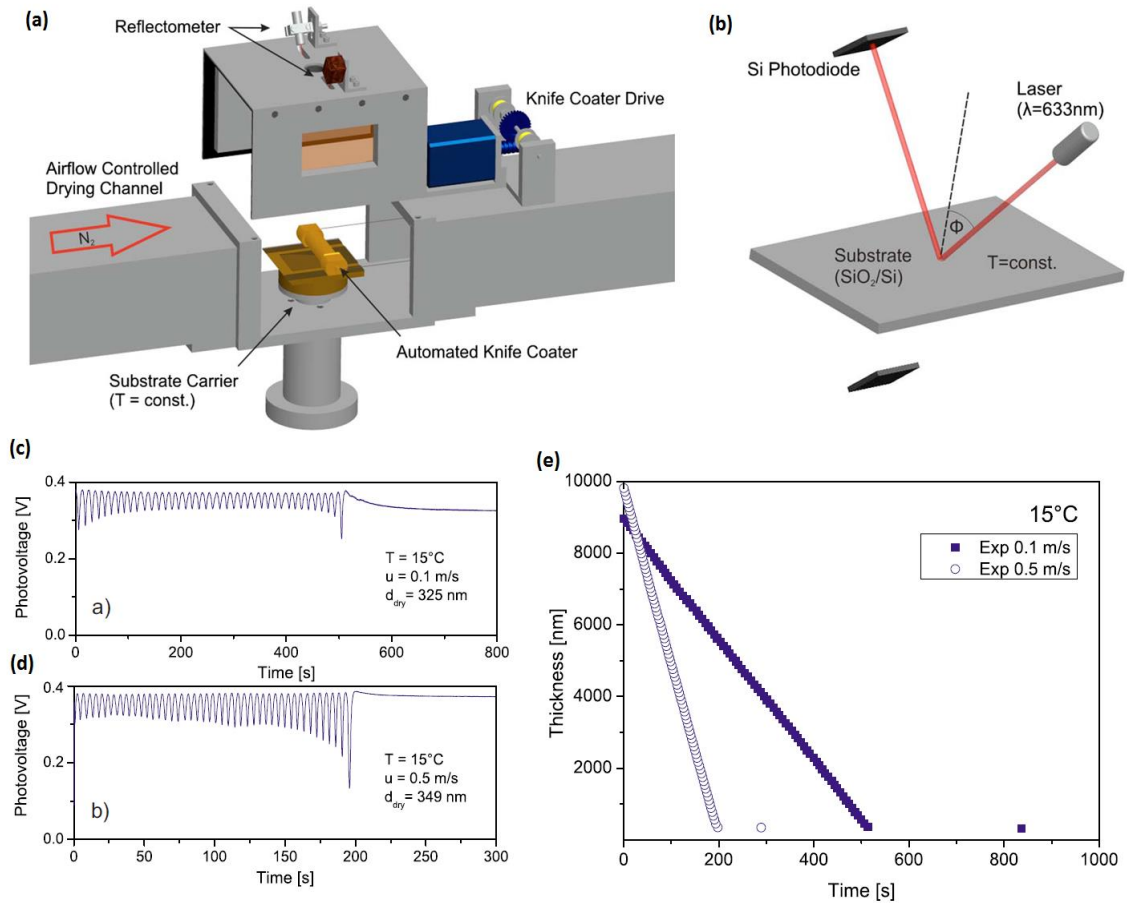


**Figure 2.6** (a) & (b) Schematics represent integrated knife coater with drying setup and laser reflectometry setup, respectively. Photovoltage vs time measured *in situ* during blade-coating of at  $15^\circ\text{C}$  and air speed of 0.1 and 0.5 m/s in (c) and (d) respectively. (e) Calculated time-dependent film thickness from (c) and (d).<sup>[124]</sup>

Off-specular scattering was utilized to investigate the mechanism of phase separation by monitoring the drying kinetics together with microscale phase separation during spin coating of blended films.<sup>[24,25]</sup> Light from laser was used whereas the scattered light from the sample was captured on CCD camera. The characteristic length of emerging

phases can be estimated from reciprocal space  $q$ -vector during film formation. In situ reflectance measurements were used to reveal the mechanism of co-solvents in preventing the formation of large fullerene-rich domains in BHJ solar cells.<sup>[24]</sup> The formation of these oversized fullerene domains is attributed to liquid–liquid phase separation that occurs in various fullerene-based BHJ systems, such as PDPP5T, PTB7, PBDTTPD, PDPPTPT, PDTG-TPD, and PBnDT-FTAZ blends with fullerene, typically when they are cast from pure solvents.<sup>[24,71,82,99,115,128]</sup> Solvent additive-processing was found to be effective in prohibiting the oversized fullerene domains and attaining the desired morphology for these systems. The study used laser reflectometry to investigate the mechanism of liquid-liquid phase separation in PDPP5T: PC<sub>70</sub>BM blends cast from pure CF and with co-solvent of CF and oDCB. Notably, oDCB is poor solvent for the polymer but good solvent for PC<sub>70</sub>BM. The intensity of specular reflected laser light (**Figure 2.7a**) was used to calculate the thickness and hence the solvent content evolution (**Figure 2.7c**) during spin coating. At the moment liquid–liquid phase separation occurs, scattering intensity arises in the out of specular direction driven by the refractive index contrast between the emerging phases; the PC<sub>70</sub>BM-rich droplets and the PDPP5T-rich solution, see **Figure 2.7b**, the onset of light scattering for pure CF case is marked by dark blue dashed line indicating the onset of liquid–liquid phase separation. For pure CF case, complete CF evaporation occurred within 0.8 s whereas the liquid–liquid phase separation occurred after 0.6 s from starting spin coating at a solute concentration of 20 vol%. On the other hand, for CF with 5% oDCB case, the film drying was prolonged to 6

s whereas no strong scattering signal was observed. However a small step, marked by dark red dashed line in **Figure 2.7b**, was detected that was attributed to scattering from small inhomogeneities caused by polymer aggregation. The thickness evolution happened in two steps; one dominated by CF evaporation that happened within 0.7 s and the other dominated by oDCB evaporation during the remaining evaporation time. This explains why a small amount of the solvent additive can induce significant changes in the morphology. Regardless of the small content of the additive in the initial formulation, the solvent mixture gets concentrated during solvent evaporation with the high boiling point solvent that is usually a poor solvent for the polymer and is believed to induce polymer aggregation. In fact, oDCB was found to force the polymer aggregation that was detected in a separate experiment using combined interference and absorption measurements. Polymer aggregation occurred at lower solute concentrations with more oDCB in the initial formulation, see **Figure 2.7c**. At a certain oDCB content (3% oDCB and above), polymer aggregation occurred early preventing liquid–liquid phase separation. However, it was found that polymer pre-aggregation alone didn't prevent the liquid–liquid phase separation. This was found by soaking a CF solution for days to induce polymer pre-aggregation but still liquid–liquid phase separation occurred when casting the pre-aggregated solution. The prevention of liquid–liquid phase separation by the co-solvent processing was attributed to the induced aggregation under supersaturated conditions at low solute content in a solvent mixture enriched by the poor solvent. The polymer aggregation, under these



supersaturated conditions, was hypothesized to form fibrillar networks that gelate the solution, thus increasing the viscosity and preventing liquid–liquid phase separation.

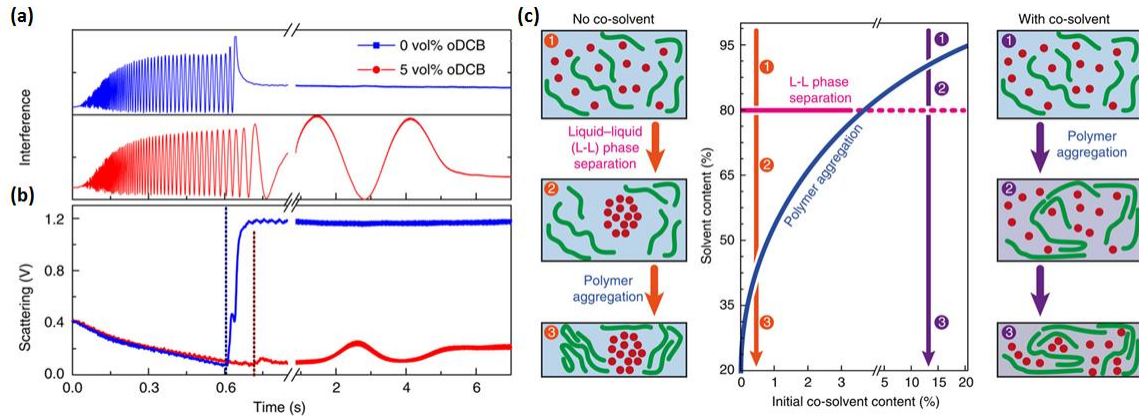


**Figure 2.7** Normalized specular interference and off-specular light scattering during spin coating of PDPP5T: PC<sub>70</sub>BM from pure CF (blue) and CF with 5 vol% oDCB (red) in (a) & (b), respectively. (c) Schematic represents the role of co-solvent preventing large-scale liquid–liquid phase separation by inducing early polymer aggregation at high solvent contents.<sup>[24]</sup>

#### 2.4.2 Spectroscopic Ellipsometry (SE)

Spectroscopic Ellipsometry (SE) is widely used technique for characterizing optical properties of thin films. Through modelling, calculation of both optical constants and film thickness can be achieved.<sup>[127,129,130]</sup> This offers the calculation of extinction coefficient that provides information about photo-physical aggregation in conjugated materials.<sup>[127]</sup> In addition, it can provide quantification of anisotropy of the optical constants in lateral and vertical directions.<sup>[129]</sup> In blended systems, quantification of the

phases is achievable via modeling such as effective medium approximation (EMA) model providing insight into vertical phase separation.<sup>[130]</sup>

For instance, spectroscopic ellipsometry was used to study the kinetics of film formation during blading of P3HT: PCBM by monitoring thickness and extinction coefficient ( $k$ ) evolution (**Figure 2.8**).<sup>[127]</sup> The roles of coating temperature and the casting solvent on the BHJ morphology were investigated. Thinning behavior was found to occur in three different stages, namely rapid, moderate and slow evaporation rates; as shown in **Figure 2.8b** for coating the blends from CB. P3HT remained solvated at the first stage as revealed by the absence of the aggregation peak at 605 nm (0-0 transition). At the second stage, rapid aggregation of P3HT was observed once the volume fraction of solutes approached 50%; indicated by sharp increase in  $k$  at 605 nm. The third stage was characterized by slow and steady aggregation after removal of most of the solvent. Coating the films at lower temperatures has resulted in the formation of coarser features, as observed in atomic force microscopy images, in correlation with the improved P3HT aggregation driven by the slower drying kinetics. Similar behavior was observed when the films were cast from 1,2,4-Trichlorobenzene (TCB) at different temperatures. More aggregation and coarser features were attained for coating conditions at lower temperatures. Moreover, at the same temperature, the samples casted from the higher boiling point TCB exhibited coarser features than the samples coated from CB, again due to the slower drying kinetics.

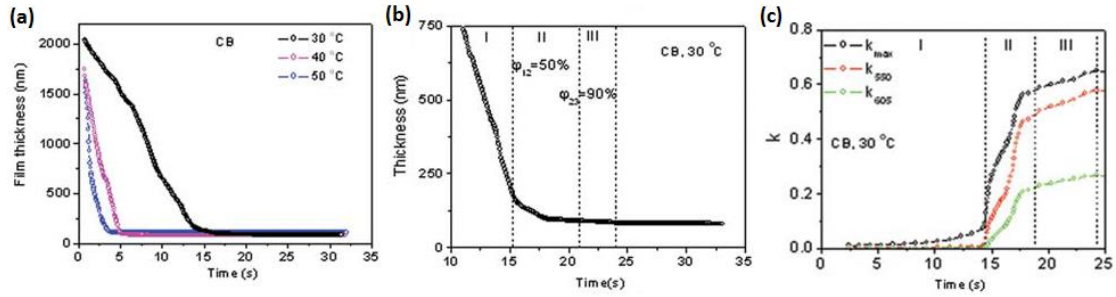


**Figure 2.8** (a) The thickness evolution of a P3HT:PCBM blend film as a function of time for blade coating blend films from CB onto a substrate held at a temperature of 30, 40 and 50 °C. (b) Re-plot the data shown in (a) for 30 °C substrates with showing the three stages of film formation. (c) The evolution of extinction coefficient ( $k$ ) at specific wavelengths during drying for 30 °C sample. <sup>[127]</sup>

### 2.4.3 UV-vis absorption

UV-vis absorption has been routinely used for measuring optical properties of semiconductors in both films and in solution state. It offers direct measurement of the optical properties, typically the absorbance, without requiring modeling. In situ UV-vis absorption can be used to monitor photo-physical aggregation during solution processing. The development of H- and J-aggregates leads to the appearance of UV-vis absorption features such as vibronic peaks and band edge shifts. <sup>[27,28,39,131]</sup> Through quantum mechanical calculations, qualitative and quantitative analysis of the degree of aggregation can be achieved. <sup>[27,28]</sup>

The effect of the casting solvents on the degree of P3HT aggregation was investigated by time resolved UV-vis absorption during blade-coating of P3HT:PCBM blends from

various solvents.<sup>[132]</sup> All the solvents used in the study were chosen to be good solvents for both P3HT and PCBM to highlight mainly the effect of vapor pressure of the solvent on the BHJ morphology. In situ UV-vis absorption revealed significant differences in the drying kinetics; longer aggregation time was observed for lower vapor pressure solvents, see **Figure 2.9**. The vibronic progressions appeared much weaker for films coated from CF and CB whereas they were significantly more pronounced for films coated DCB, TCB, and the mixed solvents DCB:CF correlating with the duration of film formation. Quantitative analysis of absorption spectra revealed reduced exciton bandwidth ( $W$ ) for films coated from low vapor pressure solvents (DCB, TCB, and DCB:CF) indicating enhancement in backbone planarity and increased conjugation length. Simultaneously, the hole mobility was found to increase in consistent with the improved P3HT ordering for films coated from low vapor pressure solvents. The device performance was found to increase with lower vapor pressure solvents up to a threshold value then decreased dramatically for TCB.

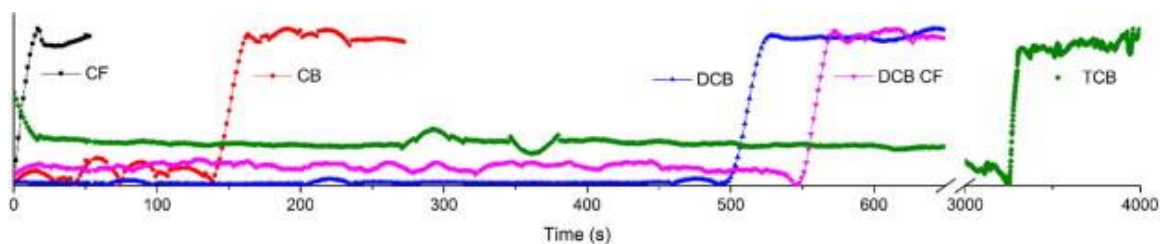


**Figure 2.9** Time evolution of  $\lambda_{\max}$  during blade coating of P3HT:PCBM from various solvents.<sup>[132]</sup>

The role of solvent additives on the film formation of PCPDTBT: PC<sub>71</sub>BM blends was investigated using time resolved UV-vis absorption.<sup>[133]</sup> UV-vis absorption was recorded on static samples directly after interrupting spin coating of PCPDTBT: PC<sub>71</sub>BM films casted from 1,2,4-trichlorobenzene (TCB) with 2% v/v 1,8-diiodooctane. Both TCB and DIO absorb near 250 nm but only TCB has vibronic structure, see absorption spectra in **Figure 2.10**. The vibronic structure near 250 nm disappeared after 18 min indicating depletion of TCB and is represented by changing color from black to blue. Simultaneously, red shift of absorption spectra and progression of PCPDTBT vibronic peaks around 800 nm were observed in consistent with TCB depletion. Vibronic progressions were found to continue to increase afterwards during the additive (DIO) evaporation. When DIO was used, the aggregation of the polymer happened in two steps; one was driven by the depletion of the host solvent TCB and the other by the slow evaporation of the higher boiling point solvent additive DIO. DIO has extended the polymer aggregation time leading to higher degree of aggregation and chain planarization for the additive-processed sample as compared to the sample coated from pure TCB.

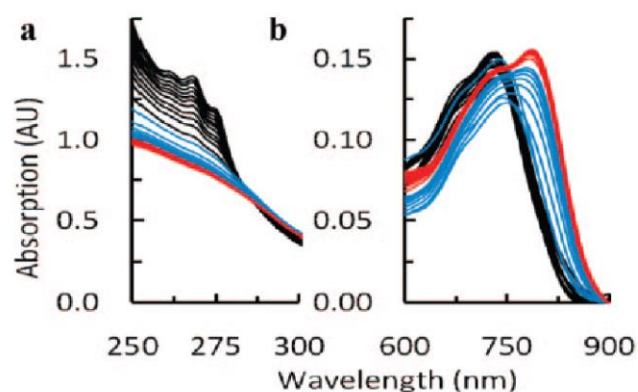


**Figure 2.10** Absorption spectra in the (a) 250-300 nm range and (b) 600-900 nm range as a function of time after spin-coating for 10 s at 2000 rpm from TCB with 2% DIO in 90 s intervals (black and blue) and then 10 min intervals (red).<sup>[133]</sup>

#### 2.4.4 Raman spectroscopy

Raman spectroscopy has been used in characterization of molecular ordering of conjugated semiconductors due to sensitivity of Raman modes to  $\pi$ -electron delocalization. Raman modes are affected by the degree of ordering and planarity of the backbone in semiconducting polymers. In P3HT, the in-plane ring skeleton modes at  $1445\text{ cm}^{-1}$  (symmetric C=C stretch mode) and at  $1381\text{ cm}^{-1}$  (C-C intra-ring stretch mode) are very sensitive to quality and quantity of aggregation.<sup>[30,31]</sup> Shift of symmetric C=C stretch mode peak to lower value besides reduction in its full width at half maximum (FWHM) are signatures of increase in ordering and planarity of P3HT backbone.<sup>[134]</sup> Broadening of that mode can be explained as contribution from ordered and disordered phase which makes quantifying degree of aggregation possible.

Time resolved Raman spectroscopy has been used to investigate the effect of solvent vapor annealing in P3HT: PCBM BHJ.<sup>[30]</sup> The as cast P3HT: PCBM film exhibited lower degree of P3HT ordering as compared to the neat P3HT sample indicated by the higher FWHM of C=C stretch mode peak, see **Figure 2.11 b**, due to the presence of PCBM that hindered P3HT aggregation in the blend sample. SVA increased P3HT ordering in the blend film as revealed by narrowing of C=C stretch mode peak after SVA treatment, see **Figure 2.11 a**. During SVA, FWHM of C=C stretch mode peak was found to decrease for both neat and blend films indicating an increase in P3HT aggregation and backbone planarity. P3HT ordering was saturated within 50 s for the neat sample but it took longer time for the blend sample; the degree of P3HT ordering in the blend sample almost approached the degree of ordering in the neat sample within 100 s. The results from Raman spectroscopy were consistent with TEM images taken for as cast and annealed films that revealed an increase in P3HT ordering and improved phase separation.

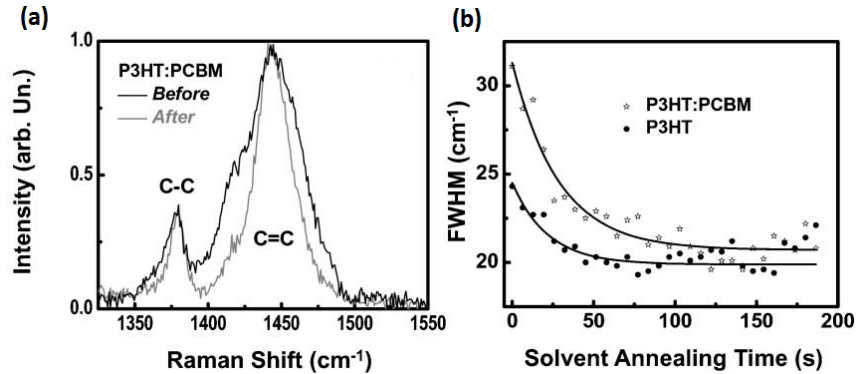


**Figure 2.11** (a) Normalized Raman spectrum of P3HT: PCBM films before and after solvent vapor annealing. (b) Time evolution of the FWHM of symmetric C=C stretching mode of P3HT (at  $1440\text{ cm}^{-1}$ ) during solvent vapor annealing of pure P3HT and P3HT: PCBM. <sup>[30]</sup>

Another study reported monitoring the morphological evolution during heating and cooling cycles of thermal annealing of P3HT: PCBM BHJ by in situ Raman spectroscopy.

<sup>[30]</sup> During heating, P3HT became disordered abruptly upon crossing  $130\text{ }^{\circ}\text{C}$ , as shown in **Figure 2.12a**, due to crossing the glassy temperature of P3HT. During cooling, P3HT ordering was observed to enhance rapidly at  $100\text{ }^{\circ}\text{C}$  into higher degree of ordering than its initial value. Investigation of the effect of annealing temperature has shown that the highest degree of P3HT ordering was attained for  $130\text{ }^{\circ}\text{C}$  annealing condition, as revealed by the lowest FWHM (**Figure 2.12b**). Devices fabricated at this temperature exhibited the highest solar cell performance as compared to other annealing temperatures.



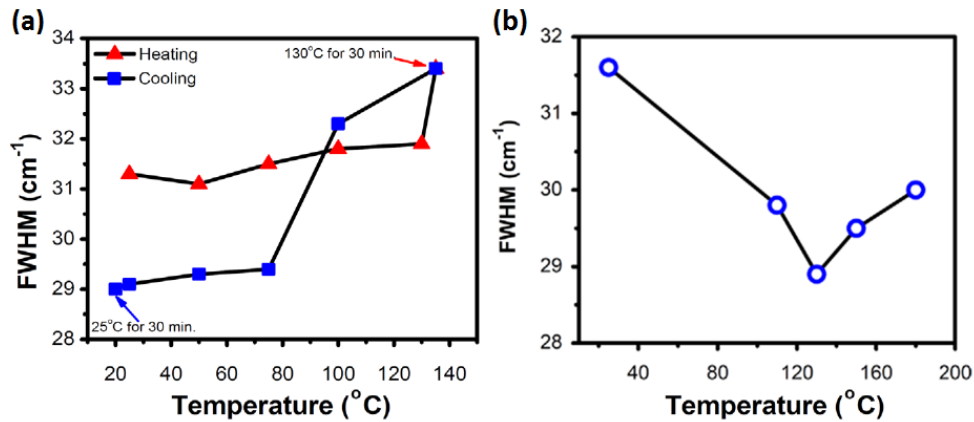


**Figure 2.12** FWHM of symmetric C=C stretching mode of P3HT versus temperature obtained by in situ Raman spectroscopy during heating and cooling cycles of of P3HT: PCBM films in (a) and static Raman at room temperature of annealed samples as a function of annealing temperature in (b).<sup>[31]</sup>

#### 2.4.5 Grazing incidence X-ray scattering

Synchrotron-based grazing incidence X-ray scattering (GIXS) has been a useful tool for characterization of crystallographic structure and nanoscale morphology in thin films.<sup>[135–140]</sup> In BHJ films, it provides unique insight into crystallization of the D & A besides the nanoscale phase separation. Although GIXS measurements can be performed at a synchrotron or at laboratory, the synchrotron source is more optimal for in situ GIXS experiments due to its high flux and collimation of the X-ray beam.<sup>[22,137]</sup> For thin film characterization, it can be done at two main configurations. One configuration is grazing incidence wide angle X-ray scattering (GIWAXS) which is sensitive to molecular scale crystal structure enabling determination of crystal structure besides estimation of the average crystal size and the texture of the crystals.<sup>[135]</sup> The other is grazing incidence

small angle X-ray scattering (GISAXS) which is sensitive to larger length scales ranging from several nanometers to tens of nanometers enabling determination of nanoscale phase separation.<sup>[135]</sup>

Dynamic investigation of BHJ formation was reported during spin coating using combined GIWAXS and GISAXS.<sup>[22]</sup> The kinetic evolution of P3HT lamellar crystallization and phase separation of PCBM and P3HT was monitored during spin coating by GIWAXS and GISAXS, respectively. BHJ formation occurred in four characteristic steps as summarized in **Figure 2.13a**, marked as circled letters (a) to (d). The first step (a) is the solution ejection that was characterized by strong increase in the scattering intensity due to the abrupt decrease in thickness of the bulk solution. At that step, no signatures of crystallinity from P3HT or PCBM were observed. In the second step (b), a weak texturing of lamellar formation of P3HT was observed oriented parallel to substrate. At the third step (c), sharp increase in intensity of both GIWAXS and GISAXS indicating rapid lamellar crystallization of P3HT and phase separation of PCBM. At the final step (d), the morphology evolution was saturated; both crystallization and phase separation reached plateau during this step. The effect of PCBM loading on the onset and period of film formation was investigated. **Figure 2.13b** shows the dependence of the onset ( $t_{\text{onset}}$ ) and period ( $\Delta t_{\text{formation}}$ ) of film formation on P3HT: PCBM ratio. Adding PCBM was found to decrease the time before the onset of film formation; however it resulted in an increase in the period of film formation that peaked at 1:1 ratio then decreased for more PCBM loading.

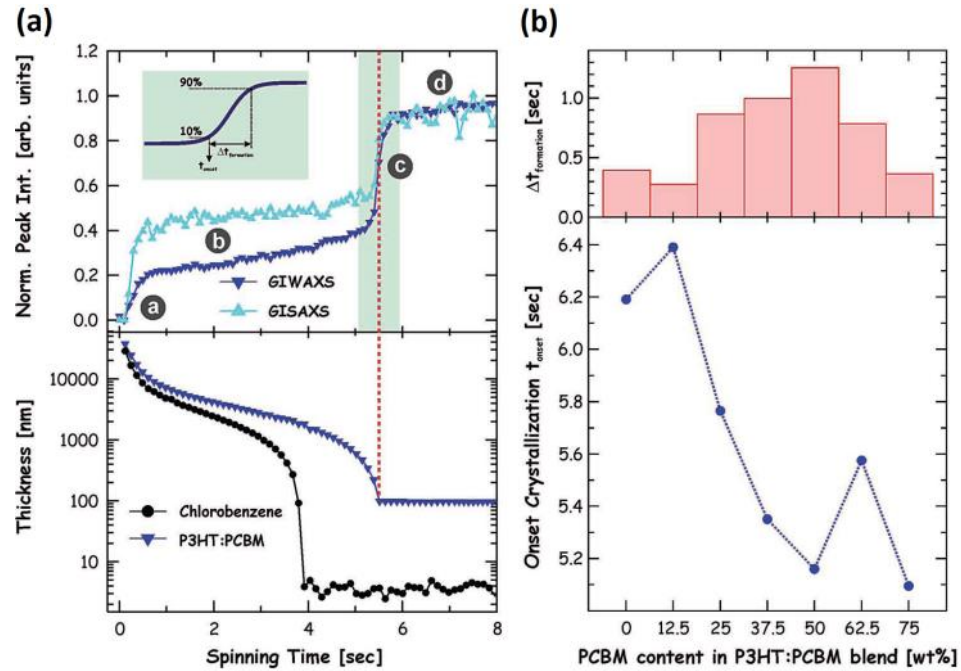


**Figure 2.13** (a) Normalized GIWAXS and GISAXS scattering intensities as a function of the spinning time during spin-coating of P3HT: PCBM (62.5 wt%:37.5 wt%) on the top and time-resolved thickness for the same sample on the bottom. (b) The onset of film formation ( $t_{onset}$ ) and its duration ( $\Delta t_{formation}$ ) for different P3HT: PCBM blend ratios. <sup>[22]</sup>

In PCPDTBT:PC<sub>71</sub>BM BHJ system, addition of small amount of ODT into casting solution from CB was found to induce polymer crystallinity and enhance phase separation. <sup>[141]</sup>

In situ GIWAXS measurements were used to reveal the solvent additive effects on the BHJ formation. The in situ experiments were done just after spin coating. <sup>[141]</sup> For the films coated from pure CB, the films suffered from poor polymer crystallinity revealed by isotropic amorphous scattering pattern. No microstructure development was

observed for the completely dry film after spin coating. On the other hand, for the additive-processed sample, nucleation of PCPDTBT crystallites was observable immediately after spin coating (possibly induced during spin coating) and crystallization continued for more than an hour, see the evolution of total scattering intensity in **Figure 2.14a**. The early polymer crystallization was attributed to reduction of the nucleation barrier for polymer crystallization induced by ODT at early stage of film formation, possibly induced during spin coating. ODT was found to promote the formation of specific polymorphs of the polymer. The polymer alkyl stacking appeared with two peaks; one observed near  $5 \text{ nm}^{-1}$  oriented mainly out-of-plane (labeled (100) ) and the other observed near  $5.5 \text{ nm}^{-1}$  oriented mainly in-plane (labeled (100)'), see **Figure 2.14b**. The crystallites of (100) peak were found to densify during film drying indicated by shift of the peaks towards higher q-space (i.e lower d-spacing). It is worth to note that thermal annealing failed to induce the polymer crystallization and attain the desired morphology that was achievable by the solvent additives.

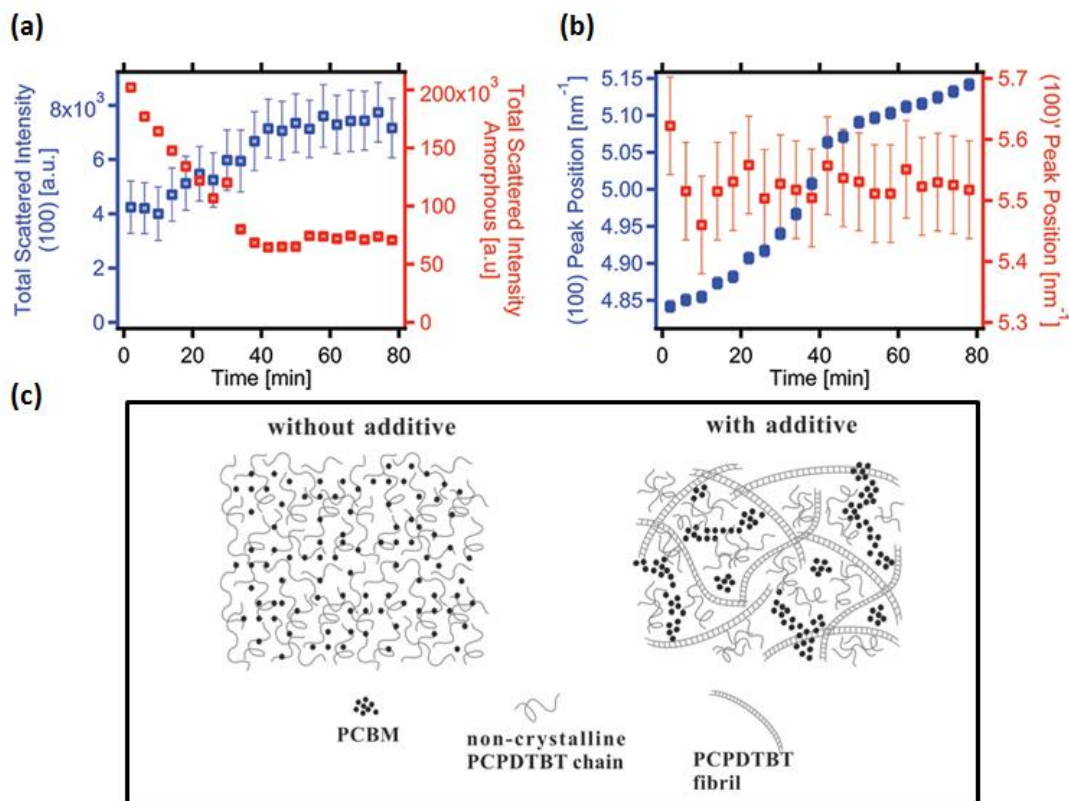


**Figure 2.14** (a) Evaluation of total scattered intensities from the alkyl stacking peak (blue) and the amorphous region (red) versus time after spin coating of PCPDTBT:PC70BM from CB containing 3% ODT.<sup>[141]</sup> (b) Time-evolution of the peak position of the (100) peak (blue) and the (100)' peak (red) of the same sample in (a).<sup>[141]</sup> (c) Schematic represents the morphology of PCPDTBT:PC<sub>70</sub>BM with and without additives.<sup>[142]</sup>

Another *in situ* study of the same system used in situ GIWAXS to monitor the structural evolution of drop-cast PCPDTBT:PC<sub>71</sub>BM blends from solution state to solid state.<sup>[142]</sup>

Again, the blend film cast from pure CB appeared amorphous with only scattering from PC<sub>71</sub>BM. A variety of additives were used in this study, including 1,8-diiodooctane (DIO),

1,8-octanedithiol (ODT), and 1,8-dichlorooctane (DCO). All additives were found to improve the crystallinity and phase separation in the casted film and enhanced the performance of the fabricated devices. Amongst all additives, DIO was found to give the highest performance and the in situ experiments were focused on the DIO additive effect. The in situ study revealed insight into the mechanism of the additive DIO that also can be translated to the other additives. During CB evaporation, DIO gets concentrated in the solution which is poor solvent for the polymer and good solvent for PC<sub>71</sub>BM. This forces the polymer to crystallize early forming fibrillar network while PC<sub>71</sub>BM remains solubilized. As DIO evaporates, the remaining polymer crystallizes and PC<sub>71</sub>BM aggregates filling the spaces between the initially formed PCPDTBT fibrillar crystallites. A schematic represents the morphology of the BHJ with and without additives is presented in **Figure 2.14c**.

Another study used combined in situ GIWAXS and GISAXS to investigate the effect of the solvent additives in pDPP:PC<sub>71</sub>BM blends.<sup>[143]</sup> On the contrary to the previous example, the additive function in this system is reducing the over-coarsening of PC<sub>71</sub>BM domains that occur when the blends are cast from pure solvents such as CF. The co-solvent CF/oDCB was found to be effective in attaining more finely mixed morphology. BHJ structural evolution occurred in four distinct stages. At the initial stage of solvent evaporation, the increase of oDCB concentration in the solution, which is a poor solvent for pDPP, was found to force pDPP crystallites formation whereas PC<sub>71</sub>BM remains solubilized. In the second stage, after CF complete evaporation, the deterioration of

solvent quality resulted in more pDPP crystallization forming networks of pDPP fibrils. In the third stage, the remaining pDPP crystallized and PC<sub>71</sub>BM segregated between the spaces of the fibrillar network. This view was confirmed by the calculated characteristic length scale of PC<sub>71</sub>BM domains that was found to be smaller than the mesh size of the fibrillar network. Finally, the structural evolution reached a steady state after complete evaporation of the solvents. The mechanism of the additive in this system wasn't so different from the previous example (PCPDTBT:PC<sub>71</sub>BM), however, leading to opposite function.

## Chapter 3

### Methodology and general description of the work

#### 3.1 Introduction

In this chapter, we present the general experimental methodology used throughout the dissertation. These include in situ characterization to monitor thin film formation, ex situ measurements to characterize the microstructure and properties of the thin films. Solar cell devices fabrication and characterization was done to investigate the correlation between solution ink formulation, processing conditions, thin film structure and morphology, and solar cell device performance.

#### 3.2 *In situ* characterization techniques

##### 3.2.1 Thickness evolution measurements by combined spectroscopic reflectometry and ellipsometry

Spectroscopic reflectometry is a commonly used technique for thickness measurement. A collimated white light source specularly reflects from the sample and collected and analyzed to estimate the thickness of thin films. The thickness is determined by analyzing interference fringes of the reflected light while the positions of maxima and minima of constructive and destructive interference, respectively, provide an easy way to deduce the thickness using the standard interference condition formula <sup>[124]</sup>:

$$\Delta = 2d \sqrt{n^2 - (\sin(\theta))^2}$$



$$\Delta_{\text{constructive}} = m\lambda \quad \text{and} \quad \Delta_{\text{destructive}} = (m-1/2)\lambda \quad (3.1)$$

where  $\theta$  is the incidence angle (the angle between the normal and the incident beam),  $n$  is refractive index,  $d$  is thickness and  $m = 1, 2, 3, \dots$

Optical reflectometry is thus used to monitor the thinning behavior of solutions during film formation.

Spectroscopic Ellipsometry (SE) is widely used optical technique for characterizing optical properties of thin films. It uses the change in light polarization as the light interacts with the thin film to characterize its optical properties, see **Figure 3.1**.<sup>[144]</sup> The change in the state of polarization of light is usually measured and recorded as two angles ( $\Psi$  and  $\Delta$ ) which are related to the ratio of the field reflection coefficients,  $R$ , for p-polarized vector (electric field in the plane of incidence) or s-polarized vector (electric field perpendicular to the plane of incidence) ( $R_p:R_s$ ) as<sup>[144]</sup>:

$$\rho = \frac{R_p}{R_s} = \tan(\Psi)e^{i\Delta} \quad (3.2)$$

where ( $\rho$ ) is the ratio of the reflectivity for p-polarized light ( $R_p$ ) divided by the reflectivity for s-polarized light ( $R_s$ ). Upon light reflection, the reflected light undergoes amplitude and phase changes which are quantified by the two parameters;  $\tan(\Psi)$  and  $\Delta$  correspond to the amplitude ratio upon reflection and the phase shift, respectively. The measured ellipsometric parameters ( $\Psi$  and  $\Delta$ ) are related to the material optical constants  $n$  and  $k$  through the complex dielectric function by the following equation<sup>[144]</sup>:

$$\langle \varepsilon \rangle = \langle \varepsilon_1 \rangle + i \langle \varepsilon_2 \rangle = (\langle n \rangle + i \langle k \rangle)^2 = \sin^2(\theta_i) \cdot \left[ 1 + \tan^2(\theta_i) \cdot \left( \frac{1-\rho}{1+\rho} \right)^2 \right] \quad (3.3)$$

Where “ $\varepsilon_1$ ” and “ $\varepsilon_2$ ” are the complex dielectric function values,  $n$  and  $k$  are refractive index and extinction coefficient, respectively.  $\theta_i$  is the incident angle.

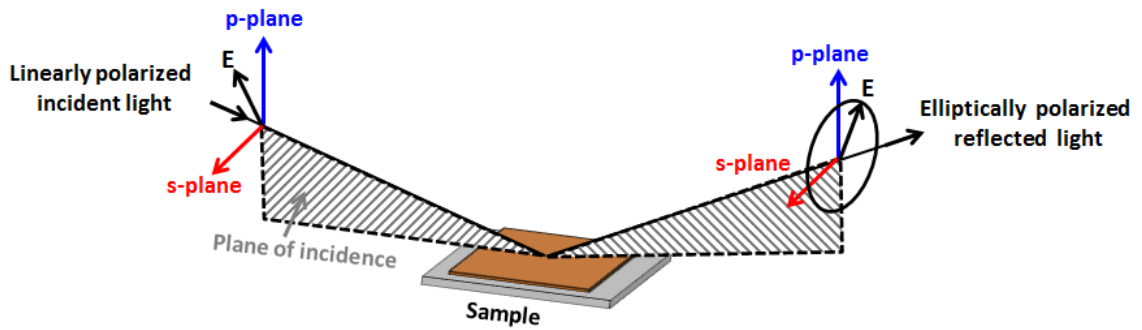


**Figure 3.1** Schematic represents the interaction of an incident linearly polarized light with a sample.

An optical multilayer model calculation is required to get optical constants and film thickness. Models allow introducing non-idealities such as layer non-homogeneities, interface mixing and surface roughness.<sup>[144]</sup> One of the benefits of the technique is that it allows estimation of thickness and dielectric constants simultaneously. Extinction coefficient provides information about J and H photophysical aggregates in conjugated materials as discussed in the previous chapter.<sup>[127]</sup> Besides, anisotropy of optical constants for uniaxial films (symmetric in-plane with different out of plane component) and biaxial films (asymmetric in plane besides out of plane component) can be modeled effectively.<sup>[129]</sup> In addition to that, quantification of vertical composition profile (donor and acceptor ratio) of bulk heterojunction can be obtained via effective medium

approximation model.<sup>[130]</sup> On the other hand, being model dependent technique is the main limitation. Prior information about the film and substrate is required for adequate modelling. Samples with thick films, high roughness and multilayered films are difficult to characterize its optical properties via modeling. For *in situ* experiments, particularly, spectroscopic ellipsometry at single acquiring angle is required for fast measurement. In single angle configuration, the technique suffers from weakness in reliability of modeling.

*In situ* spectroscopic ellipsometry (M-2000XI, J. A. Woollam Co., Inc) measurements and *in situ* reflection measurements were performed simultaneously to monitor the thinning of the solution and thin film formation during the spin coating process. For these reflection-mode measurements, a single crystal silicon wafer (100) with a 300 nm-thick thermal oxide was used as substrate, in otherwise identical processing conditions. The reflection spectra were analyzed using the Fast Fourier Transform method, which provides a first order estimate of solution thickness over the thickness range from  $\sim 10^5$  to  $\sim 10^3$  nm for white light sources without requiring an elaborate model fit. The SE spectra were obtained at an incidence angle of  $70^\circ$  from substrate normal and were analyzed in the transparent spectral range of P3HT, namely from 750 to 1700 nm. The optical properties of blend solutions and thin films were modelled assuming a Cauchy dispersion relation and an isotropic thin film using the EASE<sup>TM</sup> and WVASE32 software packages (J. A. Woollam Co., Inc).

### 3.2.2 Time resolved UV-vis absorption measurements

We have performed in situ absorption measurements using a F20-UVX spectrometer (Filmetrics, Inc.) equipped with tungsten halogen and deuterium light sources (Filmetrics, Inc.) and were restricted to a wavelength range of interest. Measurements were performed with an integration time of 0.1-0.5 s per absorption spectrum.

A collimated beam of white light in the UV-vis range (350 -1100 nm) is shined onto the sample and the fraction of absorbed light is estimated using transmittance measurements. Transmittance measurements are performed through films coated on a transparent substrate and absorbance can be calculated directly from the measured transmittance using Beer–Lambert law ( $A_\lambda = -\log_{10} T$ ; where  $A_\lambda$  is the absorbance at a certain wavelength ( $\lambda$ ) and  $T$  is the transmittance at corresponding wavelength ( $\lambda$ )). No modeling is required to extract absorbance in transmission mode.

#### 3.2.2.1 Quantitative analysis of P3HT thin films

Quantitative analysis of the degree of photo-physical aggregation in organic semiconductors can be done by modeling the absorption spectra. Two types of photo-physical aggregates should be considered in conjugated oligomers and polymers; namely J-aggregates and H-aggregates.<sup>[27]</sup> For oligomers, J-aggregates correspond to chromophores oriented in a head-to-tail stack, whereas H-aggregates correspond to chromophores oriented in a side-by-side stack. For polymers, a single polymer chain can be considered as head-to-tail arrangements of monomer repeat units constituting J-aggregate, however, in bulk, polymers exhibit hybrid photo-physical behaviour, whereas

there is a competition between interchain interactions, which favor H-like behaviour, and intrachain interactions, which favor J-like behaviour.

We have analysed the absorption spectra using a model introduced by Spano and modified by Silva and Neher.<sup>[27,28,131]</sup> The absorption spectrum was fitted using the equation below<sup>[39,131]</sup>:

$$A(E) \propto \sum_{m=0} \left( \frac{S^m}{m!} \right) \times \left( \mathbf{1} - \frac{W e^{-S}}{2E_p} \sum_{n \neq m} \frac{S^n}{n!n - (m)} \right)^2 \times \exp \left( \frac{\left( E - E_{0-0} - m E_p - \frac{1}{2} W S^m e^{-S} \right)^2}{2 \sigma^2} \right) \dots (3.4)$$

where  $A$  is the absorbance as a function of the photon energy ( $E$ ).  $E_{0-0}$  and  $E_p$  are the 0-0 transition energy and the intermolecular vibrational energy, respectively.  $W$  is the free exciton bandwidth.  $\sigma$  is the Gaussian linewidth.  $S$  is the Huang-Rhys factor.  $m$  and  $n$  are differing vibrational levels.

### 3.2.3 *In situ* Grazing incidence wide angle X-ray scattering (GIWAXS) measurements

*In situ* and *ex situ* two-dimensional (2D) GIWAXS experiments were performed at beamline D1 at the Cornell High Energy Synchrotron Source, Wilson Lab, NY, USA. A fast 2D detector (PILATUS 100 k from Dectris) was used with a framing rate of 10 Hz and an exposure time of 0.1-0.5 seconds, to record the scattering pattern during the spin coating process. The used CCD camera allows rapid acquisition of large range of scattering angles simultaneously and thus it is the typical used configuration for *in situ* experiments. On the other hand, it lacks resolution and accuracy compared to point and line detector configurations. *In situ* GIWAXS measurements during spin coating were

performed in ambient air. A schematic representation of the GIWAXS experiments is shown in **Figure 3.2**. The wavelength of incident X-ray beam was 1.1555 Å and the width of the beam was about 1 mm. Silver behenate is used to calibrate the lengths in the reciprocal space. In situ GIWAXS experiments were done at a shallow angle of 0.17° with respect to the sample plane. Ex situ GIWAXS experiments were performed at variable angles ranging from angles below the critical angle to above the critical angle of the organic film.

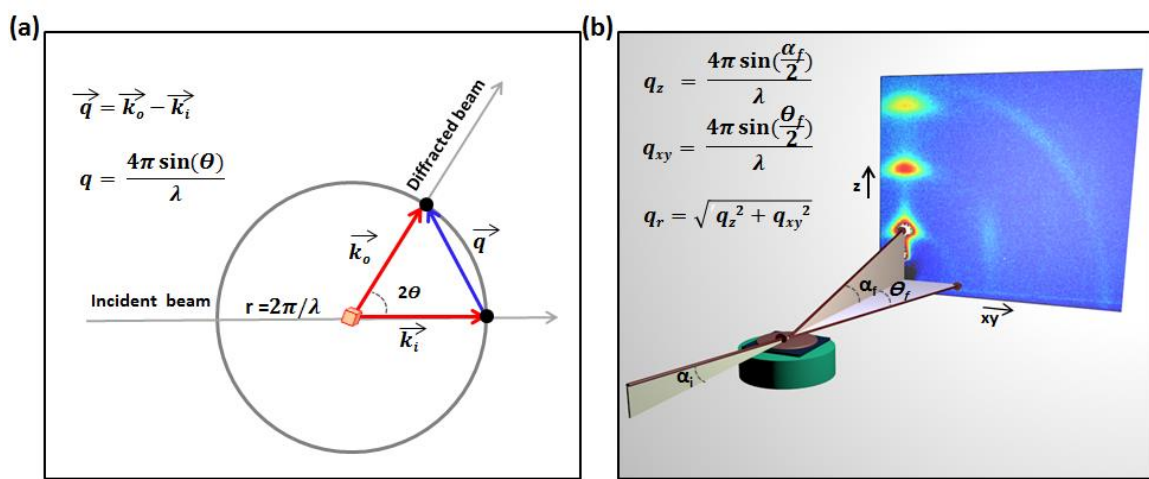


**Figure 3.2** (a) Simplified schematic represents the scattering experiment; diffraction peak appear when the reciprocal-space of a crystal (black dot) intersects the Ewald sphere. (b) Schematic represents GIWAXS experiments; scattering is collected by 2D detector.  $q_z$  and  $q_{xy}$  correspond to the scattering in the out-of-plane and in-plane directions, respectively.  $\alpha_i$ ,  $\theta_f$  and  $\alpha_f$  correspond to incident angle, out-of-plane scattering angle and in-plane scattering angle, respectively.

Three regimes should be considered for GIWAXS<sup>[135]</sup>: (1) For incidence angles lower than the critical angle (the angle below which total external reflection occurs), the beam forms an evanescent wave and the penetration of the beam is limited to several nanometers near the surface and this configuration allows probing crystalline structures near the surface. (2) For incidence angles larger than the critical angle of both the film and the substrate, scattering from both the film and the substrate is attained. However, this configuration suffers from a strong background from the substrate. (3) In the most common configuration for organic thin films, the incidence angle is tuned between the critical angle of the film and the substrate in order to probe the entire film and exclude substantial background scattering from the substrate. Here, the materials in the study have critical angles ( $\sim 0.12$  -  $0.13^\circ$ ), whereas the substrates (typically Si or SiO<sub>2</sub>/Si) have critical angle ( $\sim 0.23$  -  $0.25^\circ$ ). Two of these configurations were used in the studies reported in this dissertation. The first and third configurations were used to probe the top surface of the film and the entire thin film, respectively, with minimal contribution from the substrate.

We have used GIWAXS measurements to probe the microstructure, texture and polymorphism of organic thin films, and to estimate the relative crystallinity and average crystallite size.<sup>[135,136,138]</sup> The shape and azimuthal distribution of the diffraction peaks can be related to the texture of the crystals orientation see **Figure 3.3**. For crystallites with lattice planes oriented perfectly parallel to the substrate, well pronounced Bragg peaks appear in the out-of-plane direction (**Figure 3.3a**). In case of

crystallites oriented in parallel and perpendicular orientations, well pronounced Bragg peaks appear in both the out-of-plane and in-plane directions (**Figure 3.3b**). When the crystallites have more textured orientations with angular distribution around the horizontal alignment, Bragg diffraction broadens and appears as partial arc in the out-of-plane direction (**Figure 3.3c**). For randomly oriented crystals, Bragg peaks exhibit powder-like diffraction patterns and appear as full scattering rings (**Figure 3.3d**).

The average crystal size ( $D_c$ ) of the crystallites can be defined by Scherrer equation<sup>[145]</sup>:

$$D_c = \frac{K \cdot \lambda}{B \cdot \cos(\theta_B)} \quad (3.5)$$

Here,  $K$  is dimensionless shape factor and is used as  $K=1$ .  $\theta_B$  is the Bragg angle.  $B$  is the line broadening at FWHM and can be calculated by  $B = \Delta(2\theta_{FWHM}) = 2(\Delta q_{FWHM} \cdot \lambda/4\pi)$ . Alternatively, crystalline Correlation length (CCL) can be calculated by (CCL =  $2\pi/\text{FWHM}$ ).

The relative degree of crystallinity (RDC) can be compared between different films by integrating the GIWAXS intensity across all orientations using the following equation<sup>[115,140]</sup>:

$$RDC \propto \int_0^{\pi/2} \sin(\chi) I(\chi) d\chi \quad (3.6)$$

where  $\chi$  is the orientation angle.  $\sin(\chi)$  is geometrical correction factor.  $I$  is the GIWAXS intensity.



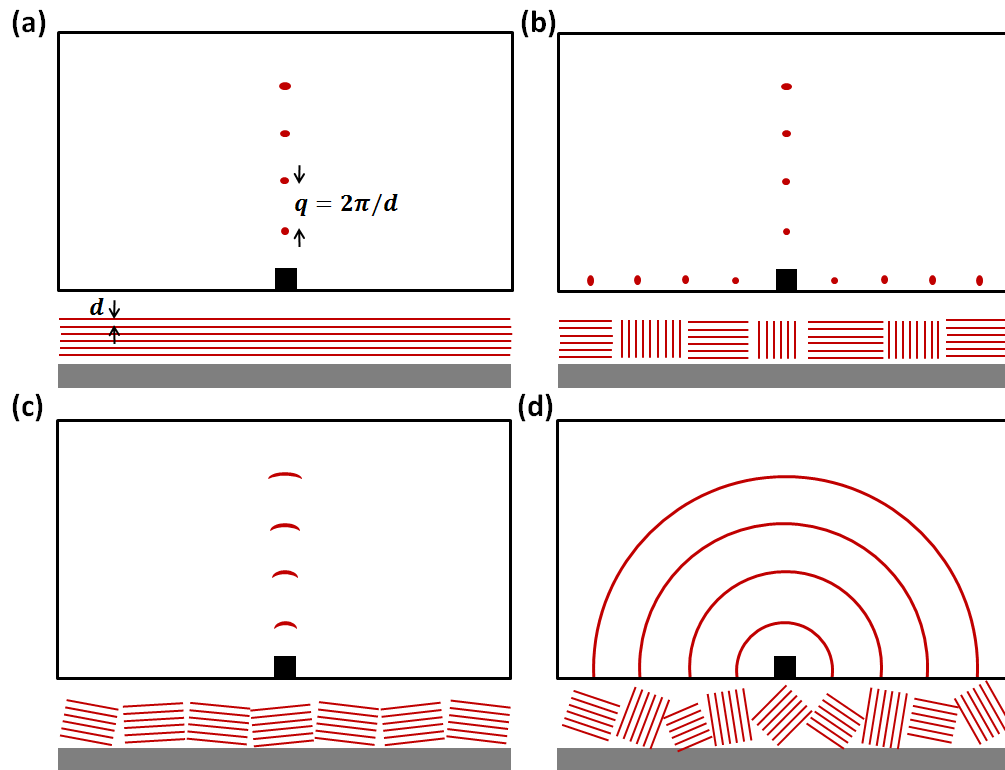


**Figure 3.3** Schematics represent 2D GIWAXS scattering of crystallites at different orientations. The crystallites are represented as red lines corresponding to crystallographic planes with spacing ( $d$ ) between the planes. (a-d) Crystallites with crystallographic planes: (a) oriented parallel to the substrate, (b) oriented in both directions, parallel and vertical to the substrates, (c) oriented with an angular distribution around the horizontal alignment, and (d) randomly oriented crystallites. Schematics are adapted from reference<sup>[135]</sup>.

### **3.3 *Ex situ* characterization techniques**

#### **3.3.1 Transmission Electron microscopy (TEM)**

TEM microscopy images were acquired using transmission electron microscope (Titan Cryo Twin, FEI Company, Hillsboro, OR) with a 4k x 4k charged couple device (CCD) camera model US4000 and an energy filter model GIF Tridiem from Gatan, Inc. (Gatan Inc., Pleasanton, CA). The GIF was utilized in energy-filtered TEM (EF-TEM) mode to image the Carbon and Sulfur distribution in the sample. The Carbon edge located at 284 eV and Sulfur edge at 165 eV were selected to generate the EF-TEM maps using a 3-window method. The samples were prepared by floating the active layer on water and transferring onto a copper (400 mesh) grid.

#### **3.3.2 Atomic force microscopy (AFM)**

Atomic force microscopy (AFM) images were taken by a high precision Agilent 5400 SPM/AFM housed in an isolation chamber. Atomic force microscopy measurements were performed to investigate the surface topography of the thin films and to calculate their surface roughness. Phase imaging by AFM reveal information about the size and shape of existing phases on the top surface.

#### **3.3.3 Transmission polarized optical microscopy (POM)**

Transmission polarized optical microscopy was performed on a Zeiss Axio Imager Z1m microscope. The temperature dependent transmission polarized optical microscopy was collected with an Olympus BX51 (with LMPlanFL N 50x objective) in combination with a

temperature-controlled microscope stage (Linkam LTS 420). In both cases, micrographs were taken with a Canon 5D Mark II.

### **3.3.4 Flash Differential Scanning Calorimetry (F-DSC)**

Differential scanning calorimetry (DSC) has been widely used to study crystallization of materials during heating and cooling cycles.<sup>[146–149]</sup> Most of reported DSC studies of solution-processed organic and inorganic materials rely on conventional DSC with typical low heating/cooling rate (ca. 10 °C/min). However, solution processing may involve metastable transitions that appear at fast film formation conditions and thus are difficult to detect by conventional DSC. The ultra-fast flash DSC (F-DSC), which is not yet widely adopted by organic/inorganic electronic community to the best of our knowledge, enables to mimic practical conditions and to study crystallization dynamics and (meta)stability at conditions far from equilibrium with the notion of possible differences between crystallization from melt and from solution.<sup>[150–156]</sup>

Flash Differential Scanning Calorimetry (F-DSC) was performed with a Mettler-Toledo Flash DSC 1 under N<sub>2</sub> atmosphere. The UFS1 differential scanning calorimeter chips (i.e. a thin film chip sensor composed of a thin free standing SiN<sub>x</sub> film on a silicon frame with a measuring area of 60 μm by 60 μm) were calibrated by the manufacturer and conditioned prior to use. Powder samples were then placed directly in contact with the sensor. Before data were recorded, the samples were heated to 400 °C and back to -80

°C at a rate of 5000 K/s, which erased the thermal history and ensured sufficient contact between the sample and sensor.

### **3.4 Solar cell devices fabrication and characterization**

#### **3.4.1 Solar cell devices fabrication**

Devices were fabricated on cleaned, UV/Ozone treated corning glass patterned with 140 nm of Indium Tin Oxide. We follow a standard cleaning procedure through sequential sonication in sodium dodecyl sulfate solution (SDS), deionized water, acetone and isopropanol for 15 min each. Substrate cleaning was completed through exposure to UV-ozone treatment for 15 min. A hole transporting layer is deposited on ITO –glass substrates; either solution-processed PEDOT:PSS or thermally-evaporated MoO<sub>x</sub> are used as the hole transporting layer. The PEDOT:PSS (Baytron-P 4083, used as received) solution was spin-coated onto substrates with spinning speed of 4000 rpm for 30 sec. MoO<sub>x</sub> (7-9 nm) was thermally evaporated at a rate of 0.1 Å/s under a constant pressure of less than 10<sup>-6</sup> torr . The organic films were deposited by solution processing. Several solution processing methods were used in the studies, including spin coating, blade-coating and wire-bar coating. Finally, the cathode was deposited by sequential evaporation of calcium (10 nm) and aluminum (100 nm) through a shadow mask at a constant pressure of less than 10<sup>-6</sup> torr.

### 3.4.2 Current density–voltage characteristics

The current density–voltage characteristics of the solar cells were measured using a Keithley 2400 under a simulated AM 1.5G solar irradiation at  $100 \text{ mW cm}^{-2}$ . Solar simulator irradiance was calibrated using a standard silicon photovoltaic with a KG1 filter calibrated by the National Renewable Energy Laboratory.

### 3.4.3 External quantum efficiency (EQE)

To measure external quantum efficiency (EQE) spectra, the fabricated devices were illuminated by monochromatic light and the generated current was recorded as a function of the wavelength of the light. The EQE spectra were generated by calibrating the device current with a current generated by photodiode with a known EQE. The EQE measurements were performed by an Oriel Quantum Efficiency Measurement Kit (Newport).

### 3.4.4 Sub-gap EQE

The EQE spectra of the fabricated devices were taken at short circuit condition under focused monochromatic illumination from xenon arc. A lock-in amplifier (Stanford Instruments SR 830) was used to measure the device output current as a function of photon energy. An optical chopper (275 Hz) was used to modulate the light beam. Calibration of lamp intensity was performed with Ge and Si photodiodes. The EQE spectra were fitted on sub-gap region to the equation<sup>[67,157]</sup>:

$$\text{EQE}(E) = \frac{f}{E\sqrt{4\pi\lambda kT}} \exp\left(\frac{-(E_{CT} + \lambda - E)^2}{4\lambda kT}\right) \quad (3.7)$$

Where  $E$  and  $E_{CT}$  are the photon energy (eV) and the energy of the charge transfer state, respectively.  $f$  is a term proportional to the number of CT states and the square of the electronic coupling element.  $\lambda$  is the reorganization energy.

### **3.4.5 Mobility measurements by metal-insulator-semiconductor charge extraction by linearly increasing voltage (MIS-CELIV)**

Metal-insulator-semiconductor diode devices were prepared on 2.5 cm × 2.5 cm ITO substrates cleaned with the same procedure as described for the solar cells. Illustration of the measurement setup is shown in **Figure 3.4**.<sup>[158,159]</sup> The architecture of hole transport and electron transport devices were ITO/MgF<sub>2</sub>/Active layer/MoO<sub>3</sub>/Ag and ITO/MgF<sub>2</sub>/Active layer/Ca/Al, respectively. Each substrate had 6 pixels (0.1 cm<sup>2</sup> each). A 70 nm layer of magnesium fluoride (MgF<sub>2</sub>) was then evaporated under a 10<sup>-6</sup> mbar vacuum. The active layer was spin coated on the top of MgF<sub>2</sub> layer. For electron-only devices a Ca(5nm)/Al (100) electrode and for hole-only devices a MoO<sub>3</sub> (5 nm)/Ag (50 nm) electrode were evaporated on the semiconductor layer by thermal evaporation under similar vacuum conditions. For MIS-CELIV measurements, a commercial available platform, PAIOS Fluxim, was used. With PAIOS setup and its operation software, the pulse shape had adjustable voltage slope and offset. The offset was such that the Ca/Al electrode was negatively biased to inject electrons and MoO<sub>3</sub>/Ag electrode was positively biased to inject holes. The transient signal was also recorded by the software. Finally, the measurement was performed in a dark box. For each case 12 cells on two

separate substrates were tested.

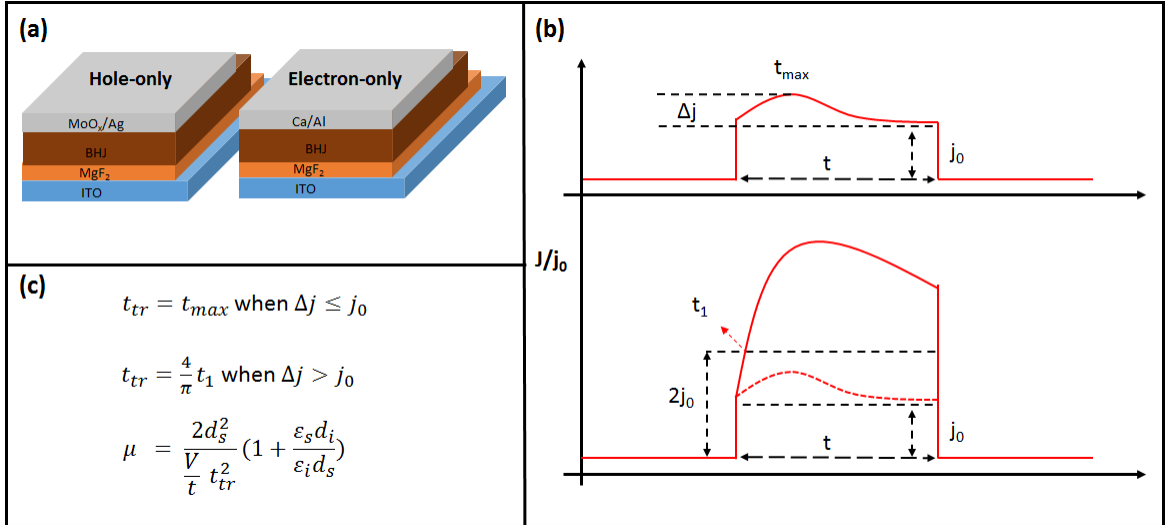


**Figure 3.4** (a) Schematics of the devices structure for electron-only and hole-only devices. (b) Illustration of MIS-CELIV extraction currents transients. Two behaviors are illustrated; (top curve) when  $\Delta j \leq j_0$ , the carrier transit time ( $t_{tr}$ ) is calculated by  $t_{tr} = t_{max}$ , (bottom curve) when  $\Delta j > j_0$ , the carrier transit time is calculated by  $t_{tr} = \frac{4}{\pi} t_1$ . (c) The equations for the mobility calculation. <sup>[158,159]</sup>

## Chapter 4

# In situ UV-visible absorption during spin-coating of organic semiconductors: a new probe for organic electronics and photovoltaics

### 4.1 Introduction

As summarized in chapter 2, understanding the mechanism of film formation and in particular the role of kinetics of the solution process on film formation is crucial for tuning the BHJ morphology and improving the performance of organic photovoltaics. However, one key challenge is the availability of laboratory-based in situ characterization techniques to monitor transformation from the solution to solid-state during the solution process used to deposit the photoactive layer, namely spin coating. Synchrotron-based techniques, such as GIWAXS and GISAXS, have been shown previously by our group but they require the use of a synchrotron X-ray source, making it difficult to perform routinely in lab-based experiments.<sup>[22]</sup> In this chapter we demonstrate a spin-coating experiment monitored *in situ* by time resolved UV-visible absorption, the most commonly used, simplest, most direct and robust optical diagnostic tool used in organic electronics. We demonstrate a new spin-coater design, which integrates the hardware to perform UV-vis absorption measurements during spin-coating and thus monitor the absorption spectrum from the solution state all the way up to the solid film state. This technique yields absorption spectra without data analysis,



and can thus be used for robust process monitoring and to establish a feedback loop.

Part of this work has appeared in *Journal of Materials Chemistry C*.<sup>[160]</sup>

In the first part of this chapter, we monitor the solution-to-solid phase transformation and thin film formation of poly(3-hexylthiophene) (P3HT), the *de facto* reference conjugated polymer in organic electronics and photovoltaics at the time this work was being performed in 2014. We do so in two scenarios which differ by the degree of polymer aggregation in solution, prior to spin-coating. We find that a higher degree of aggregation in the starting solution results in small but measurable differences in the solid state, which translate into significant improvements in the charge carrier mobility of organic field-effect transistors (OFET). In the second part of the chapter, we monitor the formation of a bulk heterojunction photoactive layer based on a P3HT-fullerene blend. We find that the spin-coating conditions that lead to slower kinetics of thin film formation favor a higher degree of polymer aggregation in the solid state and increased conjugation length along the polymer backbone. Using this insight, we devise an experiment in which the spin-coating process is interrupted prematurely, *i.e.*, after liquid ejection is completed and before the film has started to form, so as to dramatically slow the thin film formation kinetics, while maintaining the same thickness and uniformity. These changes yield substantial improvements to the power conversion efficiency of solar cells without requiring additional thermal annealing, or the use of solvent additives. Through these simple examples, we demonstrate that gaining insight

into the thin film formation process can inspire the development of new processing strategies. The insight into the inner workings of spin-coating may be increasingly important to improving the performance or efficiency of roll-to-roll manufactured devices.

#### **4.2 Design of the new spin coater setup for *in situ* UV-vis absorption measurements**

We have developed a new spin coater setup that enables for the first time acquiring UV-Vis absorption spectra during spin coating. In **Figure 4.1**, we illustrate the new spin-coater design allowing the *in situ* UV-vis absorption measurements to be performed during the process. The instrument is made of two main parts. The first part (left side) consists of a rotatable hollow tube mounted with a transparent (quartz) sample holder combined with a light source and a spectrometer, which allow light transmission through the sample mounted on the hollow tube to be collected by an optical fiber. The second part (right) is a motor controlled by a software program to adjust the acceleration, the top speed and the duration of spin-coating and which uses a rubber belt to transfer the motion of the motor shaft to the hollow sample holder. The inset in **Figure 4.1** shows a photograph of the setup. The UV-vis absorption spectra are calculated from the transmission spectra, as explained in methodology chapter 3.

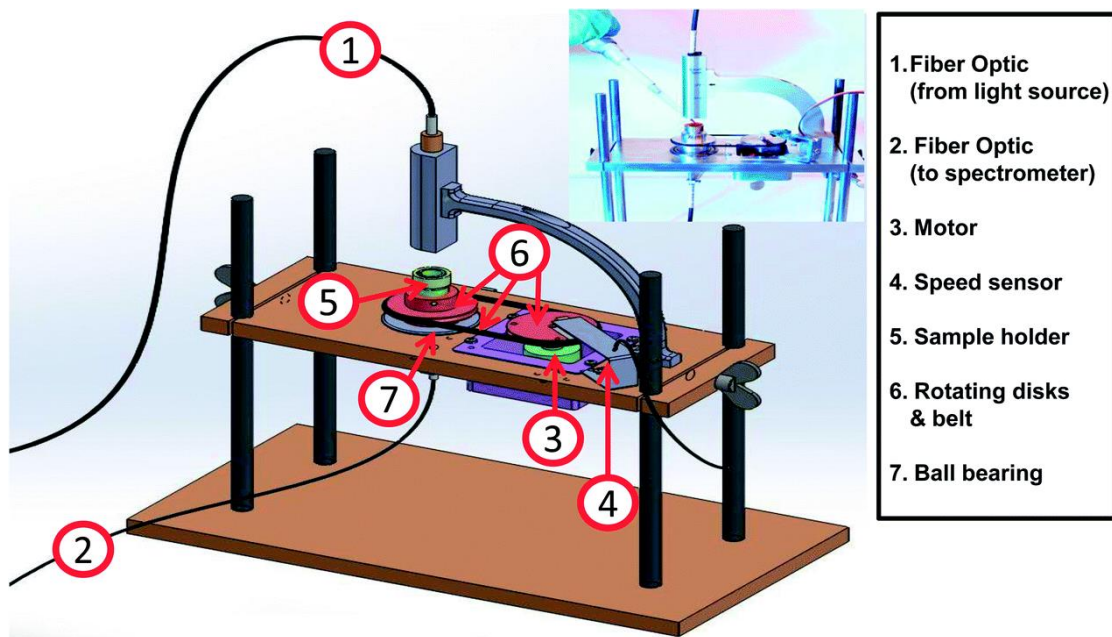


**Figure 4.1** Schematic represents the newly developed spin coater combined with in situ UV-vis absorption. An actual photo of the setup is shown in the inset of the figure.

#### 4.3 Stages of thin film formation during spin coating

Monitoring the evolution of the photo-physical aggregation provides an overview of the stages of the thin film formation during spin coating. In **Figure 4.2**, we show an overview of the time evolution of the UV-vis absorption spectra collected during the spin-coating of P3HT:PC<sub>61</sub>BM in o-DCB solution. The spectra show the P3HT phase transition from the dissolved state to the solid state, starting with a continuous decrease in the intensity of the amorphous peak at ca. 460 nm, followed by an increase in the intensity of the two well-defined peaks at ca. 550 nm and 605 nm, which are designated to be intrachain (0–1) and interchain (0–0) vibronic transitions, respectively, indicating an increased aggregation of the polymer. The evolution of the absorption

spectra follows three distinct stages, as marked in **Figure 4.2b**. In the first stage, we observe a steady and dramatic reduction in the absorption intensity of the solution peak, as a result of loss of the initial volume of the solution *via* ejection. The second stage is characterized by a steady absorption of the solution peak, indicating the solvent evaporation process is underway without inducing any change in the solution state of the P3HT. The third stage corresponds to the solid state thin film formation process, whereby the P3HT absorption peaks associated to aggregation increase dramatically and subsequently reach a plateau. We look more closely at these three stages in the next two sections, both in the context of thin film transistors and solar cells.

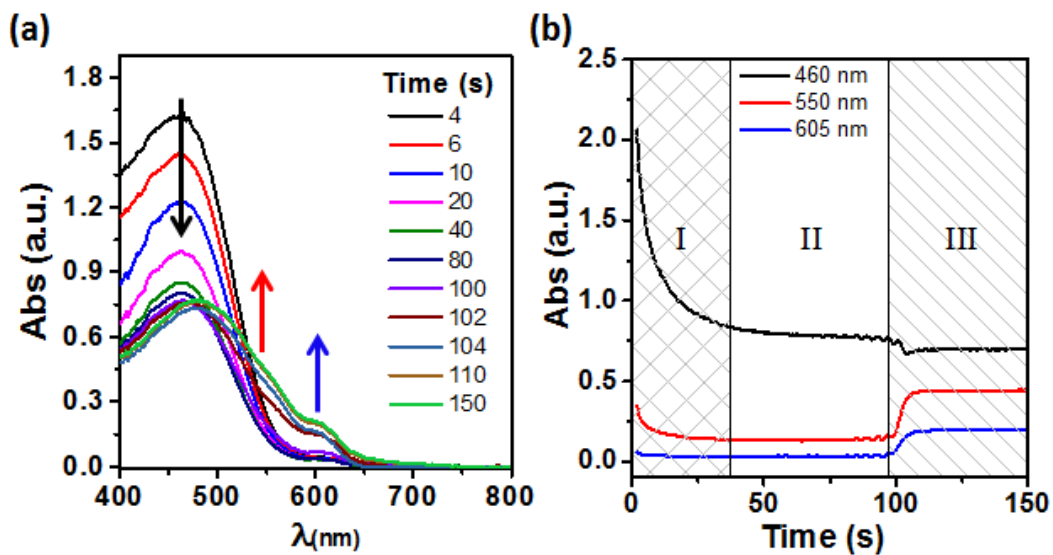


**Figure 4.2** (a) Time resolved *in situ* UV-vis absorbance spectra obtained during spin-coating of P3HT:PCBM (1 : 1) blend solution in o-DCB at 900 rpm for 120 s. (b) Time evolution of absorption intensity at the solution peak (460 nm) and at the aggregation peaks ( (0-1) at 550 nm and (0-0) at 605 nm).

#### 4.4 Neat P3HT in toluene for organic thin film transistors

##### 4.4.1 Effects of the P3HT solution state on the kinetics of film formation

The aggregation state of the neat P3HT in toluene can be controlled by adjusting the solution temperature.<sup>[39,161]</sup> A solution stirred at 65 °C (well-dissolved solution) appears transparent with a yellowish color, whereas a solution stirred at 25 °C (pre-aggregated solution) appears to be dark brown in color, as a result of significant polymer aggregation in solution. The difference between the state of the P3HT solute in these two solutions is demonstrated by the UV-vis absorption spectra at the moment of starting the spin-coating, which show clear intermolecular and intramolecular absorption peaks for the pre-aggregated solution and only the amorphous peak for the well-dissolved solution (**Figure 4.3a-b**). As the spin-coating progresses in identical conditions, we observe differences in the kinetics of the drying and polymer aggregation from the two solutions, by monitoring the intermolecular absorption peak at 605 nm (**Figure 4.3c**). In the well dissolved case, the aggregation peak is absent throughout the process until film formation is initiated. In the pre-aggregated solution, the aggregation peaks are always present; we observe a rapid decrease of the absorption at 605 nm during the initial seconds of the spin-coating due to loss of aggregates *via* ejection of the bulk solution. The absorption at 605 nm does not reach zero, indicating the remaining solution is significantly aggregated just prior to film formation. It takes ~10 s for the pre-aggregated solution to form a dry film and only 8 seconds for the well-dissolved

solution. In addition, the thin film formation kinetics – characterized by the step-like increase in the absorption at the final stages of solution drying – are drastically different in both cases, lasting  $\sim 1.3$  s in the case of the pre-aggregated solution and no more than 0.4 s for the well-dissolved solution. In **Figure 4.3c**, we observe an identical thinning behaviour in the ejection regime, followed by a deviation in the thinning behaviour of the two solutions as the solution thinning becomes dominated by solvent evaporation. Clearly, the pre-aggregated room temperature solution dries more slowly than the well-dissolved warm solution (65 °C). This can be understood to be due to the difference in the evaporation rate. Considering that both spin-coating experiments are completed with only a difference of 2 s ( $\sim 25\%$  difference in duration), it is quite remarkable that the film formation should be approximately 3 times slower in the pre-aggregated case. However, this significant difference in the kinetics of thin film formation illustrates that small to moderate differences in the duration of the drying process can have disproportionate implications on the film formation kinetics.

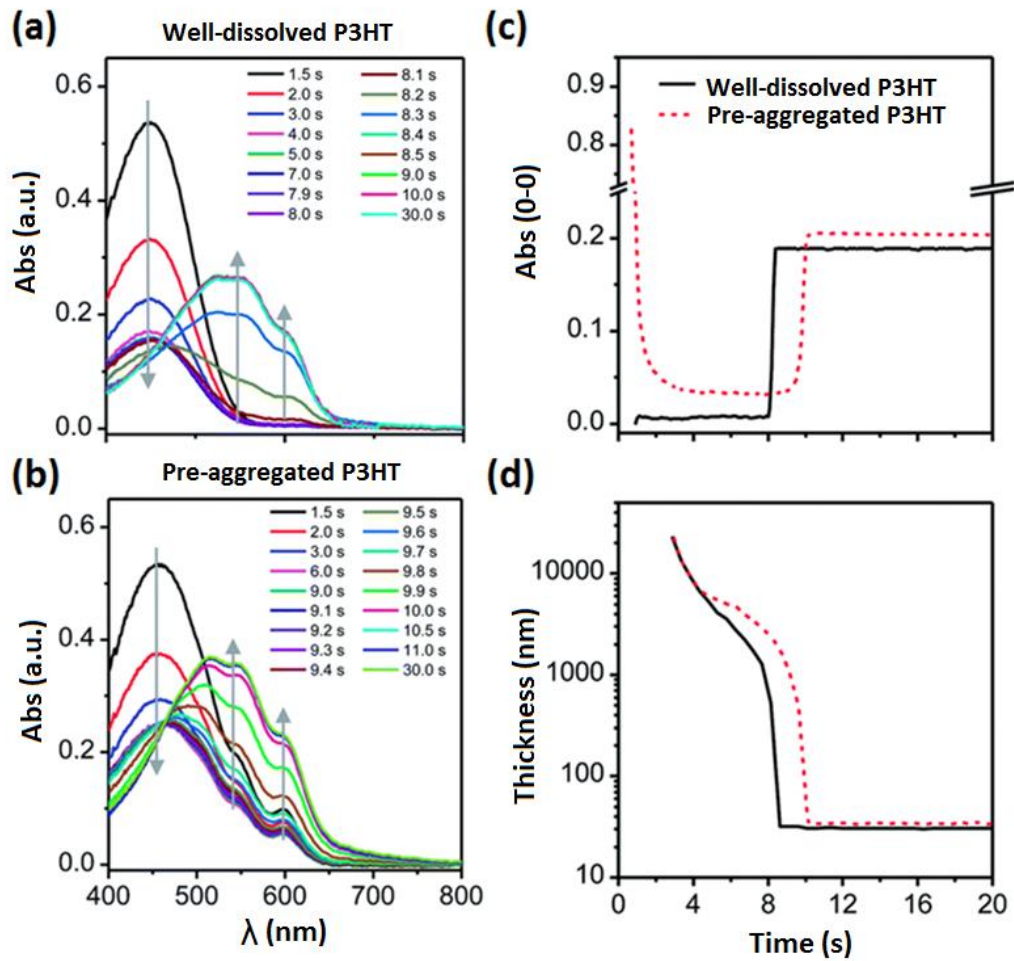


**Figure 4.3** Time resolved *in situ* UV-vis absorbance spectra obtained during spin-coating of (a) a well-dissolved solution of P3HT in warm toluene (stirred overnight at 65 °C) and spin coated at 900 rpm for 30 seconds, (b) a pre-aggregated solution of P3HT in toluene (stirred overnight at room temperature) and spin coated at 900 rpm for 30 s. (c) Time evolution of the aggregation peak ( $\lambda = 605$  nm, namely 0-0 transition) during spin-coating for the well-dissolved and pre-aggregated solutions. (d) Time evolution of solution and film thickness.

#### 4.4.2 Quantitative analysis of the degree of aggregation in neat P3HT films

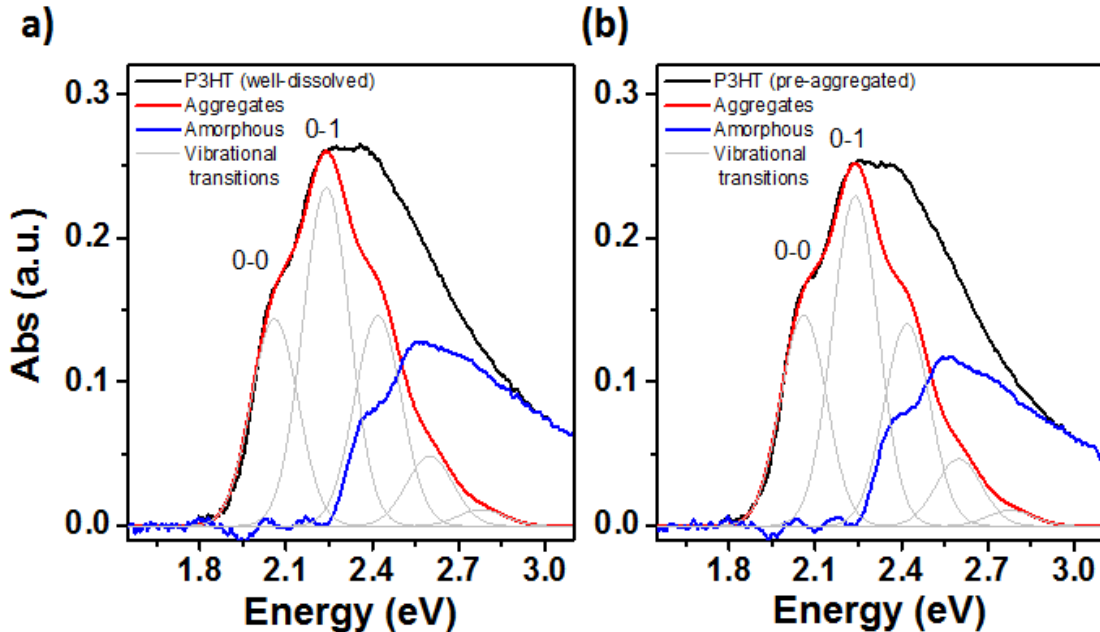


**Figure 4.4** Absorption spectra of P3HT subjected to Spano model analysis for dry films coated from (a) well-dissolved P3HT in toluene and (b) pre-aggregated P3HT in toluene.

In **Figure 4.4**, we plot absorption spectra of P3HT subjected to Spano model analysis for dry films coated from well-dissolved P3HT and pre-aggregated P3HT in toluene. We have analyzed the absorption spectra using a variant of a method first proposed by Spano to investigate excitonic (intermolecular) coupling, exciton–phonon (EP) coupling and site-energy disorder.<sup>[162]</sup> Silva modified this method to account for the effect of aggregation on the relative vibronic intensities.<sup>[163]</sup> Subsequently Neher added a weak excitonic coupling assumption and included a correction to the transition energy, by adding half of the vibronic bandwidth.<sup>[164]</sup> The absorption spectrum was fitted using the



equation (3.4 mentioned in chapter 3), which has been successfully implemented and described in detail elsewhere.<sup>[162–165]</sup>

Based on this analysis, we have calculated the aggregation fraction of the P3HT crystallites in the thin films and the exciton bandwidth,  $W$ , a parameter that has been linked to the conjugation length and backbone planarity in P3HT.<sup>[163,164]</sup> As shown in **Table 4.1**, the values for  $W$  are *ca.* 128 meV and 119 meV, and the aggregation fractions are *ca.* 52% and 54%, respectively, for the thin films prepared from the well-dissolved and pre-aggregated solutions. Quantum-chemical calculations of excitonic coupling in aggregates of conjugated oligomers and polymers have previously revealed  $W$  to be inversely proportional to the number of interacting thiophene repeat units,  $N$ , in the limit of strong interchain interactions.<sup>[164,166–170]</sup> This means that the excitonic bandwidth,  $W$ , decreases as the number of interacting thiophene repeat units,  $N$ , along the backbone increases, indicating the increased conjugation length along the backbone. We have previously observed experimentally that  $W$  decreases with an increasing lamellar thickness of P3HT fibrils obtained by ultrasonication of the high Mw P3HT solution in toluene.<sup>[165]</sup> The results of the current study indicate a larger fraction of photophysical aggregates and a longer conjugation length within the P3HT aggregates, when thin films are processed from the pre-aggregated solution, as opposed to the well-dissolved solution. This is probably due to a combination of factors, such as the fact that some of the polymer aggregates were already present in the solution

before the thin film formation, but also the fact that film formation kinetics are slower, which may have promoted more intermolecular interactions in the thin film.

**Table 4.1** Spano model parameters of P3HT films coated from well-dissolved and pre-aggregated solutions

	Aggregation [%]	W [meV]
P3HT (Well-dissolved in solution)	52 +/- 0.7	128 +/- 2
P3HT (Aggregated in solution)	54 +/- 1.3	119 +/- 1

#### 4.4.3 The impact of the aggregation state in P3HT films on the hole mobility and film morphology

We fabricated top-contact, bottom-gate field effect transistors on a SiO<sub>2</sub> as gate dielectric, to further investigate the influence of the aggregation state of the films on the carrier transport properties. The transfer curves for the two representative devices are shown in **Figure 4.5** and the associated device properties are summarized in **Table 4.2**. We found that the saturation hole mobilities are 0.011 cm<sup>2</sup> V<sup>-1</sup> s<sup>-1</sup> and 0.0012 cm<sup>2</sup> V<sup>-1</sup> s<sup>-1</sup> for the devices fabricated from the pre-aggregated and well-dissolved solutions, respectively.

**Table 4.2** Field effect transistor performance of P3HT transistor devices

	Mobility [cm <sup>2</sup> V <sup>-1</sup> s <sup>-1</sup> ]	V <sub>TH</sub> [V]	ON/OFF
P3HT (Well-dissolved in solution)	0.0012	54.27	34
P3HT (Aggregated in solution)	0.011	56.14	72

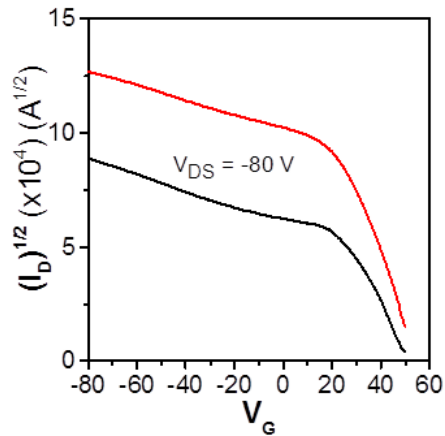


**Figure 4.5** Transfer characteristics of top-contact, bottom gate OFET devices  $[(I_D)^{1/2}-V_G]$ .

The increase in the carrier mobility is quite remarkable in the case of the pre-aggregated solution, given the marginal differences detected in the fraction of the photo-physical aggregates. To shed more light on the performance boost, we have evaluated the morphology and microstructure of the P3HT thin films using atomic force microscopy (AFM), transmission electron microscopy (TEM), and selected area electron diffraction (SAED), as shown in **Figure 4.6**. The AFM and TEM analyses reveal the formation of P3HT fibrils only in the case of films cast from pre-aggregated solution, indicating that the fibrils are seeded in the pre-aggregated solution. In both films, the SAED reveals the (020) diffraction ring associated to  $\pi$ -stacking, however the (020) intensity plotted from normalized line-scan profiles indicates a greater crystallinity in the  $\pi$ -stacking direction in the pre-aggregated films. We therefore believe the increased conjugation length indicated by a reduced  $W$  is due to the formation of crystalline fibrils, wherein the P3HT chains are stacked along the long axis and run along the lamellar thickness direction.

The improved carrier mobility in the P3HT thin film transistors can therefore be understood to be due to the formation of thin films, with a network of interconnected fibrils. Considering the Mw (68 kDa) of the P3HT used, tie-molecules play an important role in linking the fibrils to their surroundings, including neighboring fibrils. In a previous work, our group has shown the bottleneck to carrier transport in this regime of high Mw to be the degree of crystallinity and backbone planarity within the P3HT domains, whereas the presence of tie-molecules was found to be the key bottleneck to carrier transport in low-Mw P3HT, far more important than the degree of crystallinity.<sup>[165]</sup> The pre-aggregation of high-Mw P3HT solutions in marginal solvents therefore promotes carrier transport in thin films transistors, by forming an interconnected network of crystalline fibrils.

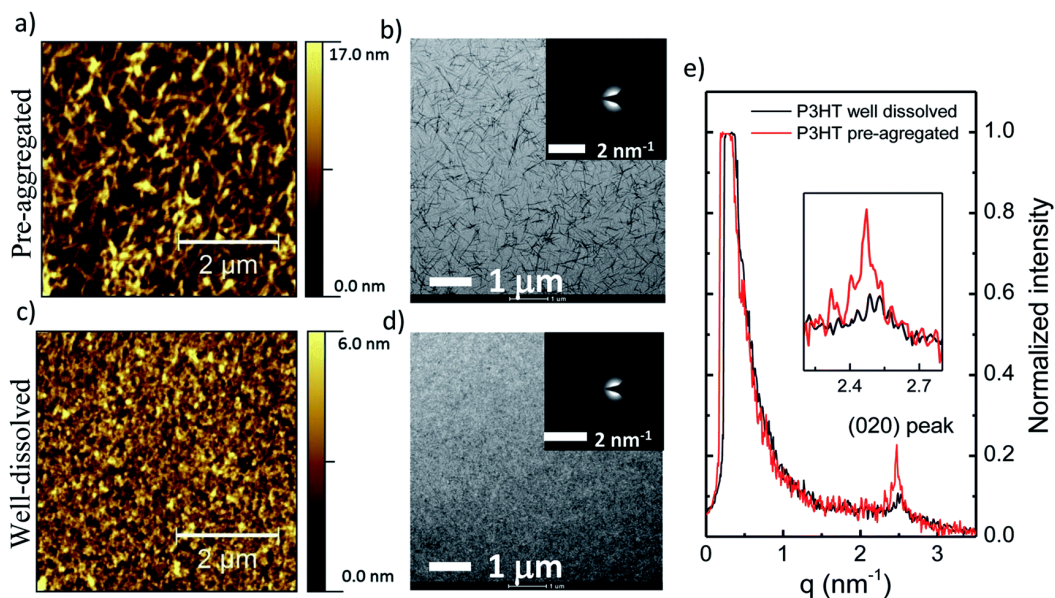


**Figure 4.6** Atomic force microscopy (AFM) and transmission electron microscopy (TEM) micrographs for P3HT thin films prepared from a pre-aggregated P3HT solution (a and b)

and a well dissolved P3HT solution (c and d), respectively. The insets of (b) and (c) show selected area electron diffraction (SAED) patterns for the same samples. The normalized intensity line scans obtained from the SAED images are plotted in (e).

#### 4.5 P3HT:PC<sub>61</sub>BM blend in *o*DCB for organic solar cells

##### 4.5.1 Effects of the spin coating speed and duration on the kinetics of film formation

We prepared spin-cast warm P3HT:PC<sub>61</sub>BM blend solutions based on *o*-DCB in different processing conditions, namely varying the spin speed and duration. In doing so, we sought to compare the experiments and thin films, where the dry film formation may occur during, or after the substrate stops spinning. In **Figure 4.7a**, we plot the thickness evolution of the solutions in the different conditions explored herein. As expected, the rate of thinning is faster when the spin-coating is performed at 1200 rpm, as compared to 900 rpm. An inspection of the time-evolution of the absorption peak at 460 nm in **Figure 4.7b** reveals this difference is partly due to more solution being ejected at 1200 rpm in the first few seconds of the spin-coating process. This is confirmed by comparing the final film thickness, which suggests more solute remains on the surface at 900 rpm (thicker film) than at 1200 rpm. An inspection of the time-evolution of the absorption at 605 nm, in **Figure 4.7c**, reveals the film is completely formed well before the substrate stops spinning at 120 s. The spinning speed appears to influence the duration of the film formation, which lasts ~7 s at 1200 rpm and ~12 s at 900 rpm, an increase of 70% of the duration of phase transformation.

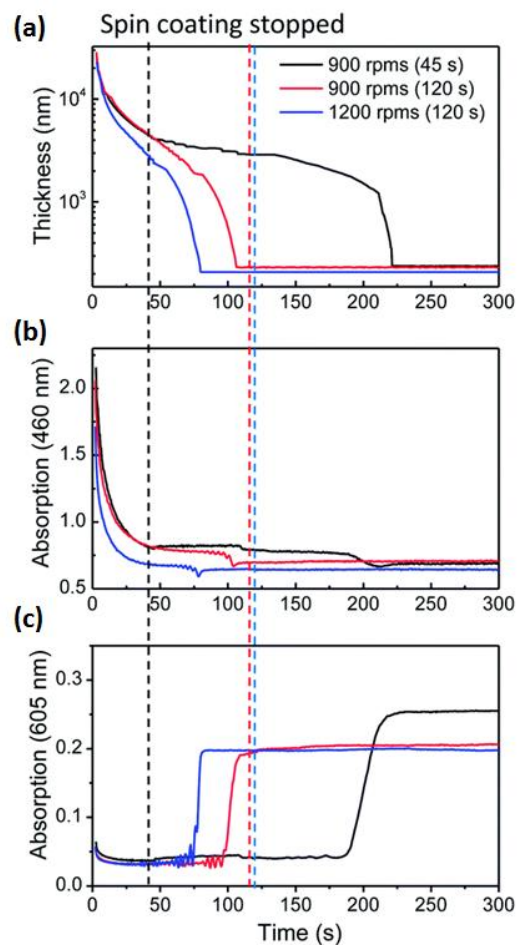


**Figure 4.7** (a) Time evolution of solution and film thickness during spin coating of P3HT:PC<sub>61</sub>BM (1 : 1) blends in different processing conditions. Spin coating of the solution of P3HT:PC<sub>61</sub>BM (1:1) in o-DCB was performed at 900 rpm for 45 s (black), 900 rpm for 120 s (red) and 1200 rpm for 120 s (blue). (b) & (c) Time evolution of absorption at the solution peak (460 nm) and at the intermolecular aggregation peak (605 nm), respectively.

We utilized the insight provided by the *in situ* UV-vis absorption measurements about the onset and end of the film formation to halt the spin-coating process prematurely, with the aim of drastically slowing down the drying rate, without changing the total film thickness, which is determined in the first few seconds of the spin-coating process. In doing so, we reduced the evaporation rate of the solvent quite drastically, more than doubling the total process duration from  $\sim 105$  s to  $\sim 225$  s, even as both films have the same final thickness. The duration of the film formation process was more than tripled to  $\sim 38$  s. These kinetic differences appear to matter, as we observed a remarkable 25% increase in the intermolecular absorption peak of P3HT, at the end of the process.

#### **4.5.2 Quantitative analysis of the degree of P3HT aggregation in P3HT: PC<sub>61</sub>BM films**

The improvements in absorption are clearly visible in **Figure 4.8a**, where the UV-vis absorption spectra (normalized to the PC<sub>61</sub>BM absorption peak) of the BHJ films dried overnight in the nitrogen glove box are compared to each other and to a neat PC<sub>61</sub>BM film. As expected, small gains can be made when the P3HT is prepared at a slower spin speed, but the improvements of the intermolecular and intramolecular transition peaks are most dramatic in the case where the spinning is suspended before the film drying is complete.

To quantify and compare the photo-physical aggregation in these samples, we subtracted the absorption spectrum of PC<sub>61</sub>BM from that of the BHJ films and then fitted the curves by using the Spano model; the fitted curves and parameters are shown

in **Figure 4.8 b-d** and **Table 4.3**, respectively. The fraction of the aggregates is lower than in the neat P3HT films and increases slightly from 38% to 40%, when reducing the spin speed from 1200 rpm to 900 rpm. We see no clear difference in the value of  $W$ , which at  $\sim 173$ – $175$  meV is quite a bit higher than in the neat P3HT films prepared from toluene, pointing to a more twisted polymer backbone in the blended films as compared to the neat films. Suspending the spin-coating process at 45 s, instead of 120 s, results in a substantial increase of the fraction of aggregation to 44.9% and a substantial decrease of  $W$  to 112 meV, which is comparable to the outcome of neat P3HT spin-coating from a toluene solution. These results indicate that the prolonged drying induced by the premature interruption of spin-coating can yield P3HT domains within the BHJ film, with a level of photo-physical aggregation and backbone planarity comparable to neat P3HT thin films prepared from a toluene solution.

**Table 4.3** Spano model parameters for P3HT : PC<sub>61</sub>BM films

Spin coating conditions		Spano Model parameters	
Speed [rpms]	time [s]	Aggregation [%]	W [meV]
1200	120	37.6 +/- 0.3	175 +/- 5
900	120	39.9 +/- 0.5	173 +/- 4
900	45	44.9 +/- 0.4	112 +/- 3



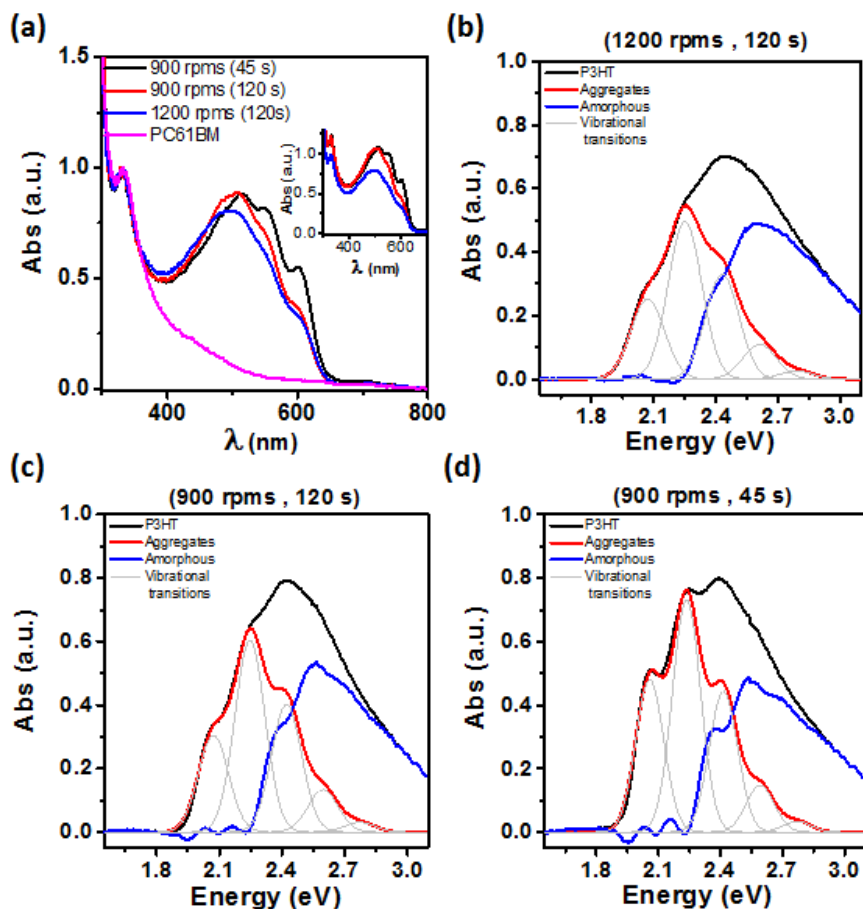


**Figure 4.8** (a) Absorption spectra of the dried films normalized to the PC<sub>61</sub>BM absorption peak (at 330 nm). The inset in (a) shows the actual absorption spectra of the dried films. Absorption spectra of P3HT subjected to Spano model analysis for P3HT: PC<sub>61</sub>BM dry films coated from oDCB at 1200 rpms for 120 s in (b), at 900 rpms for 120 s in (c) and 900 rpms for 45 s in (d). Absorption spectra of P3HT were obtained by subtraction of PC<sub>61</sub>BM absorption from P3HT:PCBM (1:1) absorption.

#### 4.5.3 The impact of the aggregation state in P3HT:PC<sub>61</sub>BM films on the solar cell device performance and BHJ morphology

Organic solar cells based on these photoactive layers were fabricated using the following standard architecture: *Glass/ITO/PEDOT:PSS/P3HT:PC<sub>61</sub>BM/Ca/Al*. We did not use any thermal annealing following deposition of the BHJ films, so as to evaluate only the performance differences due to variations in the spin-coating conditions. The *J–V* characteristics, shown in **Figure 4.9a**, indicate an increase in the power conversion efficiency (PCE), from 2.3% to 2.6%, when reducing the spin-speed from 1200 rpm to 900 rpm, and up to 3.0% when further reducing the duration of the spin-coating from 120 s to 45 s (**Table 4.4**). The most substantial differences in the PCE stem from an increased short circuit current, from 6.25 to 6.7 and 9.1 mA cm<sup>-2</sup>. This may be due to a substantially increased phase separation and P3HT  $\pi$ -stacking crystallinity in the latter case, as indicated by the TEM and SAED data, in **Figure 4.10**, and the optical analysis of the samples in **Table 4.3**. It is also noteworthy that the fill factor suffers only when spinning is stopped prematurely, decreasing from ~62–64% for the 120 s experiments, down to 55% for the 45 s experiment. The cause of this negative difference can be partially attributed to the much higher surface roughness (~13 nm) of the films spin cast at 900 rpm for 45 s, compared to the much smoother (~0.5 nm) films spin cast for 120 s, as indicated by the AFM images in **Figure 4.10**.

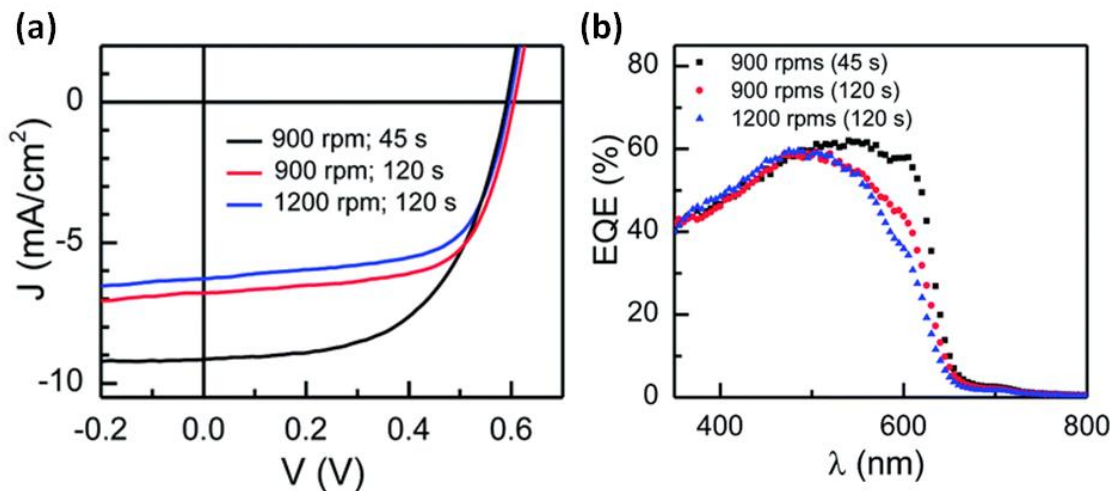


**Figure 4.9** (a) J–V characteristics of P3HT:PCBM BHJ solar cells fabricated from coated films at 900 rpm for 45 s (black), 900 rpm for 120 s (red) and 1200 rpm for 120 s (blue). (b) External quantum efficiency (EQE) spectra for these devices.

**Table 4.4** Solar cell device parameters for P3HT:PC<sub>61</sub>BM solar cells

Spin coating conditions		Solar cell devices performance parameters			
Speed [rpms]	time [s]	J <sub>sc</sub> [mA.cm <sup>-2</sup> ]	V <sub>oc</sub> [V]	FF [%]	Efficiency [%]
1200	120	6.25 +/- 0.02	0.595	62 +/- 0.2	2.3 +/- 0.1
900	120	6.7 +/- 0.2	0.604	64 +/- 0.8	2.6 +/- 0.1
900	45	9.1 +/- 0.1	0.589	55.5 +/- 0.5	3.0 +/- 0.1

We have established that decreasing the spin-speed from 1200 rpm to 900 rpm decreases the amount of solution ejected initially during acceleration, thus increasing the BHJ thickness from 208 nm to 232 nm, as verified by ellipsometry. The inset of **Figure 4.8a** compares the raw absorption spectra of the two films and shows a

significantly greater absorption across the spectrum for the films prepared at 900 rpm, as opposed to the film prepared at 1200 rpm, both below 400 nm (PC<sub>61</sub>BM contribution) and between 500 and 600 nm (P3HT contribution). The increased absorption due to the greater thickness results in only a small increase of  $J_{sc}$  by 0.5 mA cm<sup>-2</sup> in the case of the 120 s duration and in a much larger 2.9 mA cm<sup>-2</sup> increase in the case of the 45 s duration. The absorption spectra, normalized to the PC<sub>61</sub>BM absorption peak, are shown **Figure 4.8a**; these spectra better reflect the observed changes in the device performance and allow us to conclude that the PCE improvements are more closely related to the inherent structural improvement of the P3HT domains, as opposed to the overall amount of the P3HT or PC<sub>61</sub>BM absorption. To confirm this, we measured the external quantum efficiency (EQE) for all three cases, as shown in **Figure 4.9b**. The EQE is strongly modulated in the spectral region, where the P3HT vibronic transitions lie, strongly affecting the EQE in the spectral range from 550 nm to 650 nm. It is noteworthy that the EQE increases only in the area of the intermolecular vibronic transition when the film thickness increases from 208 nm to 232 nm in the case of the 120 s duration. By contrast, reducing the spin-coating duration to 45 s at 900 rpm further improves the EQE significantly, this time both in the areas of the intermolecular and intramolecular vibronic transitions. This confirms that most of the performance increases achieved are due to the greater fraction of the P3HT photo-physical aggregates and to the improvement of the intermolecular and intramolecular interactions within the P3HT domains of the bulk heterojunction film, which indicate a greater phase separation and

point to an increased crystallinity. This is confirmed by the TEM and AFM measurements, indicating a substantially coarser phase separation. The SAED data also confirm a greater crystallinity in the  $\pi$ -stacking direction, when spin coating is interrupted prior to solution drying.

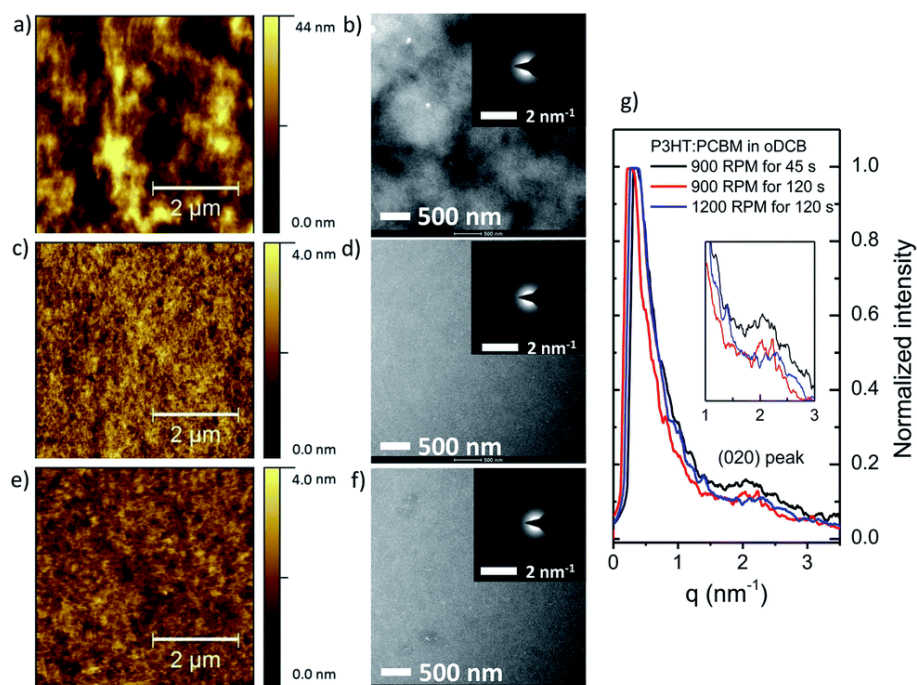


**Figure 4.10** Atomic force micrographs and transmission electron micrographs, respectively, of P3HT:PC<sub>61</sub>BM blend thin films spin-cast at (a, b) 900 rpm for 45 s, (c, d) 900 rpm for 120 s and (e, f) 1200 rpm for 120 s, respectively. Selected area electron diffraction (SAED) showing the (020) diffraction ring of P3HT are shown as insets in the respective electron micrographs. The corresponding normalized intensity line scan profiles are shown in (g).

#### 4.6 Conclusions

We have demonstrated a new experimental capability, combining everyday spin-coating with everyday UV-vis absorption to obtain, for the first time, time-resolved UV-vis absorption spectra during the spin-coating of organic semiconductor thin films, both for electronic and photovoltaic applications. We have used a reference conjugated polymer, P3HT, to demonstrate the ability of this technique to detect the solution-state of the solute in terms of the degree of aggregation, as well as to detect the transition from the liquid ejection regime of the spin-coating to the evaporation-dominated regime, as well as the onset, evolution and end of the solution-to-solid phase transformation process, also known as the thin film formation process.

In the context of electronics, we have demonstrated that the presence of large differences in the aggregation state of P3HT in the solution can induce small changes in the solid state UV-vis absorption spectrum, but which can still have important implications on the carrier transport in the context of OTFTs, mainly due to morphological and microstructural differences – namely fibril formation – detected by AFM and TEM.

In the context of photovoltaics, we have demonstrated the spinning conditions can select the amount of solute remaining on the substrate, as well as the film thickness and kinetics of crystallization. Using this insight, we proceeded to show that interrupting the spin-coating process in the evaporation-dominated thickness regime can lock in the

desired thickness, while extending the duration of the film formation quite dramatically. This is shown to have an important positive influence on the intermolecular and intramolecular interactions in the film, and the EQE as well as the power conversion efficiency of organic solar cells.

## Chapter 5

# Roles of the donor crystallization dynamics and pathway on bulk heterojunction formation in small-molecule organic solar cells

### 5.1 Introduction

The main aspects that govern BHJ formation include thermodynamics aspects such as the ease of crystallization of the BHJ components, their mutual interaction (*ca.* their miscibility in each other) and their interaction with the solvents during processing, and kinetics aspects related to the processing conditions. In the previous chapter, we have demonstrated a new capability for monitoring the kinetics of film formation by UV-vis absorption measurements. In this chapter, we use this capability combined with in situ grazing incidence wide angle x-ray scattering (GIWAXS) and flash differential scanning calorimetry (F-DSC) to perform a fundamental study of the crystallization dynamics of a variety of small-molecule donors to reveal its effect on the processing routes to attaining high-performance photovoltaics. Part of this work has appeared in *Advanced Materials*.<sup>[171]</sup>

We propose a generalized concept linking the crystallization dynamics of molecular organic semiconductors and the processing routes needed for fabricating bulk heterojunction (BHJ) solar cell devices. The study reveals the reason behind the need of empirically-adopted processing strategies such as solvent additives or alternatively thermal or solvent vapor annealing for achieving optimal performance – all of which are



incompatible with high throughput environmentally friendly manufacturing. We demonstrate that the resistance to crystallization and phase separation is the main obstacle that additives help overcome and which prevents obtaining an optimal performance from a single processing step without the need for high boiling point halogenated additives.

We investigate the ability of crystallization of several donor materials that cover a broad range of crystallization behaviors, namely p-DTS(FBTTh<sub>2</sub>)<sub>2</sub>, p-SIDT(FBTTh<sub>2</sub>)<sub>2</sub> and X2.<sup>[120,121,172]</sup> The molecular structures of the materials used in the study are shown in **Figure 5.1**. We find that crystallization of some donor materials goes through a transient disordered or liquid crystalline phase that acts as a barrier for their crystallization at fast film formation conditions such as solution processing. In such conditions, the donor-fullerene phase separation is inhibited. With this enhanced understanding of phase transformation of donor small-molecules: fullerene blends, we demonstrate state-of-the-art 7.6% small-molecule BHJ solar cells prepared additive-free and in a single step. The enhanced understanding of the crystallization dynamics is expected to curb the challenges in achieving high performance solar cells via more facile, reproducible and environmentally friendly manufacturing.

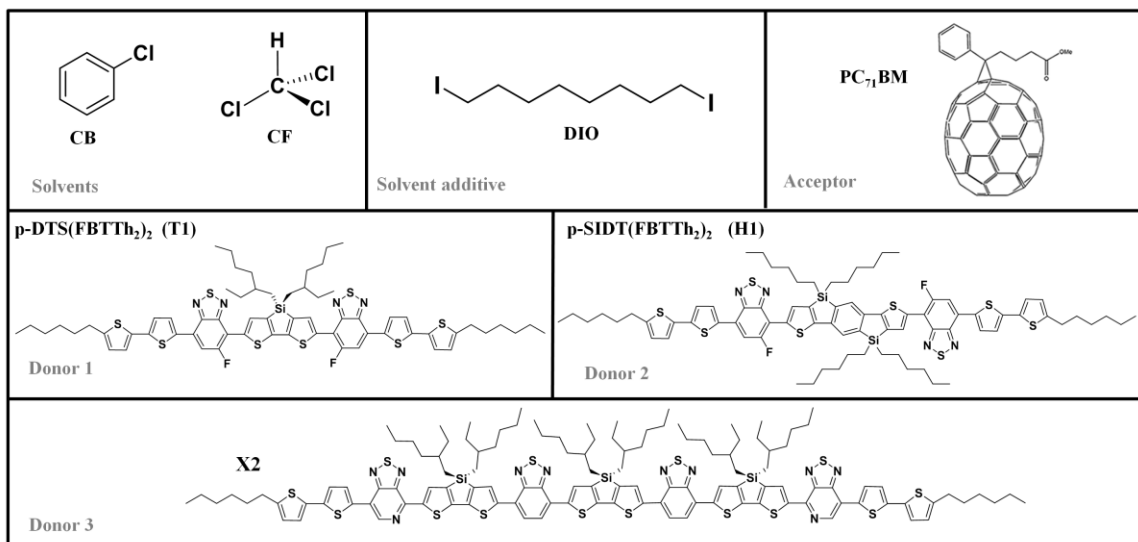


**Figure 5.1** Molecular structure of the materials in the study.

## 5.2 Roles of the donor crystallization in small-molecule organic solar cells

Generally, crystallization of donor molecules is necessary for facilitating phase separation from acceptor molecules and ensuring high carrier mobility. As discussed previously, the optimum bulk heterojunction morphology of organic solar cells requires domains of donor and acceptor that are large enough to form a bicontinuous network and small enough –or finely intermixed– for efficient charge generation.<sup>[6,23,64,65,69]</sup> For small-molecule-based devices, the crystallization of the donor strongly correlates with the BHJ phase separation. In a recent study, it was shown that donor crystallization is often the driving force for phase separation in the small-molecule BHJ system consisting of DPP(TBFu)<sub>2</sub> as the donor and PC<sub>71</sub>BM as the acceptor.<sup>[173]</sup> Donor crystallization requirements can be relaxed for polymer solar cells since it has been shown that the presence of interconnected aggregates, even for amorphous polymers, acts as the main

requirement for high carrier mobility, where long polymer chains act as tie-molecules that connect donor domains.<sup>[38,39]</sup> On the other hand, small-molecule donors, unlike polymers, lack this benefit and require crystallization to ensure intermolecular interactions required for the efficient charge transport.<sup>[17,40]</sup>

### **5.3 The need of flash differential scanning calorimetry (F-DSC) for detecting the metastable phases**

When considering the crystallization of small-molecules via solution processing, metastable transitions en route toward crystallization need to be taken into account at fast film formation conditions. These are impacted and mediated by the use of solvent additives.<sup>[174]</sup> For instance, the solution processable small-molecule BHJ system which contains a blend of p-DTS(FBTTh<sub>2</sub>)<sub>2</sub><sup>[120]</sup> and PC<sub>71</sub>BM, which has been responsible for extraordinary gains in power conversion efficiency (PCE) from ca. 1.8 to ca. 9% by the use of processing additives, exhibits unexpected features and transient phases that remain poorly understood.<sup>[120,175]</sup> Unfortunately, these metastable transitions are difficult to detect by conventional differential scanning calorimetry (DSC)<sup>[146–149]</sup>, owing to typically low heating/cooling rates (ca. 10 °C/min), and thus their role in the phase transformation outcome of donor-acceptor blends in the absence or presence of additives remains unknown. The ultra-fast flash DSC (F-DSC) technique – an approach not yet widely adopted by the organic electronics community – can mimic the kinetics of practical processing conditions such as spin coating and study crystallization

dynamics and (meta)stability in conditions far removed from equilibrium,<sup>[150–156]</sup> and can potentially reveal new insights on the phase transformation behavior of small-molecule donors and the role of additives, especially in combination with in situ diagnostics of the solution-to-solid phase transformation studies.<sup>[174]</sup>

In order to emphasize that the cooling rates from F-DSC align with the film formation rates from spin coating, it is useful to define a parameter, what we call the effective cooling rate (the cooling rate that mimics the film formation rate obtained from solution processing), by the cooling rate that would correspond to cooling of the sample from melt to room temperature in a similar time interval of the film formation by solution processing. This time interval can be estimated from the point at which the solute reaches supersaturation and starts to aggregate until the end of the solid-state film formation.<sup>[43]</sup> To do so, we have performed in situ UV-Vis absorption during spin coating to monitor the photo-physical aggregation during film formation (**Figure 5.2**). The following conditions have been used for spin coating three donor molecules in the study; p-DTS(FBTTh<sub>2</sub>)<sub>2</sub> (@ concentration 21 mg/ml in CB and coating speed 1750 rpms for 60 s), p-SIDT(FBTTh<sub>2</sub>)<sub>2</sub> (@ concentration 20 mg/ml in CB and coating speed 1750 rpms for 60 s) and X2 (@ concentration 10 mg/ml in CF and coating speed 2000 rpms for 60 s). As explained in the previous chapter, spin coating can be expressed as three distinct stages ; (1) initial loss of solution due to ejection, characterized by a drop in absorption intensity, (2) solvent evaporation stage in which the solvent evaporates

without observable change in the aggregation state of solution, characterized by steady absorption (this stage is negligible here) and (3) solid-state film formation in which the solute starts to aggregate at the end stage of solvent evaporation till the final solid-state film formation (see **Figure 5.2d-f**). Importantly, the time interval of the actual film formation can be estimated precisely from the third stage (from the red arrow till the blue arrow in **Figure 5.2d-f** and is found to be 1.9 s, 1.4 s and 0.5 s for p-DTS(FBTTh<sub>2</sub>)<sub>2</sub>, p-SIDT(FBTTh<sub>2</sub>)<sub>2</sub> and X2, respectively. We estimate the effective cooling rate by the difference between melting temperature and room temperature divided by the time interval of film formation by solution processing. The onset of melting of the three molecules is estimated from the heating thermograms in **Figure 5.3** to be ~ 190 °C for p-DTS(FBTTh<sub>2</sub>)<sub>2</sub>, ~ 138 °C for p-SIDT(FBTTh<sub>2</sub>)<sub>2</sub> and ~ 249 °C for X2, respectively. The approximate effective cooling rates calculated using these values are estimated to be 87 K/s, 81 K/s and 448 K/s for p-DTS(FBTTh<sub>2</sub>)<sub>2</sub>, p-SIDT(FBTTh<sub>2</sub>)<sub>2</sub> and X2, respectively. This value should be considered as a first approximation of the effective cooling rate as it can vary with different coating conditions, though it highlights a clear alignment between film formation rates by solution processing and the cooling rates that can be obtained by F-DSC.

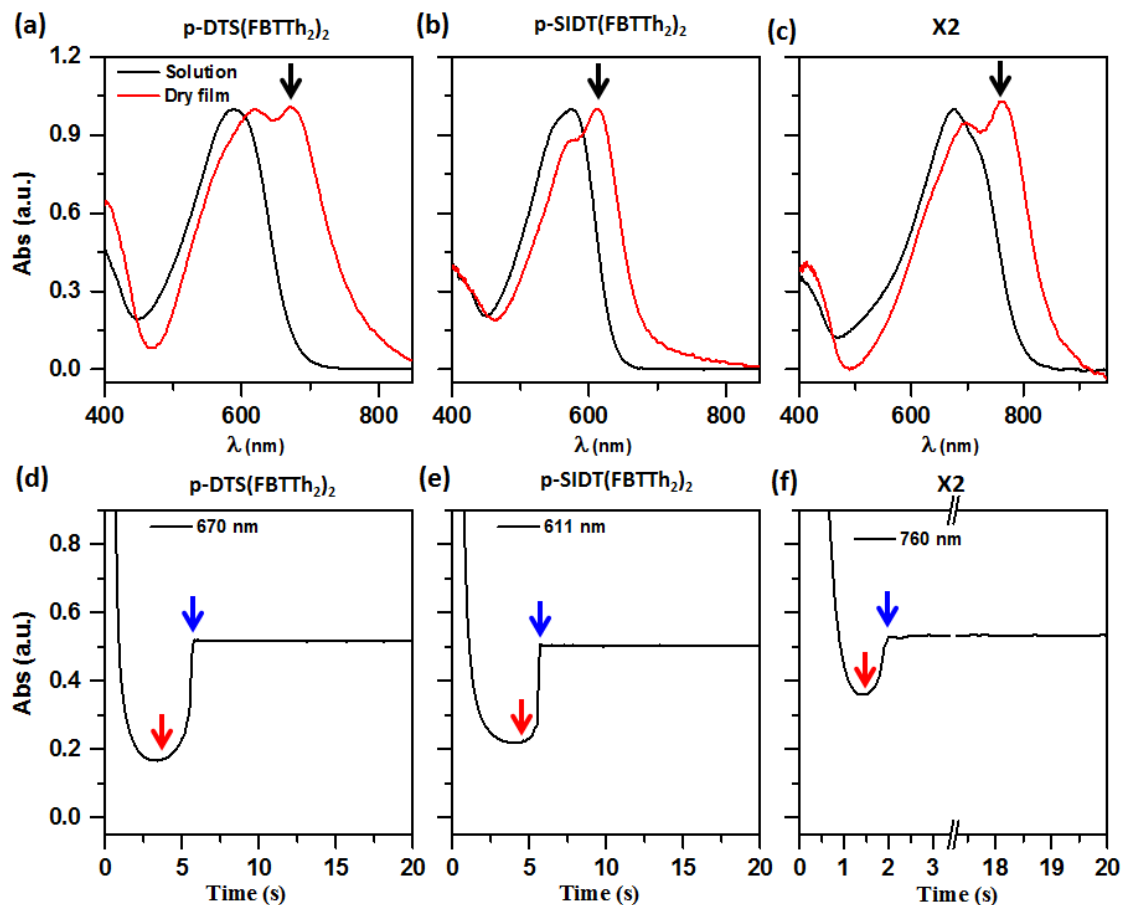


**Figure 5.2.** (a-c) UV-Vis absorption spectra of solution (dark curve) and dry film (red curve) of neat p-DTS(FBTTh<sub>2</sub>)<sub>2</sub> [T1] in (a), p-SIDT(FBTTh<sub>2</sub>)<sub>2</sub> [H1] in (b) and X2 in (c). (d-f) Time evolution of absorption at the vibronic peak marked by the black arrows in (a-c), which corresponds to an absorption characteristic of the photo-physical aggregates. The start and end of aggregation during film formation are marked by red and blue arrows, respectively.

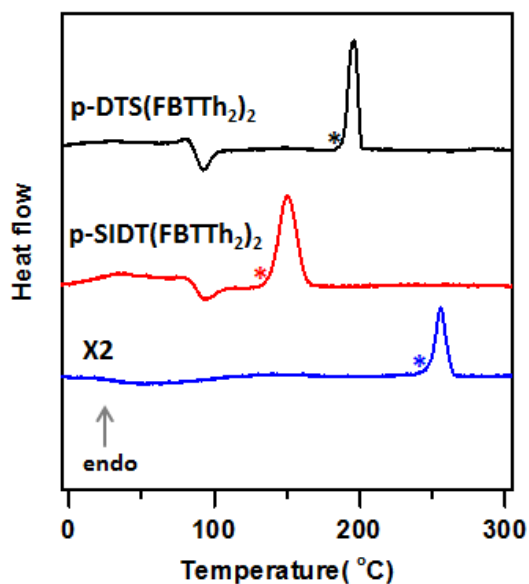


**Figure 5.3.** Heating thermograms at rate ( $100 \text{ K s}^{-1}$ ) of p-DTS(FBTTh<sub>2</sub>)<sub>2</sub> (black), p-SIDT(FBTTh<sub>2</sub>)<sub>2</sub> (red) and X2 (blue). The onset of melting for the three molecules is marked as asterisk.

#### 5.4 Liquid crystalline mesophase of p-DTS(FBTTh<sub>2</sub>)<sub>2</sub>

##### 5.4.1 Evidence of Liquid crystalline nature of p-DTS(FBTTh<sub>2</sub>)<sub>2</sub> by flash differential scanning calorimetry (F-DSC)

We recall that the as-cast p-DTS(FBTTh<sub>2</sub>)<sub>2</sub>:PC<sub>71</sub>BM film prepared without any additive remains in a largely vitrified metastable state that remains unchanged for an extended period of time.<sup>[174]</sup> We sought evidence of a LC phase by F-DSC. F-DSC allows to vitrify kinetically-inhibited phase transitions and thereby the detection of the isotropic-LC

phase transitions that are not observable by conventional DSC.<sup>[176]</sup> This is made possible by collecting thermograms at ultrafast heating and cooling rates that are up to five orders of magnitude faster than conventional DSC. In **Figure 5.4a**, we summarize F-DSC measurements performed on neat p-DTS(FBTTh<sub>2</sub>)<sub>2</sub> at different heating rates, all from an initially vitrified state. At 100 K/s, we first observe a weak endothermic transition centered at 80.0°C ( $T_{sm}^h$ ) followed by an exothermic transition related to cold crystallization ( $T_{cc}$ , i.e. crystallization in the solid state) of p-DTS(FBTTh<sub>2</sub>)<sub>2</sub> at 92.2°C and finally followed by its peak melting temperature ( $T_m$ ) at 196.1°C. Subsequent cooling at 100 K/s produces a nearly featureless curve with two weakly exothermic transitions centered at 149.6°C and at 72.0°C indicating significant vitrification of p-DTS(FBTTh<sub>2</sub>)<sub>2</sub> (**Figure 5.4b**). Increasing the rate from 100 to 500 to 1000 and to 2000 K/s leads to notable increases in  $T_{sm}^h$  from 80.0°C to 82.9°C to 85.5°C to 89.4°C and a significant shift in the  $T_{cc}$  from 92.2°C to 118.7°C to 136.5°C to 166.8°C, respectively, until a heating rate of 2000 K/s, where the cold crystallization begins to overlap with the melting point (**Figure 5.4a**). The onset of melting is estimated to be 189.4 °C, 190 °C and 190.3 °C for heating rates of 100 K/s, 500 K/s and 1000 K/s, respectively.

The notable, but relatively small, increase in  $T_{sm}^h$  with heating rate indicates a phase transition with a small activation energy barrier, which is consistent with what can be expected from a transition from a more ordered to a less ordered state such as a LC phase transition. Following similar reasoning, the pronounced  $T_{cc}$  shift suggests a phase



transition with a significant activation energy barrier, which is consistent with what is expected from a nucleation and growth process that can be described by classical nucleation theory.<sup>[45]</sup> This view is supported by F-DSC cooling data. At all cooling rates, we observe two exothermic transitions, which we from now on describe as  $T_{NI}^c$  and  $T_{Sm}^c$ , respectively, the first ( $T_{NI}^c$ ) centered at 149.6°C, 149.0°C, 147.1°C, and 143.6°C and the second ( $T_{Sm}^c$ ) centered at 71.9°C, 68.3°C, 64.8°C, 60.0°C for 100, 500, 1000, and 2000 K/s, respectively. Both exotherms are weak and show only a small rate dependence, supporting the notion of them being phase transitions with a small change in heat capacity and a minute activation energy barrier, both of which are characteristic of a LC phase transition.<sup>[46, 47]</sup>

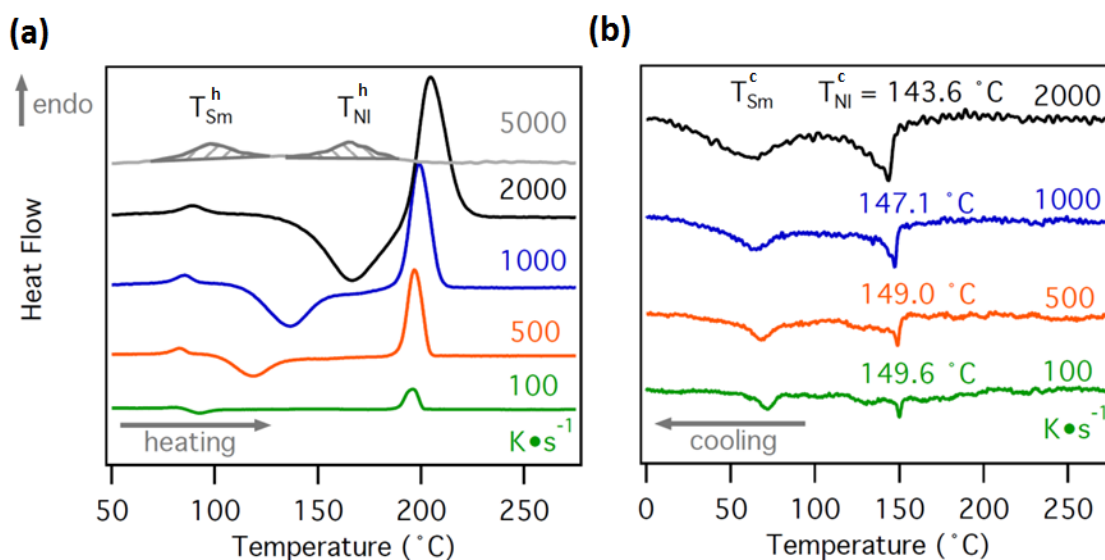


**Figure 5.4** Differential scanning calorimetry thermograms of p-DTS(FBTTh<sub>2</sub>)<sub>2</sub> at different heating (a) and cooling (b) rates revealing the liquid crystalline nature of the molecule.

#### 5.4.2 Observation of long range liquid crystalline order in p-DTS(FBTTh<sub>2</sub>)<sub>2</sub> films by cross-polarized optical microscopy (X-POM)

Further evidence was collected by optical microscopy. In **Figure 5.5**, we show typical room temperature X-POM images of neat p-DTS(FBTTh<sub>2</sub>)<sub>2</sub> film coated from pure CB and p-DTS(FBTTh<sub>2</sub>)<sub>2</sub>:PC<sub>71</sub>BM films coated from pure CB and CB with 1.5% v/v DIO. All films display similar features at the microscale and reveal a birefringent threaded texture indicating a structure with local order and planar alignment relative to the substrate that form discrete domains due to defects; such microstructures are reminiscent of the typical structure of LC phases with Schlieren textures (i.e. birefringent domains surrounded by a network of black lines). We find that this microstructure is independent of the inclusion of the DIO or PC<sub>71</sub>BM, as seen in X-POM images in **Figure 5.5**. By combining this observation with the results from F-DSC thermograms, we conclude that the crystallization of p-DTS(FBTTh<sub>2</sub>)<sub>2</sub> during the fabrication of BHJ thin films proceeds through an isotropic-LC phase transition before crystallizing along the LC phase director vectors. Furthermore, based on the X-POM data, we can tentatively attribute the first weak exothermic transition observed during cooling in F-DSC to an isotropic-nematic mesophase transition and, through deduction, the second to a nematic-smectic mesophase transition. In accordance with this assignment, we observe in thermograms collected at heating rates of 5000 K/s where we prevent cold crystallization by the ultra-high heating rate two exothermic transitions; beside the one at 99°C observed also at slower rates, we also record a weak exotherm at 165°C, which

coincide well with the transitions observed in the cooling cycles. Hence, we attribute them to the thermotropic smectic-nematic and nematic-isotropic mesophase transitions, respectively. Notable, although p-DTS(FBTTh<sub>2</sub>)<sub>2</sub>:PC<sub>71</sub>BM films coated from CB with DIO exist in a crystal phase, X-POM (**Figure 5.5c**) shows LC disclinations indicating that those crystals grow at the expense of the LC phase while maintaining the original LC disclinations.

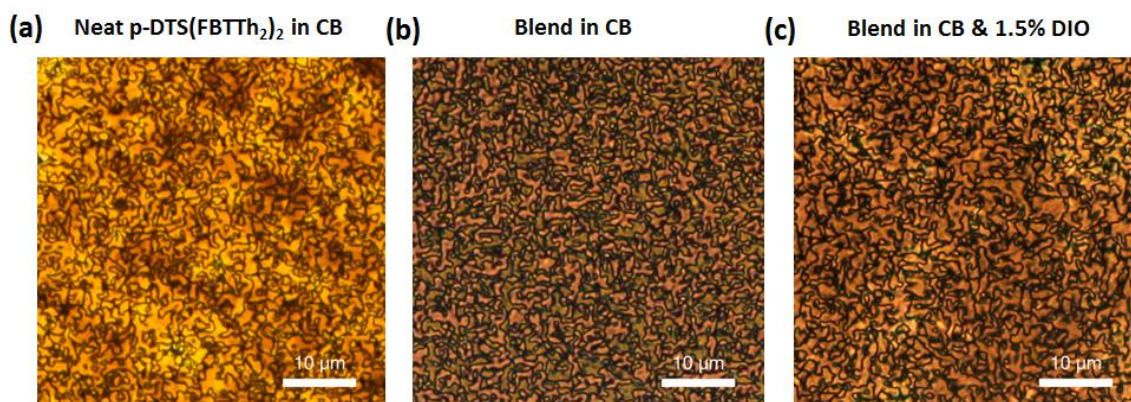


**Figure 5.5** Cross-polarized transmission optical microscopy (X-POM) of neat p-DTS(FBTTh<sub>2</sub>)<sub>2</sub> film cast from CB in (a), p-DTS(FBTTh<sub>2</sub>)<sub>2</sub>:PC<sub>71</sub>BM film cast from CB in (b) and CB with 1.5% DIO in (c).

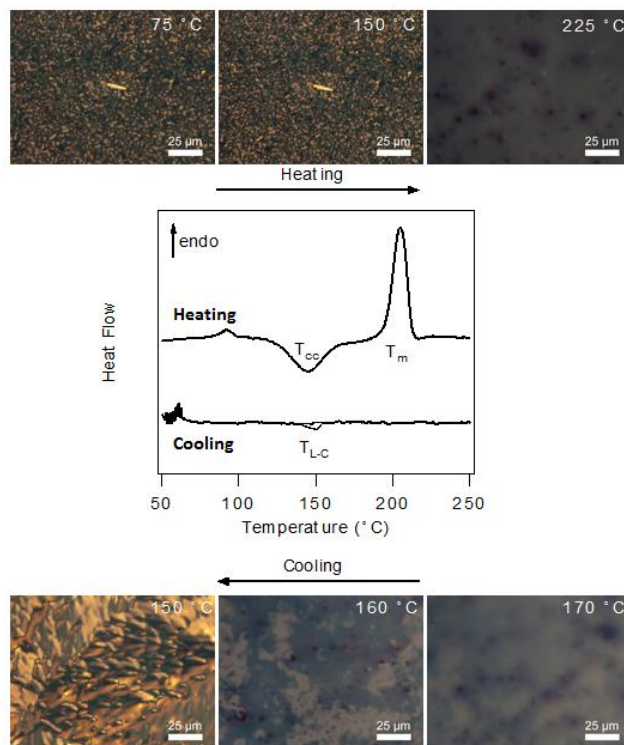


**Figure 5.6** Cross-polarized transmission optical microscopy (XPOM) of neat p-DTS(FBTTh<sub>2</sub>)<sub>2</sub> film during heating on top and cooling in bottom. Differential scanning calorimetry thermograms during heating and cooling in the middle.

Further evidence supporting these conclusions can be found in temperature-dependent X-POM measurements. In **Figure 5.6**, we show X-POM micrographs of neat p-DTS(FBTTh<sub>2</sub>)<sub>2</sub> film coated from CB at different heating temperatures on top and during cooling from melt on bottom. F-DSC thermograms in the middle were taken at 100 K/s. Upon heating to 225 °C (above the melting temperature), we observe the transformation into an isotropic phase due to melting, see XPOM image at 225 °C. When cooling from melt, XPOM images show a transition from an isotropic to nematic

phase at  $\sim 160^\circ\text{C}$  as evidenced by the appearance of weakly ordered domains (birefringent domains) within the isotropic liquid phase, followed by crystallization of p-DTS(FBTTh<sub>2</sub>)<sub>2</sub> from this phase (see appearance of crystalline domains at  $150^\circ\text{C}$ ). Thus, thin spin coated films made of p-DTS(FBTTh<sub>2</sub>)<sub>2</sub> first undergo an isotropic to LC mesophase transition after which the nucleation and growth of crystallites may proceed, while maintaining the mesoscale disclinations of the original LC phase.

#### 5.4.3 Grazing incidence x-ray diffraction confirms p-DTS(FBTTh<sub>2</sub>)<sub>2</sub> LC nature

We recall that a previous work by our group has shown, by *in situ* GIWAXS during the formation of p-DTS(FBTTh<sub>2</sub>)<sub>2</sub>:PC<sub>71</sub>BM film, the transformation of a transient and weakly ordered state of p-DTS(FBTTh<sub>2</sub>)<sub>2</sub> into thermodynamically stable state at the presence of additives in the casting solution. We therefore conclude, based on the above F-DSC and X-POM analyses, that this transient and weakly ordered state of p-DTS(FBTTh<sub>2</sub>)<sub>2</sub> is due to an LC phase.<sup>[174]</sup> This picture is further strengthened by *in situ* GIWAXS measurements performed over a period of several days at room temperature on a neat p-DTS(FBTTh<sub>2</sub>)<sub>2</sub> film cast without any additive processing ( **Figure 5.7a**). The data reveal a slow but steady evolution from the quenched LC state to the crystalline state and confirm that the film is kinetically trapped in the LC phase of p-DTS(FBTTh<sub>2</sub>)<sub>2</sub>.

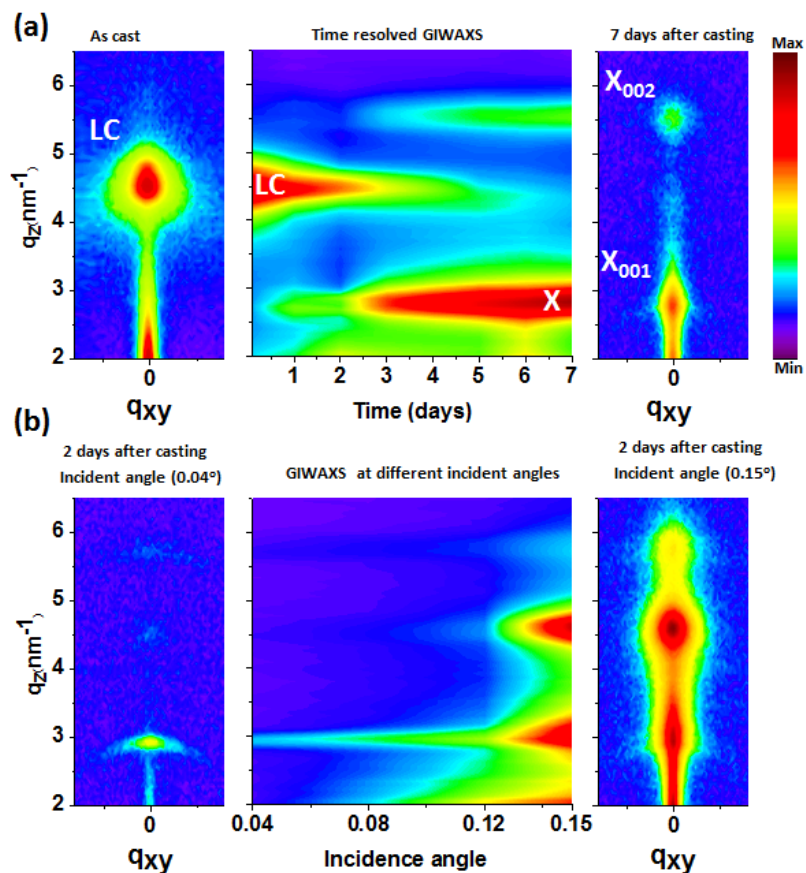


**Figure 5.7** Time evolution of p-DTS(FBTTh<sub>2</sub>)<sub>2</sub> crystallization from LC phase. (a) 2D plot of GIWAXS of neat p-DTS(FBTTh<sub>2</sub>)<sub>2</sub> as cast from pure CB (LC phase) on left, after 7 days (crystal phase) on right and time resolved integrated intensity of GIWAXS measurements over days on the middle. (b) 2D image plots of GIWAXS of p-DTS(FBTTh<sub>2</sub>)<sub>2</sub> film cast from CB soaked for two days after casting at incident angle 0.04° (below critical angle of X-ray beam) on left, 0.15° (above critical angle of X-ray beam) on right and integrated scattering intensity of GIWAXS performed at different incident angles on the middle.

We look more closely at the vertical distribution of LC and crystalline phases in partially converted sample after 2 days of ageing by angle-dependent GIWAXS measurements (**Figure 5.7b**). Tuning the incident angle with respect to the critical angle of the film can be used as waveguide for the penetration depth of the X-ray beam which can be a few nanometers below the top surface at very shallow angle.<sup>[135]</sup> At very shallow angle (ca.  $0.04^\circ$ ), we observe that crystalline phase dominates at the top surface (**Figure 5.7b**). As we increase the penetration depth of the incident beam at higher incidence angles, diffraction of the LC phase starts to appear. At an angle above the critical angle of the film (ca.  $0.15^\circ$ ), we observe the diffraction from both LC and crystalline phases. Knowing that the film was initially vitrified at LC phase indicates that crystallization is initiated at the top surface. This can be understood by the fact that molecules at the top surface are less kinetically hindered.

On the other hand, the presence of DIO during casting accelerates this transition, reducing its duration from days to minutes if not seconds, as can be seen by in situ GIWAXS measurements during spin-coating for neat p-DTS(FBTTh<sub>2</sub>)<sub>2</sub> (**Figure 5.8a**) and its blends with PC<sub>71</sub>BM (**Figure 5.8b**). In the coming chapter, we investigate in detail the roles of solvent additives in the LC to crystalline transformation and BHJ morphology evolution in p-DTS(FBTTh<sub>2</sub>)<sub>2</sub>:PC<sub>71</sub>BM system.

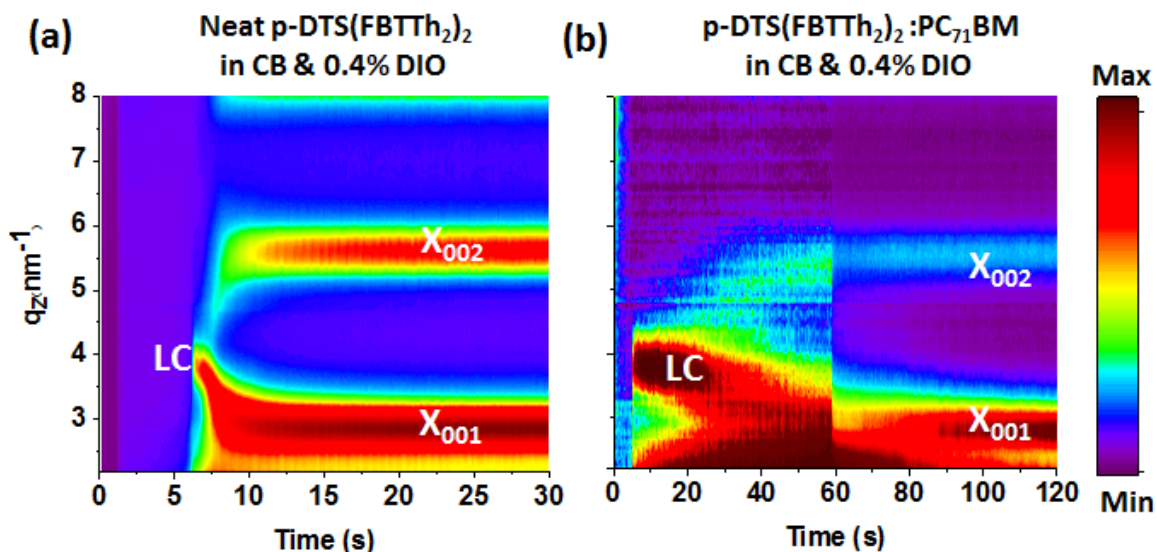


**Figure 5.8** *In situ* 2D GIWAXS image plots (Integrated scattering intensity is shown in logarithmic color scale versus  $q$  (nm<sup>-1</sup>) and time(s)) of spin-casting neat p-DTS(FBTTh<sub>2</sub>)<sub>2</sub> and p-DTS(FBTTh<sub>2</sub>)<sub>2</sub>:PC<sub>71</sub>BM blends from CB with 0.4 % DIO, in (a) and (b), respectively.

#### 5.4.4 Crystal growth of p-DTS(FBTTh<sub>2</sub>)<sub>2</sub> is templated by its liquid crystalline order

We have observed in the previous sections that the p-DTS(FBTTh<sub>2</sub>)<sub>2</sub>:PC<sub>71</sub>BM films cast from additives appear with LC disclinations under XPOM although p-DTS(FBTTh<sub>2</sub>)<sub>2</sub> has already become crystalline. This observation indicates that crystal growth of p-DTS(FBTTh<sub>2</sub>)<sub>2</sub> is templated by the initial liquid crystalline order before crystallization. This view is supported by energy filtered transmission electron microscopy (EF-TEM) images of crystallized p-DTS(FBTTh<sub>2</sub>)<sub>2</sub>:PC<sub>71</sub>BM samples that reveal the remnant LC nature of p-DTS(FBTTh<sub>2</sub>)<sub>2</sub> within the crystallized and phase-separated domains



(**Figure 5.9**). In **Figure 5.9a**, we show an EF-TEM image of p-DTS(FBTTh<sub>2</sub>)<sub>2</sub>: PC<sub>71</sub>BM film coated from CB with 1.5% v/v DIO. A composite image of sulfur (green) and carbon (red) mapping the mesoscale composition is shown in **Figure 5.9b**. The sulfur-rich regions correspond to p-DTS(FBTTh<sub>2</sub>)<sub>2</sub> rich domains while carbon-rich regions correspond to PC<sub>71</sub>BM rich domains. The images show wire-like p-DTS(FBTTh<sub>2</sub>)<sub>2</sub> structures that maintain the LC fingerprint and seem to crystallize and phase separate from molecules that were initially ordered in a preferred orientation within the LC domains.

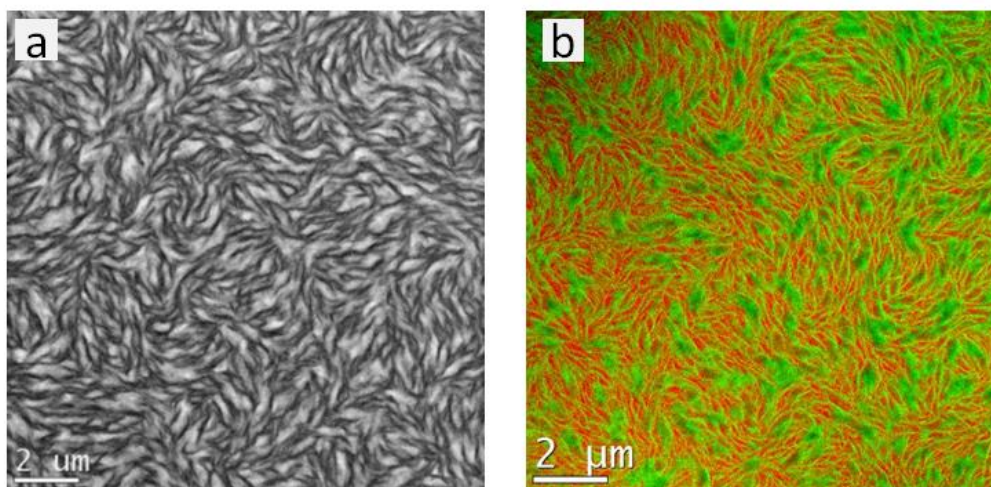


**Figure 5.9** (a) Energy-filtered transmission electron micrographs (EFTEM) with elemental mappings of carbon (284 eV) and sulfur (165 eV) performed on the plan-view of p-DTS(FBTTh<sub>2</sub>)<sub>2</sub>:PC<sub>71</sub>BM film, coated from CB with 1.5% DIO. (b) Composite color image of EF-TEM image in (a). Red and green colors represent carbon rich phase [PC<sub>71</sub>BM], sulfur rich phase [p-DTS(FBTTh<sub>2</sub>)<sub>2</sub>], respectively.

### **5.5 Generalization of the relationship between the ease of crystallization of donor molecules and the need for additives**

We deduce from all the previous observations that because p-DTS(FBTTh<sub>2</sub>)<sub>2</sub> undergoes kinetically hindered mesophase before crystallizing, it requires additives or thermal annealing to get over the hindered state and allow the crystallization and phase separation.<sup>[177]</sup> A key objective is, however, to produce high-efficiency BHJ devices in a single-step procedure. Indeed, despite the performance value added of additive processing, thermal and solvent annealing, there are doubts regarding their compatibility with large-scale continuous manufacturing. Both thermal and solvent annealing require extra processing steps. Furthermore, it is not particularly easy to use high boiling point halogenated additives in continuous manufacturing in ambient air for practical reasons such as very slow drying and toxicity to operators. We therefore sought to further explore the generality of our findings of limiting specific phase transitions to control BHJ formation with the aim of identifying relevant features to incorporate into the design of new materials that could circumvent the need for additive processing or subsequent annealing steps. We selected two donor materials, namely p-SiDT(FBTTh<sub>2</sub>)<sub>2</sub> and X2, which a priori are kinetically either more or less hindered compared to p-DTS(FBTTh<sub>2</sub>)<sub>2</sub>.

### 5.5.1 Ease of crystallization of p-SIDT(FBTTh<sub>2</sub>)<sub>2</sub>

Structurally, p-SIDT(FBTTh<sub>2</sub>)<sub>2</sub> is similar to p-DTS(FBTTh<sub>2</sub>)<sub>2</sub> but for a larger central donor moiety. The crystallization of this material is kinetically more prohibited than that of p-DTS(FBTTh<sub>2</sub>)<sub>2</sub> as confirmed by F-DSC thermograms. In **Figure 5.10**, we summarize F-DSC thermograms of p-SIDT(FBTTh<sub>2</sub>)<sub>2</sub> at different heating and cooling rates. From heating thermogram of p-SIDT(FBTTh<sub>2</sub>)<sub>2</sub> at 100 K/s (**Figure 5.10a**), we observe cold crystallization transition ( $T_{CC}$ ) of p-SIDT(FBTTh<sub>2</sub>)<sub>2</sub> centered at 93.2°C followed by its peak melting temperature ( $T_m$ ) centered at 150.3°C. Significant shift in the  $T_{CC}$  from 93.2°C to 105.6°C was observed when increasing heating rate from 100 to 200 K/s. At heating rate 400 K/s, we observe overlapping of  $T_{CC}$  with the melting point and the appearance of endothermic transition ( $T_{sm}^h$ ) centered at 96.8°C indicating vitrification of the sample. The onset of melting is estimated to be 138 °C and 138.4 °C for heating rates of 100 K/s and 200 K/s, respectively, before melting overlaps with  $T_{CC}$  at a heating rate of 400 K/s. The complete vitrification of the sample appears clearly at thermograms taken at heating rates of 500 and 1000 K/s in which we observe a notable shift of  $T_{sm}^h$  to 99.1°C and 103°C and the appearance of an endothermic transition ( $T_{NI}^h$ ) at 127.2°C and 128.1°C, respectively. The two transitions show weak rate dependence indicating a phase transition with small activation energy barrier, characteristic of LC transitions, and therefore are assigned to smectic to nematic ( $T_{sm}$ ) and nematic to isotropic ( $T_{NI}$ ) transitions, respectively. This is supported by cooling themograms of p-SIDT(FBTTh<sub>2</sub>)<sub>2</sub> (**Figure 5.10b**) in which two weak exothermic and weakly rate dependent transitions are

observed;  $T_{NI}^c$  centered at 122.3°C, 121.6°C, 119.4°C, 118.8°C and 112.6°C and  $T_{Sm}^c$  centered at 80.3°C, 79.9°C, 79.5°C, 78.2°C and 76.4 for 100, 200, 400, 500 and 1000 K/s, respectively. These observations reveal the ease of vitrification of p-SIDT(FBTTh<sub>2</sub>)<sub>2</sub>; it can be vitrified easily under fast film formation conditions such as spin coating. Moreover, the vitrification of p-SIDT(FBTTh<sub>2</sub>)<sub>2</sub> occurs at 5 times lower rate than what was observed for p-DTS(FBTTh<sub>2</sub>)<sub>2</sub>, indicating more kinetically hindered crystallization for p-SIDT(FBTTh<sub>2</sub>)<sub>2</sub>.

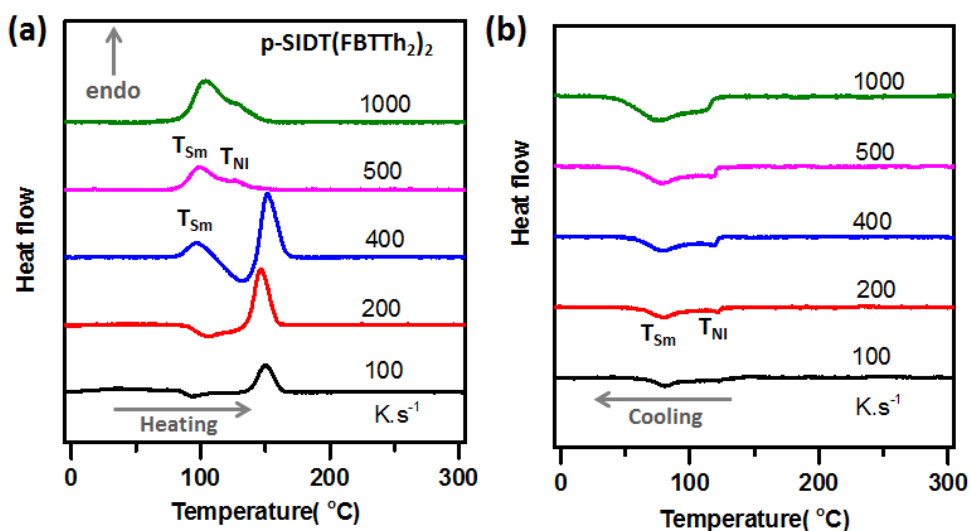


**Figure 5.10** Differential scanning calorimetry thermograms at different heating (a) and cooling (b) rates of p-SIDT(FBTTh<sub>2</sub>)<sub>2</sub>.

### 5.5.2 Ease of crystallization of X2

In contrast, X2, a medium-size molecule that has similar structure to p-DTS(FBTTh<sub>2</sub>)<sub>2</sub> but for the elongated chromophore, is found to crystallize remarkably easily compared to p-

DTS(FBTTh<sub>2</sub>)<sub>2</sub> and p-SIDT(FBTTh<sub>2</sub>)<sub>2</sub>. In **Figure 5.11**, we summarize X2 heating and cooling thermograms. It wasn't possible to vitrify X2 at all cooling and heating rates up to 5000 K/s (**Figure 5.11a**). Furthermore, no cold crystallization transition or glass transition were detected at all heating rates indicating lack of initially amorphous or LC vitrified state (**Figure 5.11a**). From heating thermograms, we observe the onset of melting at 248.9 °C, 248.9 °C, 249.3 °C, 249.4 °C and 253 °C, that peaks at 256 °C, 259 °C, 262 °C, 266 °C and 284 °C, for heating rates 100 K/s, 500 K/s, 1000 K/s, 2000 K/s and 5000 K/s, respectively. Crystallization from melt occurs at all cooling rates revealing the ease of crystallization of X2 (**Figure 5.11b**). All these observations highlight its strong ability to crystallize. As a consequence, we found that this material does not require additives to achieve a sufficiently high degree of crystallinity when processing it from solution. This likely explains the fact that BHJ solar cells can be produced even without additive processing.<sup>[178]</sup>

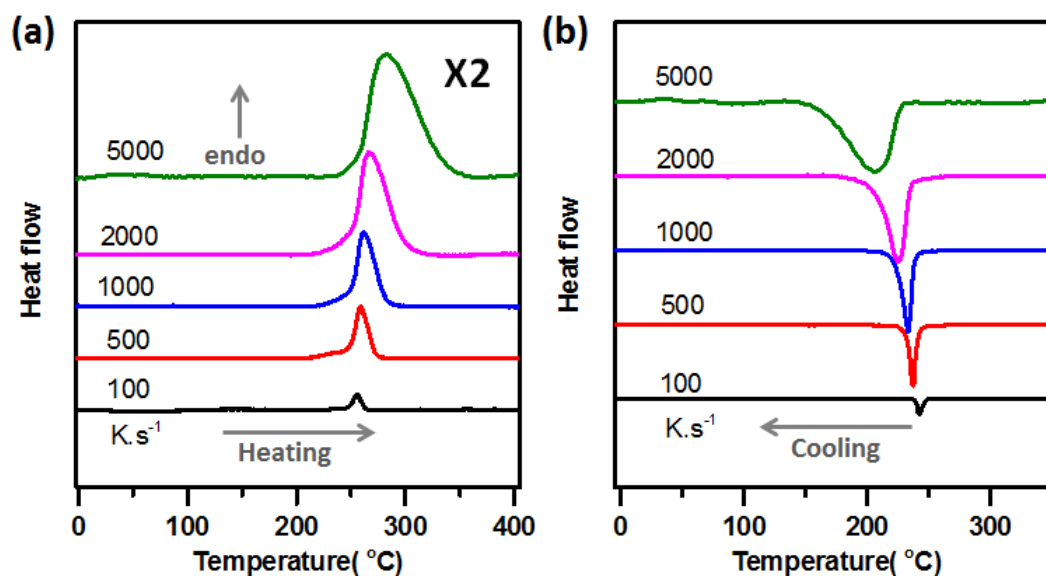


**Figure 5.11** Differential scanning calorimetry thermograms at different heating (a) and cooling (b) rates of X2.

### 5.5.3 Comparison of the ability of crystallization of p-SIDT(FBTTh<sub>2</sub>)<sub>2</sub>, X2, and p-DTS(FBTTh<sub>2</sub>)<sub>2</sub>

In order to obtain an overall picture we summarize and compare the heating and cooling thermograms at a rate 100 K/s for the three materials in **Figure 5.12**. Heating thermograms of X2 do not show cold crystallization, unlike p-DTS(FBTTh<sub>2</sub>)<sub>2</sub> and p-SIDT(FBTTh<sub>2</sub>)<sub>2</sub>, indicating high crystallinity in the sample and confirming the absence of an initially amorphous or LC vitrified state. X2 crystallizes from the melt even at high cooling rates with the appearance of a strong exothermic transition relating to hot crystallization (crystallization from melt), as concluded from cooling thermograms of X2. Moreover, hot crystallization occurs at relatively low supercooling (i.e. the difference

between the melting temperature and the hot crystallization temperature) suggesting low activation energy for crystallization, as seen in **Figure 5.12**. This is in contrast to the cases of p-DTS(FBTTh<sub>2</sub>)<sub>2</sub> and p-SIDT(FBTTh<sub>2</sub>)<sub>2</sub> in which solidification seems to first lead to liquid crystalline phases.

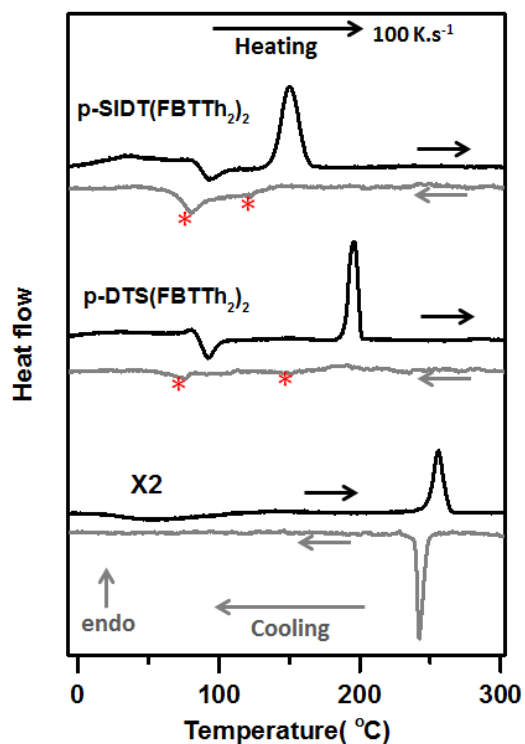


**Figure 5.12** Heating and cooling thermograms at rate (100 K s<sup>-1</sup>) of p-SIDT(FBTTh<sub>2</sub>)<sub>2</sub>, X2, and p-DTS(FBTTh<sub>2</sub>)<sub>2</sub>.

#### 5.5.4 Effect of the ease of vitrification/crystallization on crystallization behavior during solution processing

A key test of the relevance and impact of the observations made by F-DSC of the relative ease of crystallization of the three neat materials in question is whether they directly impact crystallization behavior during solution casting of BHJ blends. We have therefore monitored the crystallization behavior during solution-processing of blends with these donors and PC<sub>71</sub>BM both with and without additive processing. In **Figure 5.13**, we have plotted line cuts of the integrated intensity of the alkyl stacking peak derived from *in situ* GIWAXS measurements performed during spin-coating. 2D GIWAXS images of p-SIDT(FBTTh<sub>2</sub>)<sub>2</sub>:PC<sub>71</sub>BM, p-DTS (FBTTh<sub>2</sub>)<sub>2</sub>:PC<sub>71</sub>BM and X2:PC<sub>71</sub>BM samples are shown in **Figure 5.14**, **Figure 5.15** and **Figure 5.16**, respectively.

Starting with the p-SIDT(FBTTh<sub>2</sub>)<sub>2</sub>:PC<sub>71</sub>BM binary (**Figure 5.13a** and **Figure 5.14**), the measurements reveal no trace of long range order in the absence of additive. However, substantial crystallization is observed during spin-coating in the presence of additive. For p-DTS(FBTTh<sub>2</sub>)<sub>2</sub>:PC<sub>71</sub>BM, absence of additive leads to quenching into the LC phase (**Figure 5.13b** and **Figure 5.15**). With the inclusion of additive, the film crystallizes after briefly transitioning from solution to the LC phase. These observations match our expectation confirming the ease of vitrification of p-SIDT(FBTTh<sub>2</sub>)<sub>2</sub> and p-DTS(FBTTh<sub>2</sub>)<sub>2</sub>. Thus, both molecules require additives to overcome the hindered state and facilitate their crystallization.



On the other hand, in situ GIWAXS measurements performed on X2:PC<sub>71</sub>BM reveal that it crystallizes immediately during solution processing without any need for additives, whereas the crystallinity of X2 increases at the presence of additives (**Figure 5.13c and Figure 5.16**). This observation confirms the strong ability of crystallization of X2, unlike of p-SIDT(FBTTh<sub>2</sub>)<sub>2</sub> and p-DTS(FBTTh<sub>2</sub>)<sub>2</sub>.

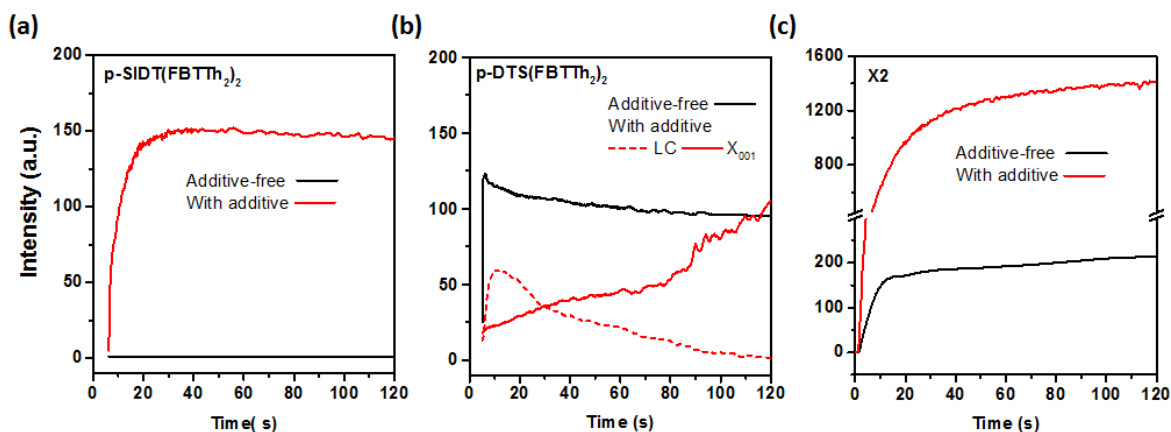


**Figure 5.13** Integrated intensity of alkyl stacking peak derived from in situ GIWAXS during spin coating of the three molecules blends with PC<sub>71</sub>BM; p-SIDT(FBTTh<sub>2</sub>)<sub>2</sub>:PC<sub>71</sub>BM from CB and CB with 0.4% DIO in (a), p-DTS(FBTTh<sub>2</sub>)<sub>2</sub>:PC<sub>71</sub>BM from CB and CB with 0.4% DIO in (b) and X2: PC<sub>71</sub>BM from CF and CF with 0.4% DIO in (c). The thickness of the coated film in (a), (b) and (c) is ~ 100 nm, ~ 103 nm and ~ 108 nm, respectively.

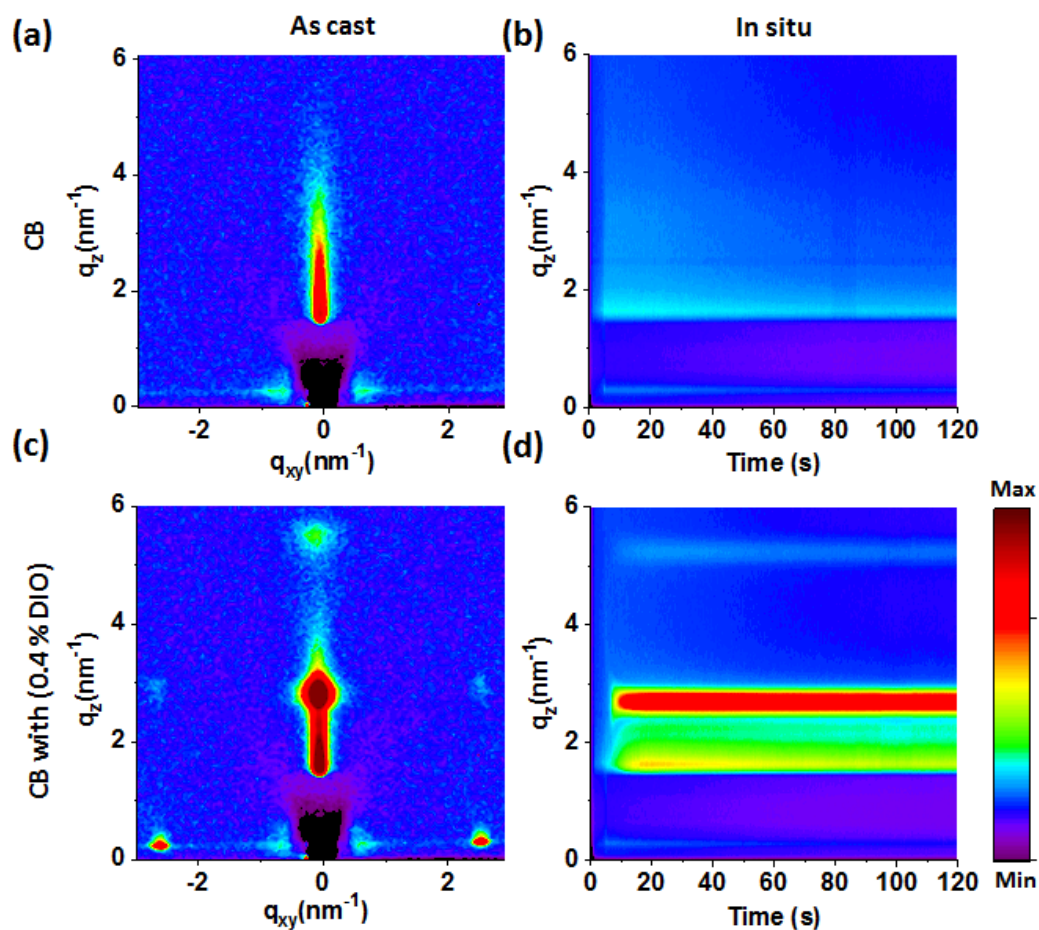


**Figure 5.14** 2D GIWAXS image plots of as cast p-SIDT(FBTTh<sub>2</sub>)<sub>2</sub>:PC<sub>71</sub>BM film from CB in (a) and CB with 0.4% DIO in (c). Time evolution of integrated scattering intensity of *in situ* GIWAXS performed during spin coating of p-SIDT(FBTTh<sub>2</sub>)<sub>2</sub>:PC<sub>71</sub>BM from CB in (b) and CB with 0.4% DIO in (d).

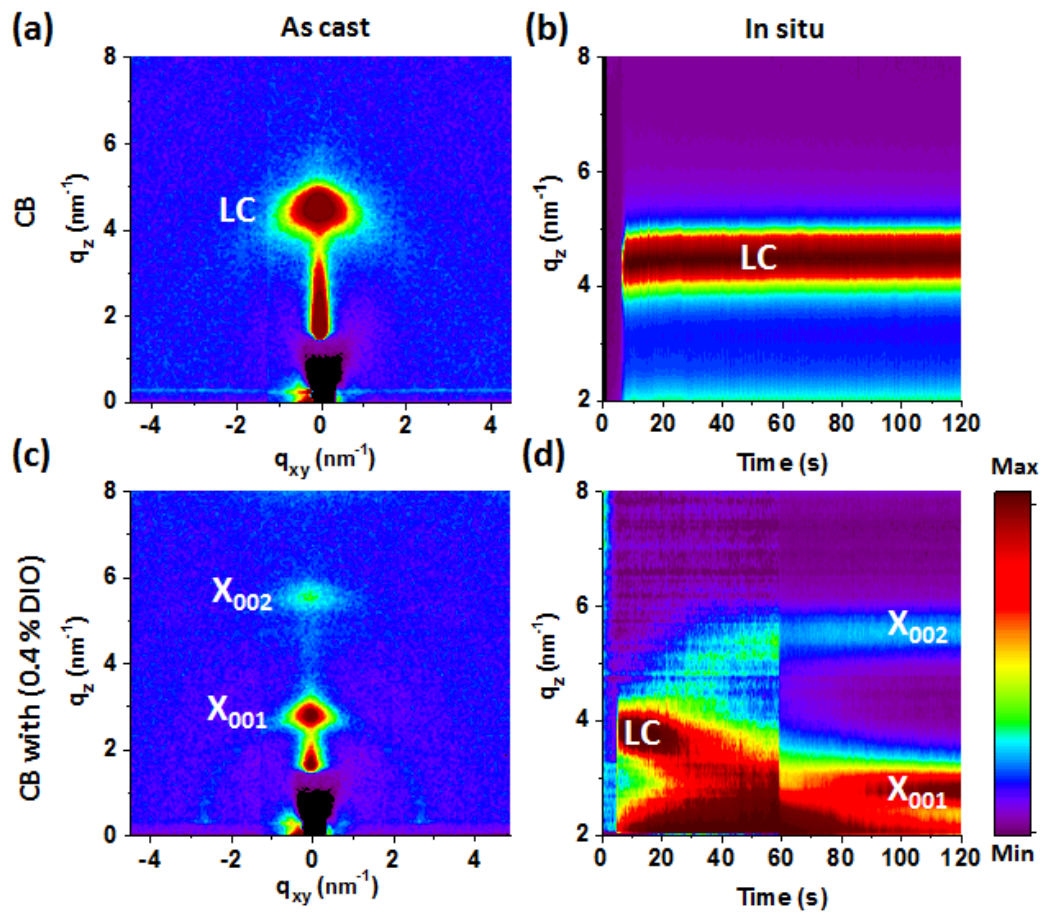


**Figure 5.15** 2D GIWAXS image plots of as cast p-DTS(FBTTh<sub>2</sub>)<sub>2</sub>:PC<sub>71</sub>BM film from CB in (a) and CB with 0.4% DIO in (c). Time evolution of integrated scattering intensity of *in situ* GIWAXS performed during spin coating of p-DTS(FBTTh<sub>2</sub>)<sub>2</sub>:PC<sub>71</sub>BM from CB in (b) and CB with 0.4% DIO in (d).

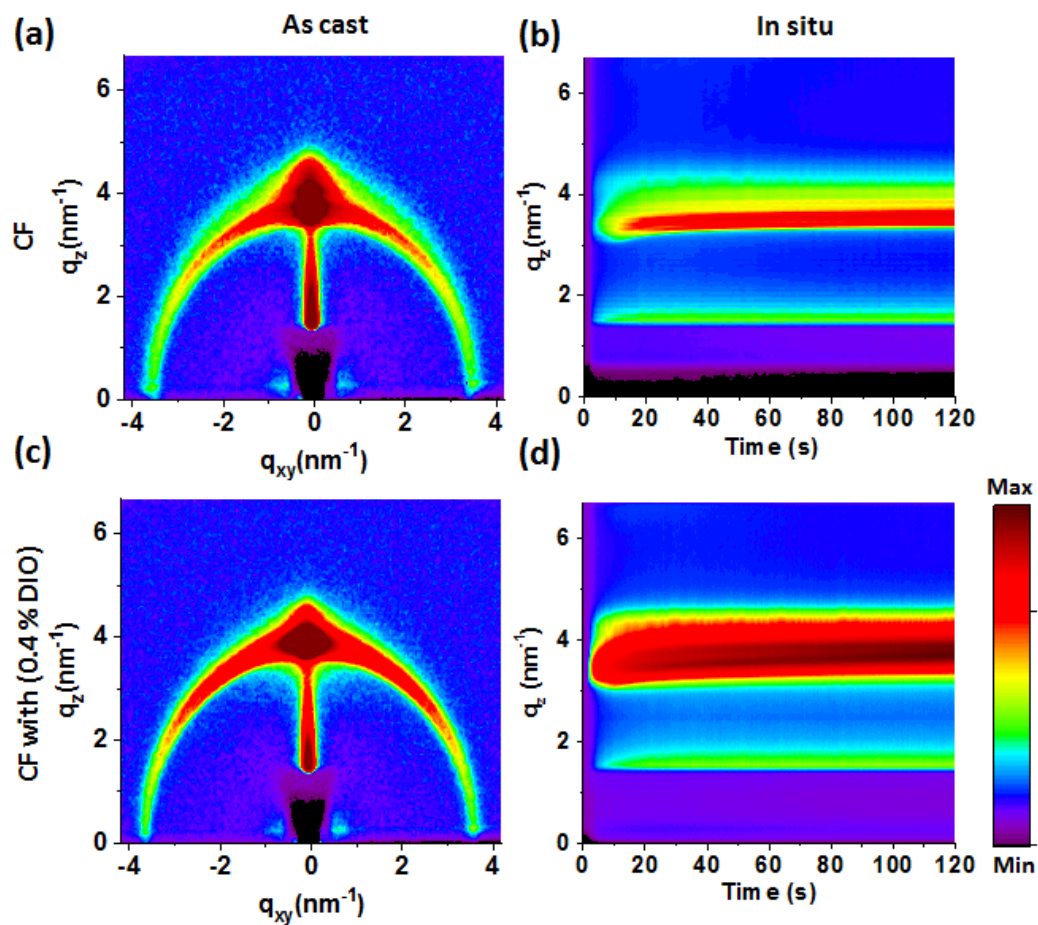


**Figure 5.16** 2D GIWAXS image plots of as cast X2:PC<sub>71</sub>BM film from CF in (a) and CF with 0.4% DIO in (c). Time evolution of integrated scattering intensity of *in situ* GIWAXS performed during spin coating of X2:PC<sub>71</sub>BM from CF in (b) and CF with 0.4% DIO in (d).

### 5.5.5 Effect of the ease of vitrification/crystallization on BHJ morphology and solar cell device performance

For the two donors, p-DTS(FBTTh<sub>2</sub>)<sub>2</sub> and p-SIDT(FBTTh<sub>2</sub>)<sub>2</sub>, that suffer from ease of vitrification, it has been shown that a vitrified and low phase separated films are attained when coating their blends with fullerene from pure CB. While addition of DIO into casting solution helps in promoting donor crystallization and BHJ phase separation. We refer to the TEM images in the references [121,177] for phase separation. Extra content of DIO leads to excessive domain coarsening and deterioration of device performance.<sup>[121]</sup> On the other hand, TEM images of X2 in reference [179] have shown remarkable ability to phase separate from fullerene at wide range of donor-acceptor ratio. The phase separation was observed even at low donor content. Indeed, this can be understood by its ease of crystallization as discussed above. For X2:PC<sub>71</sub>BM system, the device performance and morphology with using additives are not yet reported. We compare the device performance and morphology of X2:PC<sub>71</sub>BM coated from pure CF and CF with 0.4%DIO (**Figure 5.17**). Addition of DIO results in slight decrease in open circuit voltage (Voc) from 693 mV to 655 mV which is compensated by slight increase in short circuit current density (Jsc) from 15.7 to 16.1 and fill factor (FF) from 67.6 to 69.6 leading to negligible change in overall power conversion efficiency (PCE) (Device parameters and J-V curves are shown in **Table 5.1** and **Figure 5.17a**, respectively). Notably, the attained high PCE with an average (maximum) of 7.4% (7.6%) both in additive-free and additive-based processes is the highest PCE reported thus far for

small-molecule BHJ solar cells prepared without use of additives or post-process annealing. In **Figure 5.17b-c**, we show composite color image of energy-filtered E-FTEM images of the two cases, with green and red colors representing sulfur rich phase [X2] and carbon rich phase [PC<sub>71</sub>BM], respectively. EF-TEM images reveal satisfactory phase separation and well-connected domains of X2 for samples coated from pure CF. Domain coarsening is observed for samples coated from CF with 0.4% DIO. It is surprising that use of additives does not harm the device performance despite significant differences in crystallization and phase separation, because solution-processed small-molecule BHJ solar cells are known to be extremely sensitive to additive processing.<sup>[120,121]</sup> Again, this result points to the intriguing process-insensitivity of X2.<sup>[178]</sup> Whether this insensitivity is due to the ease of crystallization and to an absence of intermediate disordered or LC states of the donor material – which could otherwise make the phase transformation outcome arguably more dependent upon formulation and processing conditions – can only be speculated upon at this time. Importantly, X2, without the need of additives, is able to attain sufficient crystallization and phase separation from fullerene and form well connected domains, as expected from its strong ability to crystallize as revealed by F-DSC.

**Table 5.1** Average device parameters of solar cell devices fabricated from X2:PC<sub>71</sub>BM

	<b>J<sub>sc</sub></b> (mA/cm <sup>2</sup> )	<b>V<sub>oc</sub></b> (mV)	<b>FF</b> (%)	<b>PCE</b> (%)
No DIO	15.7±0.3	693±3	67.6 ±1.0	7.4 ±0.1
0.4% DIO	16.1±0.6	655±3	69.6 ±0.8	7.4 ±0.2

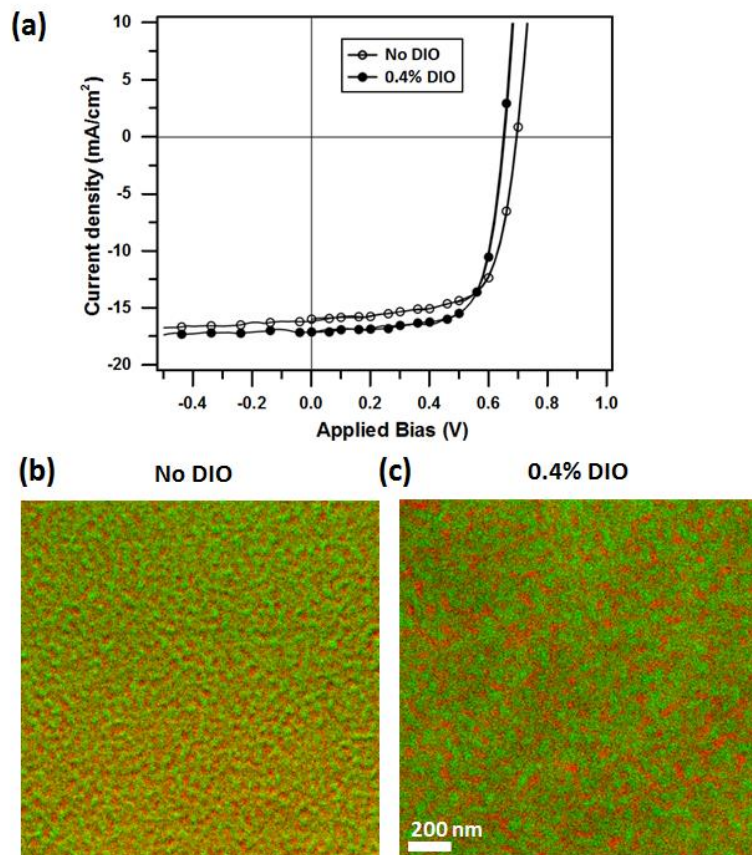


**Figure 5.17** (a) Current density-voltage (J-V) characteristics of two champion solar cells, both exhibiting PCE = 7.6%, fabricated using X2:PC<sub>71</sub>BM blend spin-cast from pure chloroform (open circles) and from chloroform with 0.4 % DIO (solid circles). (b) & (c)

Composite color image of energy-filtered transmission electron micrographs (EFTEM) with elemental mappings of carbon (284 eV) and sulfur (165 eV) performed on the plan-view of X2:PC<sub>71</sub>BM film coated from CF (b) and CF with 0.4 % DIO (c). The film thicknesses in (a) and (b) are ~ 108 nm and ~ 109 nm respectively. Green and red colors represent sulfur rich phase [X2] and carbon rich phase [PC<sub>71</sub>BM], respectively.

## 5.6 Conclusion

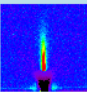
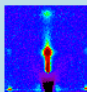
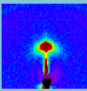
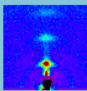
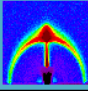
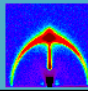
Overall, a generalized concept is proposed revealing the correlation between the ease of crystallization of donor molecules and the required processing routes for achieving high performance solar cells. The extent of kinetic hindrance and formation or not of metastable intermediate phases in a wide range of donor small-molecules can be used to directly inform the solution processing recipes and formulations needed to generate highly efficient BHJ solar cells. F-DSC is thereby a powerful tool to determine relevant phases and transitions. With the observations that some materials can be processed into highly efficient solar cells without being vitrified in the absence of additives during common solution-manufacturing, it is now possible to focus further synthetic efforts on the development of high performing small-molecule donor materials which lend themselves well to continuous, high throughput roll-to-roll manufacturing in environmentally friendly conditions in ambient air.

We have demonstrated that the ease with which donor small-molecules crystallize and their solidification pathways heavily influences whether additive processing, or



alternatively added annealing steps, are required to achieve high performance BHJ solar cells. In **Table 5.2**, we summarize the ability of crystallization and crystallization behavior of p-SIDT(FBTTh<sub>2</sub>)<sub>2</sub>, p-DTS(FBTTh<sub>2</sub>)<sub>2</sub> and X2 and the relative processing routes needed for attaining high efficiency solar cell performance . Using F-DSC, we have shown that donor materials which can be easily quenched and vitrified, such as p-DTS(FBTTh<sub>2</sub>)<sub>2</sub> and p-SIDT(FBTTh<sub>2</sub>)<sub>2</sub>, form a metastable intermediate state, either amorphous or liquid crystalline, from which the crystalline state forms, as confirmed by in situ GIWAXS measurements. In these circumstances, the solvent additives and/or annealing are required to kinetically favor crystallization and phase separation. On the other hand, donor materials with a strong ability to crystallize, such as X2, can phase separate from the fullerene without requiring additives/annealing, perhaps showing the way forward with the design of next generation donor small-molecules with the ability to yield highly efficient organic solar cells via continuous, high throughput and environmentally friendly manufacturing routes.

**Table 5.2** Comparison of the ability of crystallization, crystallization behavior and processing routes between p-SIDT(FBTTh<sub>2</sub>)<sub>2</sub>, p-DTS(FBTTh<sub>2</sub>)<sub>2</sub> and X2.

	Quenching by cooling	Vitrification by heating	As-cast donor phase w/o additives	As-cast donor phase w additives	Need for additive?	PCE (%) w/o additive	PCE (%) w/ additive	
Ease of crystallization ↓	p-SIDT(FBTTh <sub>2</sub> ) <sub>2</sub>	Quenched @ 100 K/s	Vitrified @ 400 K/s	 Amorphous	 Crystal	Yes	1.7 % <sup>a</sup>	6.4 % <sup>a</sup>
	p-DTS(FBTTh <sub>2</sub> ) <sub>2</sub>	Quenched @ 100 K/s	Vitrified @ 2000 K/s	 Liquid Crystal	 Crystal	Yes	1.8 % <sup>b</sup>	7 % - 9 % <sup>b</sup>
	X2	Not quenched up to 5000 K/s	Not vitrified up to 5000 K/s	 Crystal	 Crystal	No	7.4 % <sup>c</sup>	7.4 % <sup>c</sup>

Results (a & b) are from references [120,121,175] . Results (c) are from this work.

## Chapter 6

### **Impact of solvent additives on the mechanism of film formation in small-molecule bulk heterojunction solar cells**

#### **6.1 Introduction**

In the previous chapter, we have investigated the roles of crystallization dynamics and pathway in small-molecule BHJ layers revealing the correlation between the ease of crystallization of donor molecules and the required processing strategies used for attaining high performance solar cells. We have demonstrated that the presence of intermediate mesophase on the route of donor crystallization is the main obstacle that the solvent additives help overcome, allowing donor crystallization and donor-acceptor phase separation. In this chapter, we provide in-depth investigation of the mechanism of microstructure formation based on the interaction of the solvent additives with the components of the BHJ system including the phases in which they present. Part of this work was submitted to Chemistry of Materials (under review).

We first investigate the effects of the additive [1,8-diiodooctane (DIO)] on the solar cell device performance and active layer morphology in p-DTS(FBTTh<sub>2</sub>)<sub>2</sub>:PC<sub>71</sub>BM system cast from pure chlorobenzene (CB) and CB with different amount of the additives. Then, we use state-of-the-art in situ characterization techniques to investigate the solution to solid film transformation during spin coating of the active layer aiming to reveal the mechanism of the solvent additive effect in this BHJ system. Whereas selective solubility

of one of the BHJ components in the solvent additives is known to impact the microstructure formation of the BHJ, the phases in which each component may present is less considered in the literature. We show in this study that the interaction of the additive with the BHJ components depends on their phase; whether they present in a molecularly mixed phase, or transient phase such as liquid crystal, or crystalline phase, all of which has different interaction with the additive. Now, based on the interaction of the additive DIO with the components/phases of the system, in-depth understanding of the mechanism of microstructure formation can be achieved. DIO is shown to selectively dissolve PC<sub>71</sub>BM more than p-DTS(FBTTh<sub>2</sub>)<sub>2</sub>, enabling demixing and phase separation. Interestingly, DIO is found to interact preferentially with the LC phase promoting formation of p-DTS(FBTTh<sub>2</sub>)<sub>2</sub> crystals out of the LC phase while maintaining the liquid crystalline disclinations. The crystal phase is much less interactive with DIO promoting saturation of the microstructure development after transformation. Our results provide the evidence that nucleation density and growth of the crystalline phase of p-DTS(FBTTh<sub>2</sub>)<sub>2</sub> can be controlled by the amount of DIO which manipulates the diffusivity of the small-molecule donor and acceptor species in the wet film and consequently determines the extent of phase separation. We show that moderate kinetics of film formation is favored for achieving optimum phase separation leading to optimum device performance.

## 6.2 Effects of solvent additives on solar cell devices performance and BHJ morphology

We begin by investigating the influence of the solvent additives on the solar cell device performance of p-DTS(FBTTh<sub>2</sub>)<sub>2</sub>:PC<sub>71</sub>BM system. We have fabricated the solar cells devices using identical solution preparation and spin coating conditions to those used in previous reports <sup>[120]</sup>; 3.5% wt/v solutions of p-DTS(FBTTh<sub>2</sub>)<sub>2</sub> and PC<sub>71</sub>BM (60:40 weight ratio) from CB, 0.4 v/v% DIO-CB and 1% v/v% DIO-CB were cast at 1750 rpms for 60 s. The current density versus voltage (J-V) characteristic curves are shown in **Figure 6.1**. A modest efficiency of 2.3 % was observed for the samples casted from CB, while addition of 0.4 v/v% DIO into casting solution improved the efficiency significantly to 7.6 %. In case of 1% v/v DIO-CB, devices show extreme deterioration of device performance with efficiency around 1%.

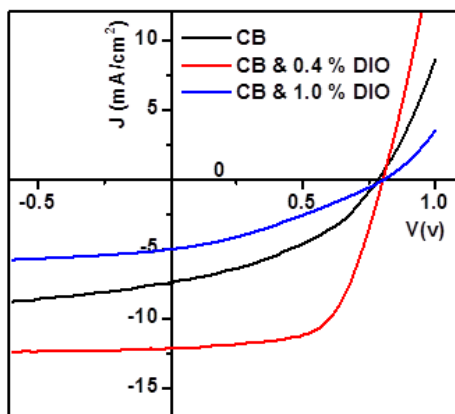


**Figure 6.1** Current density- Voltage (J-V) curves of solar cell devices fabricated from p-DTS(FBTTh<sub>2</sub>)<sub>2</sub>:PC<sub>71</sub>BM blends cast from pure CB (black), CB with 0.4% DIO (red), and CB with 1.0% DIO (blue).

These dramatic changes in device performance are mainly due to morphological differences influenced by the inclusion of additives. Thus, we investigated the impact of the additive content on the BHJ morphology. We performed cross polarized optical microscopy and energy filtered transmission electron microscopy (EF-TEM) with elemental mapping of sulfur (green; donor) and carbon (red; acceptor) to reveal the macroscale ordering and the nanoscale phase separation, respectively. As shown in the previous chapter, films cast with and without additive (**Figure 6.2a-c**) exhibit the liquid crystalline disclinations as remnants of the LC mesophase initially adopted by p-DTS(FBTTh<sub>2</sub>)<sub>2</sub>. BHJ films cast from neat CB exhibit very little phase separation, as shown in **Figure 6.2d**. The slight phase separation is not surprising as the initially quenched films tend to crystallize over a period of days in ambient conditions as we have shown in the previous chapter. As expected, the devices fabricated with this condition exhibit poor performance due to the null phase separation and the weakly ordered donor phase. On the other hand, BHJ film cast with 0.4% (**Figure 6.2e**) is more phase separated, with wire-like extended domains of p-DTS(FBTTh<sub>2</sub>)<sub>2</sub> crystals. The 0.4% DIO sample appears with well-connected domains of both p-DTS(FBTTh<sub>2</sub>)<sub>2</sub> and PC<sub>71</sub>BM. The sharp increase in power conversion efficiency of the fabricated devices under this condition correlates with the improved phase separation and increased ordering of the donor phase after crystallization. For 1% DIO case, the sample exhibits over-coarsening of PC<sub>71</sub>BM domains and p-DTS(FBTTh<sub>2</sub>)<sub>2</sub> crystals that are found to extend to the length

of microns. Clearly, this over-coarsening is counterproductive to charge generation leading to reduction in the devices performance.

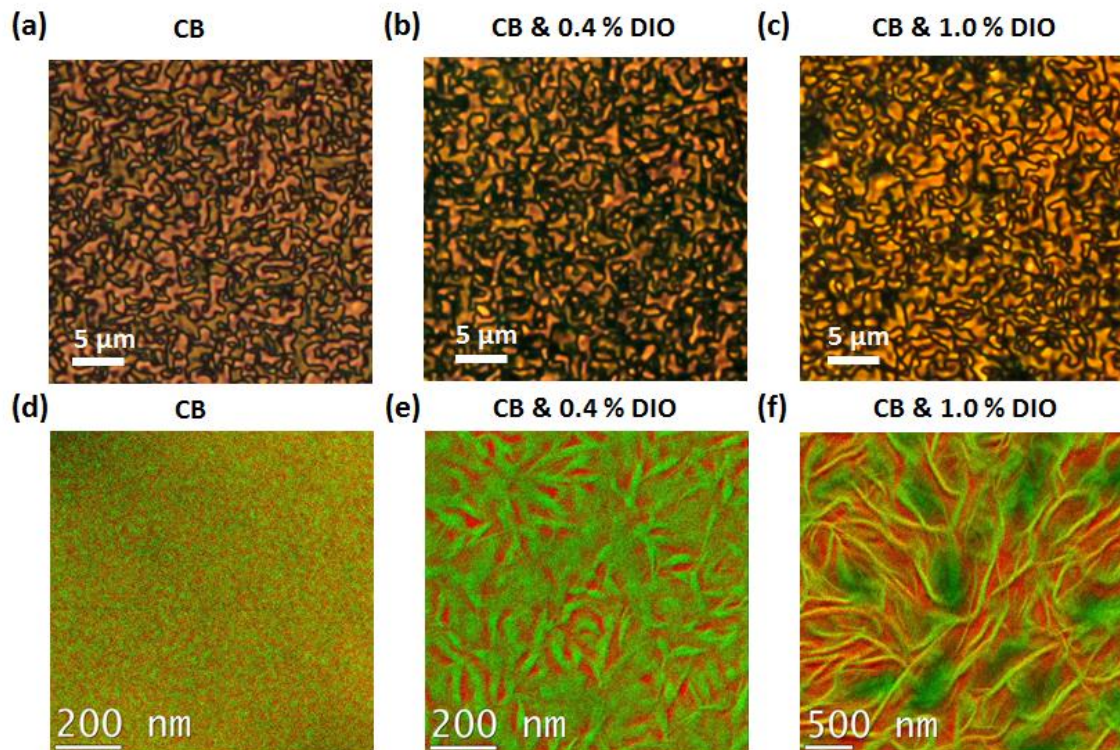


**Figure 6.2** Cross-polarized optical microscopic (X-POM) images of p-DTS(FBTTh<sub>2</sub>)<sub>2</sub>:PC<sub>71</sub>BM films cast from CB in (a), CB & 0.4% DIO in (b) and CB & 1.0% DIO in (c). Composite color images of EF-TEM with elemental mappings of carbon (284 eV) (red) and sulfur (165 eV) (green) performed on the plan-view of p-DTS(FBTTh<sub>2</sub>)<sub>2</sub> : PC<sub>71</sub>BM film coated from CB in (d), CB & 0.4% DIO in (e) and CB & 1% DIO in (f).

We have evaluated the nature and relative area of the D-A interface in the BHJ films by performing sensitive external quantum efficiency (EQE) measurements in the sub-gap region of the D and A semiconductors (**Figure 6.3**).<sup>[157,180,181]</sup> The charge transfer (CT) states in the sub-gap region can be directly excited by incoming photons and contributes to photocurrent generation.<sup>[182-184]</sup> Fitting the CT band in the EQE spectra determines the energy of the CT states and its strength is proportional to the number of such states. Despite the changing appearance of the BHJ, we find the energy of the sub-gap CT states (1.6 eV) is not affected by the presence or amount of additives, while their intensity exhibits important changes (**Figure 6.3a**). This feature suggests that the nature of the D-A interactions at the interfaces resulting in free carrier generation is essentially unchanged. The electronic coupling term ( $f$ ), which is directly proportional to the number of interfacial CT complexes that are able to generate free charges quantifies the intensity of the sub-gap EQE. We find that  $f$  decreases in devices containing DIO when compared to devices prepared without additive, consistent with increasing domain coarsening and phase separation (**Figure 6.3b**). Previous studies have suggested that devices fabricated using neat CB and known to form the liquid crystalline mesophase of the donor suffer from poor charge transport, voltage dependent geminate recombination and strong bimolecular recombination.<sup>[185]</sup> On the other hand, 1% DIO devices, which are known to crystallize the donor, exhibit a reduction in the number of interfacial CT complexes by more than one order of magnitude, correlating with the extensive coarsening of domains observed by EFTEM images. We attribute the dramatic



drop in performance of the 1% DIO devices to the extensive reduction in functional interfacial area. Devices prepared with 0.4% DIO appear to exhibit a suitable balance between phase separation of donor and acceptor domains, crystallization of the donor phase needed for charge extraction and formation of sufficient D-A interfacial area needed for charge generation.

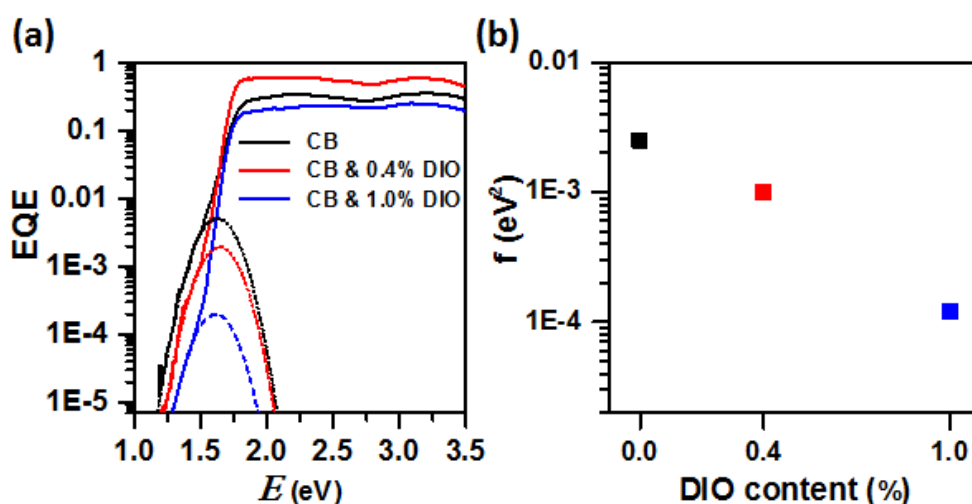


**Figure 6.3** (a) External quantum efficiency of solar cell devices fabricated from p-DTS(FBTTh<sub>2</sub>)<sub>2</sub>:PC<sub>71</sub>BM blends cast from pure CB (black), CB with 0.4% DIO (red), and CB with 1.0% DIO (blue). Fitting of the charge transfer (CT) states intensity is shown in dashed lines for the three cases. (b) The electronic coupling term ( $f$ ) versus DIO content calculated from fitting CT states in (a).

Nguyen and coworkers used time-delayed collection field (TDCF) and photocharge extraction by linearly increasing voltage (photo-CELIV) measurements to investigate the charge carrier transport properties in p-DTS(FBTTh<sub>2</sub>)<sub>2</sub>:PC<sub>71</sub>BM.<sup>[185]</sup> The study revealed the low FF and  $J_{sc}$  in the as cast devices to both strong geminate and bimolecular recombination, whereas using 0.4% DIO helped to overcome geminate recombination and reduce bimolecular recombination resulting in improved FF and  $J_{sc}$ , thereby enhancing PCE.<sup>[185]</sup> The study also revealed an increase in hole mobility by an order of magnitude for 0.4% DIO as compared to the as cast condition, which was also observed in other studies.<sup>[185,186]</sup> Friend and coworkers investigated charge carrier dynamics in p-DTS(FBTTh<sub>2</sub>)<sub>2</sub>:PC<sub>71</sub>BM system using transient absorption (TA) spectroscopy.<sup>[187]</sup> For the optimum condition (0.4% DIO), charge generation occurred at two-time scales; subpicosecond time-scale which was attributed to the dissociation of photogenerated excitons at the heterojunction and subsequent evolution in the picosecond to nanosecond time-scales which was attributed to the dissociation of photogenerated excitons at the bulk that diffuse to the heterojunction before dissociation.<sup>[187]</sup> Global analysis of TA measurements revealed two charge generation pathways; an ultrafast pathway with a rate constant of ~ 82 femtoseconds and a diffusion-limited pathway with a rate constant of ~ 22 picoseconds.<sup>[187]</sup> Interestingly the ultrafast pathway had the major contribution (~70% weight) of charge generation.<sup>[187]</sup> Furthermore, using electroabsorption measurements, electrostatic energy per charge pair and hence electron-hole separation was calculated as a function of time revealing an instant charge separation

within 40 femtoseconds of excitation to ~ 4-5 nm electron-hole separation.<sup>[187]</sup> In the absence of PC<sub>71</sub>BM aggregation (achieved by processing samples with low PC<sub>71</sub>BM content ~ 10% w/w), strong bound excitons with electron-hole separation of ~ 1.5 nm were generated upon photoexcitation, highlighting the importance of PC<sub>71</sub>BM aggregation in charges separation.<sup>[187]</sup> Similar observation was reported by Nguyen and coworkers where instant excitons dissociation was observed.<sup>[188]</sup> In addition, investigation of the charges generation and recombination dynamics with TA measurements revealed efficient charge generation after excitation where a large fraction of free charge carriers (as high as ~ 85%) was generated upon photoexcitation.<sup>[188]</sup> Modeling TA spectra with two-pool model (geminate and bimolecular recombination contributions) revealed similar geminate recombination rate but much higher effective bimolecular recombination (BMR) coefficient for p-DTS(FBTTh<sub>2</sub>)<sub>2</sub>:PC<sub>71</sub>BM as compared to the typical polymer–fullerene blends (one or two order of magnitude higher than P3HT:PC<sub>60</sub>BM or PCDTBT:PC<sub>60</sub>BM, respectively).<sup>[188]</sup> Regardless of the higher BMR for p-DTS(FBTTh<sub>2</sub>)<sub>2</sub>:PC<sub>71</sub>BM, efficient charges extraction can be obtained in this system, which was attributed to the high hole mobility in p-DTS(FBTTh<sub>2</sub>)<sub>2</sub>:PC<sub>71</sub>BM that can facilitate fast carrier extraction, thereby helping to overcome bimolecular recombination.<sup>[188]</sup>

### 6.3 Monitoring microstructure evolution during solution processing

#### 6.3.1 Thickness evolution during film formation

We investigated the thinning of the p-DTS(FBTTh<sub>2</sub>)<sub>2</sub>:PC<sub>71</sub>BM formulation based on neat CB and with the addition of 0.4 v.% and 1 v.% DIO by performing *in situ* spectroscopic reflectometry and ellipsometry during spin coating (**Figure 6.4**) under conditions identical to those used for solar cell fabrication. For the pure CB case, we observe rapid thinning and drying of the solution within 6 s, followed by a steady-state thickness indicating the film is dry (**Figure 6.4a**). In the presence of DIO, we observe identical thinning behavior initially, but this gives way to the formation of a heavily swollen, slow-drying wet film. The thickness of the wet film decreases over a period of an hour, highlighting the slow drying of DIO. After an hour, we still observe that the films processed with DIO remain swollen with the solvent additive. To fully dry the wet films, they were heated at 70 °C for 10 min. The volume fraction of the trapped solvent calculated with respect to the dry film thickness after heating is shown in **Figure 6.4b**. This indicates that 18% and 30% by volume of DIO are trapped in the wet films ( $t = 6$  s) formed, respectively, from 0.4% and 1% DIO formulations. The final thickness of the dry films is identical for all cases (*ca.* 100 +/- 5 nm) revealing that DIO processing has null effect on the thickness of the BHJ.

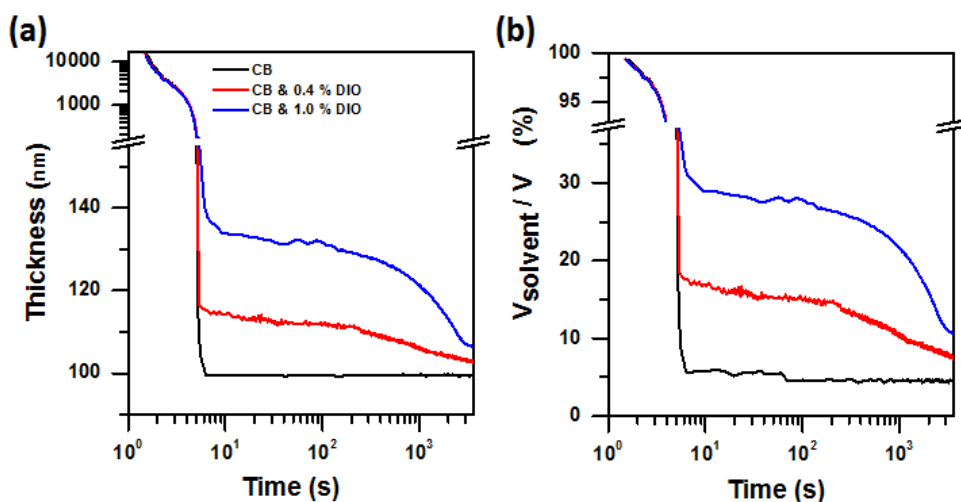


**Figure 6.4** (a) The thickness evolution during and thereafter spin-coating p-DTS(FBTTh<sub>2</sub>)<sub>2</sub>: PC<sub>71</sub>BM from CB solution and with different DIO content (0.4% and 1%). (b) The calculated retained solvent in the “wet” film during and thereafter spin-coating for the three cases in (a).

### 6.3.2 Evolution of the photo-physical aggregation and crystallization of p-DTS(FBTTh<sub>2</sub>)<sub>2</sub>

Time-resolved measurements of film thickness were complemented with UV-visible transmission measurements also performed during spin-coating. These measurements provide a means to monitor the absorption spectra of the solute at different states of thinning and BHJ formation.<sup>[160]</sup> In **Figure 6.5**, we plot a two-dimensional intensity map of the absorption spectra collected during spin-coating of p-DTS(FBTTh<sub>2</sub>)<sub>2</sub>: PC<sub>71</sub>BM from CB solution and with different DIO content. The color scale represents the strength of absorption, whereas time is represented on a logarithmic scale. A broad absorption peak (dark red) centered around 590 nm observed at the initial stage of spin coating in

all three formulations corresponds to the solution absorption peak of p-DTS(FBTTh<sub>2</sub>)<sub>2</sub>. As the solution is spun, the fluid thins out very rapidly, leading to the disappearance of the intense solution absorption peak within 2-3 s of starting the sample rotation. As the processing solvent (CB) thins and dries out by ~6 s, the film solidifies as indicated by the redshift of the absorption edge toward  $\lambda \sim 750$  nm. Absorption spectra of the dry films are shown in **Figure 6.6a**. For films processed with DIO, the solution peak of p-DTS(FBTTh<sub>2</sub>)<sub>2</sub> gives way to the formation of vibronic progressions at  $\lambda_1 = 625$  nm and at  $\lambda_2 = 682$  nm (**Figure 6.5b-c, Figure 6.6a**). The strength of the vibronic progressions is highly sensitive to the formation of local intermolecular and intramolecular aggregates.<sup>[39,189]</sup> The observation of the two vibronic features at  $\lambda_1$  and  $\lambda_2$  is indeed different from what is seen in as-cast films without DIO (**Figure 6.5a, Figure 6.6a**), where the vibronic features do not appear. By contrast, use of 1% DIO results in qualitatively similar vibronic features at  $\lambda_1$  and  $\lambda_2$ , but we find the intensity of these features, and in particular their ratio, to differ (**Figure 6.5c, Figure 6.6a**). Since an increase in the strength of vibronic progressions is indicative of further ordering and increasing conjugation length – also known to cause a red shift in the absorption spectra<sup>[39,160,190,191]</sup> – we interpret the 1% DIO spectra as being indicative of more pronounced aggregation and perhaps long-range crystalline order.

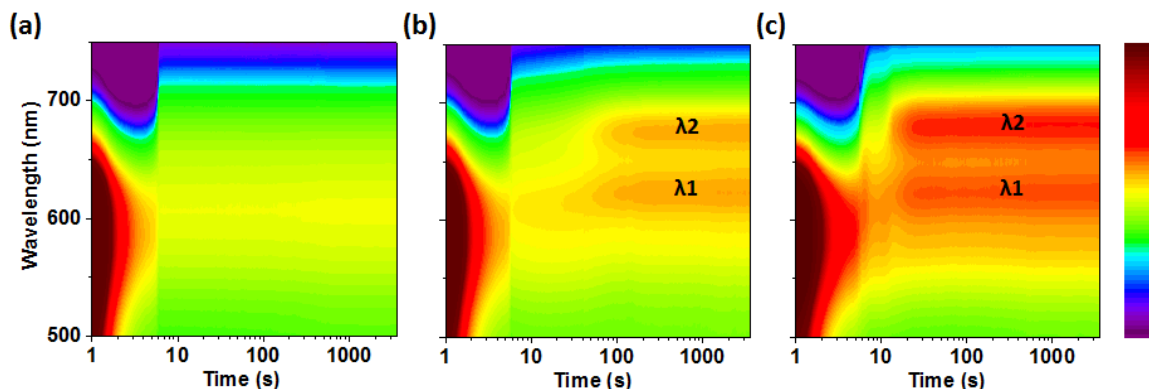


**Figure 6.5** Time-resolved UV-vis absorption color plot (absorption intensity is shown as logarithmic color scale versus wavelength ( $\lambda$ ) and time (s)) of coating p-DTS(FBTTh<sub>2</sub>)<sub>2</sub> : PC<sub>71</sub>BM from CB in (a) , CB with 0.4 % DIO in (b) and CB with 1.0 % DIO in (c).

In **Figure 6.6b**, we plot the time-evolution of the ratio of vibronic absorptions  $A(\lambda_2)/A(\lambda_1)$ , which we refer to as the vibronic ratio. As expected,  $A(\lambda_2)/A(\lambda_1)$  is identical for all formulations and remains unchanged while the cast solution is still in the liquid state ( $t < 6$  s). The DIO-free formulation is rapidly quenched into a solid state mesophase as indicated by the saturation and stabilization of the vibronic progressions for  $t > 6$  s. This mesophase is known to be liquid crystalline and is responsible for the appearance of macroscopic disclinations in the thin films (as shown earlier in **Figure 6.2a**). When DIO is present in the formulation,  $A(\lambda_2)/A(\lambda_1)$  reaches the same level as for neat and quenched formulation, and subsequently undergoes a second increase for  $t > 6$  s as the quenched mesophase of p-DTS(FBTTh<sub>2</sub>)<sub>2</sub> transitions to the crystalline phase. This is supported by the appearance of the crystalline phase of p-DTS(FBTTh<sub>2</sub>)<sub>2</sub>

by *in situ* time-resolved GIWAXS measurements (**Figure 6.7b-c**). The data reveals a strong positive correlation between the formation of vibronic progressions with a large vibronic ratio and the crystallization of the donor phase (**Figure 6.6b, Figure 6.7b-c**). The LC transition to crystal happens relatively slowly in the presence of only 0.4% DIO (**Figure 6.6b, Figure 6.7b**) and much more rapidly for 1% DIO (**Figure 6.6b, Figure 6.7c**), effectively occurring an order of magnitude faster. In all cases the final films show evidence of the LC disclinations (**Figure 6.2a-c**), proving that the as-cast film transitions through the LC mesophase prior to crystallizing (**Figure 6.7b-c**). It is worth noting that the exact timescales of phase transformation can vary by up to several seconds from run to run, but the important take away message is that kinetics of conversion may differ substantially when the amount of DIO is varied. The film is still wet and loaded in DIO when the vibronic progressions plateau (as shown previously in **Figure 6.4**). The observations that donor crystallization occurs in the wet BHJ film indicate that the additive is phase segregated within the wet BHJ. Presumably, the DIO in the wet film is segregated in the acceptor domains, where DIO is known to dissolve PC<sub>71</sub>BM.



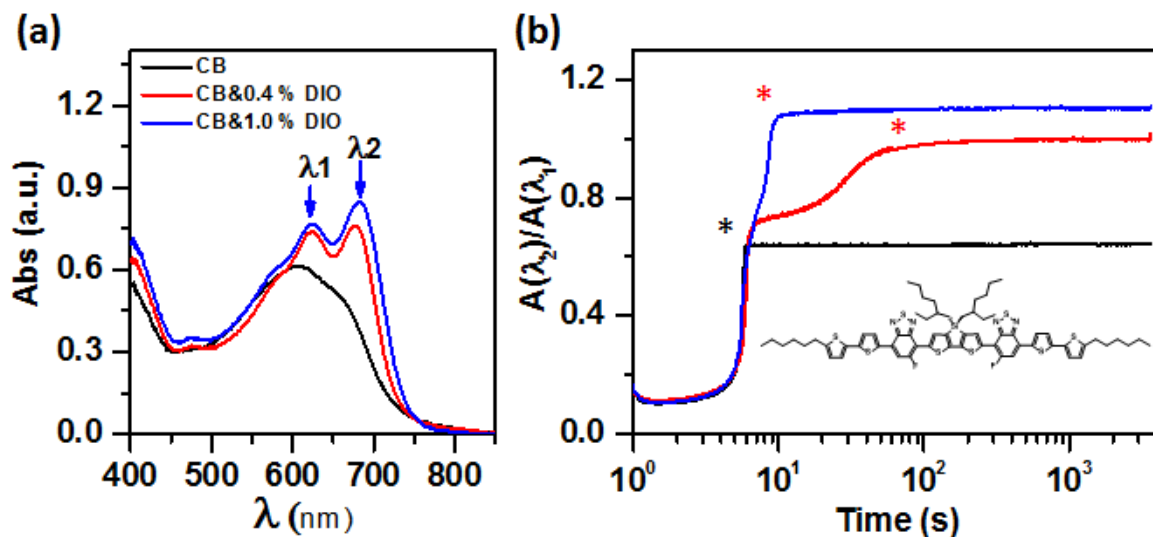


**Figure 6.6** (a) UV-vis absorption spectra of as cast dry films of p-DTS(FBTTh<sub>2</sub>)<sub>2</sub>:PC<sub>71</sub>BM coated from CB (black), CB with 0.4 % DIO (red) and CB with 1.0 % DIO (blue). (b) The vibronic ratio with respect to time for the donor represented as the ratio of absorption at  $\lambda_2 = 682$  nm and  $\lambda_1 = 625$  nm for the three formulations. The point at which CB is removed is indicated by a black asterisk and the saturation of photo-physical aggregation in the presence of DIO is marked with red asterisks.

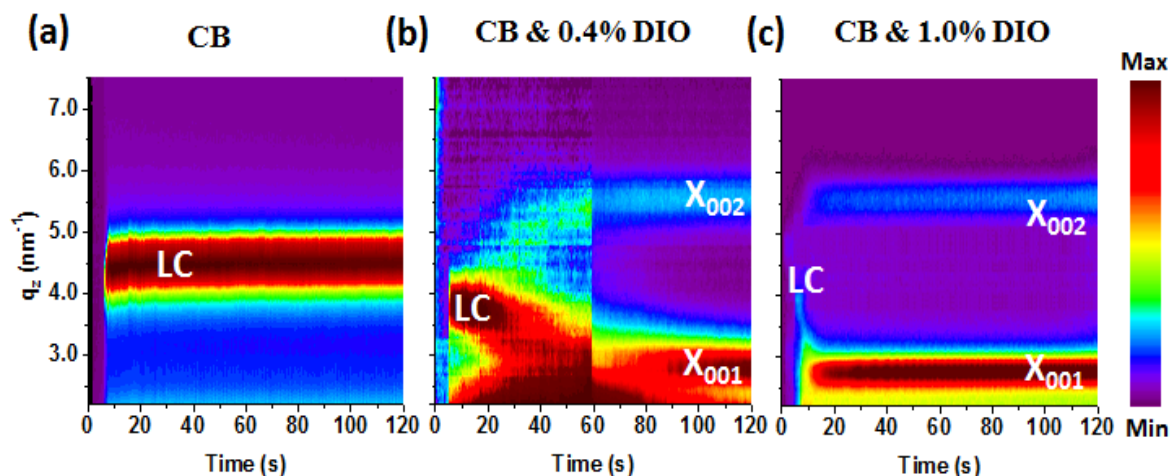


**Figure 6.7** (a) *In situ* GIWAXS color image plot (Integrated scattering intensity is shown in logarithmic color scale versus  $q$  ( $\text{nm}^{-1}$ ) and time(s)) of casting p-DTS(FBTTh<sub>2</sub>)<sub>2</sub> : PC<sub>71</sub>BM from CB in (a) , CB with 0.4 % DIO in (b) and CB with 1.0 % DIO in (c).

### 6.3.3 Evolution of PC<sub>71</sub>BM aggregation

Aggregation of PC<sub>71</sub>BM should therefore only occur upon removal of DIO. It is normally challenging to probe the state of the fullerene phase through *in situ* GIWAXS, or even by *in situ* UV-Vis absorption, measurements performed on BHJ blends. The spectra of p-DTS(FBTTh<sub>2</sub>)<sub>2</sub> and PC<sub>71</sub>BM overlap too strongly to monitor the optical absorption changes associated with the aggregation of the latter. Instead, we blended PC<sub>71</sub>BM with a transparent polymer binder poly(methyl methacrylate) (PMMA) and processed the blend in identical conditions to those used to solution-process the BHJ layers, allowing us to monitor *in situ* the aggregation behavior of PC<sub>71</sub>BM in the absence and presence of DIO. Comparison between the solution and solid state absorption spectra of PC<sub>71</sub>BM

normalized to the absorption peak at 465 nm are shown in **Figure 6.8a**. These spectra are obtained by subtracting the absorption of PMMA from the blend. The resulting absorption spectra exhibit a detectable red shift between the solution and the solid state. We monitor the time-evolution of the ratio of the absorption peaks at  $\lambda_1 = 465$  nm and  $\lambda_2 = 550$  nm and plot in **Figure 6.8b** the evolution of PC<sub>71</sub>BM aggregation for neat solutions and in the presence of DIO (0.4% and 1%). As expected, the neat solution dries within 6 s, resulting in the rapid increase and saturation of aggregation. In the presence of DIO, part or all of the PC<sub>71</sub>BM remains solvated for an extended duration with a gradual increase in aggregation closely tracking the slow evaporation of DIO. The comparison between 0.4% and 1% DIO cases reveals that the amount of DIO used in optimal BHJ formulations is insufficient to solubilize all of the PC<sub>71</sub>BM, whereas use of 1% DIO appears to solubilize almost all of the PC<sub>71</sub>BM present in the BHJ. The clear observation that PC<sub>71</sub>BM is partially solubilized by the remaining DIO in the wet film in optimal conditions demonstrates that the additive drives a two-step BHJ formation whereby the aggregations of the donor and acceptor are decoupled in time thanks to the additive, starting with LC to crystal transition of the donor, with the DIO demixing from the donor and migrating into the acceptor domains, where it remains until complete evaporation of DIO is achieved. The fact that only part of PC<sub>71</sub>BM is solubilized when 0.4% DIO is used indicates that some of the PC<sub>71</sub>BM is aggregated early or allowed to mix with the donor. After all, the selective solubility of PC<sub>71</sub>BM within the BHJ can lead to excessive undesirable phase separation.

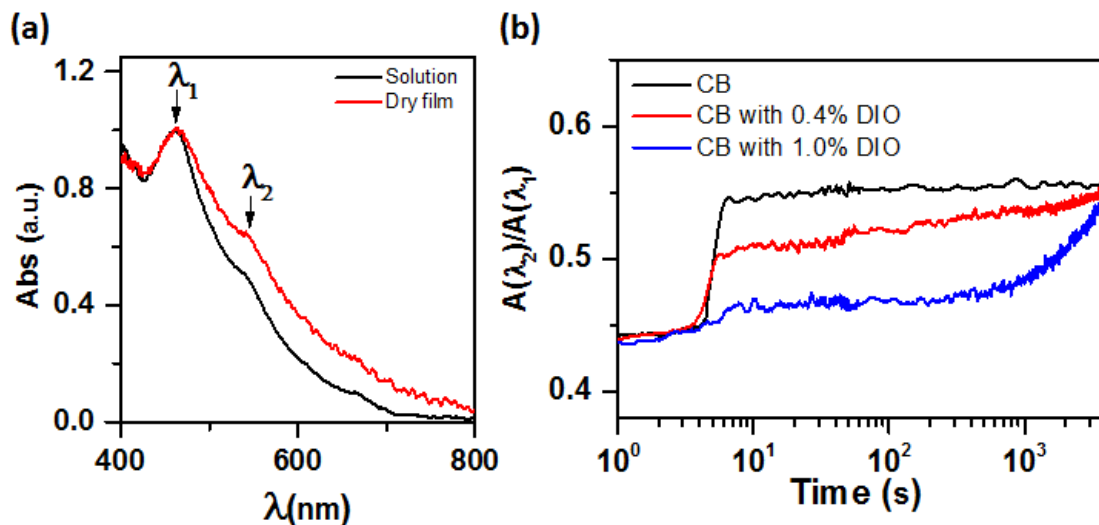


**Figure 6.8** UV-Vis absorption spectra of PC<sub>71</sub>BM: PMMA (40: 60) in solution and solid state (normalized to PC<sub>71</sub>BM absorption peak ( $\lambda_1 = 465$  nm)). (b) Time-evolution of PC<sub>71</sub>BM aggregation as represented by the ratio of absorption peak intensities at  $\lambda_2 = 550$  nm and  $\lambda_1$  during spin-coating of a PC<sub>71</sub>BM: PMMA blend. In all experiments reported here, spin-coated lasted 60 seconds, while in situ measurements were performed for at least one hour.

#### 6.4 Relative solubility of BHJ components/phases in DIO

The dramatic differences in the timelines of aggregation of p-DTS(FBTTh<sub>2</sub>)<sub>2</sub> and PC<sub>71</sub>BM in the presence of DIO highlight the impact of solubility differences between the donor and the acceptor on the pathway to BHJ formation. Differences in the solubility of the donor and acceptor in the solvent additive have been known to be important for BHJ formation in polymer:fullerene solar cells.<sup>[99,143,192]</sup> However, we have not encountered

a situation where the phase of the donor impacts its solubility and determines the outcome of solution processing. To confirm this observation more directly, we designed a new set of experiments, which we illustrate in **Figure 6.9a**. Pre-coated films of p-DTS(FBTTh<sub>2</sub>)<sub>2</sub>:PC<sub>71</sub>BM and neat p-DTS(FBTTh<sub>2</sub>)<sub>2</sub> exhibiting the liquid crystalline donor phase (no DIO) and crystalline donor phase (0.4% DIO), are soaked in DIO while monitoring the absorption of the sample *in situ*. Practically, this experiment is carried out by casting a drop of DIO while spinning the pre-coated substrate and simultaneously performing *in situ* UV-Vis absorption measurements. Soaking the neat LC donor films in DIO (**Figure 6.9b**) leads to formation of the crystalline phase with a characteristic sharpening and increase of the vibronic features. Conversion of the p-DTS(FBTTh<sub>2</sub>)<sub>2</sub> LC phase into a crystalline phase after treatment is confirmed by GIWAXS measurements on the treated film (inset of **Figure 6.9b**). As expected, the absorption characteristics of the pre-crystallized neat donor film (**Figure 6.9c**) are unaffected by DIO soaking, indicating it is far less soluble in the additive. Dropping DIO on neat PC<sub>71</sub>BM sample results in complete dissolution of the sample leaving only bare substrate, not shown here, further confirming the greater solubility of PC<sub>71</sub>BM in DIO as compared to p-DTS(FBTTh<sub>2</sub>)<sub>2</sub>.

Similar experiments were performed on p-DTS(FBTTh<sub>2</sub>)<sub>2</sub>:PC<sub>71</sub>BM blends based on the LC and crystalline phases of the donor. Here, we see that DIO selectively dissolves PC<sub>71</sub>BM from the blends with crystalline donor, as indicated by the sharp loss of absorption associated with PC<sub>71</sub>BM, while crystalline p-DTS(FBTTh<sub>2</sub>)<sub>2</sub> remains intact (**Figure 6.9e**).

For blends with LC donor, both the donor and acceptor are dissolved by DIO, resulting in a significant loss of material during spin coating of DIO (**Figure 6.9d**). The remaining p-DTS(FBTTh<sub>2</sub>)<sub>2</sub> crystallizes, but its loss indicates that a significant fraction of p-DTS(FBTTh<sub>2</sub>)<sub>2</sub> in the quenched LC blend is intimately mixed with the highly soluble PC<sub>71</sub>BM. The striking difference in the level of loss of the LC p-DTS(FBTTh<sub>2</sub>)<sub>2</sub> in the neat and blend films suggests that it is intimately mixed with PC<sub>71</sub>BM in the blend prepared without additive. The comparison between the level of loss of p-DTS(FBTTh<sub>2</sub>)<sub>2</sub> in the neat LC (none) and blend LC (nearly half) films suggests that DIO aids to rapidly crystallize the LC phase without substantially or fully dissolving p-DTS(FBTTh<sub>2</sub>)<sub>2</sub> in the LC phase.

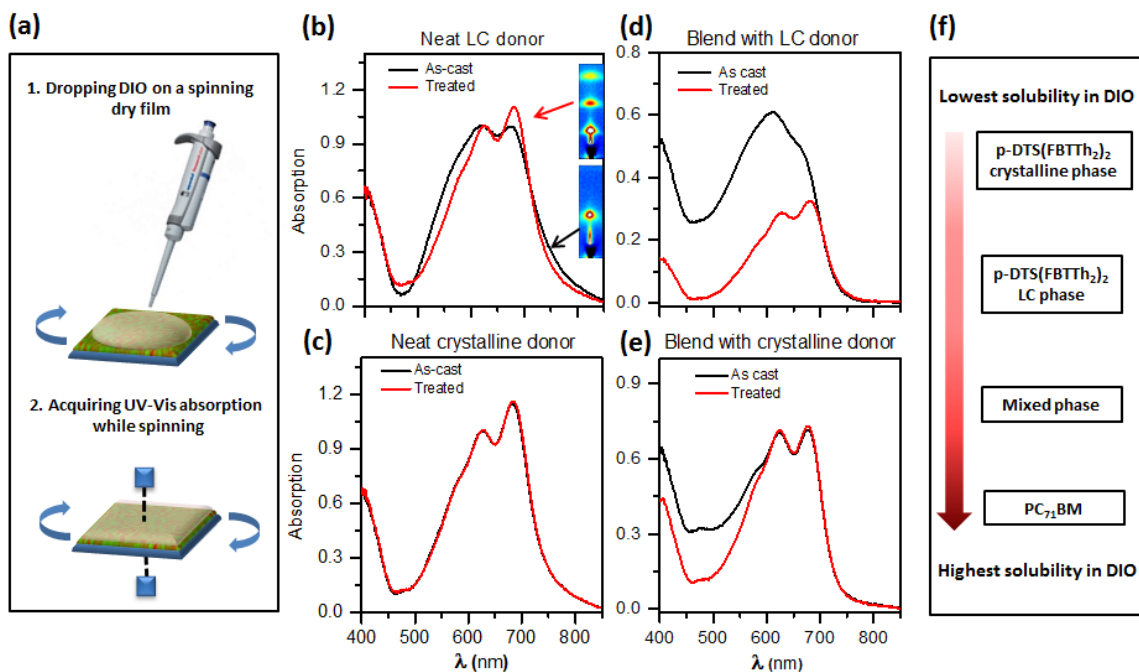


**Figure 6.9** (a) Schematic figure represents drop-spin experiment in which DIO is dropped on a dry film followed by spinning the sample, while acquiring UV-vis absorption measurements. Spin coating was done at two steps; initially at low speed (600 rpms) for 20 s in order to achieve uniform distribution of DIO followed by spinning at 1750 rpms for 5 min. UV-vis absorption of as cast and DIO treated films of neat p-DTS(FBTTh<sub>2</sub>)<sub>2</sub> prepared from CB in (b) and CB with 0.4 % DIO in (c). In the inset of figure (b), GIWAXS of as cast film from CB and after treatment indicates the transformation of the liquid crystal phase to crystal phase upon treatment with DIO. UV-vis absorption of as cast and DIO treated films of p-DTS(FBTTh<sub>2</sub>)<sub>2</sub>:PC<sub>71</sub>BM prepared from CB in (d) and CB with 0.4 % DIO in (e). (f) Schematic summarizing the solubility of different components of the BHJ in DIO relatively.

The time-evolution of the absorption intensities during these experiments are shown in **Figure 6.10**, where we plot the  $A(\lambda_2)/A(\lambda_1)$  vibronic ratio as an indicator of the evolution of photophysical aggregation and ordering of p-DTS(FBTTh<sub>2</sub>)<sub>2</sub> (**Figure 6.10 a-b**). An increase of  $A(\lambda_2)/A(\lambda_1)$  indicates a red shift of the absorption spectra and increasing aggregation and ordering. A decrease points to a blue shift and to a reduction in ordering due to solvation of p-DTS(FBTTh<sub>2</sub>)<sub>2</sub> by DIO. The initial values of as-cast films are shown as markers [black and red triangles for CB and CB with 0.4% DIO, respectively] at  $t = 0$  and dashed lines are drawn for comparison. In case of the LC donor film, we observe a reduction of normalized absorption  $A(\lambda_2)/A(\lambda_1)$  from 0.98 to 0.74 immediately upon dropping DIO, followed by a recovery of this ratio and an irreversible increase to 1.1. The initial reduction of normalized absorption points to partial solvation of the liquid crystal phase by DIO. Subsequent increase indicates an increase in the degree of molecular ordering and is consistent with the formation of the crystalline phase of p-DTS(FBTTh<sub>2</sub>)<sub>2</sub>, as confirmed by GIWAXS. On the other hand, the crystalline donor film undergoes much smaller variations when DIO is cast, indicating far weaker interactions between the DIO and the crystalline phase of the donor.

In **Figure 6.9f**, we summarize the relative solubility in DIO of different components and phases, showing the highest solubility for PC<sub>71</sub>BM followed by the mixed phase then p-DTS(FBTTh<sub>2</sub>)<sub>2</sub> LC phase and finally p-DTS(FBTTh<sub>2</sub>)<sub>2</sub> crystal phase. That p-DTS(FBTTh<sub>2</sub>)<sub>2</sub> can be soluble in DIO up to  $(24 \pm 3)$  mg/mL<sup>[193]</sup> should not be interpreted as a



contradiction of our findings. Instead, this solubility measurement was performed by dispersing p-DTS(FBTTh<sub>2</sub>)<sub>2</sub> in a large amount of DIO. The interaction of DIO with p-DTS(FBTTh<sub>2</sub>)<sub>2</sub> as isolated molecules appears to be far from its interaction with a p-DTS(FBTTh<sub>2</sub>)<sub>2</sub> thin film where the donor is aggregated in the LC or crystalline phases. These experiments indicate that direct measurements via *in situ* diagnostics can reveal unexpected behavior that appear to go against conventional wisdom but are crucial to explaining the formation of the BHJ.

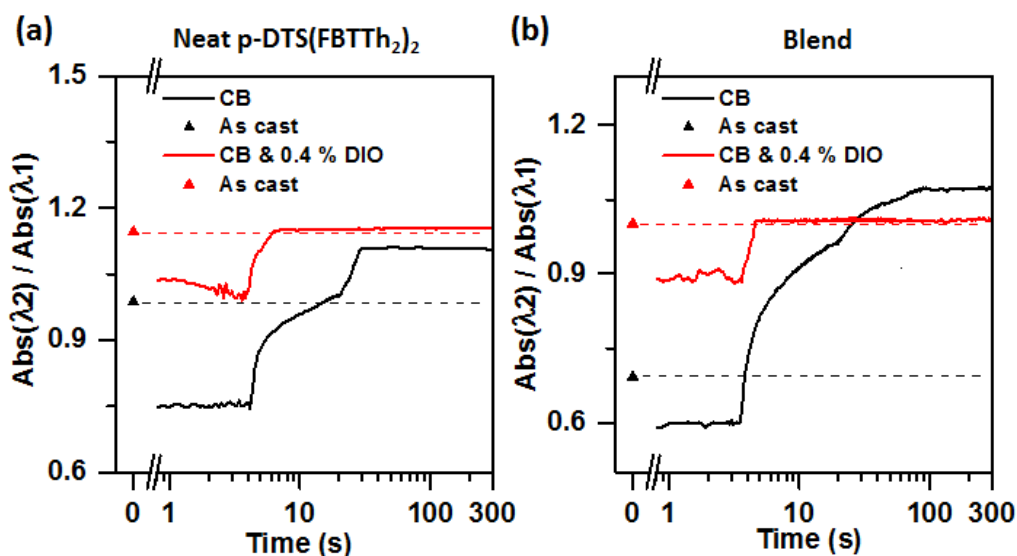


**Figure 6.10** Time evolution of the relative absorption intensity at the two vibronic peaks, V2 (at 682 nm) and V1 (at 625 nm), of the drop-spin experiment on neat p-DTS(FBTTh<sub>2</sub>)<sub>2</sub> films in (a) and p-DTS(FBTTh<sub>2</sub>)<sub>2</sub> : PC<sub>71</sub>BM films in (b). Initial values of the as cast films are shown as black triangle (CB) and red triangle (CB & 0.4% DIO) at t=0 and dashed line for comparison.

### 6.5 Mechanism of the solvent additive effect on microstructure evolution

To sum up the previous discussions, several important qualitative observations can be made: (i) LC transition to crystal is initiated immediately after removal of CB and when the film is in the wet state in the presence of DIO. (ii) The transition requires the presence of DIO in order to occur during the film formation process. (iii) The rate of the transition depends on DIO content. (iv) The amount of donor aggregation depends on additive content. (v) The transition is completed within minutes if not seconds (when more additive is present), long before the DIO leaves the film, which can take an hour or more in ambient conditions. (vi) The additive is segregated in the wet film, having been expelled by the crystalline donor into the fullerene domains. (vii) The donor is effectively insoluble in DIO after it crystallizes. (viii) The segregation process facilitates the demixing of the donor and acceptor phases. (ix) The fullerene acceptor is aggregated with removal of the additive through evaporation.

Insights gained from *in situ* diagnostics and *ex situ* micrographs can be combined together to generate a mechanistic rationale for p-DTS(FBTTh<sub>2</sub>)<sub>2</sub>:PC<sub>71</sub>BM BHJ formation, as schematically summarized in **Figure 6.11**, with the top row showing the molecular scale behavior and the two bottom rows showing the nanometer to micrometer scale. At the macroscopic scale, we have established that all formulations lead to the formation of LC disclinations of p-DTS(FBTTh<sub>2</sub>)<sub>2</sub> which persist in the solid state after crystallization and phase separation, even in the presence of additive. These disclinations have been represented as a large scale network of domains. At the

nanoscale, the as-formed LC phase of p-DTS(FBTTh<sub>2</sub>)<sub>2</sub> incorporates fullerene and DIO molecules, which are relatively well mixed (see the top left schematic of **Figure 6.11**). The LC phase of the donor is represented by yellow molecules, whereas its crystalline phase is represented as orange. This picture summarizes the state of the BHJ at the moment of CB removal and transition of the donor through its LC mesophase. In the absence of DIO, the quenched metastable film transitions very slowly to the crystalline phase, as shown in the previous chapter. The orientation of the donor crystallites formed within the LC phase is most likely templated in part by the overall starting molecular orientation within the LC disclinations and by the fact that the LC phase of the donor is not fully solubilized in the presence of DIO.

When DIO is present in the formulation, a significant amount of DIO remains in the as-cast film, initially solubilizing parts of the LC phase of the donor and the PC<sub>71</sub>BM. The presence of DIO promotes the crystallization of the LC phase. The crystalline phase is far less soluble than the LC phase, which is also far less soluble than the acceptor. Hence, significant solubility and mobility gradients are present within the wet BHJ film laden with DIO. The solubility gradient provides a driving force for the DIO and PC<sub>71</sub>BM to demix from the donor, whereas the mobility gradient gives significant kinetic facility for the DIO and PC<sub>71</sub>BM to diffuse and for the donor crystallization front to propagate. This therefore leads to the *de facto* segregation of DIO within the BHJ film toward PC<sub>71</sub>BM-rich regions, aided by the crystallization of the donor. It is understandable then that the amount of DIO present in the wet film will determine the solubility gradient as well as

the mobility gradient, effectively dictating how quickly the LC phase crystallizes and how large the crystalline domains can grow. The demixing is expected to self-terminate on the time-scale of the solution process as soon as the DIO has been segregated into pockets and all the mobile species in regions rich in DIO have migrated to their respective phases. Notably, since p-DTS(FBTTh<sub>2</sub>)<sub>2</sub> as isolated molecules has reasonable solubility in DIO, it is expected to have portion of p-DTS(FBTTh<sub>2</sub>)<sub>2</sub> solubilized at the interface between p-DTS(FBTTh<sub>2</sub>)<sub>2</sub> crystals and DIO-PC<sub>71</sub>BM domains. Nevertheless, the overall microstructure is defined and templated after demixing. The amount of DIO present in the wet film determines what fraction of the PC<sub>71</sub>BM present in the BHJ can be solubilized and rendered kinetically mobile and thus capable of demixing from the donor. Our experiments suggest that the optimal DIO fraction does not allow all of the PC<sub>71</sub>BM to be solubilized in the as-cast wet film, limiting the extent of demixing and donor crystallization. By contrast, 1% DIO may solubilize all of the PC<sub>71</sub>BM, rendering it mobile and allowing the donor crystallization to proceed unhindered. As the additive leaves the film, more and more of the PC<sub>71</sub>BM molecules become aggregated until the BHJ solidifies fully. The speed with which the donor crystallizes can vary by more than an order of magnitude and may be simply too fast in the presence of 1% DIO to assure sufficient domain purity. Indeed, a previous study has shown that films cast from the optimal formulation (0.4% DIO) exhibit the highest phase purity, whereas higher DIO content led to a deterioration of phase purity, with implications on recombination.<sup>[194]</sup> It therefore appears that the presence of DIO and the dosing of its quantity have very

significant and intricate effects on the kinetics and extents of crystallization and phase separation of the BHJ layer.

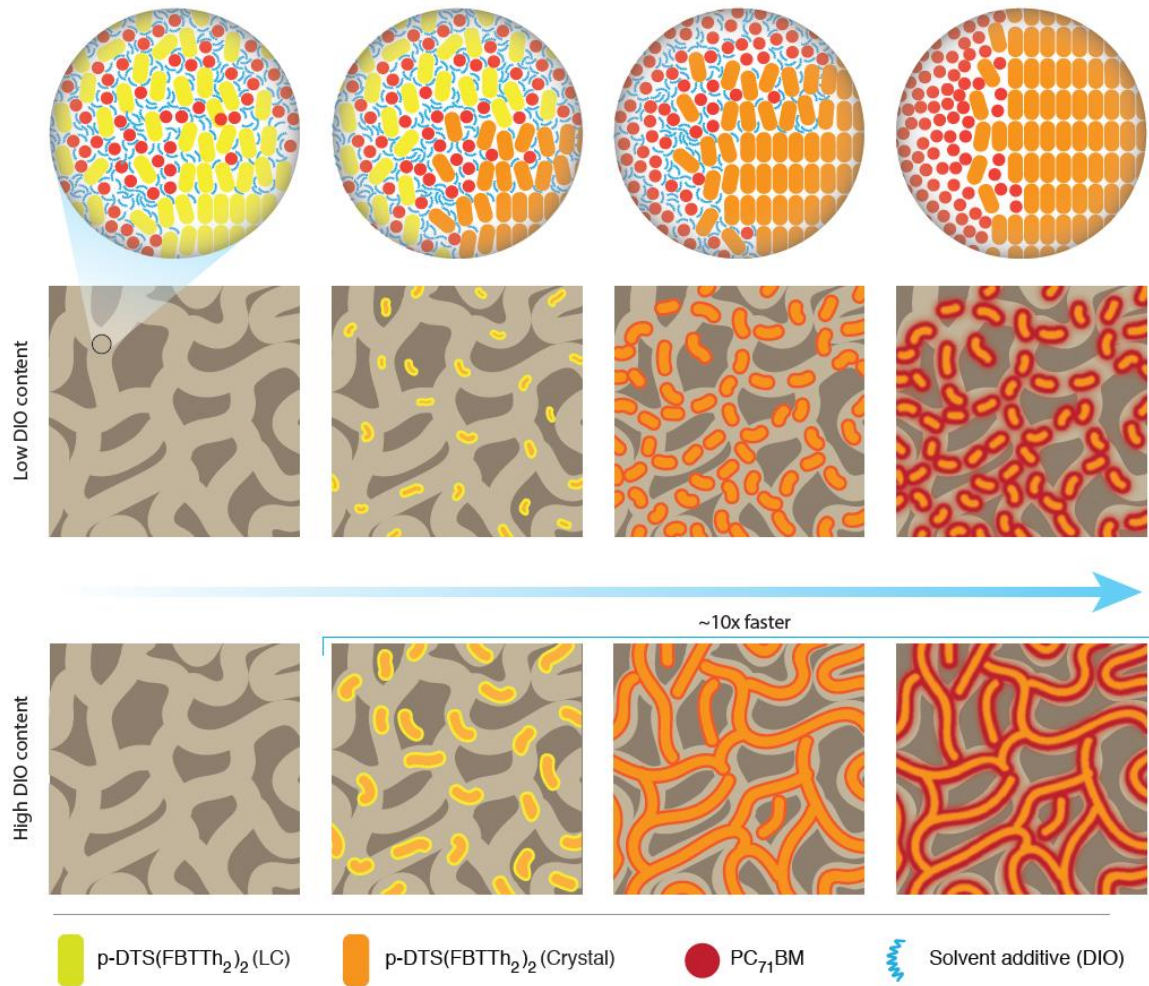


**Figure 6.11** Schematic representation of thin film microstructure just after evaporation of the process solvent (CB) in two scenarios of DIO content (0.4% and 1%). The top row shows a molecular-level view of the LC to crystal transformation accompanied by segregation of PCBM and p-DTD(FBTTh<sub>2</sub>)<sub>2</sub> phases in the presence of DIO. The middle and bottom rows show a more microscale picture of crystallization of the as-cast LC phase

(LC disclinations shown for illustration purposes) of p-DTD(FBTTh<sub>2</sub>)<sub>2</sub> and its phase separation from PC<sub>71</sub>BM for low (0.4%) and high (1%) DIO content scenarios. The aggregation and phase separation processes are both faster and more complete in the presence of large amounts of DIO, and tend to promote formation of microscale fibrils of p-DTD(FBTTh<sub>2</sub>)<sub>2</sub>.

## 6.6 Conclusions

In summary, this study reveals the importance of in situ characterization tools that provide a valuable approach towards understanding mechanisms of film formation. Our findings highlight that the interaction of the DIO additive with the BHJ components depends on the phase in which they present. Through deliberate investigation of these interactions, we attained in-depth understanding of the mechanism of microstructure formation in p-DTS(FBTTh<sub>2</sub>)<sub>2</sub>: PC<sub>71</sub>BM BHJ system. In the case of casting from CB, a highly quenched film with low phase separation is formed. p-DTS(FBTTh<sub>2</sub>)<sub>2</sub>, regardless of being well-mixed with PC<sub>71</sub>BM, exhibits micron-scaled liquid crystalline ordering. However, addition of DIO into casting solution leads to a wet, heavily swollen film wherein diffusion of the molecules is allowed, and this motion facilitates consequent structural and morphological changes. At first, DIO interacts with the p-DTS(FBTTh<sub>2</sub>)<sub>2</sub> liquid crystalline phase and allows its conversion into a crystalline phase. The crystalline phase is much less interactive with DIO ensuring its stability. Secondly, differential solubility of p-DTS(FBTTh<sub>2</sub>)<sub>2</sub> and PC<sub>71</sub>BM in DIO drives their phase segregation. DIO

content is a critical parameter that needs to be tuned carefully in order to achieve optimized performance. It influences the degree of solvation of PC<sub>71</sub>BM and consequently diffusion in the wet film. More additives seem to increase growth rate at the expense of nucleation density leading to coarsening and excessive phase segregation. We expect these findings to be insightful for other efficient small-molecule systems and should serve in better understanding of the mechanism of additive processing in organic solar cells in general.

## Chapter 7

### Polymer-fullerene bulk heterojunction solar cells: Role of solvent additives in fullerene aggregation

#### 7.1 Introduction

Generally speaking, solvent additives can either promote phase separation or control/inhibit it to avoid excessive coarsening, which is detrimental to photovoltaic operation.<sup>[99]</sup> In the previous chapter, we have investigated the role of solvent additives on the formation mechanism of a small-molecule donor and fullerene acceptor BHJ system in which the additive facilitates the donor crystallization and promotes donor-acceptor phase separation. Herein, we investigate a polymer donor and fullerene acceptor BHJ system in which the solvent additives appear to prevent excessive phase separation and domain coarsening. Specifically, the effects of solvent additives are investigated in the BHJ system composed of poly(di(2-ethylhexyloxy)benzo[1,2-*b*:4,5-*b'*]dithiophene-co-octylthieno[3,4-*c*]pyrrole-4,6-dione) (PBDTTPD) donor polymer blended with PC<sub>71</sub>BM.<sup>[115,195]</sup> In this system, the additive 1-chloronaphthalene (CN) was found to be successful in improving the device performance of this BHJ system compared to the additive-free case, whereas other additives such as 1,8-octanedithiol (OT) and 1,8-diiodooctane (DIO) comparatively failed to improve the PCE, providing us with an interesting model system to interrogate the different effects of these additives on BHJ formation. The materials used in the study are summarized in **Figure 7.1**.



Our investigation starts with a comparison of the solar cell performance when using CN and OT additives with the chlorobenzene solution. We will compare the charge carrier mobility in these devices as well as the morphology of the active layer of PBDTTPD:PC<sub>71</sub>BM. These *ex situ* investigations are followed by *in situ* monitoring studies of the solution process, emphasizing solution thinning behavior, as well as aggregation and crystallization of the donor and the acceptor, with the aim of revealing the mechanism by which the solvent additives affect BHJ formation, morphology and ultimately its photovoltaic operation.

We show that PBDTTPD, with sufficiently high Mw, pre-crystallizes early in the CB solution facilitating subsequent PBDTTPD growth during evaporation of the CB solvent. The presence of PBDTTPD pre-aggregates appears to hinder large-scale segregation of PC<sub>71</sub>BM, but to a limited extent. CN further improves the relative crystallinity of PBDTTPD and reduces the aggregation of PC<sub>71</sub>BM. *In situ* investigations show that CN slows down the crystallization of the polymer and promotes the formation of face-on crystallites. Simultaneously, CN inhibits PC<sub>71</sub>BM aggregation until the polymer crystallites constitute fibrillar networks which prevent large-scale phase segregation of PC<sub>71</sub>BM. On the other hand, OT is found to hinder the polymer crystallization when it is present in the film leading to larger scale segregation of PC<sub>71</sub>BM into micron-sized domains before the formation of polymer fibrils.

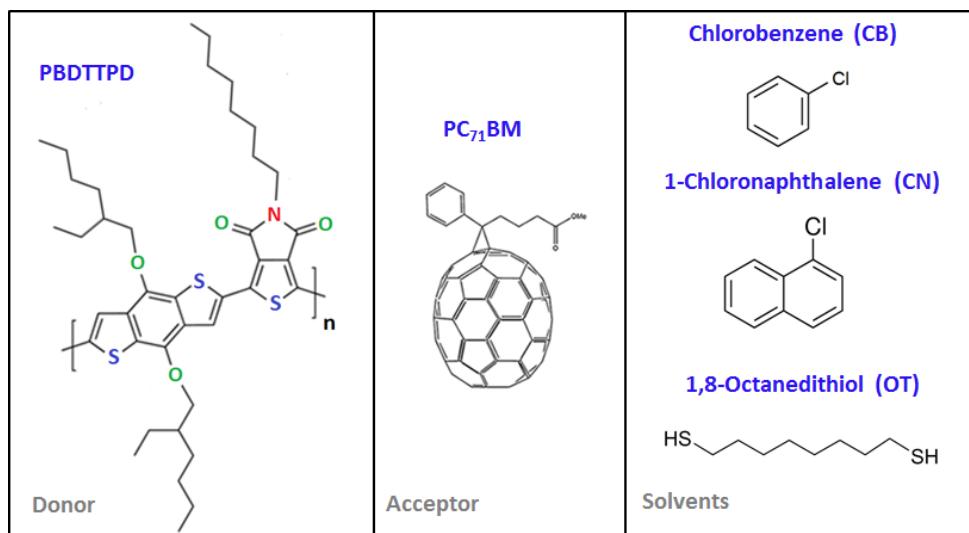


**Figure 7.1** Molecular structure of the materials in the study.

## 7.2 Effects of solvent additives on solar cell devices performance

We begin by investigating the influence of the solvent additives on the solar cell device performance of the PBDTTPD:PC<sub>71</sub>BM system. We have fabricated the solar cell devices using the following conditions for the active layer; 2% wt/v solutions of PBDTTPD:PC<sub>71</sub>BM (40:60 w%) from CB, 5 v/v% CN/CB and 5 v/v% OT/CB were cast at 1200 rpm for 45 s. The current density versus voltage (J-V) characteristics and the extracted device figures of merit are shown in **Figure 7.2** and **Table 7.1**, respectively. For devices fabricated from pure CB, a fairly good efficiency of 6.4 % was obtained, whereas addition of 5 v/v% CN into the casting solution enhanced the efficiency to 7.1 %. The increase in efficiency was mainly due to improved  $J_{sc}$ , while FF and  $V_{oc}$  remained unchanged. By contrast, the addition of 5% v/v OT into the casting solution deteriorates the device performance below the levels produced by the additive-free solution,

reaching an efficiency of 5.4%. Both the  $J_{sc}$  and the FF were found to be lower for the OT-processed devices.

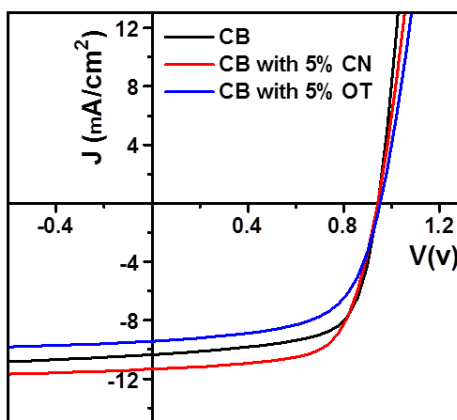


**Figure 7.2** Current density- Voltage (J-V) curves of solar cell devices fabricated from PBDTTPD: PC<sub>71</sub>BM blends processed from pure CB (black), CB with 5% CN (red), and CB with 5% OT (blue).

**Table 7.1** Device performance parameters of the solar cells fabricated from PBDTTPD: PC<sub>71</sub>BM blends processed from pure CB and CB with solvent additives

	Jsc	Voc	FF	PCE
	[mA/cm <sup>2</sup> ]	[mV]	[%]	[%]
CB	10.3	942	66	6.4
CB with 5% CN	11.3	944	66	7.1
CB with 5% OT	9.4	952	61	5.4

### 7.3 Effects of solvent additives on the BHJ morphology

We have investigated the effect of the additives on the BHJ morphology by performing TEM and EF-TEM analysis on the three aforementioned PBDTTPD: PC<sub>71</sub>BM films. In all cases, we observe fibrils of the polymer throughout the film revealing evidence of significant aggregation and order of the polymer as indicated from TEM. The sample prepared with 5% CN has enhanced fibrillar structure as compared to the other two samples. In the OT sample we observe dark regions in TEM that appear throughout the film (see the inset in **Figure 7.3f**), indicating reduced fibril content locally. To gain closer insight into the phase separation, we have performed EF-TEM on the samples as shown in **Figure 7.3d-f**. Sulfur and carbon rich domains are shown in green and red which represent the polymer and PC<sub>71</sub>BM, respectively. EF-TEM images reveal major differences in the blend morphology. In the additive-free sample, we observe the formation of large PC<sub>71</sub>BM domains with sizes on the order of ~40-100 nm. By contrast, the presence of CN leads to more a finely mixed BHJ with smaller acceptor domains, indicating that CN helps prevent the excessive coarsening of PC<sub>71</sub>BM domains. EF-TEM reveals that the dark regions observed by TEM in the OT sample are in fact large PC<sub>71</sub>BM-rich domains, as shown in **Figure 7.3f** (EF-TEM was performed on the marked area with red square in the inset of **Figure 7.3f**). The approximate size of these domains is on the order of microns. Notably, these micron-sized PC<sub>71</sub>BM domains appear throughout the film (as shown in the inset of **Figure 7.3f**). Put aside these large PC<sub>71</sub>BM domains, the rest of the film appears to have finely mixed domains. The formation of

micron-sized PC<sub>71</sub>BM domains in the presence of OT presents the intriguing possibility that the acceptor was depleted from the finely mixed BHJ elsewhere. This behavior may explain the reduction in FF and Jsc.

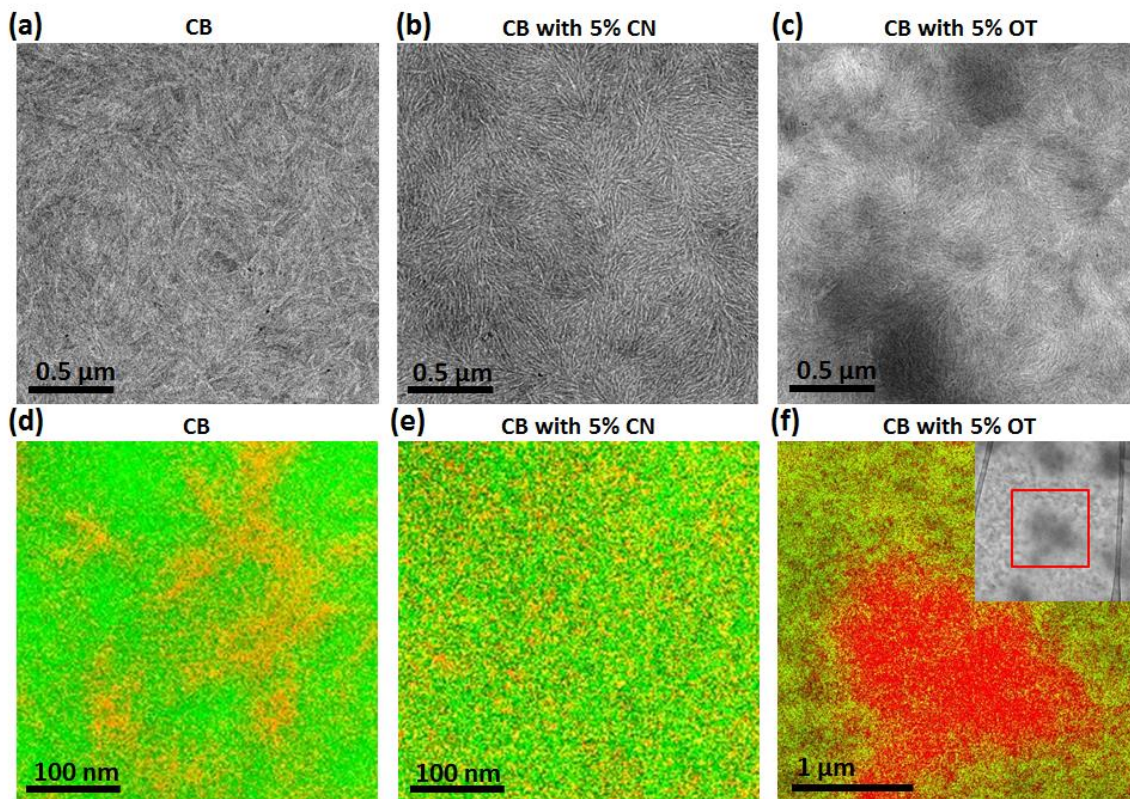


**Figure 7.3** TEM images of PBDTTPD : PC<sub>71</sub>BM films coated from: (a) CB, (b) CB with 5% CN, and (c) CB with 5% OT. Composite color images of EF-TEM with elemental mappings of carbon (284 eV) (red) and sulfur (165 eV) (green) performed on the plan-view of PBDTTPD : PC<sub>71</sub>BM films coated from; (d) CB, (e) CB with 5% CN, and (f) CB with 5% OT. EF-TEM in (f) was performed on the marked area with red square in the inset of the figure (f).

To reveal the impact of the additives on the crystalline order and texture within the BHJ, we have investigated the three samples above *ex situ* by two-dimensional (2D) grazing incidence wide angle X-ray scattering (GIWAXS; **Figure 7.4**). The 2D GIWAXS plots of the three films are shown in **Figure 7.4a-c**, while line-cuts of the integrated scattering intensity are shown in **Figure 7.4d**. In all cases, we observe reflections from the lamellar stacking ( $q \sim 3.00\text{--}3.06 \text{ nm}^{-1}$ ) both in-plane and out-of-plane, while the  $\pi$ - $\pi$  stacking ( $q \sim 17.7 \text{ nm}^{-1}$ ) is observed in the out-of-plane direction. The average d-spacing for the sample coated from pure CB was slightly lower than the additive-processed samples indicated by the shift of the scattering to higher  $q$  values for the pure CB sample ( $q$  is centered around  $\sim 3.06 \text{ nm}^{-1}$ ) as compared to the additive-processed samples ( $q$  is centered around  $\sim 3.00 \text{ nm}^{-1}$ ). The calculated relative crystallinity (normalized to the pure CB sample) and the crystalline correlation length are reported in **Table 7.2**. Both additives (CN and OT) increase the relative crystallinity of the polymer in the dry films as indicated by the increase in the normalized intensity of the scattering. The relative crystallinity increased with respect to the pure CB sample by  $\sim 78\%$  and  $\sim 62\%$  for CN-processed and OT-processed samples, respectively. The crystalline correlation length, parameter related to the average crystallite size, increased from 11 nm for pure CB sample to 16.1 nm and 16.5 nm for CN-processed and OT-processed samples, respectively. The scattering from  $\pi$ - $\pi$  stacking reveals the formation of crystallites with face-on orientation for all samples with enhancement in the scattering intensity for the

additive-processed samples indicating improved long-range order along the  $\pi$ - $\pi$  stacking direction.

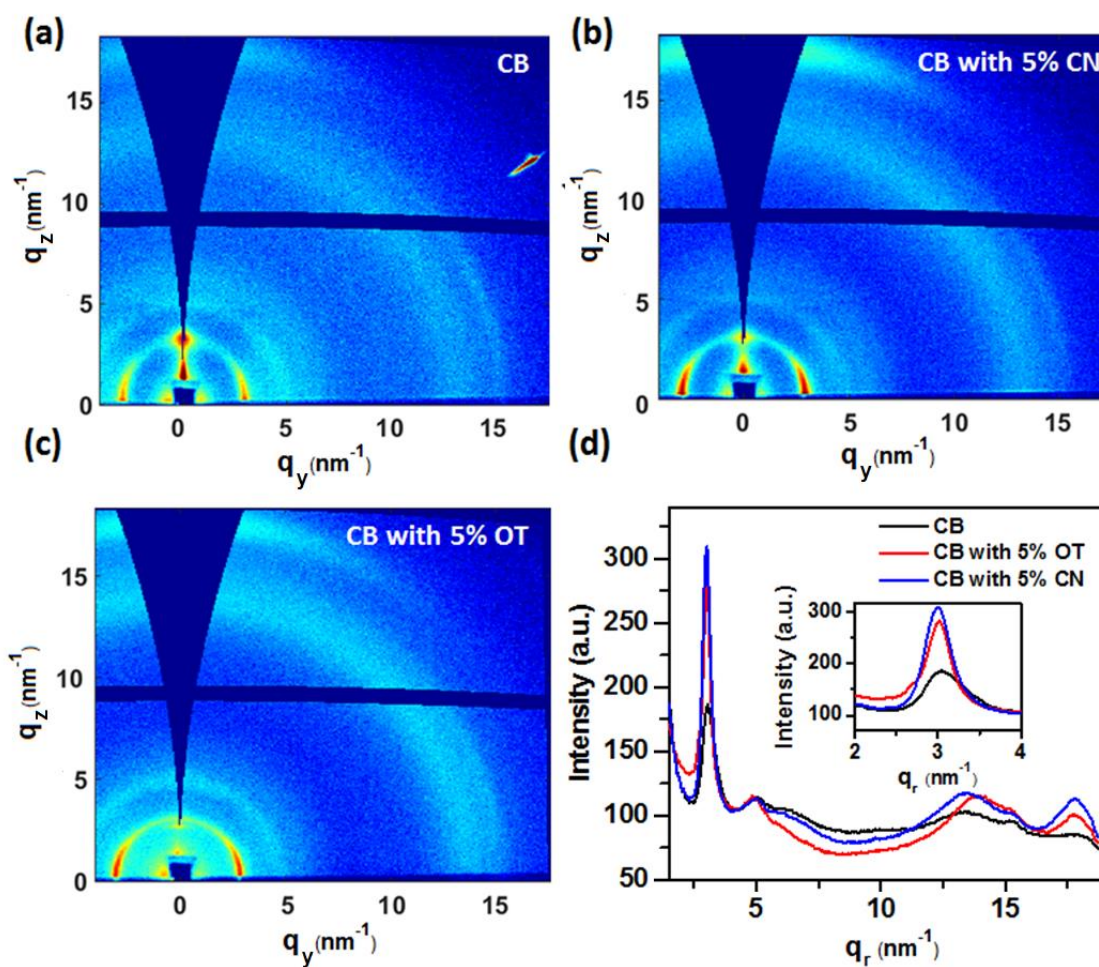


**Figure 7.4** (a-c) 2D GIWAXS plot of PBDTPD:PC<sub>71</sub>BM films coated from; (a) pure CB, (b) CB with 5% CN, and (c) CB with 5% OT. (d) Line cuts of integrated scattering intensity versus  $q$  (nm<sup>-1</sup>) of the three samples (a-c). Inset of (d) shows zoomed-in plot highlighting scattering from BDTTPD lamellar-stacking peak (100).

**Table 7.2** Summary of the relative crystallinity and crystalline correlation length of PBDTPD in the dry blend films, calculated from lamellar-staking (100) scattering.

	Relative crystallinity	FWHM <sub>(100)</sub> (nm <sup>-1</sup> )	CCL <sub>(100)</sub> (nm)
CB	1	0.57	11
CB with 5% CN (dry)	1.78	0.39	16.1
CB with 5% OT (dry)	1.62	0.38	16.5

#### 7.4 Effects of solvent additives on the carrier mobility

We have evaluated the charge carrier mobility within the BHJ layers to see the impact of the morphological and microstructural differences reported above on carrier mobility and its balance. We have used a recently developed technique, known as metal-insulator-semiconductor charge extraction by linearly increasing voltage (MIS-CELIV), to measure the charge carrier mobilities.<sup>[158]</sup> In **Table 7.3**, we summarize the mobilities of the PBDTPD:PC<sub>71</sub>BM films coated using the three formulations; the calculation of carrier mobility was performed as described in chapter 3. In all cases, the hole mobility is lower than electron mobility. However, it is worth pointing out that additives increase both hole and electron mobilities compared to the additive-free formulation. The slight increase of hole mobility is consistent with an increase of the relative degree of crystallinity of the polymer. Interestingly, the CN additive appears to selectively boost



the hole mobility (~60%) while the OT additive primarily boosts the electron mobility and by a much larger amount (~500%). The significant boost of electron mobility in the OT case is consistent with the formation of significant PC<sub>71</sub>BM aggregation as indicated by EF-TEM images in **Figure 7.3f**. As a result, the device prepared with CN had a more balanced carrier mobility ratio than OT and comparable to the additive-free case, perhaps explaining the significant difference in FF between CN and OT processed films.

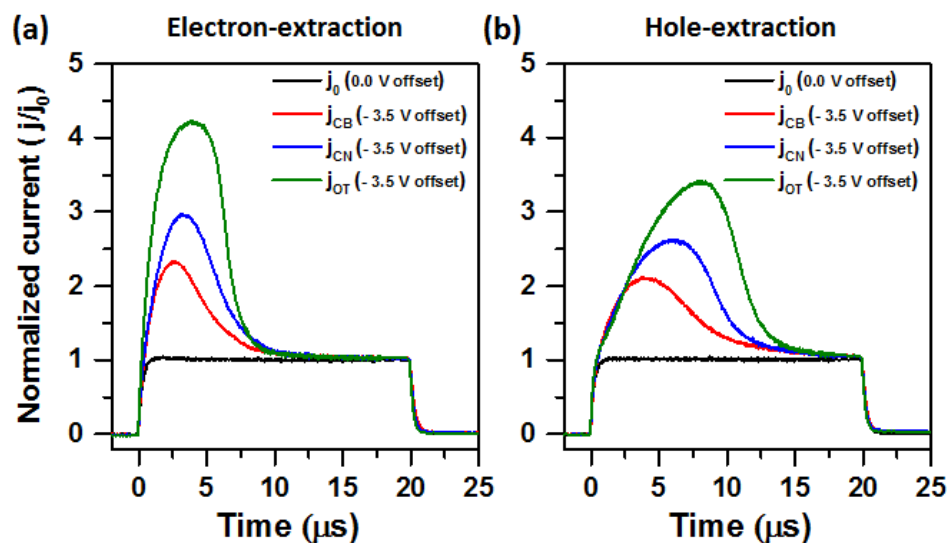


**Figure 7.5** MIS-CELIV extraction currents transients of the charge carriers injected into: (a) electron-only extraction devices; ITO/MgF<sub>2</sub>/ PBDTTPD: PC<sub>71</sub>BM /Ca/Al and (b) hole-only extraction devices; ITO/MgF<sub>2</sub>/ PBDTTPD: PC<sub>71</sub>BM /MoO<sub>3</sub>/Ag. The active layer of PBDTTPD: PC<sub>71</sub>BM was processed from; pure CB (red curves), CB with 5% CN (blue curves), and CB with 5% OT (green curves).

**Table 7.3** Calculated electron and hole mobilities of PBDTTPD: PC<sub>71</sub>BM films coated with and without additives

	Mobility (cm <sup>2</sup> V <sup>-1</sup> s <sup>-1</sup> )		$\mu_{\text{Hole}}/\mu_{\text{Electron}}$
	$\mu_{\text{Hole}} \times 10^{-5}$	$\mu_{\text{Electron}} \times 10^{-4}$	
CB	3.51±0.09	1.48±0.03	0.24
CB with 5% CN	5.65±0.22	2.01±0.02	0.28
CB with 5% OT	4.20±0.17	8.85±0.03	0.05

## 7.5 Monitoring microstructure evolution during solution processing

### 7.5.1 Thickness evolution during film formation

The key question which arises from these experiments is why do the additives result in such drastically different morphologies and how do they do it? To begin answering this question, we have investigated the thinning behavior and kinetics of the three formulations in question during spin coating, as shown in **Figure 7.6a**, using a combination of *in situ* ellipsometry and reflectometry during spin coating and thereafter. We observe identical thinning behaviors at the beginning of spin coating for all samples, where fluid ejection and outflow dominate the thinning. The thinning deviates afterwards for the formulations containing additive. For the pure CB sample, the thinning ends with the near complete evaporation of CB after ~ 13 s from the start of the spin coating. In the presence of additives, a wet and swollen BHJ film is formed upon

evaporation of the primary solvent thanks to the high boiling point of solvent additive. Subsequent thinning therefore occurs at a much slower rate. Complete film drying is attained upon transferring the samples into a vacuum chamber, which allows us to estimate the volume fraction of solvent retained during spin coating and until full drying. This is shown in **Figure 7.6b**. For additive processed samples (both CN and OT), the wet films were almost five times thicker, at the point of CB removal, as compared to the completely dry films. The volume fraction of the swollen wet film after CB removal was 82% v/v and 78 % v/v for CN-processed and OT-processed samples, respectively. The final thickness of the dry films didn't change significantly for the additive processed samples as compared to the pure CB sample; an average thickness ( $\sim 100\text{--}110\text{ nm}$ ) was attained for all samples.

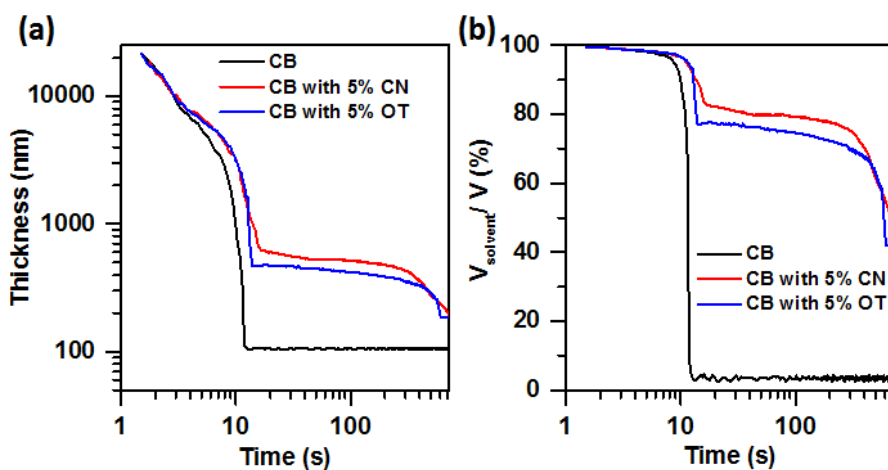


**Figure 7.6** (a) The thickness evolution during spin-coating and subsequent drying for PBDTPD: PC<sub>71</sub>BM spin-cast from pure CB, CB with 5% CN, and CB with 5% OT. (b) The

calculated retained solvent in the “wet” film during and thereafter spin-coating for the three cases in (a).

### 7.5.2 Aggregation behavior of PC<sub>71</sub>BM acceptor in different formulations

PC<sub>71</sub>BM is known to be highly soluble in CB as well as in the solvent additives used in this study.<sup>[99]</sup> However, the evolution of aggregation of PC<sub>71</sub>BM during solution processing in the presence of the solvent additives is difficult to monitor. In the previous chapter, we monitored the photo-physical aggregation of PC<sub>71</sub>BM blended with poly(methyl methacrylate) (PMMA) in the presence of DIO and we have shown that PC<sub>71</sub>BM remains solvated in DIO for prolonged durations during film formation. Herein, we have blended PC<sub>71</sub>BM with a transparent polymer binder (polystyrene (PS)) using similar solution formulation used for the BHJ blends with the exception of donor. We note that using PMMA or PS with low molecular weight (Mw) as the transparent binder results in complete outflow of the solution leading to bare substrates upon spin-coating with additives. We have therefore used high Mw PS (average Mw = 650 KDa). The PC<sub>71</sub>BM absorption spectra exhibit a modest but detectable red shift between the solvated and aggregated states of the molecule, as shown in **Figure 7.7a**. We monitor the time-evolution of the ratio of the absorption peaks at  $\lambda_1 = 465$  nm and  $\lambda_2 = 550$  nm and plot in **Figure 7.7b** the evolution of PC<sub>71</sub>BM aggregation for solutions cast from pure CB and at the presence of additives. For the pure CB sample, the solution dries within ~ 13-15 s (just like the BHJ) resulting in rapid increase in PC<sub>71</sub>BM aggregation and this behavior

persists and is frozen in time after CB removal. For CN- and OT-processed samples, a significant portion of PC<sub>71</sub>BM remains solvated in the presence of the additive for a prolonged time similar to our previous observation with DIO, confirming the high solubility of PC<sub>71</sub>BM in the additives.

Surprisingly, we observe fluctuations with time of the aggregation signature of PC<sub>71</sub>BM in the case of CN. We speculate this may be due to competing aggregation and redissolution effects as the amount of additive trapped in the wet BHJ film decreases and the additive diffuses toward the surface for subsequent evaporation. It is not clear why the same behavior is not seen in the case OT. Nevertheless, it is important to note that these experiments should be approached qualitatively as replacing of the donor with PS leads to different solubility and miscibility behavior between the fullerene and polymer which can influence the fullerene aggregation in complex ways.

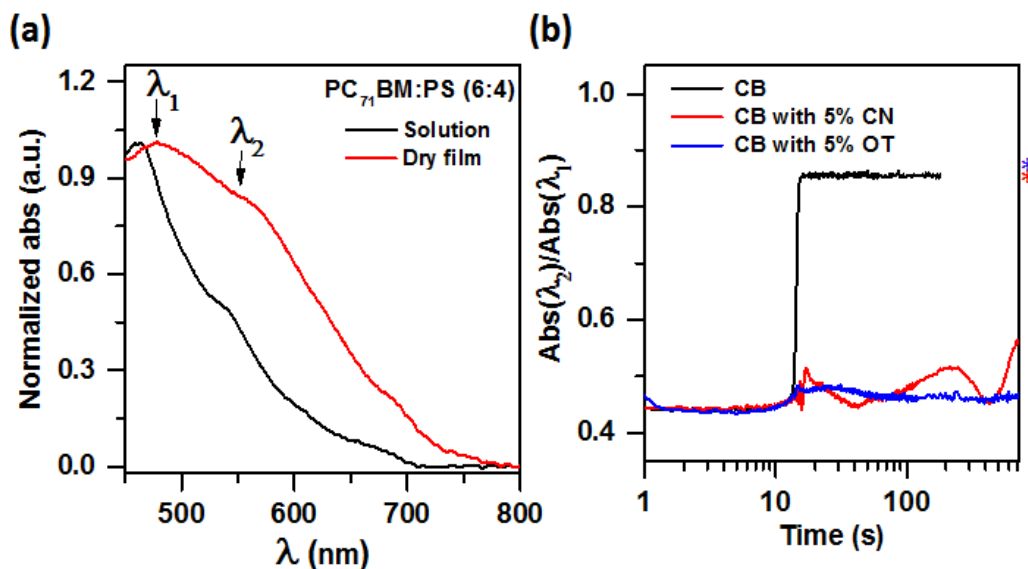


**Figure 7.7** UV-Vis absorption spectra of PC<sub>71</sub>BM: PS (60:40) in solution and solid state (normalized to PC<sub>71</sub>BM absorption peak ( $\lambda_1 = 465$  nm)). (b) Time-evolution of PC<sub>71</sub>BM aggregation as represented by the ratio of absorption peak intensities at  $\lambda_2 = 550$  nm and  $\lambda_1$  during spin-coating and thereafter of a PC<sub>71</sub>BM: PS blend. The values of  $Abs(\lambda_2)/Abs(\lambda_1)$  of the dry additive-processed films are shown as asterisks in figure (b) (right). PS with high Mw (650 KDa) was used in this experiment.

### 7.5.3 Evolution of PBDTTPD donor crystallization during BHJ film formation

We investigated the effect of additives on the crystallization behaviour of PBDTTPD in the BHJ blends by performing *in situ* GIWAXS measurements during spin coating and thereafter for the three formulations in question. 2D plots of the integrated scattering intensity, shown in logarithmic color scale, versus  $q$  ( $\text{nm}^{-1}$ ) and time (s) are shown in

**Figure 7.8** for the three cases on hand. The beginning of spin coating experiments is characterized by broad liquid solvent scattering feature ( $11 \text{ nm}^{-1} < q < 18 \text{ nm}^{-1}$ ) in all cases, giving way to the polymer's lamellar scattering  $q \sim 2.85 \text{ nm}^{-1}$  even before the bulk solvent has evaporated. This is further highlighted in GIWAXS line cuts (**Figure 7.9**) taken at 6 s and 10 s, which prove the coexistence of PBDTTPD crystallites and bulk solvent scattering features. Interestingly, these early crystallites have larger d-spacing than in the subsequent dry film, indicating the pre-aggregates may be somewhat solvated by taking up solvent molecules between lamellae. Additional increase in the PBDTTPD scattering signal coincides with significant reduction of solvent scattering, as seen in **Figure 7.8**, for all three cases. In **Figure 7.10a-b**, we plot the time evolution of the peak position and integrated intensity of PBDTTPD lamellar stacking peak (100), calculated by fitting the scattering peak to a Gaussian function. For pure CB sample, we observe an increase and plateau of the scattering intensity after 10 s indicating the formation of PBDTTPD crystallites (**Figure 7.10a**). Simultaneously, we observe a shift of the lamellar peak positions towards higher  $q$  values (lower d-spacing) upon crystallization during CB removal, indicating densification of the crystallites consistent with removal of small amounts of CB intercalated between the lamellae of PBDTTPD pre-aggregates.

For the CN-processed sample, the crystallization occurs in three main steps. In the first step, similar to the pure CB sample, PBDTTPD pre-crystallization is initiated in the solution-state. The second step is characterized by fast crystallization coinciding with

the removal of the primary solvent (CB). The third step is characterized by very slow crystallization of PBDTTPD that follows closely the evaporation of CN, indicating that CN delays and slows the crystallization of the polymer compared to the additive-free case; crystallite formation thus ceases after the initial pre-crystallization in solution, developing after ~23 s (**Figure 7.10a**). Again, we observe densification of PBDTTPD crystallites during crystallization indicated by the shifting of the peak position towards higher  $q$  values, but this behaviour does not follow CB removal anymore.  $q$  values of the lamellar stacking remains close to  $\sim 2.8 \text{ nm}^{-1}$  in the first step of PBDTTPD crystallization, and shifts to  $2.9 \text{ nm}^{-1}$  during the second step. During the third step of PBDTTPD crystallization with CN removal,  $q$  initially remains close to  $2.9 \text{ nm}^{-1}$  and shifts slowly to  $3 \text{ nm}^{-1}$  afterwards. This indicates that CN is intercalated within PBDTTPD lamellae and does not inhibit its crystallization. Notably, significant crystallization occurs even in the presence of CN intercalated within PBDTTPD crystallites, as can be seen **Figure 7.10 a-b**. Further crystallization occurs after vacuum drying, see the asterisk for the completely dried film in **Figure 7.10a**. Line-cuts of integrated scattering intensity of the as-cast and dry films processed from CB with 5% CN are shown in **Figure 7.10c**. The relative crystallinity and CCL of PBDTTPD in the as cast CN-processed sample before complete drying is reported in **Table 7.4**. The relative crystallinity is improved in the as cast CN-processed sample by 36 % even in the presence of CN, as compared to the pure CB sample (see **Table 7.4**), and increases further after vacuum drying as shown previously in **Table 7.2**.



On the other hand, OT is found to inhibit the crystallization of PBDTTPD significantly as compared to the pure CB and CB/CN solutions. The integrated scattering intensity of PBDTTPD remains very low up to 50 s indicating null crystallization of PBDTTPD, except for the pre-crystallites that were formed in the solution. The subsequent increase of PBDTTPD crystallization plateaus after 90 s. The as cast OT-processed sample has approximately half the relative crystallinity of the pure CB sample, as shown in **Table 7.4**. PBDTTPD crystallization occurs after vacuum drying of the wet film, indicating that most of the PBDTTPD remains in a disordered state in the presence of OT, as shown in **Figure 7.10d**. Line-cuts of integrated scattering intensity of the as-cast and dry films processed from CB with 5% OT are shown in **Figure 7.10d**. The as-cast film lacks ordering in the  $\pi$ - $\pi$  stacking direction and has significantly lower scattering intensity in the lamellar stacking direction. The estimated relative crystallinity in the OT-processed sample increased by 3.5 times after vacuum drying, indicating that the as-cast film was significantly vitrified by the additive OT.

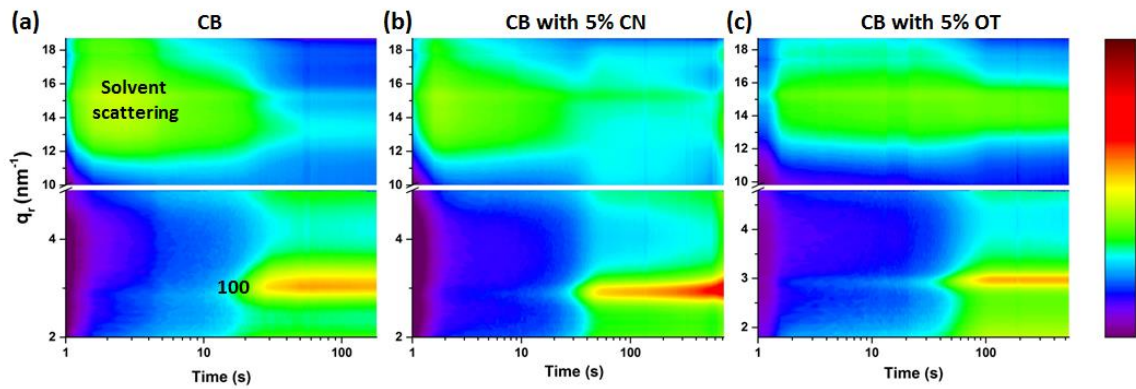


**Figure 7.8** *In situ* GIWAXS color plots (Integrated scattering intensity is shown in logarithmic color scale versus  $q$  ( $\text{nm}^{-1}$ ) and time(s)) of casting PBDTTPD: PC<sub>71</sub>BM from: (a) pure CB, (b) CB with 5% CN, and (c) CB with 5% OT.

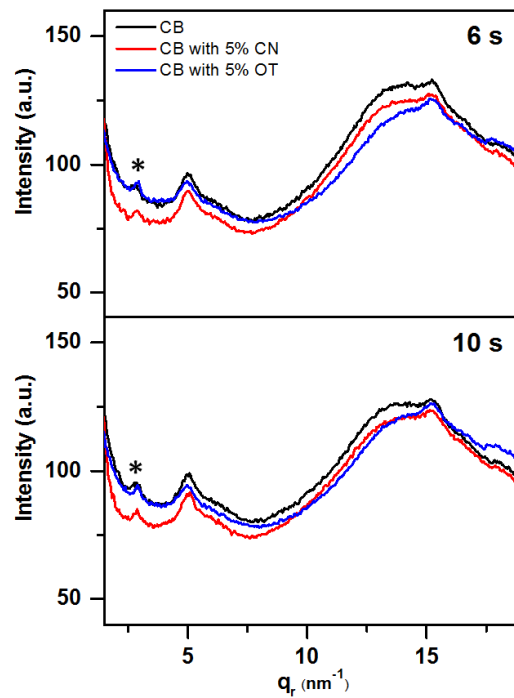


**Figure 7.9** Line-cuts of the integrated scattering intensity versus  $q$  during spin coating of PBDTTPD: PC<sub>71</sub>BM at 6 s (top) and at 10 s (bottom) from start spin coating, showing that

PBDTTPD crystallites formation occurs early in solution for additive-free and additive processed samples. The scattering around ( $q \sim 5 \text{ nm}^{-1}$ ) corresponds to a Kapton foil that was used as shield against ink splashes during spin coating. The broad scattering ( $q \sim 10\text{-}18 \text{ nm}^{-1}$ ) corresponds to solvent scattering.

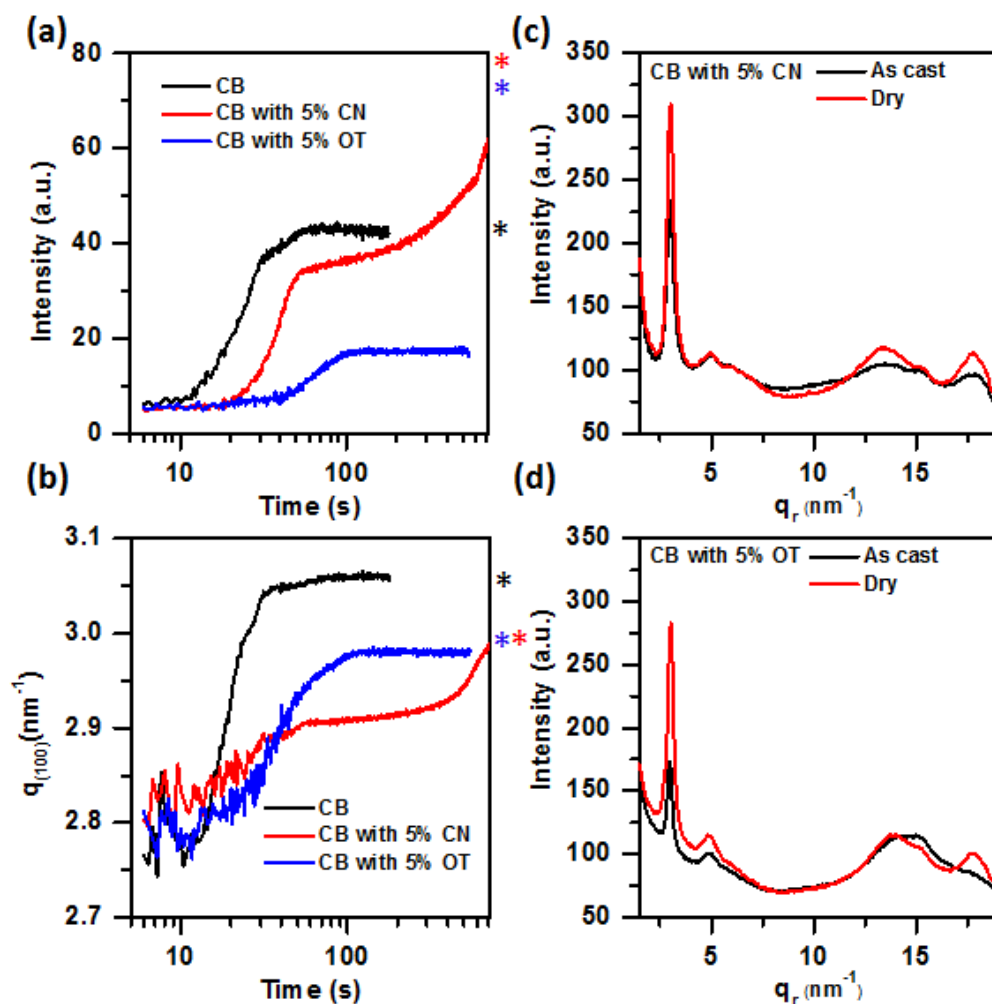


**Figure 7.10** (a) Evolution of the integrated scattering intensity of the lamellar stacking scattering peak (100) of PBDTTPD during casting of PBDTTPD: PC<sub>71</sub>BM from pure CB (black), CB with 5% CN (red), and CB with 5% OT (blue). (b) Evolution of the peak

position of the lamellar stacking peak (100) of PBDTTPD versus time (s) for the three condition in (a). The values of the integrated scattering intensity and peak position of the complete dry films are shown as asterisks on the right of the plots (a,b) with the corresponding colors of the three conditions. Line-cuts of the integrated scattering intensity versus  $q$  of the as cast and vacuum dried PBDTTPD: PC<sub>71</sub>BM films processed from CB with 5% CN (c), and CB with 5% OT (d).

**Table 7.4** Summary of the relative crystallinity and crystalline correlation length of PBDTTPD in the as cast blend films, calculated from lamellar-staking (100) scattering.

	Relative crystallinity	FWHM <sub>(100)</sub> (nm <sup>-1</sup> )	CCL <sub>(100)</sub> (nm)
CB	1	0.57	11
CB with 5% CN (as cast)	1.36	0.41	15.3
CB with 5% OT (as cast)	0.46	0.32	19.6

The as-cast samples were measured after approximately 15 min from casting, and before vacuum drying.

Further insight into the role of solvent additives on PBDTTPD crystallization can be obtained by monitoring the evolution of crystallite orientation during film formation. 2D plots of the integrated scattering intensity of PBDTTPD lamellar stacking peak, shown in logarithmic color scale, versus time(s) and azimuth angle (°) are shown in **Figure 7.11a-c**

for the three coating conditions. Line-cuts of the time-evolution of the integrated scattering intensity in the out-of-plane direction and in-plane direction are shown in **Figure 7.11d-f**. For the pure CB sample, we observe development of the scattering from the lamellar stacking in the in-plane and out-of-plane directions, simultaneously, as shown in **Figure 7.11 a,d**. The pole figure of the lamellar stacking of the as-cast pure CB sample, shown in **Figure 7.11g**, reveals that the scattering from the lamellar stacking is dominated in the out-of-plane and in-plane directions, indicating the formation of crystallites with lamellar stacking orientation dominated parallel and perpendicular to the plane of the film. For the CN-processed sample, we observe similar behavior during the first and second steps of PBDTPD crystallization in which crystallites form with lamellar orientation in both directions. However, in the third step in which crystallization is dominated by CN evaporation, CN promotes the formation of crystallites oriented with lamellar stacking parallel to the plane of the film indicated by the evolution of the scattering predominantly in the in-plane direction. Notably, these crystallites with lamellar stacking oriented parallel to the plane of the film (i.e. the plane of lamellae normal to the substrate) have their  $\pi$ - $\pi$  stacking oriented face-on. For the OT-processed sample, crystallization occurs with no preferential orientation as confirmed by the pole figure of the lamellar stacking of the as cast film. However, after vacuum drying, the lamellar stacking scattering becomes more dominant in the in-plane direction, see **Figure 7.11i**.

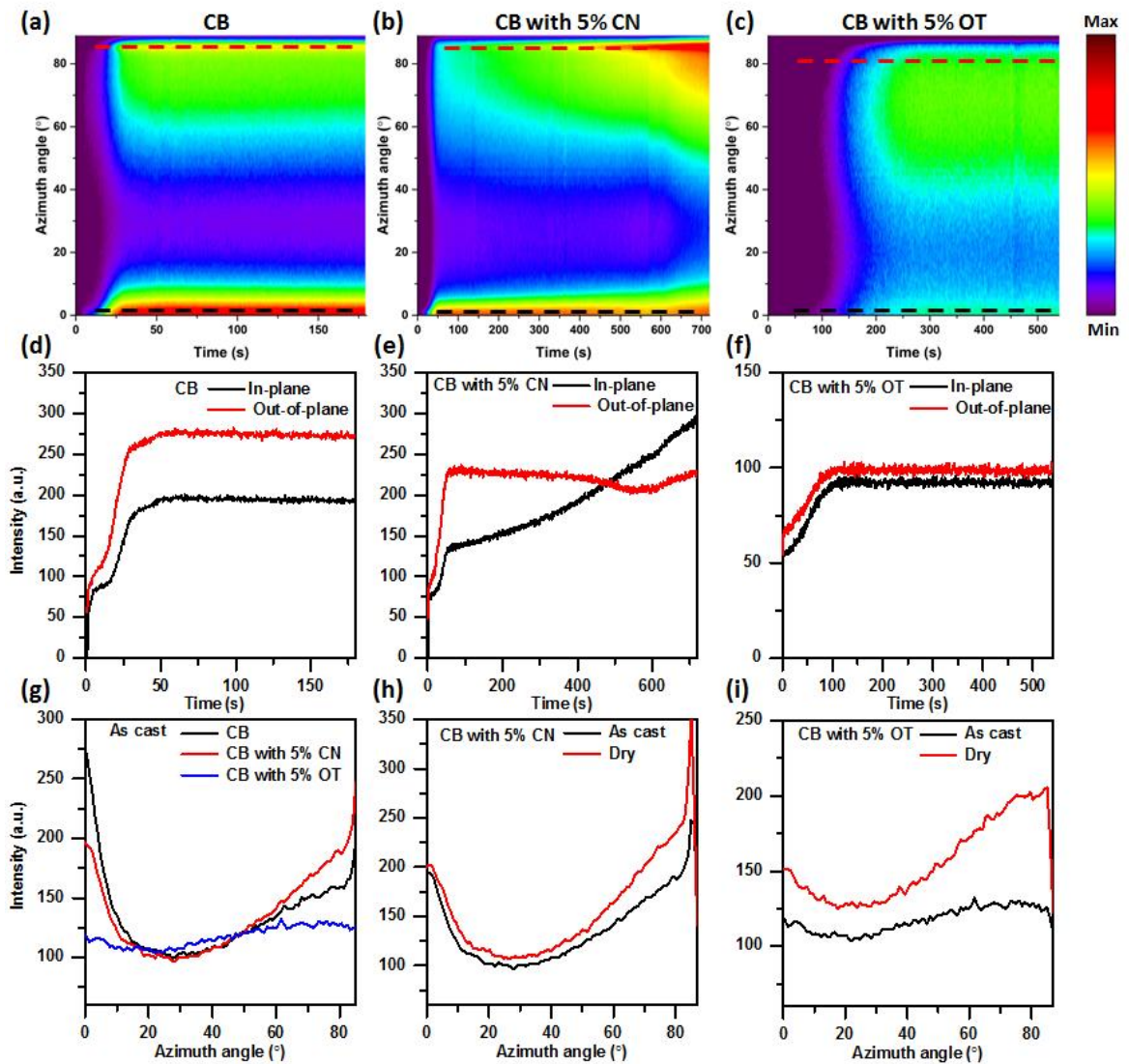


**Figure 7.11** (a-c) 2D GIWAXS color plot of integrated scattering intensity of PBDDTPD lamellar stacking peak (100), shown in logarithmic color scale, versus time(s) and azimuth angle ( $^{\circ}$ ) from out-of-plane direction at ( $0^{\circ}$ ) to in-plane direction at ( $90^{\circ}$ )); GIWAXS measurements were performed *in situ* during casting PBDDTPD: PC<sub>71</sub>BM from: (a) pure CB, (b) CB with 5% CN, and (c) CB with 5% OT. (d-f) Line-cuts of the evolution of

the integrated scattering intensity in the out-of-plane direction and in-plane direction versus time for the three conditions in (a-c); (d) pure CB, (e) CB with 5% CN, and (f) CB with 5% OT. Line-cuts were taken at the dashed lines in (a-c). (g) Line-cuts of the integrated scattering intensity versus azimuth angle ( $^{\circ}$ ) of the as cast films in (a-c). (h-i) Line-cuts of the integrated scattering intensity versus azimuth angle ( $^{\circ}$ ) of the as cast and vacuumed dried films of the additive-processed samples; (h) CB with 5% CN, and (i) CB with 5% OT.

### **7.6 Mechanism of additive-mediated bulk heterojunction formation**

Several important observations can be summarized from the results obtained thus far:

(1) PBDTTPD self-assembles early in CB solution whether an additive is present or not; (2) PC<sub>71</sub>BM remains solvated for prolonged time even after CB evaporation in the presence of the additives (CN & OT); (3) OT inhibits polymer crystallization in the wet film and solvates PC<sub>71</sub>BM as well; (4) CN promotes slow and steady polymer crystallite formation while PC<sub>71</sub>BM is mostly solvated.

We recall that PBDTTPD: PC<sub>71</sub>BM blends cast from pure CB exhibit the formation of oversized PC<sub>71</sub>BM domains on the order of hundreds of nanometers.<sup>[115]</sup> This problem is particularly severe for low Mw PBDTTPD, as shown in a previous study by McGehee and co-workers.<sup>[115]</sup> Increasing the molecular weight was found to reduce the size PC<sub>71</sub>BM domains. The authors attributed that behavior to the formation of polymer pre-aggregates in solution, leading to the formation of a framework preventing excessive

PC<sub>71</sub>BM aggregation.<sup>[115]</sup> Indeed our results reveal that, for pure CB, PBDTTPD crystallite formation occurs early in the solution and acts as a seed for further crystallization of PBDTTPD during CB evaporation, as represented schematically in **Figure 7.12a-b**. PBDTTPD crystallites form fibrillar networks that define the extent of PC<sub>71</sub>BM aggregation, as represented in **Figure 7.12b**. Since we use in this study PBDTTPD with high Mw, PBDTTPD crystallization is sufficient to prevent the over-aggregation of PC<sub>71</sub>BM to some extent, yet, PC<sub>71</sub>BM still phase separates into large domains, as shown in **Figure 7.3d**. Thus, the additive is needed to further mitigate PC<sub>71</sub>BM aggregation and promote fine BHJ morphological features. Both CN and OT can keep PC<sub>71</sub>BM solvated for extended period as shown previously in **Figure 7.7b**. However, their effect on the polymer crystallization is very different. CN promotes slow and steady PBDTTPD crystallization and self-assembly over a prolonged time leading to the formation of better developed polymer fibrillar networks in the wet film with reduced interspacing within the fibrillar networks, as represented in **Figure 7.12c**. PC<sub>71</sub>BM and a portion of PBDTTPD remain solvated in CN within these spaces in the wet film. Subsequently, upon complete removal of CN, the remaining PBDTTPD and PC<sub>71</sub>BM segregate filling the space between the polymer crystalline fibrils. The increase in the number and size of PBDTTPD fibrils, induced by CN processing, is most likely responsible for the reduced PC<sub>71</sub>BM segregation in the as cast CN-processed films.

The mechanism of CN in our study is distinguishable from the mechanism of the additive oDCB in PDPP5T: PC<sub>71</sub>BM BHJ system in CF solution in which oDCB forces PDPP5T



aggregation early in solution, discussed previously in more detail in chapter 2 (see **Figure 2.7**).<sup>[24]</sup> Herein, CN delays PBDTTPD crystallization as compared to the pure CB case, but still, the polymer fibrillar networks formation occurs before PC<sub>71</sub>BM segregation, leading to finer PC<sub>71</sub>BM phase separation. Overall, the main requirement for preventing PC<sub>71</sub>BM large segregation is the formation of the polymer-fibril networks before the PC<sub>71</sub>BM large segregation; whether the fibril-networks form early in solution or late in the wet swollen film with the additive.

In OT-processed films, the pre-aggregation of the polymer in solution clearly does not suffice. OT significantly hinders the polymer crystallization in the as-cast wet film which only crystallizes upon complete removal of OT by vacuum drying. In the presence of OT in the wet film, a portion of PC<sub>71</sub>BM is expected to phase separate into micron-sized pockets before the formation of polymer fibril-networks. The microstructure in the as cast OT-processed films before vacuum drying is represented in **Figure 7.12d** as a composition of mainly three phases; (1) pure PBDTTPD crystallites; we expect this phase to be OT-free phase because these crystallites have d-spacing identical to the final dry film, see **Figure 7.10b**; (2) Mixed PC<sub>71</sub>BM-OT phase; in the presence of OT, the polymer pre-crystals fail to form a network, instead collapsing onto themselves and promoting large scale PC<sub>71</sub>BM segregation into PC<sub>71</sub>BM-OT pockets. (3) A mixed three phase BHJ composed of amorphous PBDTTPD, PC<sub>71</sub>BM, and OT. Upon complete drying of OT, PBDTTPD and PC<sub>71</sub>BM phase segregate from phase (3) into finely mixed domains, whereas further PBDTTPD crystallization occurs. The finely mixed PBDTTPD and PC<sub>71</sub>BM

domains that appear in EFTEM images in **Figure 7.3f**, are believed to evolve from the phase (3), whereas PC<sub>71</sub>BM micron-size domains are believed to form from phase (2).

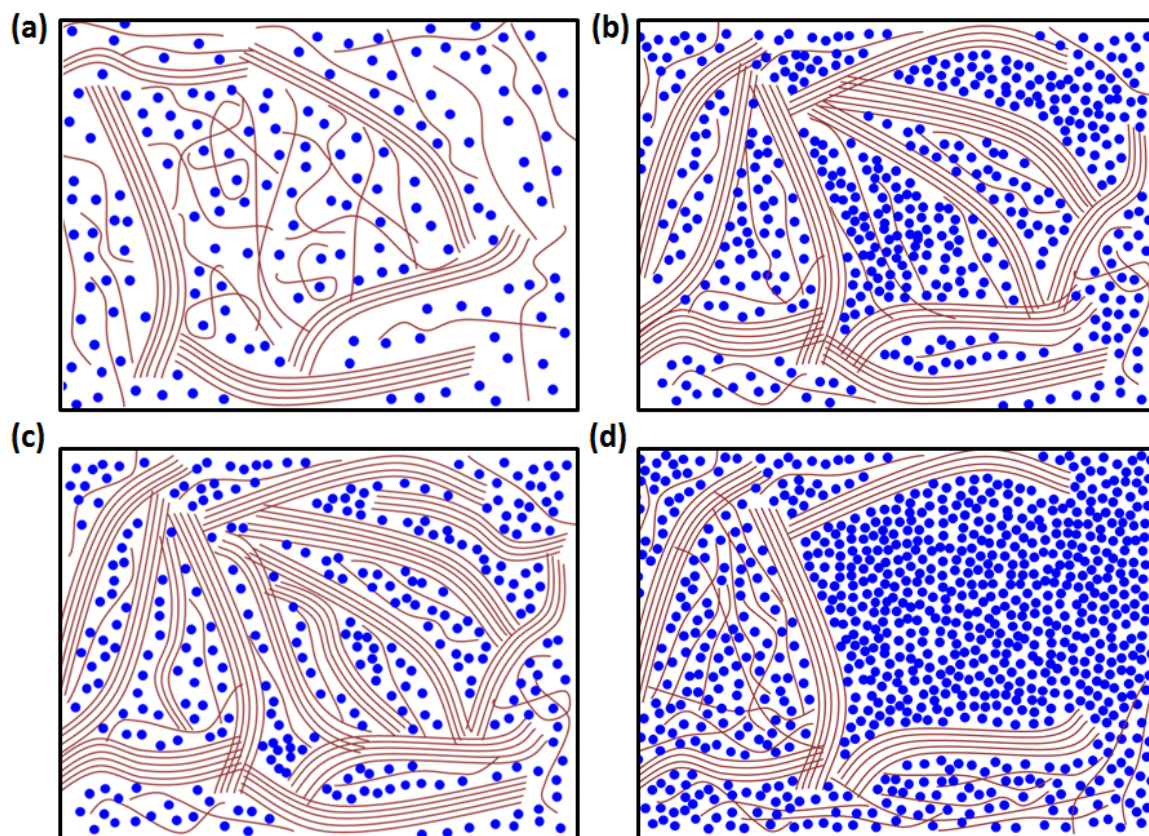


**Figure 7.12** Schematics represents the mechanisms of film formation of PBDTTPD:PC<sub>71</sub>BM blends when they are cast from pure CB, CB with CN, and CB with OT. PBDTTPD is represented as rods (dark red), PC<sub>71</sub>BM is represented as blue dots, and all solvents are transparent. (a) Schematic represents the solution-state showing PBDTTPD self-assembly in CB solution for the three conditions. (b) Schematic represents the formation of PBDTTPD fibril-network during CB evaporation for pure CB case. (c) Schematic represents the formation of PBDTTPD fibril-networks during CN evaporation for CN-

processed films revealing the formation of more fibril-networks which reduces the inter-spacing between these networks, and thus reduces PC<sub>71</sub>BM domains. (d) Schematic represents the as cast wet film, swollen with OT, for OT-processed films, revealing segregation of PC<sub>71</sub>BM into large-domains. The OT-wet film is expected to be composed of three phases; (1) pure PBDTTPD crystallites (fibrils), (2) Mixed PC<sub>71</sub>BM-OT micron-size domains (on the right of the schematic (d)), and (3) mixed phase of amorphous PBDTTPD, PC<sub>71</sub>BM, and OT (on the left and bottom of the schematic (d)). We note that this illustration (d) is zoomed-in where PC<sub>71</sub>BM aggregation occurs and shouldn't be interpreted as the film has more PC<sub>71</sub>BM than the polymer.

## 7.7 Conclusions

This study highlights the importance of the choice of the solvent additive in tuning the BHJ microstructure and emphasizes the usefulness of *in situ* monitoring of film formation in revealing the additives impact on the mechanism of film formation. Investigation of the evolution of donor and acceptor crystallization /aggregation, has provided us with in-depth understanding of the sequence and mechanism of microstructure formation in PBDTTPD: PC<sub>71</sub>BM BHJ system. In the case of casting from pure CB, polymer crystallization is induced early in the solution facilitating the formation of polymer fibril-networks before significant PC<sub>71</sub>BM segregation. Yet, the polymer crystallites formation, in terms of the number and size of the crystallites, is not sufficient to fully suppress the formation of oversized PC<sub>71</sub>BM domains. Nevertheless, the polymer

self-assembly in solution helps to attain reasonable polymer crystallinity. The formation of oversized PC<sub>71</sub>BM domains can be fully overcome by the additive CN. Our finding reveals that CN delays the polymer crystallization but promotes steady crystallization for prolonged time, leading to an enhancement in the fibrillar crystallites formation. Simultaneously, CN keeps PC<sub>71</sub>BM solvated while the polymer crystallites constitute fibril-networks that template the microstructure and prevent PC<sub>71</sub>BM large segregation. The proposed mechanism of the additive CN here is distinguished from other polymer – fullerene BHJ systems where the additive induces earlier crystallization of the polymer. Importantly, PC<sub>71</sub>BM segregation should be prevented till the polymer fibril networks formation; it doesn't matter these networks form either early in solution or much later in the wet film. For the additive OT case, although the polymer self-assembles in solution, OT inhibits further polymer crystallization when it is present in the wet film leading to severe segregation of PC<sub>71</sub>BM into micron-sized domains.

Our results reveal strong correlation between carrier's mobility and BHJ microstructure. The increase in hole mobility for the additive-processed films correlates with the enhanced polymer crystallinity. Moreover, the substantial increase in electron mobility for the OT-processed films correlates with the formation of micron-sized PC<sub>71</sub>BM domains. We attribute the reduced FF and J<sub>sc</sub> in OT-processed solar cell devices to the imbalanced electron-hole mobilities and the large PC<sub>71</sub>BM aggregates, which are expected to increase the recombination losses. It is surprising that both additive-free and CN-processed solar cell devices exhibit identical FF, regardless of their different

microstructure, but only  $J_{sc}$  increased for CN-processed solar cell devices. Perhaps, exciton splitting efficiency is identical in both cases leading to identical FF, whereas the increased  $J_{sc}$  is related to an increased interfacial area for CN-processed condition. More work is needed to fully address this hypothesis.

## Chapter 8

### Lessons for scalable processing of small-molecule bulk heterojunction solar cells while achieving microstructural and performance parity

#### 8.1 Introduction

The need for high throughput production-compatible processing has attracted attention for decades. Several efforts have been done to bridge the performance gap between lab-based processing techniques, such as spin coating, and roll-to-roll compatible manufacturing techniques, such as blade-coating, slot-die coating and wirebar coating.<sup>[21]</sup> On the context of polymer-based solar cells, achieving performance parity between spin coating and scalable techniques was attained for various systems.<sup>[196,197]</sup> On the hand for small molecule solar cells, the aggregation of small molecules, unlike polymers, is much more sensitive to process kinetics and little effort has been made to bridge the performance gap between spin coated and scalably-coated small molecule OPVs. Here, we show that scalable solution-coating of small molecule p-DTS(FBTTh<sub>2</sub>)<sub>2</sub>:PC<sub>71</sub>BM BHJ, using the conventional techniques, leads to very significant performance gaps with the optimum device performance obtained by spin coating. We investigate the origin of this difference and find that it is indeed closely linked to drying kinetics. We devise a new coating method which combines scalability with a vortex of air to emulate the drying kinetics of spin coating to demonstrate microstructural and

morphological parities which result in performance parity for small molecular organic solar cells. Part of this work is submitted for patent application.

Generally small-molecule BHJ systems have higher sensitivity to coating conditions than their polymer counterparts. For instance, for additive processed systems, the optimal content of additive is quite sharp. Minute increase in additive content than optimum leads to extreme deterioration of device performance which is also associated with significant differences in the microstructure.<sup>[121,177]</sup> On the other hand, polymer-based solar cells can perform quite efficient for wide-range of additive content, and usually, much higher additive content is used as compared to all-small-molecule solar cells.<sup>[128,137,198,199]</sup> The BHJ microstructure in polymer-based solar cells exhibits more resistance to change with additive content. We attribute this behaviour to the high diffusion of small molecules, unlike polymers, which leads to high sensitivity to the kinetics of film formation. On the other hand, polymers are much less mobile and in many systems polymer long chains create frameworks that template the microstructure, as discussed in chapter 7.

In this chapter, we investigate the effects of drying speed of small-molecule OPV formulations based on  $p\text{-DTS}(\text{FBTTh}_2)_2\text{:PC}_{71}\text{BM}$  without modifying the process temperature. We begin by demonstrating unsuccessful efforts in making working solar cells without recreating similar drying kinetics when transferring the formulation to blade- and wire-bar coating processes from spin-coating. We go on to design a new

coating apparatus that combines the benefit of an air vortex in terms of accelerated thin film drying with scalable and high speed coating methods, such as blade-coating and wire-bar-coating. *In situ* investigations performed in these processes demonstrate that process kinetics is crucial to achieving the same small-molecule BHJ formation behavior, microstructure, morphology and ultimately solar cell performance. Using the new apparatus, we could successfully attain thin film uniformity, microstructure, morphology and performance comparable to spin coated films but with 25 times less material consumption for coating speeds on the order of several meters per minute.

## **8.2 Wire-bar coating and blade-coating of p-DTS(FBTTh<sub>2</sub>)<sub>2</sub>:PC<sub>71</sub>BM films**

Let us first investigate fabrication of solar cells devices by the conventional wire-bar coating and blade-coating techniques. These conditions are used in the study. A stock solution with the optimized spin coated solution formulation was prepared; 35 mg/mL total solutes of p-DTS(FBTTh<sub>2</sub>)<sub>2</sub>:PC<sub>71</sub>BM (3:2) in CB with 0.4% (v/v) DIO (which is equivalent to 21 % w/w (DIO/solutes)). We have shown in the previous chapters that the content of the additive DIO (DIO to solute ratio) is a key factor in tuning the extent of crystallization and phase separation. Thus, for additive-processed samples, we have maintained DIO to the solute ratio identical to optimal spin coating condition (21 % w/w (DIO/solutes)).

The initial trials to fabricate solar cells were unsuccessful leading to either non-working (shorted) devices or extremely poor performance (PCE < 1%) with a few exceptions that



remained non-reproducible. This observation remained the same across the board for various coating conditions; coating with or without solvent additives, different coated thicknesses (50 to 300 nm), and varying coating temperatures (25 – 90 °C).

A closer look at the films reveals poor uniformity and the formation of over-crystallized crystals as revealed by polarized optical microscopy (POM) images (**Figure 8.1a-b**). Coffee-ring effect was observed as shown in **Figure 8.1b** indicating non-uniform drying. Further look at the nano-scale morphology by transmission electron microscopy (TEM) reveals the formation of wire-like structures that extend to the length of microns (**Figure 8.1c**). These structures are typically from p-DTS(FBTTh<sub>2</sub>)<sub>2</sub> crystals confirming over-crystallization in the film. It is not surprising that most of the fabricated devices with conventional wire-bar coating and blade-coating failed due to shorting, probably due to the presence of pinholes. To understand the reason behind these observations, we have carried out in situ investigation of the crystallization during conventional wire-bar coating.

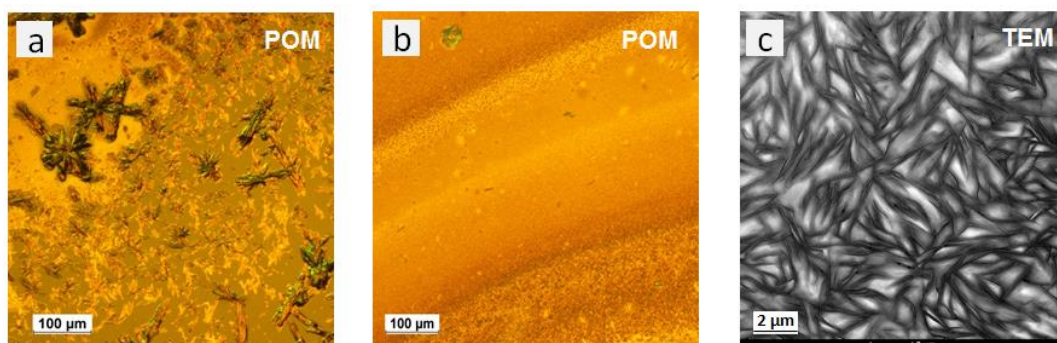


**Figure 8.1** (a) POM image of p-DTS(FBTTh<sub>2</sub>)<sub>2</sub>:PC<sub>71</sub>BM films coated by wire-bar coating from CB with 21 % w/w (DIO/solutes). (b) POM image near the edge of the sample in (a)

showing coffee-ring effect. (c) TEM image of p-DTS(FBTTh<sub>2</sub>)<sub>2</sub>:PC<sub>71</sub>BM films coated from CB with 21 % w/w (DIO/solutes).

The blade-coating and wire-bar coating speeds were varied from low-speed (0.5 mm/s to 10 mm/s) to high-speed (> 100 mm/s) in the initial trials. Afterwards, due to importance of high-speed coating in scalable manufacturing, we have maintained the coating speed at 100 mm/s for all studied conditions below.

### **8.3 Crystallization dynamics of p-DTS(FBTTh<sub>2</sub>)<sub>2</sub> during wire-bar coating of p-DTS(FBTTh<sub>2</sub>)<sub>2</sub>:PC<sub>71</sub>BM films**

In order to reveal the reason behind the over-crystallization of p-DTS(FBTTh<sub>2</sub>)<sub>2</sub> in conventional wire-bar coated samples, we have investigated the film formation by *in situ* grazing incidence wide angle X-ray scattering (GIWAXS) during wire-bar coating. In **Figure 8.2**, we show 2D GIWAXS color plot of integrated scattering intensity (shown as logarithmic color scale) versus  $q$  (nm<sup>-1</sup>) versus time; measured *in situ* during wire-bar coating of p-DTS(FBTTh<sub>2</sub>)<sub>2</sub> : PC<sub>71</sub>BM from CB with 21 % w/w (DIO/solutes) at room temperature (RT) (**Figure 8.2c**) and at 45°C (**Figure 8.2e**). Line cuts of integrated scattering intensity are shown in **Figure 8.2d,f**. For sample coated at RT, we observe broad scattering from the bulk solvent at  $q$  range from 11 nm<sup>-1</sup> to 18 nm<sup>-1</sup> that lasts up to 35 s after coating revealing significant slow evaporation for wire-bar coating at room temperature as compared to spin coating that lasts for 6 s only. We observe the formation of p-DTS(FBTTh<sub>2</sub>)<sub>2</sub> crystals at early stage (after ~ 10 s) revealed by the

scattering at  $q$  ( $\sim 2.8 \text{ nm}^{-1}$ ) corresponds to alkyl-stacking of  $\text{p-DTS}(\text{FBTTh}_2)_2$ . However, the scattering intensity remains low up to 25 s indicating that most of  $\text{p-DTS}(\text{FBTTh}_2)_2$  remains solvated by the bulk solvent at this early stage. This is followed by sharp increase in  $\text{p-DTS}(\text{FBTTh}_2)_2$  crystallization revealed by the sharp increase in the alkyl-stacking scattering intensity (**Figure 8.2d**) and the appearance of higher order reflections (namely  $X_{002}$  and  $X_{003}$ ) (**Figure 8.2c**). After bulk solvent evaporation, we observe saturation of  $\text{p-DTS}(\text{FBTTh}_2)_2$  crystallization around 40 s (**Figure 8.2c-d**). Notably, we don't observe the formation of LC phase unlike spin coating in which  $\text{p-DTS}(\text{FBTTh}_2)_2$  goes through vitrified LC phase before crystallization (**Figure 8.2c**). Furthermore, significant  $\text{p-DTS}(\text{FBTTh}_2)_2$  crystallization occurs in an environment saturated with the bulk solvent; at the moment of bulk solvent removal, the scattering intensity of  $\text{p-DTS}(\text{FBTTh}_2)_2$  alkyl-stacking was  $\sim 75\%$  of its value at the final solid-state (**Figure 8.2d**). On the other hand, for spin coating,  $\text{p-DTS}(\text{FBTTh}_2)_2$  is quenched into LC phase at the moment of CB removal and crystallization occurs afterwards. For wire-bar coated sample at RT, due to the slow drying kinetics,  $\text{p-DTS}(\text{FBTTh}_2)_2$  must have enough time for nucleation and growth to occur without going through the vitrified state. Moreover, the presence of solvent (CB) in the wet film provides the kinetics for  $\text{p-DTS}(\text{FBTTh}_2)_2$  crystallization which leads also to over-crystallization of  $\text{p-DTS}(\text{FBTTh}_2)_2$  (**Figure 8.2b**). In **Figure 8.2b**, we show line cuts of integrated scattering intensity versus  $q$  ( $\text{nm}^{-1}$ ) of wire-bar coated samples versus spin-coated reference sample. We have calculated the crystalline correlation length (CCL) and the relative crystallinity for the

samples (**Table 8.1**). Wire-bar coated sample at RT exhibits much higher CCL (~22.4 nm) than the spin coated sample (CCL~13.6 nm), indicating larger crystallites for RT wire-bar coated sample. Moreover, the relative crystallinity for RT wire-bar coated sample is more than three time higher than the spin coated samples. We recall that over-crystallization of p-DTS(FBTTh<sub>2</sub>)<sub>2</sub> occurs for spin coating samples when excessive amount of the additive DIO was used, as shown in chapter 6. We conclude that when p-DTS(FBTTh<sub>2</sub>)<sub>2</sub> crystallization occurs in an environment saturated with the solvents (either the bulk solvent or the additive solvent), over-crystallization of p-DTS(FBTTh<sub>2</sub>)<sub>2</sub> happens.

In order to accelerate the drying kinetics, we have performed wire-bar coating at elevated temperature (*ca.* 45 °C)(**Figure 8.2e-f**). Indeed, the drying time of the bulk solvent was significantly reduced to ~6.6 s, which is comparable to the drying time obtained by spin coating. However, this strategy failed to hinder the over-crystallization of p-DTS(FBTTh<sub>2</sub>)<sub>2</sub>. Again, we didn't observe LC phase on the route before crystallization. Similar to wire-bar coating at RT, significant crystallization occurs at the presence of the bulk solvent; crystallization period lasts from ~4.4 s to ~8.8 s whereas solvent scattering is observable up to 6.6 s. Wire-bar coating at 45 °C has resulted in slight reduction in CCL to 19 nm and relative crystallinity to 3.1 as compared to wire-bar coating at RT. However, these values still indicate much higher crystallinity for wire-bar coating samples than spin coating sample. We attribute the failure of wire-bar coating at 45 °C to hinder p-DTS(FBTTh<sub>2</sub>)<sub>2</sub> over-crystallization to the increase in the diffusion of p-

DTS(FBTTh<sub>2</sub>)<sub>2</sub> molecules at elevated temperatures that is expected to favor the crystal growth specially if the growth occurred in an environment saturated with a plasticizer (*ca.* CB).

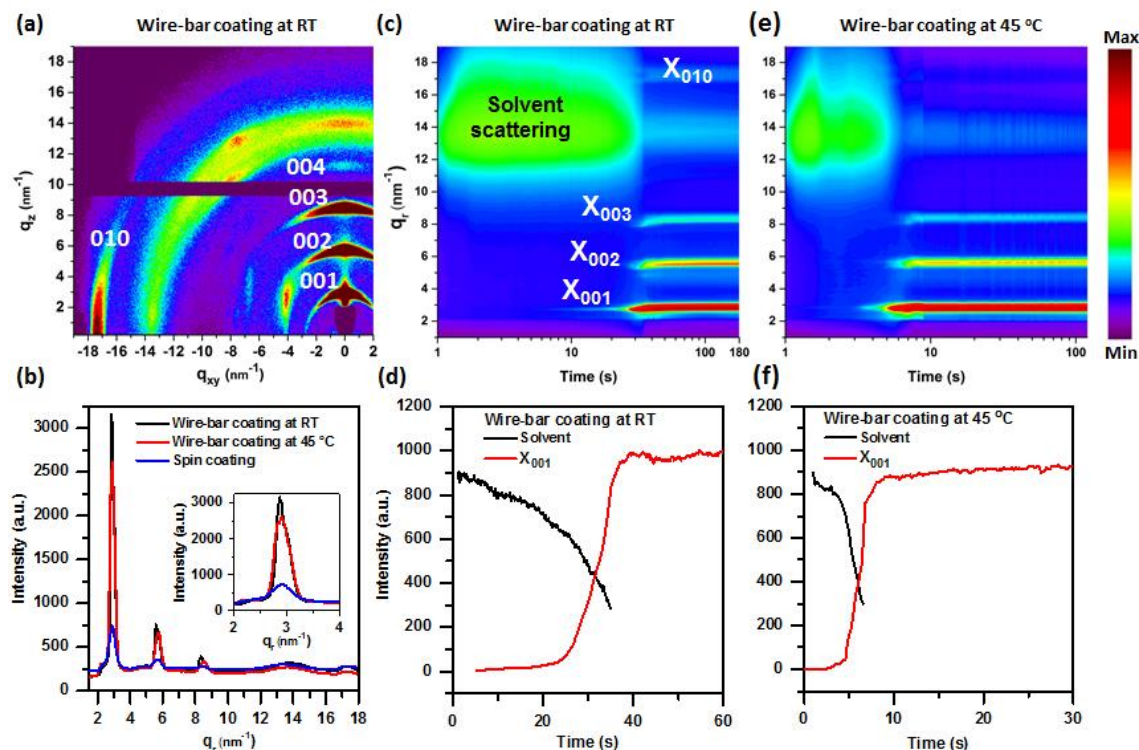


**Figure 8.2** (a) 2D GIWAXS image of p-DTS(FBTTh<sub>2</sub>)<sub>2</sub> : PC<sub>71</sub>BM film wire-bar coated from at room temperature. (b) Line cuts of integrated scattering intensity versus  $q$  ( $\text{nm}^{-1}$ ) of wire-bar coated samples at room temperature (black), at 45 °C (red) and spin-coated reference sample (blue). All samples were processed with identical DIO content; 21 % w/w (DIO/solutes). Inset of (b) shows zoomed-in plot highlighting scattering from p-DTS(FBTTh<sub>2</sub>)<sub>2</sub> alkyl-stacking peak (001). (c) & (e) 2D GIWAXS color plot (Integrated scattering intensity is shown in logarithmic color scale versus  $q$  ( $\text{nm}^{-1}$ ) and time(s));

measured *in situ* during wire-bar coating of p-DTS(FBTTh<sub>2</sub>)<sub>2</sub> : PC<sub>71</sub>BM from CB with 21 % w/w (DIO/solutes) at room temperature and at 45 °C, respectively. (d) & (f) Integrated scattering intensity of solvent scattering (black) and p-DTS(FBTTh<sub>2</sub>)<sub>2</sub> alkyl-stacking scattering ( $X_{001}$ ) (red) calculated from *in situ* GIWAXS in (c) & (d), respectively. The thickness of the wire-bar coated films was 120 +/- 10 nm.

**Table 8.1** Summary of the relative crystallinity and crystalline correlation length of p-DTS(FBTTh<sub>2</sub>)<sub>2</sub>, calculated from the alkyl-stacking peak (001)

	Relative crystallinity	FWHM <sub>(001)</sub> (nm <sup>-1</sup> )	CCL <sub>(001)</sub> (nm)
Spin coating	1	0.46	13.6
Wire-bar coating at RT	3.4 +/- 0.2	0.28	22.4
Wire-bar coating at 45 °C	3.1 +/- 0.2	0.33	19

Our hypothesis is that the observed crystallization behavior is mediated by crystal growth in an environment saturated with CB. However, DIO was used in the conditions discussed above. Therefore, we have investigated whether the same behavior is observable in the absence of DIO. Indeed, similar behavior was observed for additive-free wire-bar coated sample (**Figure 8.3**) confirming that this crystallization behavior is dominated by the presences of the CB during crystal growth.

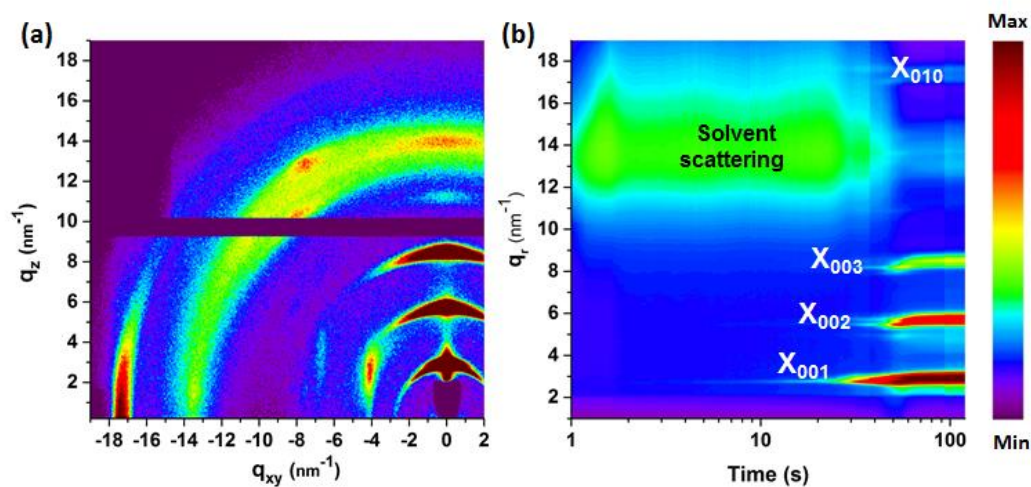


**Figure 8.3** (a) 2D GIWAXS image of p-DTS(FBTTh<sub>2</sub>)<sub>2</sub> : PC<sub>71</sub>BM film wire-bar coated from pure CB at room temperature. (b) 2D GIWAXS colour plot (Integrated scattering intensity is shown in logarithmic colour scale versus  $q$  (nm<sup>-1</sup>) and time(s)); measured *in situ* during wire-bar coating of p-DTS(FBTTh<sub>2</sub>)<sub>2</sub> : PC<sub>71</sub>BM from pure CB at room temperature.

## 8.4 Introducing modified wire-bar coating

### 8.4.1 Lessons to scalable fabrication of small-molecule solar cells

To achieve high performance solar cells with scalable manufacturing technique, we have to overcome the challenge of over-crystallization. This can be achieved by preventing the crystallization from happening in solvent-saturated environment, either the main solvent or the additive. For the bulk solvent CB, it has to be quickly evaporated and this also has to be done at low temperature (RT) enough to prevent significant crystallization. For the additive DIO, its content has to be maintained similar to the one

used in the optimized spin coated condition (21% w/w DIO/solutes). One more challenge is attaining uniformity of drying sufficiently for avoiding the formation of pinholes/cracks and coffee-ring effect. Non-uniform drying gives rise to gradient in solvent evaporation rate and consequently gradient in solute concentration. Under these circumstances, capillary forces arise in the wet film leading to random diffusion of the solutes across the wet film. Thus, pinholes or cracks can form where there is lack of the solute supply. Over-crystallization can also lead to the formation of pinholes or cracks when most of the solutes are consumed in crystal growth leading to run out of the solutes nearby. Therefore, we have looked for a solution that can handle both problems; the uniformity of drying as well as the over-crystallization. This was achieved by designing and implementing a new apparatus that can control the kinetics of drying as well as achieve sufficient uniformity of drying.

#### **8.4.2 New perspective on thin film coating: from spin coating towards modified wire-bar coating**

Spin coating is currently the most common lab-based technique used for fabrication of solution processed thin films. However, it is wasteful process and non-compatible with high throughput fabrication.<sup>[21]</sup> Let us first discuss the spin coating process aiming to attain guidelines to overcome its drawbacks. Spin coating can be partitioned into four different steps as summarized below (**Figure 8.4**)<sup>[200]</sup>:



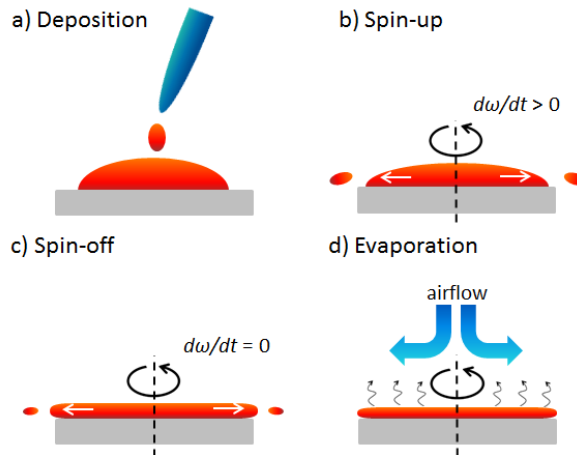


**Figure 8.4** Schematics represents the stages of spin coating process; namely (a) deposition, (b) spin-up, (c) spin-off and (d) evaporation.

1. **Deposition:** During this stage, solution is deposited onto static or rotating substrates from micro-syringes. Then, the substrate is accelerated to the desired speed while spreading of the solution occurs due to centrifugal force.
2. **Spin-up:** The second stage involves accelerating up the substrate to its final desired rotation speed and is characterized by aggressive fluid expulsion from the substrate due to rotation. During this early stage, inertia of the fluid driven by the accelerating substrate results in twisting motion of the fluid and the formation of spiral vortices leading to significant ejection of the ink out of the substrate.
3. **Spin-off (also called: stable fluid outflow):** This stage starts when the substrate is spinning at a constant rate and eventually the fluid is thin enough to be completely co-rotating with the substrate. This stage is characterized by gradual quite uniform fluid thinning while the fluid thinning behavior is mainly modulated by fluid viscous

forces. The fluid continues to flow uniformly outward, while continuous loss of the ink occurs through spinning off the ink from the edges of the substrate. Solvent evaporation occurs also during this step; however the thinning behavior is dominated by viscous flow.

- 4. Evaporation:** The fourth stage starts when the centrifugal out flow stops and consequently no further loss of the ink occurs. During this stage, the thinning behavior is dominated by solvent evaporation only. The evaporation rate is mediated by the difference in partial pressure of the ink species (volatiles) between the free surface of the ink layer and the bulk gas surrounding the ink at the liquid/vapor interface.

The primary drawback of spin coating arises from the initial steps, namely spin-up and spin-off, which involve ejection of the ink. The last step involves drying of the solution via an interaction of the ink with the surrounding environment (*ca.* air, dry  $N_2$ ). Airflow dynamics at the liquid/air interface during the evaporation step plays a decisive role on the film uniformity, one of the main benefits of spin coating. The evaporation mechanism during this step can be summarized as follows. Thin layer of the surrounding gas is spun with the substrate whereas the surrounding gas far from the substrate is much less mobile. Consequently, a gradient of the air speed further from the rotating substrate emerges leading to gradient in the partial pressure of the surrounding gas. This gradient in the partial pressure drives the evaporation of the volatiles.

Due to the drawback of the poor material usage in spin coating technique, several alternative techniques, such as wire-bar / knife coating, slot-die coating, were developed and used as replacement for spin coating due to their effective materials usage approaching 0% ink wastage. However, control of film drying after ink casting has been challenging, especially when it has unfavorable implications on the microstructure as observed in our system here. Since spin coating is known for delivering highly uniform films, we have chosen to implement its unique drying mechanism into scalable processing. Regardless of the benefits gained from substrate rotation in spin coating technique, such as uniform distribution of the ink, it is the main reason behind the material losses during the coating as discussed previously. Therefore, in order to attain effective material usage, it is essential to manage the uniformity of drying without substrate rotation. We designed a new apparatus that approaches this problem by implementing the drying mechanism of spin coating technique but without substrate rotation. The apparatus mimics the fluid dynamics on top of the substrate but avoids rotating the substrate thereby providing the advantage of curbing ink-loss and aiding film uniformity.

The new apparatus is composed of conventional wire-bar coating combined with an apparatus for film drying control, illustrated in **Figure 8.5**. The uniform distribution of the ink that is achieved at the initial steps of spin coating is managed by the alternative scalable techniques, such as wire-bar coating in our apparatus. After the ink is screened

via a high speed wire-bar coating, air is spun on the sample surface (adjustable air-substrate distance). Simply stated, instead of spinning the sample that involves ejection of the ink, the air (or inert gas) on top of the sample is spun after wet film is cast. This is done via applying vacuum or supplying an inert gas through a rotating slit on top of the sample.

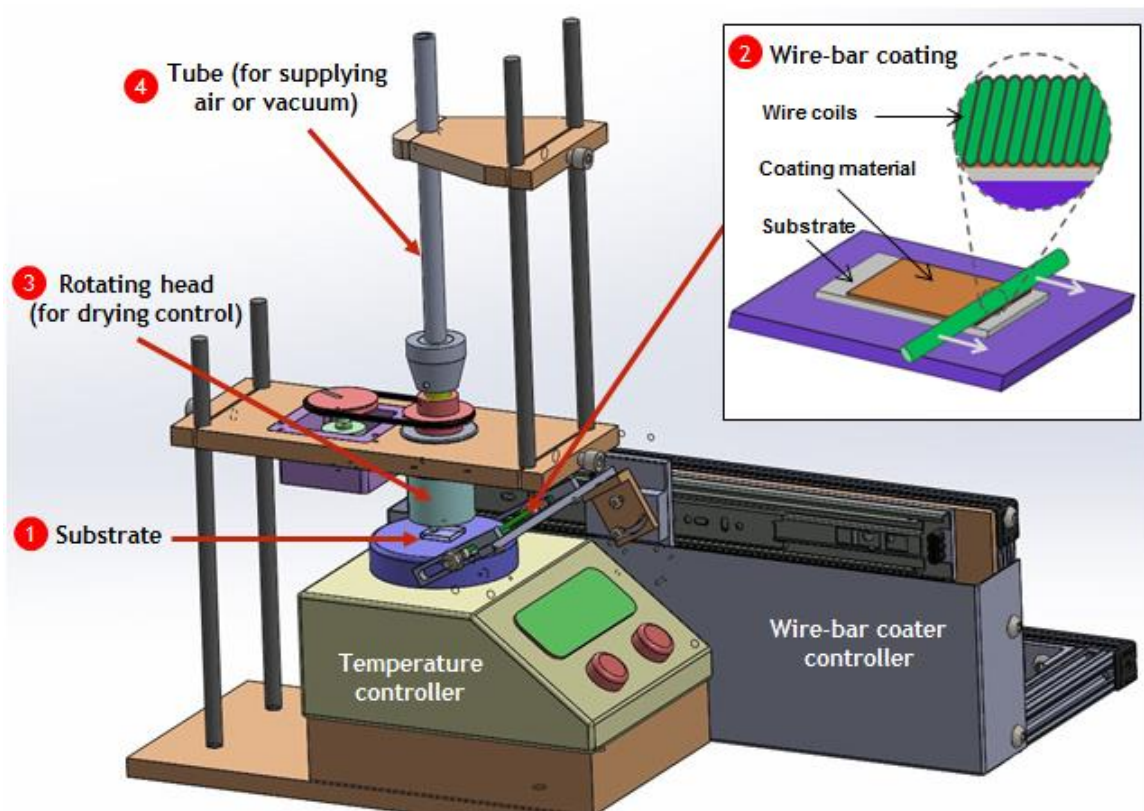


**Figure 8.5** Schematic of the apparatus for high-throughput and high-speed thin film coating. Substrate is placed on a temperature controller (1). Wire-bar coater is used to coat the solution on the substrate (2). Representation of the wire-bar coater is shown in the inset of the figure. Drying of the wet film is controlled by spinning the surrounding

gas on top of the wet film by supplying vacuum or drying gas through rotating slit in a cylindrical rotating head (3). Vacuum or drying gas is supplied via stationary tube (4).

#### **8.4.3 Film uniformity obtained by modified wire-bar coating versus spin coating**

To elucidate the effectiveness of the new apparatus in attaining film uniformity comparable with spin-cast samples, we have investigated the film uniformity of the coated samples by the new apparatus using polarized optical microscopy. We show POM images of spin coated and conventional wire-bar coated samples in **Figure 8.6a-b** for reference. Samples coated by conventional wire-bar coating appear non-uniform under POM (**Figure 8.6b**). We observe throughout the whole film the formation of randomly distributed large crystallites with size as high as hundreds of microns. Using the modified wire-bar coating setup, the formation of these large crystallites can be overcome as shown in **Figure 8.6c-d**. Notably, for samples coated by modified wire-bar coating at identical solute concentration as used for spin coating gives much thicker film (~2.5-3 times thicker films). We still observe large crystallites in thick films coated by modified wire-bar coating but their size and distribution are much less than the ones observed in conventional wire-bar coated samples (**Figure 8.6d**). However, apart from these crystallites, the film appears uniform elsewhere (**Figure 8.6c**). To attain thinner films with thickness comparable to spin coating sample, the solute concentration was diluted ~2.8 times (**Figure 8.6d**). For thinner films obtained by modified wire-bar coating,

the formation of the large crystallites was completely hindered and the films appear as uniform as the spin coated sample (**Figure 8.6d**).

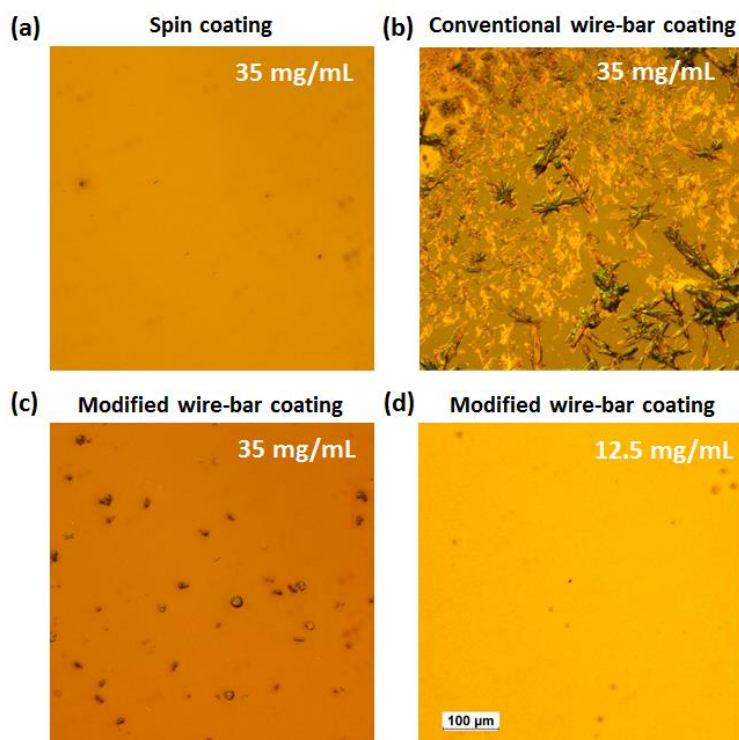


**Figure 8.6** POM images of p-DTS(FBTTh<sub>2</sub>)<sub>2</sub>:PC<sub>71</sub>BM films coated by: (a) spin coating (total solutes concentration = 35 mg/mL), (b) conventional wire-bar coating (total solutes concentration = 35 mg/mL), (c) modified wire-bar coating (total solutes concentration = 35 mg/mL), and (d) modified wire-bar coating ((total solutes concentration = 12.5 mg/mL). All samples were coated from CB with 21 % w/w (DIO/solutes). The thickness of the films in (a), (b), (c), and (d) is 100±5 nm, 290 ± 10 nm, 275 ± 10 nm, and 115±5 nm, respectively.

#### 8.4.4 Relative crystallinity of the modified wire-bar coated samples

To check the capability of the new apparatus in overcoming the over-crystallization of p-DTS(FBTTh<sub>2</sub>)<sub>2</sub> in the blend films, we have performed GIWAXS measurements on samples coated by the new apparatus and spin-cast reference samples. 2D GIWAXS plots of the dry films coated by the new apparatus and spin coating are shown in **Figure 8.7a-b**; line-cuts of the integrated scattering intensity are shown in **Figure 8.7c**. Both samples exhibit high order in the alkyl-stacking direction revealed by the appearance of alkyl-stacking reflections (001, 002 and 003) that appear as partial arc scattering but with more dominating scattering in the out-of-plane direction. The  $\pi$ - $\pi$  stacking scattering reveals preferred edge-on preferential texture for both samples. The relative crystallinity and CCL were calculated for both conditions; the calculation was done for three measurements per each condition, and reported in **Table 8.2**. The samples have average thicknesses of ~100-120 nm and ~100-105 nm for modified wire-bar coating and spin coating, respectively. Samples coated by both coating methods exhibit similar relative crystallinity and average crystal size (CCL ~13-14 nm) of p-DTS(FBTTh<sub>2</sub>)<sub>2</sub> crystallites. These results prove that the new apparatus is effective in overcoming p-DTS(FBTTh<sub>2</sub>)<sub>2</sub> over-crystallization.

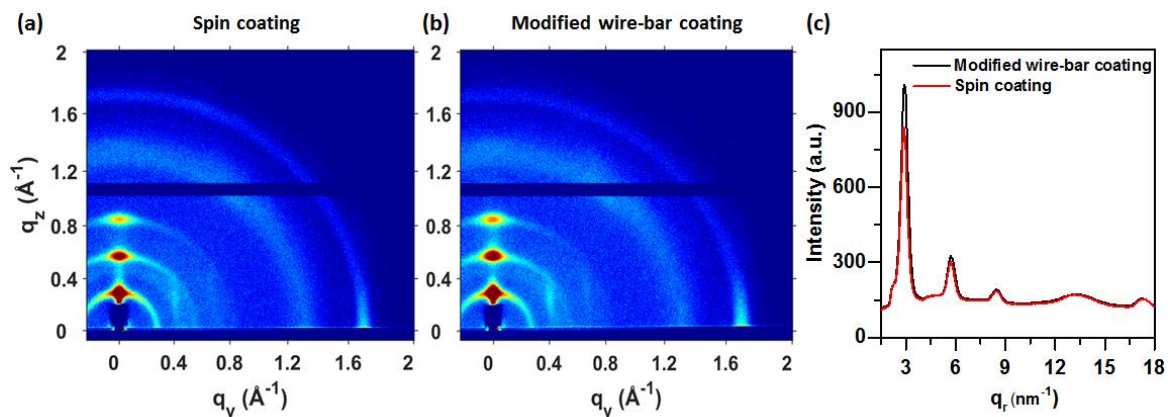


**Figure 8.7** 2D GIWAXS images of p-DTS(FBTTh<sub>2</sub>)<sub>2</sub>:PC<sub>71</sub>BM films coated by spin coating (a), and modified wire-bar coating (b). (c) Line cuts of integrated scattering intensity versus  $q$  (nm<sup>-1</sup>) of p-DTS(FBTTh<sub>2</sub>)<sub>2</sub>:PC<sub>71</sub>BM samples coated by modified wire-bar coating (black curve) and spin coated (red curve). Both samples were processed with identical DIO content; 21 % w/w (DIO/solutes).

**Table 8.2** Summary of the relative crystallinity and crystalline correlation length of p-DTS(FBTTh<sub>2</sub>)<sub>2</sub>, calculated from the alkyl-stacking peak (001)

Coating method	Relative crystallinity	FWHM <sub>(001)</sub> (nm <sup>-1</sup> )	CCL <sub>(001)</sub> (nm)
Spin coating	1	0.45+/-0.02	13.9+/-0.6
Modified wire-bar coating	1.12+/-0.08	0.47+/-0.02	13.4+/-0.6

The errors include standard deviation for three measurements.



#### 8.4.5 Solar cell devices fabrication by the modified wire-bar coating apparatus

We have fabricated solar cell devices using the modified wire-bar coating apparatus to test its applicability in attaining high performance solar cells. Solar cell device characteristics are shown in **Figure 8.8** and **Table 8.3**. For all the devices, the active layer was coated in air. The reference spin coated samples have shown slightly lower PCE (*ca.* ~ 6%) than samples coated in a nitrogen glove-box (PCE ~ 7.6%). Solar cells fabricated by modified wire-bar coating with identical solution formulation used for optimized spin coated condition have shown much lower PCE (~2 times less) than the spin-cast reference device. The samples suffered from much lower FF and also from a reduction in  $J_{sc}$ . We attribute this lower FF to the high thickness of the film (~ 2.7 times thicker than the spin-cast samples). Generally, in too thick organic photovoltaics, the photogenerated charges have to migrate larger distance before reaching the electrodes increasing the probability of the recombination losses on their way. Therefore, we have systematically reduced the thickness of the active layer by reducing the solute concentration. With lower thickness of the active layer, FF and  $J_{sc}$  get improved gradually leading to an increase in PCE. The best performance of the modified wire-bar coated devices was attained at a total solute concentration of 12.5 mg/mL which gives slightly thicker film (~118 nm) than the spin coated samples (~105 nm). The new wire-bar coated devices have slightly higher  $J_{sc}$  but lower FF resulting in slight improvement in the overall device performance. These results are promising and further improvements are expected if the devices are fabricated in controlled nitrogen

atmosphere. Overall, using the new apparatus, we could successfully attain similar, if not higher, performance than the reference spin-coated samples but with a scalable technique and with much lower materials consumption. Regardless of the success of the new apparatus in reproducing the solar cell devices performance obtained by spin coating, more work is needed to investigate the kinetics of film formation by the new apparatus.

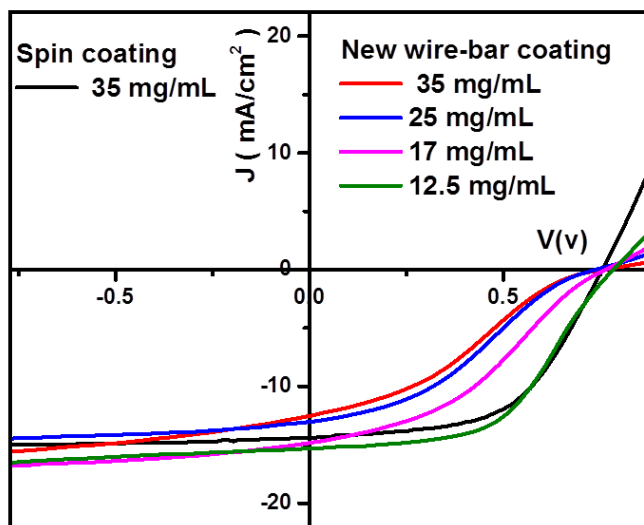


**Figure 8.8** Current density- Voltage (J-V) curves of solar cell devices fabricated from p-DTS(FBTTh<sub>2</sub>)<sub>2</sub>:PC<sub>71</sub>BM blends coated by spin coating with total solute concentration 35 mg/mL (black), new wire-bar coating at different concentrations; 35 mg/mL (red), 25 mg/mL (blue), 17 mg/mL (pink), and 12.5 mg/mL (green). All samples were coated in air from CB with 21 % w/w (DIO/solutes). Notably, fabricated solar cell devices in glove-box by spin coating have higher performance (PCE > 7%).

**Table 8.3** Device performance parameters of the solar cells fabricated from p-DTS(FBTTh<sub>2</sub>)<sub>2</sub>:PC<sub>71</sub>BM by spin coating versus the new wire-bar coating apparatus.

	Conc [mg/mL]	Thickness nm	Jsc [mA/cm <sup>2</sup> ]	Voc [mV]	FF [%]	PCE [%]
Spin coating	35	105	14.4	755	56	6.0
New wire-bar-coating	35	275	12.5	763	33	3.1
New wire-bar-coating	25	215	12.9	754	36	3.5
New wire-bar-coating	17	137	14.8	766	38	4.3
New wire-bar-coating	12.5	118	15.3	784	52	6.3

## 8.5 Conclusions

In conclusion, we have demonstrated a new capability of thin film coating that combines scalability of solar cell active layer coating with obtaining high performance solar cells comparable to the common lab-based coating method (*ca.* spin coating). We have shown that conventional wire-bar coating fails to deliver sufficient film uniformity and microstructure for obtaining high performance solar cell devices fabricated from p-DTS(FBTTh<sub>2</sub>)<sub>2</sub>:PC<sub>71</sub>BM blends. Through investigation of the crystallization behavior of p-DTS(FBTTh<sub>2</sub>)<sub>2</sub> *in situ* during conventional wire-bar coating, we have shown that p-DTS(FBTTh<sub>2</sub>)<sub>2</sub> crystallization occurs in an environment saturated with the main solvent, leading to p-DTS(FBTTh<sub>2</sub>)<sub>2</sub> over-crystallization in conventional wire-bar coated films. The latter can be responsible for the formation of cracks/pin holes in the conventional wire-

bar coated films by the depletion of the molecules that are consumed by crystal growth. To overcome the problems of film uniformity and donor over-crystallization, we have introduced a new apparatus that combines a drying mechanism, similar to spin coating, with a wire-bar coating. We have demonstrated that the new apparatus helps to overcome the over-crystallization in p-DTS(FBTTh<sub>2</sub>)<sub>2</sub>:PC<sub>71</sub>BM films and obtain film uniformity comparable to spin coated films. Using this new capability, we could successfully attain efficient solar cell devices on par with the ones fabricated by spin coating but with null material waste and scalable technique at high-speed coating compatible with industrial applications.

## Chapter 9

### Conclusions and Future Work

#### 9.1 Summary

In this dissertation, we have investigated, using state-of-the-art *in situ* characterization techniques, the mechanism of bulk heterojunction film formation during solution processing. In doing so, we have investigated the roles of processing methods (spin-coating vs wire-bar coating) and conditions (thinning and drying kinetics), type of conjugated material (small-molecule and polymer donors), and ink formulation (choice of solvent additives) in the formation behavior of the BHJ layer used in organic solar cells. Through in-depth investigation of the mechanisms of BHJ formation, we have demonstrated general concepts about the correlation between the processing conditions with the microstructure of the BHJ and the performance of the solar cell devices. Our findings have paved the way towards fabrication of small-molecule-based OPVs with high-throughput-compatible techniques while achieving performance parity. In this chapter, we summarize the conclusions of this dissertation and link our findings to the current and future challenges in the field of organic solar cells.

The main aspects that govern BHJ formation include thermodynamic aspects, such as the ease of crystallization/aggregation of the BHJ components, their mutual interactions and their interaction with the solvents used in solution processes, and include kinetic aspects related to the drying kinetics of the solvents in different processing conditions

and the time-evolution of the formulation during thinning and drying processes. In this dissertation, we have covered many of these aspects in a variety of BHJ systems in the hopes of providing general guidelines for the mechanisms of BHJ film formation by solution processing.

In chapter 4, we have demonstrated a new capability for monitoring the kinetics of thin film formation during solution processing by spin coating. We have utilized this capability to investigate the roles of solution aggregation state and the kinetics of film formation on the microstructure of organic semiconductor thin films, both for electronic and photovoltaic applications. The new experimental capability allowed, for the first time, to acquire time-resolved UV-vis absorption measurements during the spin-coating of organic semiconductor thin films. We have demonstrated the ability of this new technique to detect the evolution of the degree of solute aggregation during the spin coating from solution-ejection to solvent-evaporation-dominated thinning regimes, allowing detection of the onset, evolution, and end of thin film formation process. More precisely, we have shown that the presence of large differences in the degree of aggregation of the polymer P3HT in the solution results in small but detectable changes in the solid-state UV-vis absorption spectrum, however, this still leads to large morphological and microstructural differences. We have demonstrated that pre-aggregation of P3HT in marginal solution results in the formation of crystalline P3HT fibrils, leading to an enhancement on the carrier transport in P3HT thin films in the

context of thin film transistors. For organic photovoltaic applications, we have demonstrated how bulk heterojunction formation kinetics, controlled by varying spin coating conditions, impact the microstructure of the BHJ based on a P3HT-fullerene blend. We have shown that slower kinetics of thin film formation leads to an enhancement in the degree of polymer aggregation in the solid state, in terms of the fraction of polymer aggregates, and increased conjugation length within the aggregates. Although tuning the kinetics of thin film formation can be achieved by controlling the spin coating speed, it has implications on the solution ejection during the initial stages of spin coating, and hence the thickness of the dry film. Using this insight, we have shown that the duration of the film formation can be extended dramatically by interrupting the spin-coating process in the solvent-evaporation-dominated thinning regime, leading to significant enhancement in the degree of P3HT aggregation and crystalline P3HT fibrils formation, and improved P3HT-fullerene phase separation. This strategy has resulted in improved solar cell performance of P3HT-fullerene devices without requiring thermal annealing. Overall, our findings highlighted the importance of in situ monitoring of thin film formation and the implications of the kinetics of thin film formation on the microstructure of organic semiconductor thin films and how it impacts the relevant optoelectronics devices performance.

One of the main challenges in the OPV community is to design materials which can be processed by additive-free and annealing-free processing, however, there is still very

little knowledge about the design rules or guidelines needed to address this issue. In chapter 5, we have demonstrated, through investigation of the ease of crystallization of donor molecules, a generalized concept linking the thermodynamics and kinetics of donor crystallization and the processing routes needed for fabricating efficient BHJ solar cell devices. Our findings reveal the reason behind the need for solvent additives or alternatively thermal or solvent vapor annealing for attaining optimal performance. We have demonstrated that the presence of metastable phases on the route of crystallization is the main obstacle towards fabricating OPVs from a single processing step without the need for additives or annealing. More precisely, we have investigated the ease of crystallization/vitrification of three donor molecules, namely p-DTS(FBTTh<sub>2</sub>)<sub>2</sub>, p-SIDT(FBTTh<sub>2</sub>)<sub>2</sub> and X2, using flash-DSC at heating/cooling rates that mimic the thin film formation rate in solution processing. We have complemented these measurements by investigating the crystallization behavior during solution processing using *in situ* GIWAXS measurements. We have found that donor materials, such as p-DTS(FBTTh<sub>2</sub>)<sub>2</sub> and p-SIDT(FBTTh<sub>2</sub>)<sub>2</sub>, that can be easily vitrified, as detected by F-DSC, undergo a metastable intermediate state before crystallization, as confirmed by *in situ* GIWAXS. In such conditions, the donor crystallization and its phase separation from fullerene are inhibited at fast film formation conditions, such as spin coating, resulting in vitrified BHJ films. Hence, the solvent additives and/or annealing are needed to provide the kinetics for crystallization and phase separation. On the other hand, donor materials, such as X2, which crystallize with great ease, can phase separate from the fullerene without an aid.



Using this insight, we have demonstrated state-of-the-art 7.6% power conversion efficiency (PCE) small-molecule BHJ solar cells without using an additive or any post-process annealing steps. This enhanced understanding of the crystallization dynamics should help curb the challenges in achieving high performance solar cells via more facile and environmentally friendly manufacturing, a crucial topic for the organic photovoltaics community.

In chapter 6, we have provided more in-depth investigation of the mechanism of microstructure formation in additive-mediated processing for a BHJ system that involves the presence of donor metastable phase, namely p-DTS(FBTTh<sub>2</sub>)<sub>2</sub>: PC<sub>71</sub>BM. Through investigation of the interaction between the solvent additive DIO and the components of the BHJ system, we have demonstrated that this interaction depends on the phase in which the BHJ components are present. Our results revealed in-depth insights into the mechanism of microstructure formation in p-DTS(FBTTh<sub>2</sub>)<sub>2</sub>: PC<sub>71</sub>BM BHJ system. As expected, in the absence of additives, a highly quenched film is formed where p-DTS(FBTTh<sub>2</sub>)<sub>2</sub> is trapped into liquid crystalline phase and thus exhibits null phase separation from fullerene. On the other hand, in the presence of DIO in the initial formulation, a wet film, heavily swollen with DIO, is attained where DIO allows the diffusion of the molecules, and thus induces consequent structural and morphological changes. At first, DIO interacts with the p-DTS(FBTTh<sub>2</sub>)<sub>2</sub> liquid crystalline phase and promotes its transformation into a crystalline phase. We have found that the additive DIO affects not only the kinetics of liquid crystal to crystal phase transformation but also

the thermodynamics in the system by preferentially dissolving the LC phase more than the crystal phase. Our results reveal that solubility gradients are present in the wet film where PC<sub>71</sub>BM is the most soluble in DIO, followed by the mixed phase in which p-DTS(FBTTh<sub>2</sub>)<sub>2</sub> is present in a molecular state, then p-DTS(FBTTh<sub>2</sub>)<sub>2</sub> LC phase, while p-DTS(FBTTh<sub>2</sub>)<sub>2</sub> crystal phase is the least soluble. These solubility gradients drive the LC to crystal phase transformation and PC<sub>71</sub>BM separation where the p-DTS(FBTTh<sub>2</sub>)<sub>2</sub> crystallization front propagates at the expense of the LC phase and PC<sub>71</sub>BM diffuses out of the mixed phase. In that sense, DIO content is a critical factor in defining the degree of solvation and consequently diffusion of the molecular species in the wet film, which determines the extent of crystallization and phase separation. We found that, excessive additive content seem to increase growth rate at the expense of nucleation density resulting in excessive coarsening of donor and acceptor domains. These results highlight the importance of considering the interaction of the additives with different phases in BHJ, which has been less considered in the literature thus far.

In chapter 7, we have investigated a BHJ system in which the additives are used to reduce the donor-acceptor phase separation, unlike the previous example in which the additive promotes phase separation from initially quenched film. We have attained in-depth understanding of the mechanism of microstructure formation in PBDTTPD: PC<sub>71</sub>BM BHJ system, by monitoring the evolution of the donor crystallization and the acceptor aggregation during the BHJ film formation. Our findings reveal that the ability to form polymer fibril-networks before PC<sub>71</sub>BM segregation is the main requirement for

preventing large PC<sub>71</sub>BM phase separation. When casting the blends from pure CB, polymer crystallization is induced early in the solution, driven by the known low solubility of the high Mw PBDTTPD in CB. This early crystallites formation facilitates further crystallization during CB evaporation, which in turn constitutes polymer fibril-networks earlier than significant PC<sub>71</sub>BM aggregation. However, due to quick CB evaporation, the mesh size of fibril-networks, with large fibrils interspacing, is not sufficient to fully suppress the formation of large PC<sub>71</sub>BM domains. This insight revealed the need for an additive to further prevent PC<sub>71</sub>BM aggregation. We have investigated two additives, namely CN and OT that are known to solubilize PC<sub>71</sub>BM. We found that the additive CN helps to overcome the formation of PC<sub>71</sub>BM large aggregation but OT fails. In situ investigations of the BHJ formation reveal that CN delays the polymer crystallization but promotes slow and steady crystallization for prolonged time, resulting in an enhancement in the fibril-networks formation. At the same time, CN keeps PC<sub>71</sub>BM solvated. The prolonged crystallization, driven by CN slow evaporation, increases the number and size of the polymer fibrils, reducing the interspacing between the fibril-networks which inhibits PC<sub>71</sub>BM large segregation. On the other hand, the additive OT significantly hinders the polymer crystallization as long as it is present in the wet film, resulting in severe segregation of PC<sub>71</sub>BM before the formation of fibril-networks. Notably, the proposed mechanism in the additive-free case resembles the mechanism reported for other polymer–fullerene BHJ systems in which an additive is used to induce earlier crystallization of the polymer. However, herein, for the pure CB case, the early

crystallization is induced by the low solubility of the high Mw PBDTPD in CB. On the other hand, CN acts by a different mechanism that involves delayed and prolonged polymer crystallization. Overall, all mechanisms agree on preventing PC<sub>71</sub>BM segregation till sufficient fibril-networks formation.

In chapter 8, we have demonstrated a new apparatus for thin film coating combining attaining high performance solar cells with scalable coating of BHJ active layer. We have found that scalable techniques, such as conventional wire-bar and blade-coating, failed to deliver the appropriate microstructure for high performance solar cell devices fabricated from p-DTS(FBTTh<sub>2</sub>)<sub>2</sub>:PC<sub>71</sub>BM blends. Our results reveal that the over-crystallization of the donor p-DTS(FBTTh<sub>2</sub>)<sub>2</sub> and/or the formation of cracks/pinholes are the main obstacles. Through *in situ* investigations of the crystallization behavior, we have demonstrated the reason behind p-DTS(FBTTh<sub>2</sub>)<sub>2</sub> over-crystallization in conventional wire-bar coated films as crystallization mediated by CB-saturated environment. The over-crystallization and the non-uniformity of drying in the conventional wire-bar coating are believed to be responsible for the formation of cracks/pinholes by the depletion of the molecules that are consumed by crystal growth. The new apparatus handles these problems by implementing a drying mechanism, similar to spin coating, into a wire-bar coating. Truly, the new apparatus helps to obtain film uniformity comparable to spin coated films and overcome the donor over-crystallization. Finally, we have demonstrated the effectiveness of this new capability in

obtaining efficient solar cell devices but with high-throughput compatible technique. Overall, we believe that this new capability should pave the way for bridging the performance gap between lab-based OPVs fabrication and scalable manufacturing.

## 9.2 Future work

While we have investigated the mechanism of film formation of various BHJ systems by monitoring aggregation/crystallization of BHJ components using mainly UV-vis absorption and GIWAXS measurements, these techniques are limited to materials that exhibit detectable change in absorption characteristics and crystalline behavior during thin film formation. Many modern donor systems exhibit null change in absorption characteristics during thin film formation and others appear to exhibit no crystalline order, limiting the investigation of the film formation in these systems by the techniques proposed herein. Therefore, there is need for developing new *in situ* characterization metrologies suitable for these systems. For instance, Raman spectroscopy and photoluminescence have already been implemented during annealing of BHJ films; however, no efforts of their implementation during solution processing by spin coating were reported. Moreover, all the studied systems, herein, are binary systems of donor-fullerene blends. The mechanisms of film formation are expected to be more complex in ternary systems, requiring more efforts to reveal the mechanism of film formation in these systems. Moreover, replacing the fullerene with non-fullerene acceptors is expected to have implications on the mechanisms of film formation.<sup>[58]</sup> Luckily, the non-

fullerene acceptor materials are designed to contribute to the absorption and their absorption characteristics exhibit detectable changes with aggregation, and some of them are crystalline. Thus, the used techniques and methodology in this study should contribute toward understanding the mechanisms of BHJ formation made of these materials.

On the topic of scalability of solar cell fabrication, we have demonstrated in chapter 8 a successful example of a scalable coated BHJ system with good efficiency. However, this process involved the use of halogenated toxic additives. More efforts need to be made for materials systems that can be processed in toxic additive-free formulations. Regardless of the success of the new apparatus in attaining device performance parity with spin coating, investigation of the actual film formation is needed to fully understand the mechanism of film formation involved in this technique. Moreover, the applicability of this technique in other BHJ systems should be investigated. For instance, there are efforts in the community to develop materials that can be processed from green solvents.<sup>[100]</sup> Such materials are expected to be the best candidates for scalable manufacturing and the methods demonstrated and used in this dissertation should continue to contribute to understanding, controlling and scaling up the processing of BHJ layers.

**BIBLIOGRAPHY**

- [1] C. Battaglia, A. Cuevas, S. De Wolf, *Energy Environ. Sci.* **2016**, *9*, 1552.
- [2] E. Alsema, M. J. de Wild, E. A. Alsema, N. Jungbluth, *MRS Proc.* **2005**, *895*, 895.
- [3] V. Fthenakis, *Renew. Sustain. Energy Rev.* **2009**, *13*, 2746.
- [4] K. G. Reddy, T. G. Deepak, G. S. Anjusree, S. Thomas, S. Vadukumpully, K. R. V. Subramanian, S. V. Nair, A. S. Nair, *Phys. Chem. Chem. Phys.* **2014**, *16*, 6838.
- [5] Z. M. Beiley, M. G. Christoforo, P. Gratia, A. R. Bowring, P. Eberspacher, G. Y. Margulis, C. Cabanetos, P. M. Beaujuge, A. Salleo, M. D. McGehee, *Adv. Mater.* **2013**, *25*, 7020.
- [6] Y. Huang, E. J. Kramer, A. J. Heeger, G. C. Bazan, *Chem. Rev.* **2014**, *114*, 7006.
- [7] J. E. Coughlin, Z. B. Henson, G. C. Welch, G. C. Bazan, *Acc. Chem. Res.* **2014**, *47*, 257.
- [8] K. M. Coakley, M. D. McGehee, *Chem. Mater.* **2004**, *16*, 4533.
- [9] A. Mishra, P. Bäuerle, *Angew. Chemie - Int. Ed.* **2012**, *51*, 2020.
- [10] N.-G. Park, *Mater. Today* **2015**, *18*, 65.
- [11] B. Li, L. Wang, B. Kang, P. Wang, Y. Qiu, *Sol. Energy Mater. Sol. Cells* **2006**, *90*, 549.
- [12] J. Duan, H. Zhang, Q. Tang, B. He, L. Yu, *J. Mater. Chem. A* **2015**, *3*, 17497.
- [13] S. Torabi, F. Jahani, I. Van Severen, C. Kanimozhi, S. Patil, R. W. A. Havenith, R. C. Chiechi, L. Lutsen, D. J. M. Vanderzande, T. J. Cleij, J. C. Hummelen, L. J. A. Koster, *Adv. Funct. Mater.* **2015**, *25*, 150.
- [14] S. Gélinas, O. Paré-Labrosse, C. N. Brosseau, S. Albert-Seifried, C. R. McNeill, K. R. Kirov, I. A. Howard, R. Leonelli, R. H. Friend, C. Silva, *J. Phys. Chem. C* **2011**, *115*, 7114.
- [15] S. R. Forrest, E. I. Haskal, P. E. Burrows, *Mater. Res. Soc. Symp. - Proc.* **1995**, *392*, 77.

- [16] C. J. Bardeen, *Annu. Rev. Phys. Chem.* **2014**, *65*, 127.
- [17] R. R. Lunt, J. B. Benziger, S. R. Forrest, *Adv. Mater.* **2010**, *22*, 1233.
- [18] S. Dimitrov, B. Schroeder, C. Nielsen, H. Bronstein, Z. Fei, I. McCulloch, M. Heeney, J. Durrant, *Polymers.* **2016**, *8*, 14.
- [19] S. D. Collins, C. M. Proctor, N. A. Ran, T.-Q. Nguyen, *Adv. Energy Mater.* **2016**, *6*, 1501721.
- [20] S. M. Tuladhar, M. Azzouzi, F. Delval, J. Yao, A. A. Y. Guilbert, T. Kirchartz, N. F. Montcada, R. Dominguez, F. Langa, E. Palomares, J. Nelson, *ACS Energy Lett.* **2016**, *1*, 302.
- [21] F. C. Krebs, *Sol. Energy Mater. Sol. Cells* **2009**, *93*, 394.
- [22] K. W. Chou, B. Yan, R. Li, E. Q. Li, K. Zhao, D. H. Anjum, S. Alvarez, R. Gassaway, A. Biocca, S. T. Thoroddsen, A. Hexemer, A. Amassian, *Adv. Mater.* **2013**, *25*, 1923.
- [23] F. Liu, Y. Gu, J. W. Jung, W. H. Jo, T. P. Russell, *J. Polym. Sci. Part B Polym. Phys.* **2012**, *50*, 1018.
- [24] J. J. van Franeker, M. Turbiez, W. Li, M. M. Wienk, R. A. J. Janssen, *Nat. Commun.* **2015**, *6*, 6229.
- [25] S. Y. Heriot, R. A. L. Jones, *Nat. Mater.* **2005**, *4*, 782.
- [26] T. Wang, A. D. F. Dunbar, P. a. Staniec, A. J. Pearson, P. E. Hopkinson, J. E. MacDonald, S. Lilliu, C. Pizzey, N. J. Terrill, A. M. Donald, A. J. Ryan, R. a. L. Jones, D. G. Lidzey, *Soft Matter* **2010**, *6*, 4128.
- [27] F. C. Spano, C. Silva, *Annu. Rev. Phys. Chem.* **2014**, *65*, 477.
- [28] F. C. Spano, *J. Chem. Phys.* **2005**, *122*, 234701.
- [29] J. Peet, N. S. Cho, S. K. Lee, G. C. Bazan, *Macromolecules* **2008**, *41*, 8655.
- [30] S. Miller, G. Fanchini, Y.-Y. Lin, C. Li, C.-W. Chen, W.-F. Su, M. Chhowalla, *J. Mater. Chem.* **2008**, *18*, 306.



- [31] P. Veerender, V. Saxena, A. K. Chauhan, S. P. Koiry, P. Jha, A. Gusain, S. Choudhury, D. K. Aswal, S. K. Gupta, *Sol. Energy Mater. Sol. Cells* **2014**, *120*, 526.
- [32] G. Yu, J. Gao, J. C. Hummelen, F. Wudl, A. J. Heeger, *Science*. **1995**, *270*.
- [33] A. J. Heeger, *J. Phys. Chem. B* **2001**, *105*, 8475.
- [34] B. Yang, Y. Yi, C.-R. Zhang, S. G. Aziz, V. Coropceanu, J.-L. Brédas, *J. Phys. Chem. C* **2014**, *118*, 27648.
- [35] G. O. Ngongang Ndjawa, K. R. Graham, R. Li, S. M. Conron, P. Erwin, K. W. Chou, G. F. Burkhard, K. Zhao, E. T. Hoke, M. E. Thompson, M. D. McGehee, A. Amassian, *Chem. Mater.* **2015**, *27*, 5597.
- [36] K. R. Graham, G. O. N. Ndjawa, S. M. Conron, R. Munir, K. Vandewal, J. J. Chen, S. Sweetnam, M. E. Thompson, A. Salleo, M. D. McGehee, A. Amassian, *Adv. Energy Mater.* **2016**, 1601211.
- [37] J. Clark, C. Silva, R. Friend, F. Spano, *Phys. Rev. Lett.* **2007**, *98*, 206406.
- [38] R. Noriega, J. Rivnay, K. Vandewal, F. P. V Koch, N. Stingelin, P. Smith, M. F. Toney, A. Salleo, *Nat. Mater.* **2013**, *12*, 1038.
- [39] K. Zhao, H. U. Khan, R. Li, Y. Su, A. Amassian, *Adv. Funct. Mater.* **2013**, *23*, 6024.
- [40] K. H. Lam, T. R. B. Foong, Z. E. Ooi, J. Zhang, A. C. Grimsdale, Y. M. Lam, *ACS Appl. Mater. Interfaces* **2013**, *5*, 13265.
- [41] H. Chung, Y. Diao, *J. Mater. Chem. C* **2016**, *13*, 773.
- [42] Y. Yuan, G. Giri, A. L. Ayzner, A. P. Zoombelt, S. C. B. Mannsfeld, J. Chen, D. Nordlund, M. F. Toney, J. Huang, Z. Bao, *Nat. Commun.* **2014**, *5*, 3327.
- [43] B. Kan, M. Li, Q. Zhang, F. Liu, X. Wan, Y. Wang, W. Ni, G. Long, X. Yang, H. Feng, Y. Zuo, M. Zhang, F. Huang, Y. Cao, T. P. Russell, Y. Chen, *J. Am. Chem. Soc.* **2015**, *137*, 3886.
- [44] K. R. Graham, C. Cabanetos, J. P. Jahnke, M. N. Idso, A. El Labban, G. O. Ngongang

- Ndjawa, T. Heumueller, K. Vandewal, A. Salleo, B. F. Chmelka, A. Amassian, P. M. Beaujuge, M. D. McGehee, *J. Am. Chem. Soc.* **2014**, *136*, 9608.
- [45] J. E. Donaghey, A. Armin, P. L. Burn, P. Meredith, *Chem. Commun.* **2015**, *51*, 14115.
- [46] X. Liu, K. S. Jeong, B. P. Williams, K. Vakhshouri, C. Guo, K. Han, E. D. Gomez, Q. Wang, J. B. Asbury, *J. Phys. Chem. B* **2013**, *117*, 15866.
- [47] O. V. Mikhnenko, H. Azimi, M. Scharber, M. Morana, P. W. M. Blom, M. A. Loi, *Energy Environ. Sci.* **2012**, *5*, 6960.
- [48] B. Michl, J. Benick, A. Richter, M. Bivour, J. Yong, R. Steeman, M. C. Schubert, S. W. Glunz, *Energy Procedia* **2013**, *33*, 41.
- [49] O. V. Mikhnenko, H. Azimi, M. Scharber, M. Morana, P. W. M. Blom, M. A. Loi, *Energy Environ. Sci.* **2012**, *5*, 6960.
- [50] B. C. Schroeder, Z. Li, M. a. Brady, G. C. Faria, R. S. Ashraf, C. J. Takacs, J. S. Cowart, D. T. Duong, K. H. Chiu, C.-H. Tan, J. T. Cabral, A. Salleo, M. L. Chabinyk, J. R. Durrant, I. McCulloch, *Angew. Chemie Int. Ed.* **2014**, *53*, 12870.
- [51] S. Honda, H. Ohkita, H. Benten, S. Ito, *Chem. Commun.* **2010**, *46*, 6596.
- [52] T. Ameri, P. Khoram, J. Min, C. J. Brabec, *Adv. Mater.* **2013**, *25*, 4245.
- [53] Q. An, F. Zhang, J. Zhang, W. Tang, Z. Deng, B. Hu, *Energy Environ. Sci.* **2016**, *9*, 281.
- [54] H. K. Kodali, B. Ganapathysubramanian, *Sol. Energy Mater. Sol. Cells* **2013**, *111*, 66.
- [55] G. Dennler, M. C. Scharber, C. J. Brabec, *Adv. Mater.* **2009**, *21*, 1323.
- [56] A. C. Mayer, S. R. Scully, B. E. Hardin, M. W. Rowell, M. D. McGehee, *Mater. Today* **2007**, *10*, 28.
- [57] T. Xu, L. Yu, *Mater. Today* **2014**, *17*, 11.
- [58] Y. Lin, X. Zhan, *Mater. Horizons* **2014**, *1*, 470.

- [59] C. Zhan, X. Zhang, J. Yao, *RSC Adv.* **2015**, *5*, 93002.
- [60] S. Holliday, R. S. Ashraf, A. Wadsworth, D. Baran, S. A. Yousaf, C. B. Nielsen, C.-H. Tan, S. D. Dimitrov, Z. Shang, N. Gasparini, M. Alamoudi, F. Laquai, C. J. Brabec, A. Salleo, J. R. Durrant, I. McCulloch, *Nat. Commun.* **2016**, *7*, 11585.
- [61] A. Sharenko, C. M. Proctor, T. S. van der Poll, Z. B. Henson, T.-Q. Nguyen, G. C. Bazan, *Adv. Mater.* **2013**, *25*, 4403.
- [62] Q.-D. Ou, Y.-Q. Li, J.-X. Tang, *Adv. Sci.* **2016**, *3*, 1600123.
- [63] D. Bartesaghi, I. del C. Pérez, J. Kniepert, S. Roland, M. Turbiez, D. Neher, L. J. A. Koster, *Nat. Commun.* **2015**, *6*, 7083.
- [64] B. Huang, J. A. Amonoo, A. Li, X. C. Chen, P. F. Green, *J. Phys. Chem. C* **2014**, *118*, 3968.
- [65] S. Venkatesan, N. Adhikari, J. Chen, E. C. Ngo, A. Dubey, D. W. Galipeau, Q. Qiao, *Nanoscale* **2014**, *6*, 1011.
- [66] T. M. Burke, M. D. McGehee, *Adv. Mater.* **2014**, *26*, 1923.
- [67] K. Vandewal, S. Albrecht, E. T. Hoke, K. R. Graham, J. Widmer, J. D. Douglas, M. Schubert, W. R. Mateker, J. T. Bloking, G. F. Burkhard, A. Sellinger, J. M. J. Fréchet, A. Amassian, M. K. Riede, M. D. McGehee, D. Neher, A. Salleo, *Nat. Mater.* **2013**, *13*, 63.
- [68] G. Grancini, M. Maiuri, D. Fazzi, A. Petrozza, H.-J. Egelhaaf, D. Brida, G. Cerullo, G. Lanzani, *Nat. Mater.* **2012**, *12*, 29.
- [69] B. P. Lyons, N. Clarke, C. Groves, *Energy Environ. Sci.* **2012**, *5*, 7657.
- [70] B. Walker, A. Tamayo, D. T. Duong, X.-D. Dang, C. Kim, J. Granstrom, T.-Q. Nguyen, *Adv. Energy Mater.* **2011**, *1*, 221.
- [71] J. J. van Franeker, G. H. L. Heintges, C. Schaefer, G. Portale, W. Li, M. M. Wienk, P. van der Schoot, R. A. J. Janssen, *J. Am. Chem. Soc.* **2015**, *137*, 11783.
- [72] U. Vongsaysy, D. M. Bassani, L. Servant, B. Pavageau, G. Wantz, H. Aziz, *J. Photonics*

*Energy* **2014**, *4*, 40998.

- [73] D. T. Duong, B. Walker, J. Lin, C. Kim, J. Love, B. Purushothaman, J. E. Anthony, T.-Q. Nguyen, *J. Polym. Sci. Part B Polym. Phys.* **2012**, *50*, 1405.
- [74] H. Hoppe, T. Glatzel, M. Niggemann, W. Schwinger, F. Schaeffler, A. Hinsch, M. C. Lux-Steiner, N. S. Sariciftci, *Thin Solid Films* **2006**, *511*, 587.
- [75] S. E. Shaheen, C. J. Brabec, N. S. Sariciftci, F. Padinger, T. Fromherz, J. C. Hummelen, *Appl. Phys. Lett.* **2001**, *78*, 841.
- [76] M. A. Ruderer, S. Guo, R. Meier, H.-Y. Chiang, V. Körstgens, J. Wiedersich, J. Perlich, S. V. Roth, P. Müller-Buschbaum, *Adv. Funct. Mater.* **2011**, *21*, 3382.
- [77] S. Beaupré, M. Leclerc, *J. Mater. Chem. A* **2013**, *1*, 11097.
- [78] S. H. Park, A. Roy, S. Beaupré, S. Cho, N. Coates, J. S. Moon, D. Moses, M. Leclerc, K. Lee, A. J. Heeger, *Nat. Photonics* **2009**, *3*, 297.
- [79] P.-K. Shin, P. Kumar, A. Kumar, S. Kannappan, S. Ochiai, P.-K. Shin, P. Kumar, A. Kumar, S. Kannappan, S. Ochiai, *Int. J. Photoenergy* **2014**, *2014*, 1.
- [80] M. T. Dang, G. Wantz, H. Bejbouji, M. Urien, O. J. Dautel, L. Vignau, L. Hirsch, *Sol. Energy Mater. Sol. Cells* **2011**, *95*, 3408.
- [81] F. S. U. Fischer, K. Tremel, A.-K. Saur, S. Link, N. Kayunkid, M. Brinkmann, D. Herrero-Carvajal, J. T. L. Navarrete, M. C. R. Delgado, S. Ludwigs, *Macromolecules* **2013**, *46*, 4924.
- [82] S. Guo, E. M. Herzig, A. Naumann, G. Tainter, J. Perlich, P. Müller-Buschbaum, *J. Phys. Chem. B* **2014**, *118*, 344.
- [83] D. Chen, A. Nakahara, D. Wei, D. Nordlund, T. P. Russell, *Nano Lett.* **2011**, *11*, 561.
- [84] V. D. Mihailetschi, H. X. Xie, B. de Boer, L. J. A. Koster, P. W. M. Blom, V. D. Mihailetschi, H. Xie, *Adv. Funct. Mater.* **2006**, *16*, 699.
- [85] W. Ma, C. Yang, X. Gong, K. Lee, A. J. Heeger, *Adv. Funct. Mater.* **2005**, *15*, 1617.

- [86] Z. Xu, L.-M. Chen, G. Yang, C.-H. Huang, J. Hou, Y. Wu, G. Li, C.-S. Hsu, Y. Yang, *Adv. Funct. Mater.* **2009**, *19*, 1227.
- [87] D. S. Germack, C. K. Chan, R. J. Kline, D. A. Fischer, D. J. Gundlach, M. F. Toney, L. J. Richter, D. M. DeLongchamp, *Macromolecules* **2010**, *43*, 3828.
- [88] M. Campoy-Quiles, T. Ferenczi, T. Agostinelli, P. G. Etchegoin, Y. Kim, T. D. Anthopoulos, P. N. Stavrinou, D. D. C. Bradley, J. Nelson, *Nat. Mater.* **2008**, *7*, 158.
- [89] J. Hou, H.-Y. Chen, S. Zhang, G. Li, Y. Yang, *J. Am. Chem. Soc.* **2008**, *130*, 16144.
- [90] H.-Y. Chen, J. Hou, A. E. Hayden, H. Yang, K. N. Houk, Y. Yang, *Adv. Mater.* **2010**, *22*, 371.
- [91] M. C. Scharber, M. Koppe, J. Gao, F. Cordella, M. A. Loi, P. Denk, M. Morana, H.-J. Egelhaaf, K. Forberich, G. Dennler, R. Gaudiana, D. Waller, Z. Zhu, X. Shi, C. J. Brabec, *Adv. Mater.* **2010**, *22*, 367.
- [92] H. Lu, B. Akgun, T. P. Russell, *Adv. Energy Mater.* **2011**, *1*, 870.
- [93] Q. Zhang, B. Kan, F. Liu, G. Long, X. Wan, X. Chen, Y. Zuo, W. Ni, H. Zhang, M. Li, Z. Hu, F. Huang, Y. Cao, Z. Liang, M. Zhang, T. P. Russell, Y. Chen, *Nat. Photonics* **2014**, *9*, 35.
- [94] J. Jo, S.-I. Na, S.-S. Kim, T.-W. Lee, Y. Chung, S.-J. Kang, D. Vak, D.-Y. Kim, *Adv. Funct. Mater.* **2009**, *19*, 2398.
- [95] S. S. van Bavel, E. Sourty, G. de With, J. Loos, *Nano Lett.* **2009**, *9*, 507.
- [96] J. H. Park, J. S. Kim, J. H. Lee, W. H. Lee, K. Cho, *J. Phys. Chem. C* **2009**, *113*, 17579.
- [97] Y. Zhao, Z. Xie, Y. Qu, Y. Geng, L. Wang, *Appl. Phys. Lett.* **2007**, *90*, 43504.
- [98] K. Sun, Z. Xiao, S. Lu, W. Zajaczkowski, W. Pisula, E. Hanssen, J. M. White, R. M. Williamson, J. Subbiah, J. Ouyang, A. B. Holmes, W. W. H. Wong, D. J. Jones, *Nat. Commun.* **2015**, *6*, 1.
- [99] H.-C. Liao, C.-C. Ho, C.-Y. Chang, M.-H. Jao, S. B. Darling, W.-F. Su, *Mater. Today* **2013**, *16*, 326.

- [100] S. Zhang, L. Ye, H. Zhang, J. Hou, *Mater. Today* **2016**, *19*, 533.
- [101] C. M. Hansen, *Hansen Solubility Parameters : A User's Handbook*, CRC Press, **2007**.
- [102] X. Liu, S. Huettner, Z. Rong, M. Sommer, R. H. Friend, *Adv. Mater.* **2012**, *24*, 669.
- [103] K. R. Graham, P. M. Wieruszewski, R. Stalder, M. J. Hartel, J. Mei, F. So, J. R. Reynolds, *Adv. Funct. Mater.* **2012**, *22*, 4801.
- [104] H.-Y. Chen, H. Yang, G. Yang, S. Sista, R. Zadoyan, G. Li, Y. Yang, *J. Phys. Chem. C* **2009**, *113*, 7946.
- [105] T. Salim, L. H. Wong, B. Bräuer, R. Kukreja, Y. L. Foo, Z. Bao, Y. M. Lam, *J. Mater. Chem.* **2011**, *21*, 242.
- [106] Y. Sun, C. Cui, H. Wang, Y. Li, *Adv. Energy Mater.* **2011**, *1*, 1058.
- [107] G. Ren, E. Ahmed, S. A. Jenekhe, *Adv. Energy Mater.* **2011**, *1*, 946.
- [108] A. J. Moulé, K. Meerholz, *Adv. Mater.* **2008**, *20*, 240.
- [109] J. Yuan, Z. Zhai, H. Dong, J. Li, Z. Jiang, Y. Li, W. Ma, *Adv. Funct. Mater.* **2013**, *23*, 885.
- [110] H.-C. Liao, C.-S. Tsao, Y.-T. Shao, S.-Y. Chang, Y.-C. Huang, C.-M. Chuang, T.-H. Lin, C.-Y. Chen, C.-J. Su, U.-S. Jeng, Y.-F. Chen, W.-F. Su, *Energy Environ. Sci.* **2013**, *6*, 1938.
- [111] J. K. Lee, W. L. Ma, C. J. Brabec, J. Yuen, J. S. Moon, J. Y. Kim, K. Lee, G. C. Bazan, A. J. Heeger, *J. Am. Chem. Soc.* **2008**, *130*, 3619.
- [112] Y. Liang, Z. Xu, J. Xia, S.-T. Tsai, Y. Wu, G. Li, C. Ray, L. Yu, *Adv. Mater.* **2010**, *22*, E135.
- [113] J. S. Moon, C. J. Takacs, S. Cho, R. C. Coffin, H. Kim, G. C. Bazan, A. J. Heeger, *Nano Lett.* **2010**, *10*, 4005.
- [114] S. J. Lou, J. M. Szarko, T. Xu, L. Yu, T. J. Marks, L. X. Chen, *J. Am. Chem. Soc.* **2011**, *133*, 20661.
- [115] J. A. Bartelt, J. D. Douglas, W. R. Mateker, A. El Labban, C. J. Tassone, M. F. Toney, J. M. J.

- Fréchet, P. M. Beaujuge, M. D. McGehee, *Adv. Energy Mater.* **2014**, *4*, 1.
- [116] B. A. Collins, Z. Li, J. R. Tumbleston, E. Gann, C. R. McNeill, H. Ade, *Adv. Energy Mater.* **2013**, *3*, 65.
- [117] J. Kudrjasova, J. Kesters, P. Verstappen, J. Brebels, T. Vangerven, I. Cardinaletti, J. Drijkoningen, H. Penxten, J. Manca, L. Lutsen, D. Vanderzande, W. Maes, *J. Mater. Chem. A* **2016**, *4*, 791.
- [118] J. Min, O. K. Kwon, C. Cui, J.-H. Park, Y. Wu, S. Y. Park, Y. Li, C. J. Brabec, *J. Mater. Chem. A* **2016**, *4*, 14234.
- [119] Y. Sun, G. C. Welch, W. L. Leong, C. J. Takacs, G. C. Bazan, A. J. Heeger, *Nat. Mater.* **2012**, *11*, 44.
- [120] T. S. van der Poll, J. a Love, T.-Q. Nguyen, G. C. Bazan, *Adv. Mater.* **2012**, *24*, 3646.
- [121] J. a Love, I. Nagao, Y. Huang, M. Kuik, V. Gupta, C. J. Takacs, J. E. Coughlin, L. Qi, T. S. van der Poll, E. J. Kramer, A. J. Heeger, T.-Q. Nguyen, G. C. Bazan, *J. Am. Chem. Soc.* **2014**, *136*, 3597.
- [122] K. Gao, J. Miao, L. Xiao, W. Deng, Y. Kan, T. Liang, C. Wang, F. Huang, J. Peng, Y. Cao, F. Liu, T. P. Russell, H. Wu, X. Peng, *Adv. Mater.* **2016**, *28*, 4727.
- [123] H. Wang, F. Liu, L. Bu, J. Gao, C. Wang, W. Wei, T. P. Russell, *Adv. Mater.* **2013**, *25*, 6519.
- [124] B. Schmidt-Hansberg, M. F. G. Klein, K. Peters, F. Buss, J. Pfeifer, S. Walheim, a. Colsmann, U. Lemmer, P. Scharfer, W. Schabel, *J. Appl. Phys.* **2009**, *106*, 124501.
- [125] S. Ebbens, R. Hodgkinson, A. J. Parnell, A. Dunbar, S. J. Martin, P. D. Topham, N. Clarke, J. R. Howse, *ACS Nano* **2011**, *5*, 5124.
- [126] P. Mokarian-Tabari, M. Geoghegan, J. R. Howse, S. Y. Heriot, R. L. Thompson, R. a L. Jones, *Eur. Phys. J. E. Soft Matter* **2010**, *33*, 283.
- [127] T. Wang, A. D. F. Dunbar, P. A. Staniec, A. J. Pearson, P. E. Hopkinson, J. E. MacDonald, S.

- Lilliu, C. Pizzey, N. J. Terrill, A. M. Donald, A. J. Ryan, R. A. L. Jones, D. G. Lidzey, *Soft Matter* **2010**, *6*, 4128.
- [128] W. Kim, J. K. Kim, E. Kim, T. K. Ahn, D. H. Wang, J. H. Park, *J. Phys. Chem. C* **2015**, *119*, 5954.
- [129] M. Campoy-Quiles, M. I. Alonso, D. D. C. Bradley, L. J. Richter, *Adv. Funct. Mater.* **2014**, *24*, 2116.
- [130] A. Ashraf, D. M. N. M. Dissanayake, D. S. Germack, C. Weiland, M. D. Eisaman, *ACS Nano* **2014**, *8*, 323.
- [131] S. T. Turner, P. Pingel, R. Steyrlleuthner, E. J. W. Crossland, S. Ludwigs, D. Neher, *Adv. Funct. Mater.* **2011**, *21*, 4640.
- [132] J. L. Hernandez, E. Reichmanis, J. R. Reynolds, *Org. Electron.* **2015**, *25*, 57.
- [133] J. Peet, N. S. Cho, S. K. Lee, G. C. Bazan, *Macromolecules* **2008**, *41*, 8655.
- [134] S. Miller, G. Fanchini, Y. Lin, C. Li, C. Chen, W. Su, *J. Mater. Chem.* **2008**, *18*, 306.
- [135] P. Müller-Buschbaum, *Adv. Mater.* **2014**, *26*, 7692.
- [136] A. Hexemer, P. Müller-Buschbaum, *IUCrJ* **2015**, *2*, 106.
- [137] L. J. Richter, D. M. DeLongchamp, F. A. Bokel, S. Engmann, K. W. Chou, A. Amassian, E. Schaible, A. Hexemer, *Adv. Energy Mater.* **2015**, *5*, 1.
- [138] J. L. Baker, L. H. Jimison, S. Mannsfeld, S. Volkman, S. Yin, V. Subramanian, A. Salleo, A. P. Alivisatos, M. F. Toney, *Langmuir* **2010**, *26*, 9146.
- [139] S. Pröllner, F. Liu, C. Zhu, C. Wang, T. P. Russell, A. Hexemer, P. Müller-Buschbaum, E. M. Herzig, *Adv. Energy Mater.* **2016**, *6*, 1.
- [140] J. Rivnay, a Salleo, S. Mannsfeld, C. Miller, M. Toney, *Chem. Rev.* **2012**, *112*, 5488.
- [141] J. T. Rogers, K. Schmidt, M. F. Toney, G. C. Bazan, E. J. Kramer, *J. Am. Chem. Soc.* **2012**,



134, 2884.

- [142] Y. Gu, C. Wang, T. P. Russell, *Adv. Energy Mater.* **2012**, *2*, 683.
- [143] F. Liu, Y. Gu, C. Wang, W. Zhao, D. Chen, A. L. Briseno, T. P. Russell, *Adv. Mater.* **2012**, *24*, 3947.
- [144] M. Losurdo, M. Bergmair, G. Bruno, D. Cattelan, C. Cobet, A. De Martino, K. Fleischer, Z. Dohcevic-Mitrovic, N. Esser, M. Galliet, R. Gajic, D. Hemzal, K. Hingerl, J. Humlicek, R. Ossikovski, Z. V. Popovic, O. Saxl, *J. Nanoparticle Res.* **2009**, *11*, 1521.
- [145] D. M. Smilgies, *J. Appl. Crystallogr.* **2009**, *42*, 1030.
- [146] N. J. Jeon, J. H. Noh, W. S. Yang, Y. C. Kim, S. Ryu, J. Seo, S. Il Seok, *Nature* **2015**, *517*, 476.
- [147] Z. Li, H. C. Wong, Z. Huang, H. Zhong, C. H. Tan, W. C. Tsoi, J. S. Kim, J. R. Durrant, J. T. Cabral, *Nat. Commun.* **2013**, *4*, 2227.
- [148] H. Zhao, X. Guo, S. He, X. Zeng, X. Zhou, C. Zhang, J. Hu, X. Wu, Z. Xing, L. Chu, Y. He, Q. Chen, *Nat. Commun.* **2014**, *5*, 3108.
- [149] X. Guo, N. Zhou, S. J. Lou, J. Smith, D. B. Tice, J. W. Hennek, R. P. Ortiz, J. T. L. Navarrete, S. Li, J. Strzalka, L. X. Chen, R. P. H. Chang, A. Facchetti, T. J. Marks, *Nat. Photonics* **2013**, *7*, 825.
- [150] V. Mathot, M. Pyda, T. Pijpers, G. Vanden Poel, E. van de Kerkhof, S. van Herwaarden, F. van Herwaarden, A. Leenaers, *Thermochim. Acta* **2011**, *522*, 36.
- [151] J. Orava, a. L. Greer, B. Gholipour, D. W. Hewak, C. E. Smith, *Nat. Mater.* **2012**, *11*, 279.
- [152] M. Chen, M. Du, J. Jiang, D. Li, W. Jiang, E. Zhuravlev, D. Zhou, C. Schick, G. Xue, *Thermochim. Acta* **2011**, *526*, 58.
- [153] D. Mileva, R. Androsch, *Colloid Polym. Sci.* **2012**, *290*, 465.
- [154] N. Bosq, E. Zhuravlev, N. Sbirrazzuoli, *J. Phys. Chem. B* **2013**, *117*, 3407.

- [155] I. Stolte, R. Androsch, M. L. Di Lorenzo, C. Schick, *J. Phys. Chem. B* **2013**, *117*, 15196.
- [156] A. Mollova, R. Androsch, D. Mileva, C. Schick, A. Benhamida, *Macromolecules* **2013**, *46*, 828.
- [157] K. Vandewal, A. Gadisa, W. D. Oosterbaan, S. Bertho, F. Banishoeib, I. Van Severen, L. Lutsen, T. J. Cleij, D. Vanderzande, J. V. Manca, *Adv. Funct. Mater.* **2008**, *18*, 2064.
- [158] G. Juška, N. Nekrašas, K. Genevičius, *J. Non. Cryst. Solids* **2012**, *358*, 748.
- [159] A. Armin, G. Juska, M. Ullah, M. Velusamy, P. L. Burn, P. Meredith, A. Pivrikas, *Adv. Energy Mater.* **2014**, *4*, 1.
- [160] M. Abdelsamie, K. Zhao, M. R. Niazi, K. W. Chou, A. Amassian, *J. Mater. Chem. C* **2014**, *2*, 3373.
- [161] G. Janssen, A. Aguirre, E. Goovaerts, P. Vanlaeke, J. Poortmans, J. Manca, *Eur. Phys. J. Appl. Phys.* **2007**, *37*, 287.
- [162] F. C. Spano, *Chem. Phys.* **2006**, *325*, 22.
- [163] J. Clark, J.-F. Chang, F. C. Spano, R. H. Friend, C. Silva, *Appl. Phys. Lett.* **2009**, *94*, 163306.
- [164] S. T. Turner, P. Pingel, R. Steyrlleuthner, E. J. W. Crossland, S. Ludwigs, D. Neher, *Adv. Funct. Mater.* **2011**, *21*, 4640.
- [165] K. Zhao, H. U. Khan, R. Li, Y. Su, A. Amassian, *Adv. Funct. Mater.* **2013**, *23*, 6024.
- [166] J. Gierschner, Y.-S. Huang, B. Van Averbeke, J. Cornil, R. H. Friend, D. Beljonne, *J. Chem. Phys.* **2009**, *130*, 44105.
- [167] P. Pingel, A. Zen, R. D. Abellón, F. C. Grozema, L. D. A. Siebbeles, D. Neher, *Adv. Funct. Mater.* **2010**, *20*, 2286.
- [168] M. J. McIntire, E. S. Manas, F. C. Spano, *J. Chem. Phys.* **1997**, *107*, 8152.
- [169] E. S. Manas, F. C. Spano, *J. Chem. Phys.* **1998**, *109*, 8087.

- [170] D. Beljonne, J. Cornil, R. Silbey, P. Millié, J. L. Brédas, *J. Chem. Phys.* **2000**, *112*, 4749.
- [171] M. Abdelsamie, N. D. Treat, K. Zhao, C. McDowell, M. A. Burgers, R. Li, D.-M. Smilgies, N. Stingelin, G. C. Bazan, A. Amassian, *Adv. Mater.* **2015**, *27*, 7285.
- [172] X. Liu, Y. Sun, L. a Perez, W. Wen, M. F. Toney, A. J. Heeger, G. C. Bazan, *J. Am. Chem. Soc.* **2012**, *134*, 20609.
- [173] A. Sharenko, M. Kuik, M. F. Toney, T.-Q. Nguyen, *Adv. Funct. Mater.* **2014**, *24*, 3554.
- [174] L. a Perez, K. W. Chou, J. a Love, T. S. van der Poll, D.-M. Smilgies, T.-Q. Nguyen, E. J. Kramer, A. Amassian, G. C. Bazan, *Adv. Mater.* **2013**, *25*, 6380.
- [175] V. Gupta, A. K. K. Kyaw, D. H. Wang, S. Chand, G. C. Bazan, A. J. Heeger, *Sci. Rep.* **2013**, *3*, 1965.
- [176] V. Mathot, M. Pyda, T. Pijpers, G. Vanden Poel, E. van de Kerkhof, S. van Herwaarden, F. van Herwaarden, A. Leenaers, *Thermochim. Acta* **2011**, *522*, 36.
- [177] J. a. Love, C. M. Proctor, J. Liu, C. J. Takacs, A. Sharenko, T. S. van der Poll, A. J. Heeger, G. C. Bazan, T.-Q. Nguyen, *Adv. Funct. Mater.* **2013**, *23*, 5019.
- [178] Y. Huang, X. Liu, C. Wang, J. T. Rogers, G. M. Su, M. L. Chabiny, E. J. Kramer, G. C. Bazan, *Adv. Energy Mater.* **2014**, *4*, 1301886.
- [179] Y. Huang, X. Liu, C. Wang, J. T. Rogers, G. M. Su, M. L. Chabiny, E. J. Kramer, G. C. Bazan, *Adv. Energy Mater.* **2014**, *4*, 1.
- [180] K. Vandewal, K. Tvingstedt, A. Gadisa, O. Inganäs, J. V. Manca, *Phys. Rev. B - Condens. Matter Mater. Phys.* **2010**, *81*, 1.
- [181] K. Vandewal, K. Tvingstedt, A. Gadisa, O. Inganäs, J. V Manca, *Nat. Mater.* **2009**, *8*, 904.
- [182] K. Vandewal, S. Albrecht, E. T. Hoke, K. R. Graham, J. Widmer, J. D. Douglas, M. Schubert, W. R. Mateker, J. T. Bloking, G. F. Burkhard, A. Sellinger, J. M. Frechet, A. Amassian, M. K. Riede, M. D. McGehee, D. Neher, A. Salleo, *Nat Mater* **2014**, *13*, 63.

- [183] C. Deibe, T. Strobe, V. Dyakonov, *Adv. Mater.* **2010**, *22*, 4097.
- [184] K. R. Graham, P. Erwin, D. Nordlund, K. Vandewal, R. Li, G. O. Ngongang Ndjawa, E. T. Hoke, A. Salleo, M. E. Thompson, M. D. McGehee, A. Amassian, *Adv. Mater.* **2013**, *25*, 6076.
- [185] C. M. Proctor, S. Albrecht, M. Kuik, D. Neher, T.-Q. Nguyen, *Adv. Energy Mater.* **2014**, *4*, 1400230.
- [186] S. Mukherjee, C. M. Proctor, J. R. Tumbleston, G. C. Bazan, T.-Q. Nguyen, H. Ade, *Adv. Mater.* **2015**, *27*, 1105.
- [187] S. Gélinas, T. S. Van Der Poll, G. C. Bazan, R. H. Friend, *Science*. **2014**, *343*, 512.
- [188] A. K. Ko Kyaw, D. Gehrig, J. Zhang, Y. Huang, G. C. Bazan, F. Laquai, T.-Q. Nguyen, *J. Mater. Chem. A* **2015**, *3*, 1530.
- [189] J. Clark, C. Silva, R. H. Friend, F. C. Spano, *Phys. Rev. Lett.* **2007**, *206406*, 1.
- [190] W. Ni, M. Li, F. Liu, X. Wan, H. Feng, B. Kan, Q. Zhang, H. Zhang, Y. Chen, *Chem. Mater.* **2015**, *27*, 6077.
- [191] J. Zhao, B. Xia, K. Lu, D. Deng, L. Yuan, J. Zhang, L. Zhu, X. Zhu, H. Li, Z. Wei, *RSC Adv.* **2016**, *6*, 60595.
- [192] F. Buss, B. Schmidt-hansberg, M. Sanyal, C. Munuera, P. Scharfer, W. Schabel, E. Barrena, *Macromolecules* **2007**, *49*, 4867.
- [193] S. Engmann, F. a. Bokel, A. a. Herzing, H. W. Ro, C. Girotto, B. Caputo, C. V. Hoven, E. Schaible, A. Hexemer, D. M. DeLongchamp, L. J. Richter, *J. Mater. Chem. A* **2015**, *3*, 8764.
- [194] S. Mukherjee, C. M. Proctor, J. R. Tumbleston, G. C. Bazan, T. Q. Nguyen, H. Ade, *Adv. Mater.* **2015**, *27*, 1105.
- [195] C. Cabanetos, A. El Labban, J. A. Bartelt, J. D. Douglas, W. R. Mateker, J. M. J. Fréchet, M. D. McGehee, P. M. Beaujuge, *J. Am. Chem. Soc.* **2013**, *135*, 4656.

- [196] H. W. Ro, J. M. Downing, S. Engmann, A. A. Herzing, D. M. DeLongchamp, L. J. Richter, S. Mukherjee, H. Ade, M. Abdelsamie, L. K. Jagadamma, A. Amassian, Y. Liu, H. Yan, *Energy Environ. Sci.* **2016**, *9*, 2835.
- [197] K. Zhao, H. Hu, E. Spada, L. K. Jagadamma, B. Yan, M. Abdelsamie, Y. Yang, L. Yu, R. Munir, R. Li, G. O. N. Ndjawa, A. Amassian, *J. Mater. Chem. A* **2016**, 16036.
- [198] Y. J. Kim, S. Ahn, D. H. Wang, C. E. Park, *Sci. Rep.* **2015**, *5*, 18024.
- [199] C. J. Schaffer, J. Schlipf, E. Dwi Indari, B. Su, S. Bernstorff, P. Müller-Buschbaum, *ACS Appl. Mater. Interfaces* **2015**, *7*, 21347.
- [200] N. Sahu, B. Parija, S. Panigrahi, *Indian J. Phys.* **2009**, *83*, 493.

## Papers Published, Submitted and Under Preparation

### Refereed Publications:

- [1] **M. Abdelsamie**, N. D. Treat, K. Zhao, C. McDowell, M. A. Burgers, R. Li, D-M. Smilgies, N. Stingelin, G. C. Bazan, A. Amassian "Toward Additive-Free Small-Molecule Organic Solar Cells: Roles of the Donor Crystallization Pathway and Dynamics", *Adv. Mater.* **2015**, 27, 7285–92.
- [2] **M. Abdelsamie**, K. Zhao, M. R. Niazi, K. W. Chou, A. Amassian, "In situ UV-visible Absorption during Spin-coating of Organic Semiconductors: a New Probe for Organic Electronics and Photovoltaics", *J. Mater. Chem. C.* **2014**, 2, 3373.
- [3] C. McDowell, **M. Abdelsamie**, K. Zhao, D.-M. Smilgies, G. C. Bazan, A. Amassian, "Synergistic Impact of Solvent and Polymer Additives on the Film Formation of Small Molecule Blend Films for Bulk Heterojunction Solar Cells", *Adv. Energy. Mater.* **2015**, 5, 18.
- [4] L. K. Jagadamma, **M. Abdelsamie**, A. El Labban, E. Aresu, G. O. Ngongang Ndjawa, D. H. Anjum, D. Cha, P. M. Beaujuge, A. Amassian, "Efficient Inverted Bulk-Heterojunction Solar Cells from Low-Temperature Processing of Amorphous ZnO Buffer Layers", *J. Mater. Chem. A.* **2014**, 2, 13321.
- [5] A. R. Kirmani, G. H. Carey, **M. Abdelsamie**, B. Yan, D. Cha, L. R. Rollny, X. Cui, E. H. Sargent, A. Amassian, "Effect of Solvent Environment on Colloidal Quantum Dot Solar Cell Manufacturability and Performance", *Adv. Mater.* **2014**, 26, 4717.
- [6] M. R. Niazi, R. Li, **M. Abdelsamie**, K. Zhao, D. H. Anjum, M. M. Payne, J. E. Anthony, D-M. Smilgies, A. Amassian, "Contact-Induced Nucleation in High-Performance Bottom-Contact Organic Thin Film Transistors Manufactured by Large-Area Compatible Solution Processing", *Adv. Funct. Mater.* **2016**, 26, 2371.

- [7] M. R. Niazi, R. Li, E. Q. Li, A. R. Kirmani, **M. Abdelsamie**, Q. Wang, W. Pan, M. M. Payne, J. E. Anthony, D-M. Smilgies, S. T. Thoroddsen, E. P. Giannelis, A. Amassian, "Solution-Printed Organic Semiconductor Blends Exhibiting Enhanced Transport Properties on par with Single Crystals", *Nat. Commun.* **2015**, 6, 8598.
- [8] J. A. N. Malik, N. D. Treat, **M. Abdelsamie**, L. Yu, R. Li, A. Amassian, C. J. Hawker, M. L. Chabiny, N. Stingelin, "Controlling the Solidification of Organic Photovoltaic Blends with Nucleating Agents", *Org. Photonics Photovolt.* **2014**, 2, 59.
- [9] K. Zhao, G. O. N. Ndjawa, L. K. Jagadamma, A. El Labban, H. Hu, Q. Wang, R. Li, **M. Abdelsamie**, P. M. Beaujuge, A. Amassian, "Highly Efficient Organic Solar Cells Based on a Robust Room-Temperature Solution-Processed Copper Iodide Hole Transporter", *Nano Energy.* **2015**, 16, 458.
- [10] K. Zhao, O. Wodo, D. Ren, H. U. Khan, M. R. Niazi, H. Hu, **M. Abdelsamie**, R. Li, E. Li, L. Yu, B. Yan, M. M. Payne, J. Smith, J. E. Anthony, T. D. Anthopoulos, S. T. Thoroddsen, B. Ganapathysubramanian, A. Amassian "Vertical Phase Separation in Small Molecule:Polymer Blend Organic Thin Film Transistors Can Be Dynamically Controlled", *Adv. Funct. Mater.* **2016**, 26, 1737.
- [11] H. W. Roab, J. M. Downing, S. Engmann, A. A. Herzinger, D. M. DeLongchamp, L. J. Richter, S. Mukherjee, H. Ade, **M. Abdelsamie**, L. K. Jagadamma, A. Amassian, Y. Liue and H. Yan, "Morphology changes upon scaling a high-efficiency, solution-processed solar cell", *Energy Environ. Sci.* **2016**, DOI: 10.1039/C6EE01623E.
- [12] K. Wang, R. Liang, J. Wolf, Q. Saleem, M. Babics, P. Wucher, **M. Abdelsamie**, A. Amassian, M. R. Hansen, P. M Beaujuge, "Donor and Acceptor Unit Sequences Influence Material Performance in Benzo [1, 2-b: 4, 5-b'] dithiophene-6, 7-Difluoroquinoxaline Small Molecule Donors for BHJ Solar Cells", *Adv. Funct. Mater.* **2016**, DOI: 10.1002/adfm.201602162.

- [13] K. Zhao, H. Hu, E. Spada, L.K. Jagadamma, B. Yan, **M. Abdelsamie**, Y. Yang, L. Yu, R. Munir, R. Li, G.O. Ngongang Ndjawa, A. Amassian, "Highly efficient polymer solar cells with printed photoactive layer: rational process transfer from spin-coating", *J. Mater. Chem. A* **2016**, DOI: 10.1039/C6TA06258J.
- [14] D. Baran, R. S. Ashraf, D. A. Hanifi, **M. Abdelsamie**, N. Gasparini, J. Nelson, C. J. Brabec, A. Amassian, A. Salleo, T. Kirchartz, J. R. Durrant and I. McCulloch, "Reducing the Efficiency-Stability-Cost Gap of Organic Photovoltaics with Highly Efficient and Stable P3HT:small molecule Acceptor Ternary Solar Cells", *Nat. Mater.* **2016**, DOI: 10.1038/nmat4797.
- [15] R. Munir, A. D. Sheikh, **M. Abdelsamie**, H. Hu, L. Yu, K. Zhao, T. Kim, O. El Tall, R. Li, D-M. Smilgies, A. Amassian, "Towards Reproducible Hybrid Perovskite Thin Films: Role of the Precursor Solvate", *Adv. Mater.* **2016**, DOI: 10.1002/adma.201604113.
- [16] D. Baran, T. Kirchartz, S. Wheeler, S. Dimitrov, **M. Abdelsamie**, J. Gorman, R. S. Ashraf, S. Holliday, A. Wadsworth, N. Gasparini, P. Kaienburg, H. Yan, A. Amassian, C. Brabec, J. Durrant, I. McCulloch, "Reduced voltage losses yield 10% and >1V fullerene free organic solar cells", *Energy Environ. Sci.* **2016**, DOI: 10.1039/C6EE02598F.

**Patents:**

- [1] **M. Abdelsamie** and A. Amassian, "A Thin-Film Coating Apparatus and Methods of Forming a Thin-Film Coating", Patent filed on 16<sup>th</sup> Nov 2016. **USPTO, No. 62/422,831.**

**Publications in preparation:**

- [1] **M. Abdelsamie**, K. Zhao, G. O. N. Ndjawa, G. C. Bazan and A. Amassian, "Small-molecule Bulk Heterojunction Solar Cells: Roles of Selective Solubility & Mesophase Formation", *Chem. Mater.* (Under review).



- [2] **M. Abdelsamie**, A. El Labban, R. Munir, Z. Kan, S. Dey, D. Anjum, D-M. Smilgies, P. M. Beaujuge and A. Amassian, "Polymer-fullerene bulk heterojunction solar cells: Role of solvent additives in fullerene aggregation", (In preparation).
- [3] **M. Abdelsamie**, M.R. Niazi, D. Anjum, D-M. Smilgies, G. C. Bazan and A. Amassian, "Towards Highly Efficient Small-Molecule Organic Solar Cells: from *in-situ* Investigation to Scalable Processing", (In preparation).

#### **Conferences:**

- [1] **M. Abdelsamie**, N. D. Treat, K. Zhao, C. McDowell, N. Stingelin, G. C. Bazan, A. Amassian, **2015 MRS Fall Meeting & Exhibit**, Symposium Z: Molecularly Ordered Organic and Polymer Semiconductors-Fundamentals and Devices, *Boston, Massachusetts*, USA.
- [2] **M. Abdelsamie**, N. D. Treat, N. Stingelin, G. C. Bazan, A. Amassian, **Solar Future 2015 Symposium**, *KAUST*, Thuwal, Saudi Arabia.
- [3] **M. Abdelsamie**, A. Mansour, K. Zhao, B. Yan, T. McCarthy-Ward, M. Heeney, A. Amassian, **2013 Advanced light source user meeting**, *Lawrence Berkeley National Laboratory*, California, USA.
- [4] **M. Abdelsamie**, A. Mansour, B. Yan, A. Amassian, **SPIE Optics and Photonics symposium (2013)**, *San Diego*, California, USA, Paper No: 8811-43.
- [5] **M. Abdelsamie**, K. Zhao, M. R. Niazi, A. Amassian, **International Colloquium on Flexible Electronics and Photovoltaics [ICFE-PV] (2013)**, *KAUST*, Thuwal, Saudi Arabia.